FATIGUE GROWTH ANALYSES OF A PART-THROUGH CRACK IN A SOLID BAR UNDER COMBINED CYCLIC TENSION-TORSION LOADING

DEVI CHANDRA

FACULTY OF ENGINEERING
UNIVERSITY OF MALAYA
KUALA LUMPUR

2016

FATIGUE GROWTH ANALYSES OF A PART-THROUGH CRACK IN A SOLID BAR UNDER COMBINED CYCLIC TENSION-TORSION LOADING

DEVI CHANDRA

THESIS SUBMITTED IN FULFILMENT
OF THE REQUIREMENTS FOR THE DEGREE OF
DOCTOR OF PHYLOSOPHY

FACULTY OF ENGINEERING
UNIVERSITY OF MALAYA
KUALA LUMPUR

2016

UNIVERSITY OF MALAYA
ORIGINAL LITERARY WORK DECLARATION

Name of Candidate: **DEVI CHANDRA**

Registration/Matric No: **KHA100074**

Name of Degree: **DOCTOR OF PHYLOSOPHY**

Title of Thesis:

FATIGUE GROWTH ANALYSES OF A PART-THROUGH CRACK IN A SOLID BAR UNDER COMBINED CYCLIC TENSION-TORSION LOADING

Field of Study: **PRODUCT DESIGN AND DEVELOPMENT**

I do solemnly and sincerely declare that:

(1) I am the sole author/writer of this Work;
(2) This Work is original;
(3) Any use of any work in which copyright exists was done by way of fair dealing and for permitted purposes and any excerpt or extract from, or reference to or reproduction of any copyright work has been disclosed expressly and sufficiently and the title of the Work and its authorship have been acknowledged in this Work;
(4) I do not have any actual knowledge nor ought I reasonably to know that the making of this work constitutes an infringement of any copyright work;
(5) I hereby assign all and every rights in the copyright to this Work to the University of Malaya ("UM"), who henceforth shall be owner of the copyright in this Work and that any reproduction or use in any form or by any means whatsoever is prohibited without the written consent of UM having been first had and obtained;
(6) I am fully aware that if in the course of making this Work I have infringed any copyright whether intentionally or otherwise, I may be subject to legal action or any other action as may be determined by UM.

Candidate's Signature Date:

Subscribed and solemnly declared before,

Witness's Signature Date:

Name:

Designation:

ABSTRACT

This thesis presents evaluations of the stress intensity factors (SIFs) and the fatigue crack growths of a surface/corner crack in solid bar under combined cyclic tension-torsion loading. A surface crack in solid cylinder and a corner crack in square prismatic bar are considered. The numerical modelling was carried out using a Dual Boundary Element Method (DBEM) based software and an axial-torsion fatigue testing machine was utilized to perform the experimental works. In doing the numerical works, the J-integral technique was chosen to evaluate the stress intensity factors and the NASGRO crack growth rate equation was used to simulate the fatigue crack growths. As preliminary numerical works, fatigue crack growths of a surface crack in a notched cylinder under cyclic tension were evaluated. Crack shape evolutions for different crack aspect ratios and the corresponding stress intensity factors were correlated to study the behaviour of the crack growths. The cylinder that contains a defect which has a smaller crack aspect ratio in a notched cylinder shall be given more careful attentions. Next, the numerical works were further carried out to evaluate the stress intensity factors and fatigue crack growths of a corner crack in a square prismatic bar under combined cyclic torsion-tension loads. In this particular case, the cylinder part was needed to model the torsional loading to be transferred to the square bar. The SIFs at the initial condition and the fatigue crack growths for different loading ratios of tension stress to torsional stress are presented. For a given tension loading, the larger Mode III SIFs and the shorter fatigue life were found at the model with the crack aspect ratio $a/c \neq 1$ and having a larger torsional loading. With a consideration of a practical interest, surface crack growths in a solid cylinder under combined cyclic tension-torsion loading were particularly evaluated through experimentation and numerical modeling. The aluminium alloy 6061-T6 was used for this purpose. A guideline for introducing a semi-elliptical surface crack in a solid cylinder using the die-sinking EDM machine is presented in detail in this thesis.

The numerical simulations and experimental works showed similar crack growth paths. The fatigue lives obtained from the experimentation and numerical simulations were shown to be in good agreements. At the first increment, the torsion loading gave a more dominant effect on the crack extension angle at the crossed surface point than that due to the crack aspect ratio. Meanwhile, the effect of the crack aspect ratio on the crack extension angle was observed to be more dominant at the crack depth point. The combinations of flat and shear lips fracture surfaces, and fluctuating crack growth direction and K_{eff} values at the crossed surface points confirmed the inclined and twisted crack front during stable crack growth. The crack growth direction at the crossed surface points fluctuated significantly during stable crack growth.

ABSTRAK

Tesis ini membentangkan penilaian faktor keamatan tegangan (SIFs) dan pertumbuhan retak lelah daripada sebuah retak permukaan/sudut pada batang pepejal yang mengalami beban gabungan tarik-torsi. Sebuah retak permukaan pada silinder pepejal dan retak sudut pada batang prisma persegi menjadi perhatian. Pemodelan berangka telah dilakukan menggunakan perisian berasaskan Dual Boundary Element Method (DBEM) dan sebuah mesin uji kelelahan beban tarik-torsi telah digunakan untuk melaksanakan kerja-kerja uji kaji. Dalam melakukan kerja-kerja berangka, teknik J-integral telah dipilih untuk menilai faktor keamatan tegangan dan persamaan kadar pertumbuhan retak NASGRO digunakan untuk mensimulasikan pertumbuhan retak lelah. Diperingkat awal kerja-kerja berangka, pertumbuhan sebuah retak permukaan pada silinder bertakuk kerana beban tarik berulang telah dinilai. Perubahan bentuk retak untuk nisbah saiz retak yang berbeza dan faktor keamatan tegangannya telah dikaitkan untuk mengkaji tingkah laku pertumbuhan retak. Silinder bertakuk yang mengandungi retak dengan nisbah saiz retak yang lebih kecil hendaklah diberikan perhatian lebih berhati-hati. Seterusnya, kerja-kerja berangka dilakukan untuk menilai faktor keamatan tegangan dan pertumbuhan retak lelah sebuah retak sudut pada batang prisma persegi yang mengalami gabungan beban tarik-torsi. Dalam kes ini, sebuah silinder diperlukan untuk memodelkan beban torsi untuk dipindahkan ke batang persegi. Faktor keamatan tegangan dan pertumbuhan retak lelah dengan nisbah beban tarik-torsi yang berbeza telah dibentangkan. Untuk sebuah beban tarik yang diberikan, mod III faktor keamatan tegangan yang lebih besar dan umur yang lebih pendek ditemui pada model dengan beban torsi yang lebih besar dan nisbah saiz retak $a/c \neq 1$. Dengan mempertimbangkan kepentingan praktikal, retak permukaan pada silinder pepejal yang mengalami beban gabungan tarik-torsi telah dinilai melalui uji kaji dan pemodelan berangka. Aluminium 6061-T6 telah digunakan untuk tujuan ini. Garis panduan untuk pembuatan retak permukaan berbentuk semi-elips pada

silinder pepejal menggunakan mesin die-sinking EDM dibentangkan secara terperinci dalam thesis ini. Laluan pertumbuhan retak dengan simulasi berangka adalah terlihat sama dengan laluan pertumbuhan retak yang diperolehi dengan kerja-kerja uji kaji. Umur lelah yang diperolehi daripada ujikaji dan simulasi berangka telah dibuktikan ada dalam kesamaan yang baik. Pada tahap pertama simulasi, beban torsi memberi kesan yang lebih dominan kepada sudut pertumbuhan retak di titik perpotongan retak dengan permukaan daripada kerana nisbah saiz retak. Sementara itu, kesan nisbah saiz retak terhadap sudut pertumbuhan retak terlihat lebih dominan pada titik kedalaman retak. Kombinasi permukaan patah yang rata dan berbentuk bibir, arah pertumbuhan retak serta nilai faktor keamatan tegangan efektif yang turun naik pada titik perpotongan crack dengan permukaan mengesahkan terjadinya ujung depan retak yang miring dan berpintal semasa pertumbuhan retak. Arah pertumbuhan retak pada titik perpotongan retak dengan permukaan turun naik dengan ketara selama pertumbuhan retak yang stabil.

ACKNOWLEDGMENTS

All praises to Almighty Allah for granting me immense grace and blessings to complete my study. In this opportunity, I would like to express my biggest gratitude to my supervisors, Assoc. Prof. Dr. Nukman Yusoff and Assoc. Prof. Dr. Judha Purbolaksono for their continuous support and guidance. They have constantly given encouragement and advice throughout the time of my study.

I am also very thankful for the help of all staff in the Department of Mechanical Engineering and of the technical staff in CAD laboratory. I could not complete my study without their help and support. My thanks also go to University Malaya High Impact Research Grant and University of Andalas for their financial support.

Last but not least, I want to thank my parents for their continuous love, pray, and dedications in raising, encouraging, educating and supporting me. My last and most inexpressible gratitude goes to my wife Yulharni Eka Putri and also my beloved kids Rahmat, Salsa, Hadif and Asyfa for their sincere belief, patience, understanding, and moral support in achieving my success, particularly completing my study.

DEVI CHANDRA

February, 2016

TABLE OF CONTENTS

LIST OF FIGURES

LIST OF TABLES

LIST OF SYMBOLS AND ABBREVIATIONS

Symbols

a	:	Crack depth
c	:	Crack length
C	:	Material constant
a/c	:	Crack aspect ratio
d	:	Notch diameter
da	:	Crack extension
da/dN	:	Crack growth rate
D	:	Cylinder diameter
E	:	Modulus of Elastic
G	:	Strain energy release rate
J	:	J-integral
J_I	:	Mode I J-integral
J_{II}	:	Mode II J-integral
J_{III}	:	Mode III J-integral
K	:	Stress intensity factor
K_I	:	Mode I stress intensity factor
K_{II}	:	Mode II stress intensity factor
K_{III}	:	Mode III stress intensity factor
K_{eff}	:	Effective stress intensity factor
K_c	:	Plane stress fracture toughness
K_{IC}	:	Plane strain fracture toughness
K_{max}	:	Maximum stress intensity factor
K_{min}	:	Minimum stress intensity factor

ΔK	:	Range stress intensity factor
ΔK_{th}	:	Range threshold stress intensity factor
L	:	Length
m	:	Paris exponent
N	:	Number of cycle
n	:	Nasgro constant
p	:	Nasgro constant
q	:	Nasgro constant
R	:	Stress ratio
r_y	:	Plastic zone radius
S	:	Applied stress
S	:	Strain energy density factor
S	:	Boundary surface
T	:	Traction
U	:	Crack closure
u	:	Displacement in x direction
v	:	Displacement in y direction
W	:	Strain energy density
Y	:	Geometric correction factor
α	:	Plane stress/strain constraint factor
ε	:	Normal strain
σ	:	Tension stress
σ_{ij}	:	Stress field around crack tip
σ_{ys}	:	Yield stress
τ	:	Shear stress
υ	:	Poisson's ratio

ω	:	Plastic zone width
θ	:	Crack direction angle
Γ	:	Integration path
δ	:	Crack tip opening displacement
λ	:	Biaxiality ratio
γ	:	Surface energy density
μ	:	Shear modulus of elastic
σ_f	:	Fracture strength
$\Delta\sigma$	:	Range cyclic stress

Abbreviations

BEM	:	Boundary element method
CAD	:	Computer aided design
COD	:	Crack opening displacement
CT	:	Compact tension
CTOD	:	Crack tip opening displacement
CTD	:	Crack tip displacement
CTS	:	Compact tension shear
DBEM	:	Dual boundary element method
DBIE	:	Dual boundary integral equation
DDM	:	Displacement discontinuous method
EDM	:	Electric discharge machining
EPFM	:	Elastic plastic fracture mechanic
FCG	:	Fatigue crack growth
FDM	:	Finite different method
FE	:	Finite element

FEA	:	Finite element analysis
FEM	:	Finite element method
FVM	:	Finite volume method
HCE	:	Hybrid crack element
LEFM	:	Linear elastic fracture mechanic
MTS	:	Maximum tangential stress
MSED	:	Minimum strain energy density
MERR	:	Maximum energy release rate
MPERR	:	Maximum potential energy release rate
MVCCI	:	Modified virtual crack closure integral
SIF	:	Stress intensity factor
SERR	:	Strain energy release rate
VCCI	:	Virtual crack closure integral
VCE	:	Virtual crack extension
XFEM	:	Extended finite element method

CHAPTER 1

INTRODUCTION

1.1 Introduction

Solid cylinder and square prismatic bars are widely used in engineering components and structures. Surface defects are frequently initiated in the components due to cyclic applied loads, manufacturing imperfections, metallurgical flaws or service handling. During service loading, the cracks may grow into a critical stage and eventually causes an undesirable fracture failure which has consequences to lives, injuries and financial losses. To ensure the safety of the engineering component to be fit in service, scheduled inspections shall be performed. In doing so, accurate calculation of the stress intensity factors (SIFs) and understanding of the fatigue crack behavior are required. Linear elastic fracture mechanics (LEFM) approach has been widely used in analyzing the fatigue crack behavior where the elastic stress-strain fields in the vicinity of crack tip are usually evaluated by calculating the SIFs.

The SIF solutions for a surface crack in a solid cylinder bar have been reported by many researchers. Most of the available solutions are limited to a simple loading case such as under either of tension, bending or torsion (Raju & Newman, 1986; Shih & Chen, 2002; Shin & Cai, 2004; Carpinteri, 1992; Fonte et al., 1999). Under such loading, the fatigue crack growth and crack shape evolution of a surface crack in a smooth round bar have also been reported by Carpinteri (1993), Carpinteri and Brighenti (1996a), Carpinteri and Vantadori (2009), Couroneau and Royer (1998), Couroneau and Royer (2000), Lin and Smith (1997), Lin and Smith (1998), Thompson and Sheppard (1992), Toribio et al. (2009), Toribio et al. (2011) and Toribio et al. (2014). The stress intensity factor solutions and fatigue crack growth of a corner crack

in the non-round bar under pure tension or bending have been reported by Raju and Newman Jr (1988), Forman and Mettu (1990), Naresh et al. (2013).

In practices, engineering components or structures are often subjected to combined loading which in turn causes mixed-mode fractures (Modes I, II and III). In such cases, the calculation of stress intensity factors and the evaluation of fatigue crack growth become more complex. The complexities mainly involves the necessity to evaluate the mixed-mode elastic stress field around the crack tip by their respective SIFs (K_I, K_{II}, K_{III}) that would control the fatigue crack growth, fracture mechanism and crack growth direction. The fatigue crack growth under combined loading may differ significantly from those observed under a pure single mode loading. The other complexity is that the crack propagation under combined loads generally fluctuates in the zigzag form at which the SIFs would be difficult to calculate. Under combined loadings, the crack propagates not in a self similar manner. This would imply that the crack may grow deviated from its original direction and the crack orientation continuously changes along the fatigue loading. It is attributed to the change of the loading mode during the crack propagation. In addition, the direction of the principal stresses around the crack tip/front under combined loading leads to complex stress states. It is therefore essential and necessary to understand the effects of combined loading on fatigue crack growth behavior of the cracked components.

Many researchers have investigated the fatigue crack growths under combined loads around the world. Finite element method has been employed by Carpinteri and Brighenti (1996b) to evaluate the surface crack propagation in round bar subjected to combined axial and bending load. The path of crack propagation does not depend to the loading ratio for any input value of the total combined stress. In a study of a straight-front crack in solid cylinder under cyclic tension and steady torsion loads, Yang et al. (2006) found a significant reduction of the crack growth rate when a steady torsion

was superimposed to cyclic tension. Under combined cyclic bending and steady torsion loads, Fonte et al. (2006) investigated a surface crack growth and its evolution in a solid shaft. Similar to the result found by Yang et al. (2006), they reported that the steady torsion loading superimposed into the cyclic bending load may significantly reduce the crack growth rates. The stress-strain intensity and energy-based approaches has been used by Abreu et al. (2009) to predict the fatigue life of a notched tubular specimen under combined bending-torsion load. To verify the results reported by Fonte et al. (2006), fatigue growth simulation for a surface crack in a solid cylinder subjected to combined cyclic bending and static torsion loads has been conducted by Maligno et al. (2010) using Zencrack FE code. This code is also used to simulate the fatigue growth of an inclined outer surface crack in hollow shafts under combined cyclic torsion and axial loads. Predan et al. (2013) conducted a fatigue experiment on a hollow cylinder subjected to torsion load. They confirmed that K_{II} is found more significant for stable crack-initiation than K_{III}. Recently, Branco et al. (2014) predicted the fatigue life of a laterally-notched round bar under combined bending-torsion loads. The principle stress field criterion was used to predict the crack initiation site, surface crack path and surface crack angle. An assessment of fatigue crack growth rate and fatigue life was conducted by Tanaka (2014) on a circumferential notched round bar of steel subjected combined cyclic torsion and static axial load. Citarella et al. (2014) numerically and experimentally evaluated the crack growth behaviour of a straight front surface crack on steel cylinder bar under tension and combined tension torsion loads.

A few analyses on fatigue crack growth in the non-round components such as prismatic bar under combined loading were found in literature. The strain energy density theory was used to analyze the crack growth of edge cracked beam under Mode I, Mode II and mixed-mode I-II loads (Nobile, 2000). Rozumek and Marciniak (2008) experimentally investigated the fatigue crack growth of rectangular bar under out-of-

phase bending and torsion loadings. Varfolomeev et al. (2014) investigated mixed-mode I-II fatigue crack growth and crack path of modified single edge notch bar under bending.

Although many efforts have been devoted to evaluate the SIFs and fatigue crack behaviour under combined loading, the relevant findings of the crack analyses for the cases under combined loadings are actively sought for updating the knowledge in the areas of fatigue and fracture mechanics. In this study, numerical and experimental studies on the fatigue crack growths of a surface/corner crack in a solid were carried out. The research backgrounds, the methodology and the findings are presented in Chapters 2, 3 and 4, respectively.

1.2 Problem statement

Many failures in the engineering structures due to the fatigue crack have been widely reported in literature (Heyes, 1998; Asi, 2006; Xu et al., 2006; Urquiza et al., 2014; Savkovic et al., 2012; Infante et al., 2014; Barter, 2013; Griza et al., 2013; Liu, 2014; Sujata et al., 2014). Fatigue behaviors of a part-through crack in a solid bar under simple loading have been well analyzed and documented. The Paris law was used extensively in the fatigue crack growth simulations. There is currently insufficient information pertaining to the SIFs and fatigue crack growth behaviours of a part-through crack in a solid bar under combined load. The fatigue crack growths in the components containing a high stress concentration such as V-shaped notched round bar however always attract attentions for further investigations. Only a few studies on the fatigue crack growth in the non-round components such as prismatic bar were reported. It was known that there was an issue in modelling a torsional load in a non-round component. In doing experiments, there is no a detailed guideline for inducing an initial surface or corner crack in a specimen that has been reported in literature.

1.3 Research objectives

Relevant knowledge on the SIFs and fatigue crack growth under combined loadings is actively sought and remains open for updates. Thus, the objectives of this research may be stated as follows:

1. To evaluate numerically Mode I SIFs, the fatigue lives and the crack shape evolutions of a semi-elliptical surface crack in V-shaped notched round bar under cyclic tension.
2. To model the torsional loading and evaluate the SIFs and fatigue crack growths in a square prismatic bar under combined tension-torsion loads.
3. To investigate the effect of initial crack size, crack aspect ratio, and tension-torsion load ratio on the SIFs, crack growth direction and fatigue life of a surface crack in a solid cylinder through experimentation and numerical modeling.
4. To develop the preparation procedures of inducing an initial surface crack in a specimen.

1.4 Scope of research

The scope of this research work is within the LEFM concept. A dual boundary element method (DBEM) based software was used for all the numerical modelling. The generalized NASGRO crack propagation law that is widely used in many practical simulations in aerospace industries was chosen for simulating the crack growth rate and the *J*-integral method was used to evaluate the stress intensity factors.

1.5 Significance of outcomes

The findings are expected to give some updates in the areas of fatigue and fracture mechanics and provide some insights to those who are working in the structural integrity analysis and involved in design process of cylindrical and square shape components.

1.6 Thesis organization

This thesis is consist of five chapters which are arranged as follows:

Chapter 1 – Introduction. This chapter presents the brief background and importance of the research, the problem statement, the scope and objective of this research.

Chapter 2 – Literature Review. This chapter presents the basic theory of fracture mechanics, brief theory of FEM and BEM and the relevant previous works of evaluating mixed-mode SIFs and fatigue crack growth done by other researchers.

Chapter 3 – Methodology. This chapter describes the methods used to accomplish the research activities involving the numerical modelling, the experimental setup of fatigue crack and brief fractography technique.

Chapter 4 – Results and Discussions. This chapter presents and discusses the benchmarking of the BEASY results with those available in literature, the numerical results of the SIFs, crack evolution, crack patch and fatigue crack growths, the experimental results of fatigue crack growth and the manufacturing technique to generate an initial surface crack in a specimen.

Chapter 5 – Conclusions and Future Works. This chapter concludes all the findings from this research and presents some recommendations for future works.

CHAPTER 2

LITERATURE REVIEW

2.1 Introduction

Fatigue crack growth (FCG) behaviour is commonly evaluated by using the fracture mechanic approach. Fracture mechanics concept uses stresses and strains as the basis of the analysis and provides a number useful quantitative fracture parameters and criteria to predict whether or not a fracture may occur. The stress intensity factor is a well known and important fracture parameter in the application of Linear Elastic Fracture Mechanic (LEFM) concept to fracture problems where the crack growth and the crack direction models are often described using this factor. The basic concept of these models is necessary to understand in the context of the numerical analysis of mixed-mode FCG. A comprehensive analysis of mixed-mode FCG requires the combinations of robust modelling and computation of the cracked component, experimental work and fracture surface evaluation. The use of efficient and effective numerical methods is required to obtain the accurate fatigue crack evaluations. The BEM has been extensively used as an alternative method to the FEM in the numerical simulation of crack problems.

In this chapter, the general theory of fracture mechanics and mixed-mode FCG are presented. The brief background and application of the fractography technique in crack growth analyses are described. The uses of the analytical and numerical methods in the fracture mechanics are also presented. Next, a number of the published numerical and experimental works in evaluating the SIFs and mixed-mode FCG behaviours are reviewed.

2.2 Fracture Mechanics

Failure modes of most engineering components and structures are the fatigue fracture. Fatigue is defined as a process of the initiation and propagation of a crack under the applied cyclic loads. Fatigue fracture occurs when the crack extension attains the critical crack size at which the residual strength of cracked component is unable to withstand the applied load. It can take place at the stress levels that are less than the monotonic tensile strength of the material (Fischer-Cripps, 2007).

Studies on the fatigue fracture mainly addressed the predictions of the crack growth rate, fatigue life and fracture strength of the cracked components. It can be determined by utilizing either of stress-life, strain-life and fracture mechanics approaches. Fracture mechanics approach uses three important variables, i.e. stress strength of the material and crack size. The fracture toughness governs the criterion of the strength of the material. Fracture mechanics allows the researchers to quantify the critical combinations of applied stress, crack size and material toughness and evaluate the behavior of the cracked structures. The fracture mechanics concept then promoted the establishment of a new design philosophy, i.e. damage tolerance design concept which has been applied in many engineering structures such as aircrafts, ground and rail vehicles, nuclear generators, pressure vessels, bridges, ships, buildings, etc. The accurate predictions of the fatigue crack growth life, critical crack size and inspection intervals are of important objectives of the design concepts.

Historically, the establishment of fracture mechanics is related to some well-known disasters in last several decades such as the fracture of the Liberty Ship during World War II, the Havilland Comet Jet accident in 1954, the failure of the King Bridge in Melbourne in 1962, etc. The investigation agencies have reported that the fatigue crack was the main cause of those disasters. The development of fracture mechanics theory was initiated by Alan Griffith (1920) who proposed the energy balance-based

crack extension theory. He used a thermodynamic approach to analyze the centre cracked glass plate that was also presented in an earlier work by Inglis (1913). Griffith (1920) stated that the failure due to a crack extension would occur if the energy released due to crack extension is greater than the energy needed to create new surface. The fracture strength of a brittle material and its relationship with the crack size described by Griffith theory is given by:

$$\sigma_f = \sqrt{\frac{2E\gamma}{\pi a}} \tag{2.1}$$

Next, Irwin (1948) and Orowan (1949) separately modified the Griffith's fracture strength for an arbitrary crack in ductile materials by considering the dissipation energy due the plastic flow at the vicinity of the crack tip. In the following work, Irwin (1956) introduced a fracture criterion based on the strain energy release rate (SERR). The strain energy release rate *G* that correlates to the stress intensity factor *K* is given as follows:

$$G = \frac{K^2}{E'} \tag{2.2}$$

where $E' = E$ for the plane stress condition and $E' = E/(1-\nu^2)$ for the plane strain condition.

The other important contribution of Irwin's works was the stress analysis of the cracked problem by using the semi-inverse method of Westergaard (Westergaard, 1939). With the aid of this method, Irwin (1957) introduced the stress intensity factor to characterize the elastic stress field around the crack tip. In the early 1960s, the stress intensity factor concept by Irwin (Irwin, 1957) and the crack tip opening displacement (CTOD) concept by Wells (Wells, 1961) have been evolved and accepted as an approaches to solve fracture problems in industries. Paris et al. (1961) applied the SIF to describe the incremental fatigue crack extensions. They proposed the first empirical

equation that relates the rate of the crack growth to the cyclic range of the stress intensity factor under a constant amplitude loading. The equation was then called the Paris law that is written as:

$$\frac{da}{dN} = C\Delta K^m \tag{2.3}$$

where N is the number of cycle, a is the crack size, ΔK is the stress intensity factor range, C and m are materials constants. Paris law has become an important crack growth rate equation and its emergence has been marked as the beginning of the modern fracture mechanics era.

Generally, the fracture mechanics describes the quantitative relations of external stress acting upon a component to local stress and displacement field near the crack front for various crack sizes and geometries. It has been used in predicting the crack propagation rate at which a crack can approach a critical size for the fracture instability. Thus, the fracture mechanics have an important role in the life prediction of the cracked components under cyclic loading. The fracture mechanics is divided into two concepts based on the deformation field around the crack tip: (i) linear elastic fracture mechanics (LEFM) and (ii) elastic plastic fracture mechanics (EPFM). The LEFM concept is highly associated with the fatigue and fracture analyses on the linear elastic material or in a nonlinear condition at which the yielding at the crack tip is very small in comparison to the crack size. Conversely, when the crack tip plasticity is larger, then the EPFM concept is more appropriate approach for the crack analysis.

2.3 Linear Elastic Fracture Mechanics

The energy and stress-displacement approaches are the basic knowledge of the fracture mechanics studies in the context of the LEFM. In the energy approach, the energy release rate parameter is used to characterize the fracture behavior of the cracked component. It is a measure of the energy change and global exercise of the cracked

component during the crack extension. In the stress-displacement approach, the crack behavior is evaluated by measuring the crack tip stress-displacement field, which is characterized by the SIF. Fracture occurs when the stress intensity factor K reaches its critical value which is the fracture toughness K_c of the material. In the following section, some important terms used in the LEFM theory are described.

2.3.1 Stress intensity factors

Stress analysis of two-dimensional crack problem in the linear elasticity material has been done by Irwin (1957). Referring to Figure 2.2, the elastic stress around the crack tip is given as (Irwin, 1957):

$$\boldsymbol{\sigma_{ij}(r,\theta) = \frac{K}{\sqrt{2\pi r}} f_{ij}(\theta) + other\ terms} \qquad \textbf{(2.4)}$$

where σ_{ij} is the stress tensor component, r and θ are the polar coordinate that is originated at the crack tip and $f_{ij}(\theta)$ is trigonometric functions. As the coordinate r approach zero (at the crack tip), the first right term in Eq. 2.4 becomes dominant and the second right terms are constant or tend to zero. Thus, the stress field is dominated by the stress singularity. The parameter of the stress singularity is expressed by the stress intensity factor K. The elastic stress at any point around the crack tip can be determined when the stress intensity factor is known.

Physically, the stress intensity factor is regarded as the intensity of load transmitted through the crack-tip region caused by the introduction of a crack into the component (Tada et al., 2000). The SIFs measure theoretically the severity of the stress around the crack tip caused by the remote loading. During the crack extension, the changes of crack geometry and stresses would be followed by the corresponding instantaneous value of K. Therefore, the range of the applied cyclic stress on the cracked component would reflect the range of K around the crack tip, as given as:

$$\boldsymbol{\Delta K = K_{max} - K_{min} = \Delta\sigma . Y\sqrt{\pi a}} \text{ where } \boldsymbol{\Delta\sigma = \sigma_{max} - \sigma_{min}} \quad \textbf{(2.5)}$$

In general, the stress intensity factor *K* is dependent on the loading type, crack size and shape and component geometry. The general expression of *K* can be written as (Liu, 1998):

$$\boldsymbol{K = YS\sqrt{\pi a}} \quad \textbf{(2.6)}$$

where *a* is the crack size, *S* is the remote stress and *Y* is the dimensionless geometric correction factor. If the geometric correction factor is known, the applied *K* can be computed for any combination of stress and crack size. The applied stress intensity can then be compared to the appropriate material property, which may be fracture toughness K_c.

The SIFs have been shown to be special values for the studies of fatigue cracking. The SIF is a necessary parameter in the evaluations of crack growth rate, crack growth direction, critical crack length and fatigue life. The SIFs solutions for various structural configurations, crack types and loading condition have been presented in many handbooks, literatures and databases. If the SIF solution of a structural geometry is not available due to the complexity of geometry and loading state, the corresponding solution can be obtained through the experimental or numerical approach. The experimental measurement of SIFs is possible due some techniques such as photo-elasticity (Singh & Gope, 2013), caustics method (Mahajan & Ravi-Chandar, 1989), strain gauge (Sarangi et al., 2012), digital image correlation method (Zhang & He, 2012). However, measurements of SIF by experimental methods have been rendered virtually by the advances in the computer technology. Today, nearly all new SIFs solutions are obtained numerically (Anderson, 2005).

2.3.2 Elastic stress field near crack tip

The crack surface displacements due to the remote loading are characterized by the relative movements of the lower and upper crack surfaces. It is categorized into three cracking modes which are associated with a particular crack-tip stress field as illustrated in Figure 2.1. Mode I (opening mode) occurs when the crack surfaces are moving apart in the normal direction to the crack plane. Mode II (sliding mode) takes place when the crack surfaces are sliding each other, perpendicular to the crack edge. Mode III (tearing mode) takes places when the crack surfaces are sliding one and another but parallel to the crack edge. The local mixed-mode loading conditions at cracks tip occur in a combination of the three basic displacement modes.

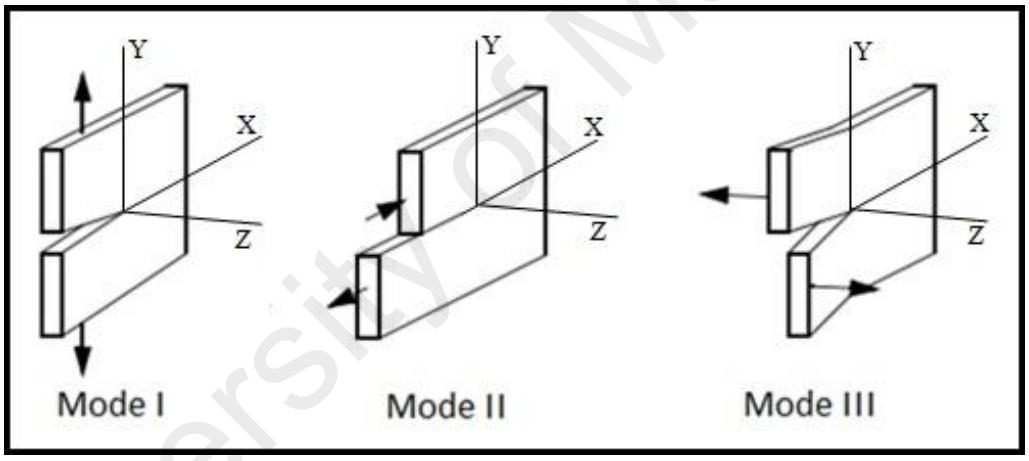

Figure 2.1: Modes of crack tip deformation.

Irwin (1957) determined the stress field around the crack tip associated with each mode of crack deformations as a function of the distance *r* from the crack tip as illustrated in Figure 2.2.

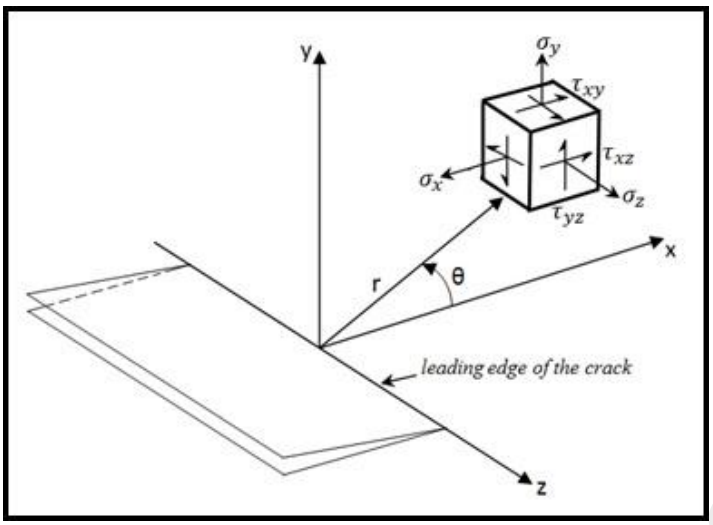

Figure 2.2: Stresses around the crack tip (Cartesian coordinate system).

Referring to the coordinate system shown in Figure 2.2, the stress fields at the vicinity of the crack tip are given by

Mode I :

$$\boldsymbol{\sigma_x = \frac{K_I}{\sqrt{2\pi r}} cos\frac{\theta}{2}\left\{1 - sin\left(\frac{\theta}{2}\right) sin\left(\frac{3\theta}{2}\right)\right\}} \quad \textbf{(2.7)}$$

$$\boldsymbol{\sigma_y = \frac{K_I}{\sqrt{2\pi r}} cos\frac{\theta}{2}\left\{1 + sin\left(\frac{\theta}{2}\right) sin\left(\frac{3\theta}{2}\right)\right\}} \quad \textbf{(2.8)}$$

$$\boldsymbol{\tau_{xy} = \frac{K_I}{\sqrt{2\pi r}} sin\frac{\theta}{2} cos\frac{\theta}{2} cos\frac{3\theta}{2}} \quad \textbf{(2.9)}$$

For plane strain :

$$\boldsymbol{\sigma_z = v(\sigma_x + \sigma_y)} \quad \textbf{(2.10)}$$

$$\boldsymbol{\tau_{xz} = \tau_{yz} = 0} \quad \textbf{(2.11)}$$

For plane stress :

$$\boldsymbol{\sigma_z = \tau_{xz} = \tau_{yz} = 0} \quad \textbf{(2.12)}$$

Mode II :

$$\boldsymbol{\sigma_x = -\frac{K_{II}}{\sqrt{2\pi r}} sin\frac{\theta}{2}\left\{2 + cos\left(\frac{\theta}{2}\right) cos\left(\frac{3\theta}{2}\right)\right\}} \quad \textbf{(2.13)}$$

$$\boldsymbol{\sigma_y = \frac{K_{II}}{\sqrt{2\pi r}} sin\frac{\theta}{2} cos\frac{\theta}{2} cos\frac{3\theta}{2}} \quad \textbf{(2.14)}$$

$$\boldsymbol{\tau_{xy} = \frac{K_{II}}{\sqrt{2\pi r}} cos\frac{\theta}{2}\left\{1 - sin\frac{\theta}{2} sin\frac{3\theta}{2}\right\}} \quad \textbf{(2.15)}$$

For plane strain :

$$\boldsymbol{\sigma_z = v(\sigma_x + \sigma_y)} \quad \textbf{(2.16)}$$

$$\boldsymbol{\tau_{xz} = \tau_{yz} = 0} \quad \textbf{(2.17)}$$

For plane stress :

$$\boldsymbol{\sigma_z = \tau_{xz} = \tau_{yz} = 0} \quad \textbf{(2.18)}$$

Mode III :

$$\boldsymbol{\tau_{xz} = -\frac{K_{III}}{\sqrt{2\pi r}} sin\left(\frac{\theta}{2}\right)} \quad \textbf{(2.19)}$$

$$\boldsymbol{\tau_{yz} = \frac{K_{III}}{\sqrt{2\pi r}} cos\left(\frac{\theta}{2}\right)} \quad \textbf{(2.20)}$$

$$\boldsymbol{\sigma_x = \sigma_y = \sigma_z = \tau_{xy} = 0} \quad \textbf{(2.21)}$$

In Equations (2.7-2.21), K_I, K_{II} *and* K_{III} are the SIFs for Mode I, Mode II and Mode III, respectively. As K_I, K_{II} *and* K_{III} are not the functions of the coordinates of r and θ, they represent the strength of stress fields surrounding the crack tip (Tada et al., 2000).

2.3.3 J-integral and crack tip opening displacement method (CTOD)

Wells (1961) observed that the initial sharp crack blunt with plastic deformation was shown to have a finite displacement δ at the crack tip, called the crack tip opening displacement (CTOD). Wells (1961) also stated that CTOD can be used to characterize the crack tip when the LEFM is no longer valid. He proposed a relationship between CTOD and K or G as:

$$\boldsymbol{\delta = \frac{4K_I^2}{\pi\sigma_{ys}E} = \frac{4G}{\pi\sigma_{ys}}} \quad \textbf{(2.22)}$$

The CTOD method employed the displacement of a point in both crack surfaces for computing the stress intensity factor as illustrated in Figure 2.3 (Carpinteri et al. 2003). Modes I, II and III SIFs at the point P can be formulated as (Carpinteri et al., 2003):

$$K_I^P = \frac{E}{4(1-\nu^2)}\sqrt{\frac{\pi}{2r}}\left(u_b^P|_{S^+} - u_b^P|_{S^-}\right) \quad \textbf{(2.23)}$$

$$K_{II}^P = \frac{E}{4(1-\nu^2)}\sqrt{\frac{\pi}{2r}}\left(u_n^P|_{S^+} - u_n^P|_{S^-}\right) \quad \textbf{(2.24)}$$

$$K_{III}^P = \frac{E}{4(1-\nu^2)}\sqrt{\frac{\pi}{2r}}\left(u_t^P|_{S^+} - u_t^P|_{S^-}\right) \quad \textbf{(2.25)}$$

where u^P is the displacement that evaluated at point *P*. u_b^P, u_n^P and u_t^P are the displacements in the *b*-direction, *n*-direction and *t*-direction respectively as the projections of the displacement u^P to the corresponding crack front coordinate directions (see Figure 2.3). S^+ and S^- denote upper and lower crack surfaces respectively. The values of $K_I^{P\prime}, K_{II}^{P\prime}$ and $K_{III}^{P\prime}$ are the approximated stress intensity factors corresponding to the point P' along the crack front (in the normal direction as illustrated in Figure 2.3).

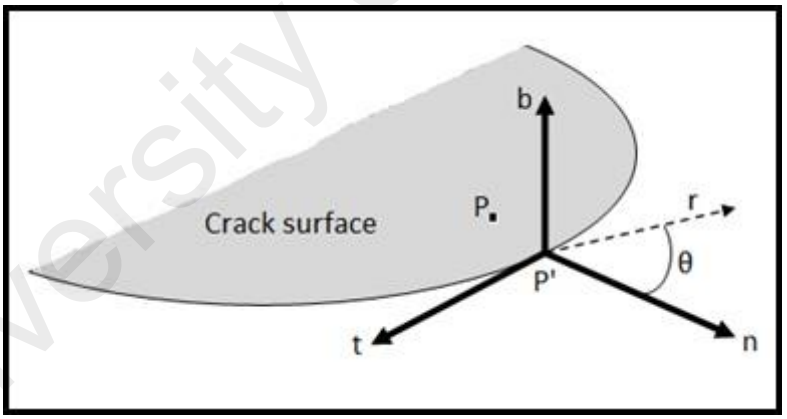

Figure 2.3: Definition of the CTOD method.

The *J*-integral is regarded as the change of potential energy of the component as a result of the crack extension. Its value is about the same wherever the path integral starts and ends on the crack face. It is also not depending on the direction of subsequent crack growth. Rice (1968) defined the general expression of the *J*-integral as

$$J = \int_\Gamma \left(W d_y - \vec{T}.\frac{\partial \vec{u}}{\partial x} ds\right) \quad \textbf{(2.26)}$$

where $\vec{T}$ is the traction vector acting on a segment *ds* of the contour Γ and $\vec{u}$ is a displacement vector (the displacement on an element along the arc *s*) and Γ is any closed contour in the *x*-*y* plane that encircles the crack tip. The closed contour Γ is taken in a counter-clockwise direction starting from one crack face and ending on the opposite face and closing the crack tip (see Figure 2.4). The corresponding strain energy density *W* is expressed by:

$$\boldsymbol{W = \int_0^{\varepsilon_{ij}} \sigma_{ij}.\, d(\varepsilon_{ij})} \qquad \textbf{(2.27)}$$

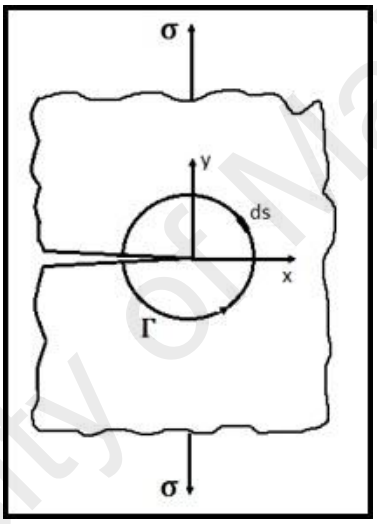

Figure 2.4: Definition of the J-Integral.

For a small scale of yielding or linear-elastic material behavior, the *J*-integral that is equivalent to the energy release rate *G* can also be corelated to the stress intensity factor as:

$$\boldsymbol{J_I = \frac{K_I^2}{E'}\ ;\ J_{II} = \frac{K_{II}^2}{E'}\ \ ;\ \ J_{III} = \frac{K_{III}^2}{2\mu}} \qquad \textbf{(2.28)}$$

In case of the mixed-mode fatigue crack growth, the *J*-integral is the summation of each the corresponding mode of the J-integral. Thus, the J-integral for the mixed-mode loading is expressed as

$$\boldsymbol{J = \frac{K_I^2}{E'} + \frac{K_{II}^2}{E'} + \frac{K_{III}^2}{2\mu}} \qquad \textbf{(2.29)}$$

2.3.4 Fatigue crack growth

In general, the fatigue failure in metal consists of three stages: (i) crack initiation, (ii) crack propagation and (iii) final failure. The crack initiation stage involves the crack nucleation and microcrack growth that primarily take place at the material surface. The growing micro-crack will then merge to form a macro crack. The crack initiation stage may cover the major part of the fatigue life because the micro-crack growth rate is often very low. The crack propagation begins when the macro crack progressively advances into the subsurface material. Here, the growing crack dependent on the fracture resistance of the material. In the final fracture, the unstable crack growth has occurred and eventually causes the catastrophic failure of the component. In many fatigue crack studies, the crack growth data are generally presented in the form of the crack length or crack depth plotted against the number of cycles (*a-N* curve), see Figure 2.5. The slope of curve indicates the crack growth rate *da/dN*. At a higher stress level, the crack growth rate becomes higher and the fatigue life is shorter.

The fatigue crack growth data are also often presented in the form of the crack growth rate against the stress intensity factor ranges (*da/dN* vs ΔK curve) in the log-log scale as shown in Figure 2.6. The data consist of the threshold region (Region I), the Paris law region (Region II) and the fracture region (Region III). Two vertical asymptotes identified at Regions I and III, respectively, represent the conditions where the crack begins to propagate and the fracture is about to occur. In Region I, if $\Delta K < \Delta K_{th}$, the crack would not grow or alternatively is growing very slowly where the ΔK is near the ΔK_{th} value. Then, the macroscopic crack will grow stably in Region II with the ΔK value above the ΔK_{th}. The crack growth rate curve is shown to have a linear relationship between *da/dN* and ΔK. In Region III, the crack growth rate can be very high in order of 10^{-3} mm/cycle and above. This stage usually undergoes a few fatigue life cycles.

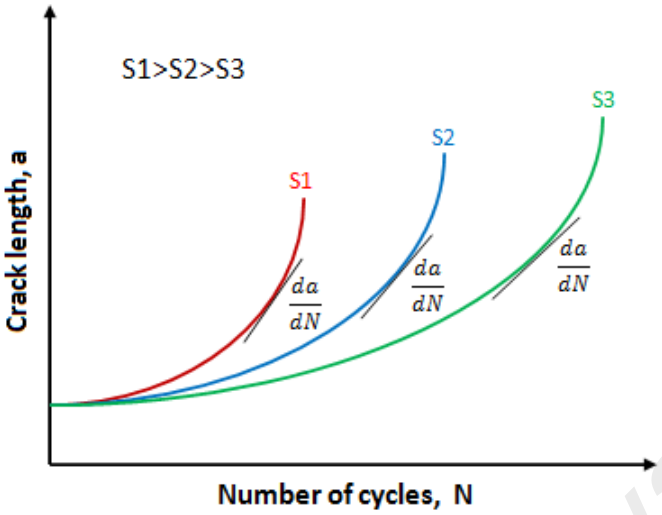

Figure 2.5: Crack growth curve.

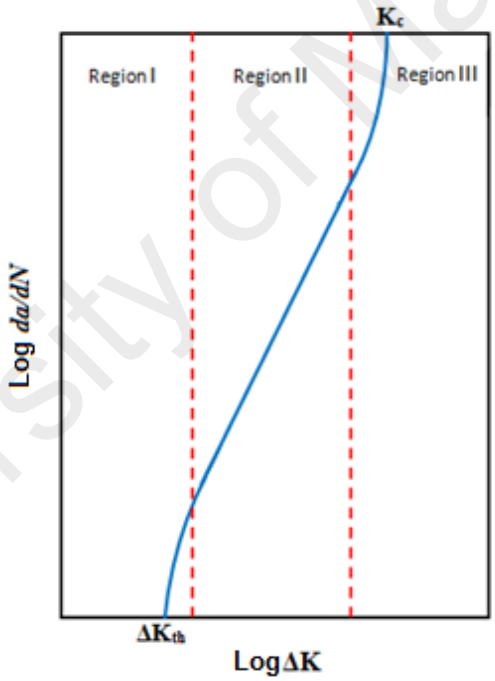

Figure 2.6: Crack growth rate curve.

2.3.5 Crack tip plasticity

Practically, the cracked components are accompanied with a small amount of plastic deformation (inelastic yielding) around the crack tip. It can be described by considering Figure 2.2 and Equation (2.8). When the distance r approaches zero, the stress σ_y in Equation (2.8) will be infinite or singular. However, the design stress does

not allow the local stress σ_y to be greater than the yield strength of the material. Otherwise, the material at the crack tip will undergo yielding. The crack problems can be treated using the LEFM principle if the yielding size is relatively small in comparison to the size of crack. Generally, the yielding size at the crack tip is called the plastic zone. The plastic zone may be assumed as a circular region with a radius r_y. Irwin and Paris (1960) have proposed the relation between the plastic zone r_y and the Mode I SIF based on the elastic stress analysis as:

$$\boldsymbol{r_y = \frac{1}{2\pi}\left(\frac{K_I}{\sigma_{ys}}\right)^2} \tag{2.30}$$

for plane stress and,

$$\boldsymbol{r_y = \frac{1}{6\pi}\left(\frac{K_I}{\sigma_{ys}}\right)^2} \tag{2.31}$$

for plane strain.

Dugdale (1960) proposed the strip yield method to define the plastic zone. For plane stress condition, the width of plastic zone is expressed as:

$$\boldsymbol{\omega = a\left[sec\left(\frac{\pi\sigma}{2\sigma_{ys}}\right) - 1\right]} \tag{2.32}$$

For a small scale of yielding, the plastic zone is defined as

$$\boldsymbol{r_y = \frac{\pi}{8}\left(\frac{K_I}{\sigma_{ys}}\right)^2} \tag{2.33}$$

2.3.6 Crack closure

The concept of the crack closure or Elber's mechanism (Elber, 1970) considers the plastic deformation that occurs at the crack tip during the crack propagation. During unloading of a tension stress cycle, it was observed that the crack would close before the tension stress reached zero. The contact between the crack surfaces will occur due to the

constraint of the surrounding elastic material. Then, the crack surfaces will not open immediately at the start of the following cycle and they remain closed for some time during the cycle. This implies that the crack only propagates at the opening portion of a stress cycle (when the crack starts to open at $K = K_{op}$ and remains open-up at $K = K_{max}$). The crack is unable to propagate while it remains closed (the crack remains partly or fully closed at $K = K_{min}$). This observation has led to reduce the driving force of crack propagation ΔK to the effective level $\Delta K_{eff,.}$ Thus, the fatigue crack growth rate as a function of ΔK_{eff} can be written as

$$\frac{da}{dN} = f(\Delta K_{eff}) \tag{2.34}$$

where $\Delta K_{eff} = K_{max} - K_{op}$, K_{op} is the stress intensity opening factor at which $K_{op} > K_{min}$. In this relation, the effect of the stress ratio R on the plastic wake field of the crack has been accounted by K_{min}. Elber (1971) characterized the crack closure U level as the ratio of the ΔK_{eff} to ΔK as follow:

$$U = \frac{\Delta K_{eff}}{\Delta K} = \frac{K_{max} - K_{op}}{K_{max} - K_{min}} \tag{2.35}$$

The experimental crack closure measurement on Al-alloy (2024-T3) fatigue crack (Elber, 1971) indicated that the crack closure U can be described as a simple function of the stress ratio R as

$$U = 0.5 + 0.4R \tag{2.36}$$

For the negative stress ratios, Schijve (1981) proposed a crack closure function as

$$U = 0.55 + 0.33R + 0.12R^2 \tag{2.37}$$

2.3.7 Fracture toughness

The fracture criterion based on the stress intensity approach postulates that a cracked component will fracture when the stress intensity factor K at the crack tip is larger than the fracture toughness K_c of the material. Therefore, the fracture toughness denotes the ability of the material to resist the crack propagation. According to the state of stress in a cracked body, the fracture toughness has two conditional states that are the plane stress fracture toughness K_c and the plane strain fracture toughness $K_{Ic.}$ The fracture toughness K_{Ic} is the critical value of the stress intensity factor K_I at which the fracture would take place. The determination of K_{Ic} can be done experimentally using the following correlation as:

$$\boldsymbol{K_{Ic} = Y.\sigma_c\sqrt{\pi a_c}} \quad \textbf{(2.38)}$$

where σ_c and a_c are the tension stress level and the crack length at the failure, respectively. The term Y is the dimensionless geometric factor. The plane strain fracture toughness K_{Ic} is independent of structural geometry but is normally associated with a structural member having thick geometry. Meanwhile, the plane stress fracture toughness K_c is a function of specimen thickness and other geometric variables. Fracture toughness can be expressed in term of the critical energy release rate G_c as (Irwin, 1957):

$$\boldsymbol{G_c = \frac{K_c^2}{E}} \quad \textbf{(2.39)}$$

for plane stress and

$$\boldsymbol{G_{Ic} = K_{Ic}^2 \frac{(1-\upsilon^2)}{E}} \quad \textbf{(2.40)}$$

for plane strain.

2.4 Mixed-mode fracture mechanics

Mixed-mode fracture condition can occur due to mainly three factors: (i) mixed-mode of loading is present on a component (normal and shear loads), where the crack front is perpendicular to the direction of normal load. (ii) normal/uniaxial loadings are applied to the component having inclined or deflected crack and (iii) combination of the pre-strain condition with the mechanical and or thermal loads (Ayhan, 2007). The analysis of mixed-mode crack requires the determinations of SIFs in a complex state of stress where the distribution of the three dimensional crack tip stress field is varied through the thickness of the solid component.

2.4.1 Crack tip-stress field

In mixed-mode fracture cases, the evaluation of the stress field near the crack tip shall take into account all modes of the SIFs (K_I, K_{II}, K_{III}). Generally, the SIFs under mixed- mode loading are determined using the superposition of the entities of all modes. Referring to the coordinate system shown in Figure 2.7, the elastic stress field at the vicinity of the crack tip for all fracture modes (Modes I, II and III) can be expressed as (Richard et al., 2014) :

$$\boldsymbol{\sigma_r = \frac{K_I}{4\sqrt{2\pi r}}\left\{5cos\left(\frac{\theta}{2}\right) - cos\left(\frac{3\theta}{2}\right)\right\} - \frac{K_{II}}{4\sqrt{2\pi r}}\left\{5sin\left(\frac{\theta}{2}\right) - 3sin\left(\frac{3\theta}{2}\right)\right\}} \quad \textbf{(2.41)}$$

$$\boldsymbol{\sigma_\theta = \frac{K_I}{4\sqrt{2\pi r}}\left\{3cos\left(\frac{\theta}{2}\right) + cos\left(\frac{3\theta}{2}\right)\right\} - \frac{K_{II}}{4\sqrt{2\pi r}}\left\{3sin\left(\frac{\theta}{2}\right) + 3sin\left(\frac{3\theta}{2}\right)\right\}} \quad \textbf{(2.42)}$$

$$\boldsymbol{\tau_{r\theta} = \frac{K_I}{4\sqrt{2\pi r}}\left\{sin\left(\frac{\theta}{2}\right) + sin\left(\frac{3\theta}{2}\right)\right\} + \frac{K_{II}}{4\sqrt{2\pi r}}\left\{cos\left(\frac{\theta}{2}\right) + 3cos\left(\frac{3\theta}{2}\right)\right\}} \quad \textbf{(2.43)}$$

$$\boldsymbol{\tau_{rz} = \frac{K_{III}}{\sqrt{2\pi r}}sin\left(\frac{\theta}{2}\right)} \quad \textbf{(2.44)}$$

$$\boldsymbol{\tau_{\theta z} = \frac{K_{III}}{\sqrt{2\pi r}}cos\left(\frac{\theta}{2}\right)} \quad \textbf{(2.45)}$$

$$\boldsymbol{\sigma_z = v(\sigma_r + \sigma_\theta)} \quad \textbf{(2.46)}$$

$$\boldsymbol{\sigma_z = v(\sigma_r + \sigma_\theta) = \frac{8v}{4\sqrt{2\pi r}}\left\{K_I cos\left(\frac{\theta}{2}\right) - K_{II} sin\left(\frac{\theta}{2}\right)\right\}} \quad \textbf{(2.47)}$$

for plane strain,

$$\sigma_z = 0 \tag{2.48}$$

for plane stress.

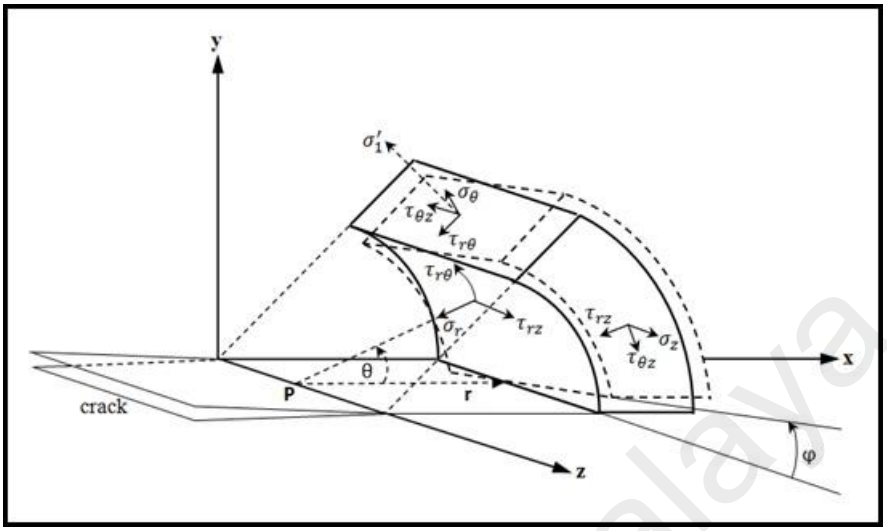

Figure 2.7: Polar coordinate system and stresses at 3D crack front (Richard et al., 2005)

2.4.2 Mixed-mode crack growth model

Over the years, a number of mixed-mode crack growth models have been proposed based on the stress field and energy approaches. The parameters such as stress intensity factor, strain energy density, strain intensity factor, energy release rate, COD and J-integral are usually employed in the development of the models. In the mixed-mode crack growth analysis, the effective stress intensity factors ΔK_{eff} are often used to calculate the crack extensions. Paris law which originally considers Mode I fatigue crack growth has been generalized to evaluate the mixed-mode fatigue crack growth as proposed by Tanaka (1974):

$$\frac{da}{dN} = C(\Delta K_{eff})^m \tag{2.49}$$

where *C* and *m* are material constant. Equation (2.49) seems adequate to portray the behavior mixed-mode crack growth in Region II, resulting in a linear relationship between *da/dN* and $\Delta K_{eff.}$ Equation (2.49) was then extended by Walker (1970) for considering the effect of mean stress or stress ratio on the crack growth rate as:

$$\frac{da}{dN} = C\left(\frac{\Delta K_{eff}}{(1-R)^{1-\gamma}}\right)^m \quad \textbf{(2.50)}$$

where R is the stress ratio ($R=S_{min}/S_{max}=K_{min}/K_{max}$) and γ is the the material constant obtained from the experimental data at various R. Both Paris and Walker models are often found to have the conservative crack growth rate estimation at Region III where the crack grows faster. However, they are found to be less conservative at Region I due to lower crack growth rates. Therefore, Forman (1972) attempted to propose a new crack growth model where the critical stress intensity factor K_c was taken into account to describe the unstable crack growth at Region III as:

$$\frac{da}{dN} = \frac{C[\Delta K_{eff}]^n}{(1-R)K_c - \Delta K_{eff}} \quad \textbf{(2.51)}$$

The more accurate fatigue crack growth model which describes all region of fatigue life curve is the FNK (Forman, Newman and de Koning) equation or also well known called the NASGRO equation. The NASGRO equation considers the effects of the crack closure, crack arrest at threshold region and crack acceleration on the crack growth rate at the fast fracture region (region III). The NASGRO equation is written as:

$$\frac{da}{dN} = \frac{C(1-f)^n \Delta K_{eff}^n \left(1-\frac{\Delta K_{th}}{\Delta K_{eff}}\right)^p}{(1-R)^n \left(1-\frac{\Delta K_{eff}}{(1-R)K_c}\right)^q} \quad \textbf{(2.52)}$$

where C, n, p and q are the NASGRO constants that are empirically derived. f is the crack opening function that is defined as:

$$f = Max(R, A_0 + A_1 R + A_2 R^2 + A_3 R^3) \quad \textbf{(2.53)}$$

For R ≥ 0 and

$$f = A_0 + A_1 R \quad \textbf{(2.54)}$$

For -2 ≤ R < 0.

The polynomial coefficients are defined as:

$$A_0 = (0.825 - 0.34\alpha + 0.05\alpha^2)(cos[\pi/2(S_{max}/S_0)])^{\frac{1}{\alpha}} \quad (2.55)$$

$$A_1 = (0.415 - 0.071\alpha)S_{max}/S_0 \quad (2.56)$$

$$A_2 = 1 - A_0 - A_1 - A_3 \quad (2.57)$$

$$A_3 = 2A_0 + A_1 - 1 \quad (2.58)$$

where α is the plane stress/strain constraint factor and S_{max}/S_o is the ratio of the peak stress to the material flow stress in a stress cycle.

The non stress intensity based crack growth models have also been proposed by many researchers. Sih and Barthelemy (1980) described the range of strain energy density factor as driving force of the mixed-mode crack growth. They expressed the mixed-mode crack growth model as:

$$\frac{da}{dN} = C(\Delta S_{eff})^n \quad (2.59)$$

where:

$$\Delta S_{eff} = 2/\pi\left[a_{11}(\theta)\Delta K_{I,eff}^2 + a_{12}(\theta)\Delta K_{I,eff}\Delta K_{II,eff} + a_{22}(\theta)\Delta K_{II,eff}^2 + a_{33}(\theta)\Delta K_{III,eff}^2\right] \quad (2.60)$$

The coefficients $a_{ij}(\theta)$ are the functions of the elastic constant and the crack growth direction relative to the original crack plane, θ. ΔK_{eff} is the range of effective stress intensity factor that considers the crack closure. Yan (2006a) implemented this criterion to calculate the crack growth of an inclined centre crack in an elastic plate under combined Modes I-II load by the boundary element method.

Li (1989) used the deformation intensity at the mixed-mode crack tip to predict the crack growth rate by defining a vector crack tip displacement (CTD). He proposed the mixed-mode crack growth model based on this vector as:

$$\frac{da}{dN} = C(\Delta CTD)^n \quad (2.61)$$

where:

$$\boldsymbol{\Delta CTD = 4/(\pi\sigma.E)\left[\left(\Delta K_I^2 + 3\Delta K_{II}^2\right)\left(\Delta K_I^2 + 2\Delta K_{II}^2 + 2\Delta K_I \Delta K_{II}\right)\right]^{1/2}} \quad \textbf{(2.62)}$$

The mixed-mode crack growth models presented above partially use ΔK_{eff} to evaluate the crack extension rates. Generally, the effective stress intensity factors K_{eff} quantify the effect of the overall mode stress acting upon the crack front to the crack growth rate by combining all three mode SIFs. There are various methods proposed in literature to calculate the effective stress intensity factor as follows:

(i) Tanaka equation

Tanaka (1974) proposed the equations for K_{eff} as:

$$\boldsymbol{K_{eff} = \sqrt[4]{K_I^4 + 8K_{II}^4 + \frac{8}{(1-\nu)}K_{III}^4}} \quad \textbf{(2.63)}$$

(ii) Yaoming Mi equation

Mi and Aliabadi (1992) applied the K_{eff} equation into the Dual Boundary Element Method to calculate the mixed-mode fatigue crack. The equation is given as:

$$\boldsymbol{K_{eff} = \sqrt{(K_I + |K_{III}|)^2 + 2K_{II}^2}} \quad \textbf{(2.64)}$$

(iii) Sum-square equation.

Shi et al. (2006) and Pirondi (2003) used the sum-square approach to quantify all modes SIFs. The expression is written as:

$$\boldsymbol{K_{eff} = \sqrt{K_I^2 + K_{II}^2 + K_{III}^2}} \quad \textbf{(2.65)}$$

(iv) Maximum principal stress equation

Chambers et al. (1991) proposed the K_{eff} equation based on the maximum principal stress where Mode III SIFs are ignored. The expression is then written as:

$$K_{eff} = cos\left(\frac{\theta}{2}\right)\left[K_I cos^2\left(\frac{\theta}{2}\right) - \frac{3}{2}K_{II} sin^2(\theta)\right] \quad (2.66)$$

2.4.3 Mixed-mode crack growth direction criteria

A proper understanding about the direction of crack extension is essential in analysing the mixed-mode fractures. The direction of crack extension is measured from the plane of the initial crack and is characterized by an angle θ. It is evident that the direction of the mixed-mode crack depends upon the ratio of modes stress intensity at the crack front. A number of the fracture parameters such as SIFs, strain energy density, *J*-integral, energy release rate and crack tip displacement have been implemented in develop the direction of crack extension criteria under the mixed-mode loads.

2.4.3.1 Maximum tangential stress criterion (MTS)

The MTS criterion which was proposed by Erdogan and Sih (1963) allow a crack to propagate along the radial direction and perpendicular to the maximum tangential stress. In two-dimensional mixed-mode I and II loading, the stresses $\sigma_{\theta\theta}$ and $\tau_{r\theta}$ at the crack tip for linear elastic condition are expressed as:

$$\sigma_{\theta\theta} = \frac{1}{\sqrt{2\pi r}} cos\frac{\theta}{2}\left(K_I cos^2\frac{\theta}{2} - \frac{3}{2}K_{II} sin\theta\right) \quad (2.67)$$

$$\tau_{r\theta} = \frac{1}{2\sqrt{2\pi r}} cos\frac{\theta}{2}\left[K_I sin\theta + K_{II}(3cos\theta - 1)\right] \quad (2.68)$$

The tangential stress $\sigma_{\theta\theta}$ will be the maximum value when $\tau_{r\theta} = 0$, that is:

$$\tau_{r\theta} = K_I sin\theta + K_{II}(3cos\theta - 1) = 0 \quad (2.69)$$

Thus, the angle θ can be given as:

$$\theta = 2tan^{-1}\left\{\frac{1}{4}\frac{K_I}{K_{II}} \pm \frac{1}{4}\sqrt{\left(\frac{K_I}{K_{II}}\right)^2 + 8}\right\} \quad (2.70)$$

and the maximum principal stress σ_1 is written as:

$$\sigma_1 = \frac{1}{\sqrt{2\pi r}} cos^2\frac{\theta}{2}\left(K_I cos\frac{\theta}{2} - 3K_{II} sin\frac{\theta}{2}\right) \quad (2.71)$$

The fracture criterion for the mixed-mode crack problems can be defined as:

$$\boldsymbol{K_I cos^3\frac{\theta}{2} - 3K_{II} cos^2\frac{\theta}{2} sin\frac{\theta}{2} = K_{Ic}} \quad \textbf{(2.72)}$$

This criterion can predict the crack growth direction for Mode I-II conditions, but it is not applicable when Mode III condition that is resulted from the circumferential stress is included in the mixed-mode fracture.

2.4.3.2 Minimum strain energy density criterion (MSED)

Sih and Macdonald (1974) proposed the crack growth direction criteria based on the minimum strain energy density (MSED (also called *S*-criterion). They described the region which has the minimum value of the strain energy density factor (*S*) is the direction of crack propagation. This criteria expressed in term of K_I, K_{II} and K_{III} as :

$$\boldsymbol{S(\theta) = \frac{1}{16\pi\mu}\left[(1+cos\theta)(\kappa - cos\theta)K_I^2 + 2sin\theta(2cos\theta - \kappa + 1)K_I K_{II} + \right.}$$

$$\boldsymbol{\left.\left((\kappa+1)(1-cos\theta) + (1+cos\theta)(3cos\theta - 1)\right)K_{II}^2 + 4K_{III}^2\right]} \quad \textbf{(2.73)}$$

where,

$$\boldsymbol{\kappa = 3 - 4\nu} \quad \text{for plane strain} \quad \textbf{(2.74)}$$

$$\boldsymbol{\kappa = \frac{(3-\nu)}{(1+\nu)}} \quad \text{for plane stress} \quad \textbf{(2.75)}$$

The angle of crack growth direction θ where the strain energy density $S(\theta)$ is minimum can be obtained numerically by solving the following expressions:

$$\frac{\partial S(\theta)}{\partial \theta} = 0 \quad , \quad -\pi < \theta < \pi \, , \quad \text{and} \quad \textbf{(2.76)}$$

$$\frac{\partial^2 S(\theta)}{\partial \theta^2} > 0 \quad \textbf{(2.77)}$$

2.4.3.3 Maximum energy release rate criterion (MERR)

Hussain et al. (1974) developed the MERR rate criterion based on the Griffith's crack analysis. The crack extension is assumed occurring along the direction of maximum energy release rate. The energy release rate of kinked crack tip is given as:

$$G_{kink} = \frac{\kappa+1}{8\mu}\left(k_I^2 + k_{II}^2\right) \tag{2.78}$$

where k_I and k_{II} are Mode I and Mode II SIFs at kinked crack tip respectively which are function of the kinked angle θ, that is :

$$k_I = \left(\frac{4}{3+cos^2\theta}\right)\left(\frac{\pi-\theta}{\pi+\theta}\right)^{\theta/2\pi}\left(K_I cos\theta + \frac{3}{2}K_{II} sin\theta\right) \tag{2.79}$$

$$k_{II} = \left(\frac{4}{3+cos^2\theta}\right)\left(\frac{\pi-\theta}{\pi+\theta}\right)^{\theta/2\pi}\left(K_{II} cos\theta - \frac{1}{2}K_I sin\theta\right) \tag{2.80}$$

The crack growth direction angle or fracture angle θ_o is thus determined by maximizing $G_{kink}(\theta)$:

$$\frac{\partial G_{kink}(\theta)}{\partial \theta} = 0 \quad \text{at } \theta = \theta_o \tag{2.81}$$

$$\frac{\partial^2 G_{kink}(\theta)}{\partial \theta^2} < 0 \quad \text{at } \theta = \theta_o \tag{2.82}$$

2.4.3.4 The J-criterion

Hellen and Blackburn (1975) used the J-integral to evaluate the mixed-mode crack growth direction. They postulated that the direction of crack extension is along the direction of vector *J*. The vector *J* for 2D mixed-mode problem is defined as:

$$J = J_I\vec{i} + J_{II}\vec{j} \tag{2.83}$$

where J_I and J_{II} are Mode I and Mode II J- integral values, respectively.

2.4.3.5 Maximum potential energy release rate criterion (MPERR)

To determine the crack direction, the MPERR criterion was proposed by Chang et al. (2006) based on the approximation of the energy release rate of mixed-mode crack. They used effective SIF of each modes fracture in developing the energy release rate which are function of K_I, K_{II}, K_{III} and the incremental direction. According to this criterion, the following expression determines the direction of mixed-mode crack extension:

$$\frac{\kappa+1}{8}\left[K_I^2\left(sin\frac{\theta}{2}+sin\frac{3\theta}{2}\right)+4K_IK_{II}cos\frac{3\theta}{2}-K_{II}^2\left(3sin\frac{3\theta}{2}-5sin\frac{\theta}{2}\right)\right]+$$

$$K_{III}^2 sin\frac{\theta}{2}=0 \qquad (2.84)$$

2.4.3.6 Vector crack tip displacement (CTD) criterion

Li (1989) proposed the CTD vector criterion where the crack propagates along the direction of the CTD vector. The CTD vector is the combination of crack tip opening displacement (CTOD) vector and the crack tip sliding displacement (CTSD) vector that are corresponding to Modes I and II fatigue crack, respectively.

2.5 Analytical method

The analyses of the in-plane elastic crack problems have been made by mathematicians since early 1900s when Inglis (1913) used an elliptic coordinate to solve a single crack problem in an infinite sheet. Since then, Griffith (1920) found the critical stress required for the crack growth. Irwin (1957) used Westergaard's method to analytically solve the crack problems based on the local stress field. Subsequently, a crack model was proposed by Barenblatt (1959), where the stress singularity can be removed by considering a cohesive zone along a line ahead of the crack. The similar methods have been used by Dugdale (1960) to study the crack tip plasticity in thin sheets. Next, Rice (1968) developed a fine mathematical formulation of *J*-integral and showed that it is independent to its path near the crack front.

The major development on the analytical technique for solving plane crack problem was proposed by Muskhelishvili (1977) where the stresses and displacements were expressed in terms of the analytic functions of complex variables. These complex variable functions can be solved by many techniques such as the conformal mapping (Bowie, 1973), Laurent series expansion (Isida, 1973), the boundary collocation (Gross et al., 1964), the asymptotic approximation (Benthem & Koiter, 1973), etc. However, the complex variable method is only applicable for two-dimensional problems. The other analytical methods for solving crack problems are the integral transform method (Sneddon, 1975), the alternating method (Hartranft & Sih, 1972) and the weight function method (Bueckner, 1971). The integral transform method used an integral transform solution of the elasticity equation to generate dual integral equations of the traction and displacement for the unknown functions. Then, the dual integral equation is reduced to a single integral equation and stress intensity factor can be calculated based on this integral equation. The Fourier, Henkel and Mellin transforms are common techniques used in the integral transform method depending upon the geometry. In the alternating method, the singular term of the stress function for traction is integrated over a contour which encloses the crack. Then, the stress functions of complex variables are solved for any integer power of the traction polynomial to obtain the SIFs.

In past several years, a number of researchers have used the aforementioned analytical methods above to solve crack problems. Cheung et al., (1989) employed the boundary collocation method to calculate the SIFs of a circular arc crack. Leblond and Amestoy (2013) used the conformal mapping to calculate the SIF of kinked and curve crack. Liu et al. (2014) used the complex variable method to produce the SIF solutions of two collinear plane edge cracks emanating from an elliptical hole in a finite plate under shear loading. Woo et al. (2013) applied the collocation method to calculate *J*-integral of an internal crack. Yang et al. (2013) used the weight function method for

determining the SIF of a high aspect ratio of a semi-elliptical crack in a cylindrical vessel. Mikheevskiy et al. (2012) evaluated the SIFs and fatigue crack of a corner crack in a lug using the weight function method.

The well-know SIF solutions for a number of crack types, component geometries and loadings have been reported by Newman and Raju (1981), Newman and Raju (1983), Raju and Newman Jr (1986). The Newman-Raju's solutions were obtained by fitting the finite element results of the corresponding crack problems. It is frequently used to validate the numerical and experimental results. The SIF equation for a surface crack in a finite plate under tension is given as:

$$\boldsymbol{K(\phi) = \sigma\sqrt{\frac{\pi a}{Q}}\left[M_1 + M_2\left(\frac{a}{t}\right)^2 + M_3\left(\frac{a}{t}\right)^4\right] f(\phi) g f_w} \qquad \textbf{(2.85)}$$

and for a corner crack in a finite plate under tension, the SIF equation is expressed as:

$$\boldsymbol{K(\phi) = \sigma\sqrt{\frac{\pi a}{Q}}\left[M_1 + M_2\left(\frac{a}{t}\right)^2 + M_3\left(\frac{a}{t}\right)^4\right] f(\phi) g_1 g_2} \qquad \textbf{(2.86)}$$

where M_i (i = 1, 2, 3) and g_i is the curve fitting function that function of the crack aspect ratio *a/c*, $f(\phi)$ is the angular function, f_w is the finite width correction factor, Q is the elliptical shape factor.

2.6 Numerical method

2.6.1 Finite element method

The rapid developments in the computer technology have encouraged researchers to evaluate fracture problems using the numerical methods. The computational solutions of complex problems can be now obtained more efficiently. Among of the numerical methods are finite element method (FEM), boundary element method (BEM), finite different method (FDM) and finite volume method (FVM). The FEM and BEM are most common methods used for numerical simulations in the fracture researches. The FEM conceptually discretizes a body/component into a number of elements and uses

approximate/shape functions within each element. The formulations of the FEM for the LEFM problem employ the Principle of Virtual Work as:

$$\int_V \boldsymbol{\sigma_{ij}\delta\epsilon_{ij}dV} = \int_S \boldsymbol{\sigma_{ij}n_j\delta u_i dS} \quad \textbf{(2.87)}$$

where $\delta\epsilon_{ij}$ is the virtual strain tensor and n_j is the normal vector to the surface of the applied traction. The FEA formulation is then arranged in the form of a system of algebraic equations in term of the nodal variables.

The applications of the FEM to LEFM problem are divided into two methods, i.e the indirect and direct methods. In the indirect method, the displacements or stresses of the elements are fitted to the elastic singular solution in the vicinity of the crack-tip, yielding the SIFs as a function of the distance from the crack-tip. The extrapolation to the crack-tip yields the approximated values for the SIFs. Examples of the indirect methods are the nodal force method, the virtual crack closure integral (VCCI), the equivalent domain integral method and the virtual crack extension (VCE) or the stiffness derivative method. The nodal force method calculates the SIF using the forces that are normal to the crack plane and ahead of the crack front. The VCCI method computes the strain energy release rates using the forces that are normal to the crack plane and the relative displacements of the crack faces behind the crack front. The SIFs are then obtained from the calculated strain energy release rate. The VCCI method was proposed firstly for 2D problems by Rybicki and Kanninen (1977) and for 3D problems by Shivakumar et al. (1988) and Fawaz (1998). Valvo (2014) used this technique for calculating the SIFs of the mixed-mode I-II-III crack problems. The VCE method was proposed by Hellen (1975). This method uses the shifted crack tip nodes Δa so that the stiffness matrix is only slightly changed in the crack region. The changes in ΔK can thus be calculated easily using a few elements. Ishikawa (1980) and Sha (1984) applied the VCE method to evaluate the mixed-mode fracture problems. Shin and Cai (2004) implemented the virtual crack extension method in ABAQUS-FEA software to

calculate the SIFs of a surface crack in a rod. In the domain integral method, a crack-tip contour integral is expressed as an equivalent domain/volume integral over a finite domain surrounding the crack tip. This method has been employed by Li et al. (1985) and Shih et al. (1986) to determine the energy release rate along the straight crack front of a 3D structure. Shivakumar and Raju (1992) applied the equivalent domain integral method for a 3D mixed-mode crack problem. Wu et al. (2012) employed the domain integral method embedded in the extended finite element to calculate the mixed-mode SIFs of a 3D model.

Generally, modelling and simulations of crack problems by using the FEM require fine elements around the crack tip regions. Therefore, in the direct method of FEA, the special singular element or crack-tip elements and hybrid element are used to model the crack-tip region. The singular elements are developed based on the employment of the asymptotic displacement field in the FE formulation. Tracey (1971) used triangular singular elements in which the approximate solution for the SIF was the average of the numerical values obtained from each element in contact with the crack tip. Shih and Chen (2002) used collapse singular element encoded into ANSYS software to calculate the SIFs of a surface crack in a rod. Tan et al. (1996) used the nodal force method together with pentahedral singular elements along the crack front to calculate the SIFs of a corner crack at a semi-circular edge notch in a plate under tension. As the alternative to special singular element, Barsoum (1976) introduced a quarter-point element by modifying isoparametric elements with a quadratic shape function such that the position of the mid-side nodes is altered. The coordinates of the nodes are shifted from the middle to the quarter-point position in the direction of the crack tip. Boljanović and Maksimović (2011) used a quarter-point singular element to evaluate the crack growth and crack direction under the mixed-mode I-II loading. The special crack tip element utilizing the higher order term of the asymptotic expansion for the elasticity

solution was developed by Wilson (1973). This special element was utilized to discretize the surroundings of the crack tip, while regular elements are used to discretize the rest of the model. Tong et al. (1974) developed a hybrid finite element procedure for treating crack problems by employing the stress and displacement distribution around the crack tip. Implementation of this method is facing difficulties due to the complexity of the formulations. To date, a number of numerical methods have been proposed to improve the computational efficiency such as extended finite element method (XFEM), scaled boundary finite element method (SBFEM), element-free Galerkin method (EFG). The applications of the FEM for the mixed-mode fatigue crack analyses are presented in Section 2.9 of this chapter.

2.6.2 Boundary Element Method

The boundary element method (BEM) has become an alternative numerical technique to solve engineering problems particularly in the scope of fracture mechanics. The BEM is known to have easy modeling steps and good accuracy in the results in the analyses of the stress singularity problems. It is an effective tool in engineering analysis and design especially when combined with CAD system due to mesh generation that is highly automated, robust in mesh refinement and in-built error estimation (Purbolaksono et al., 2009). The formulations of the BEM are developed based on the displacement boundary integral equation (DBIE). The integrals are numerically integrated over the domain boundaries that are discretized into a number of boundary elements. The most advantage of BEM as compared to the other numerical methods such as FEM is the reduction of the dimensionality of the problems by one order in the meshing/modeling stage. Only boundary lines of the domain are needed for discretization of 2D model. Meanwhile, surface boundaries of the domain needs to be modeled on 3D model. This advantage leads to simpler and faster in data preparation (Brebbia & Dominguez, 1996). The developments and applications of the BEM to

fracture mechanics problem have been reported in detail by Aliabadi (1997) and Mukhopadhyay et al. (2000).

The BEM has been successfully implemented to the linear elastic problems of cracked structures. The solutions of crack problem (crack surfaces are considered as a single region) with the standard boundary element formulation initially can not be obtained because the coincidence of crack surface leads to the singular matrix of the linear algebraic equations (Cruse, 1972). Several approaches in the scope of BEM have been proposed to overcome the problems such as Green's function method (Snyder & Cruse, 1975), sub-region method (Blandford et al., 1981) and displacement discontinuity method (DDC) Crouch et al. (1983). The Green's function method requires no of crack discretization, but it is only applicable to the problems with very simple crack geometries. The sub-region method divides the cracked body into two regions by extending the crack edges into the body artificially. This method is applicable to model any geometry of the crack shape but seems difficult to be implemented in an incremental crack analysis automatically. The DDC method that uses the Green's functions corresponds to the dislocation points (displacement discontinuities). Each pair of the coincident source points on the crack boundaries are replaced by a single source point. Finally, the DBEM proposed by Portela et al. (1992) was found to be able to overcome the issue of the crack modelling. The DBEM uses the dual boundary integral equations: the displacement integral equation that is collocated on the one crack surface and the traction integral equation that is collocated on the other crack surface. The basic theory of the DBEM is presented in Chapter 3.

The BEM has been applied for evaluating crack problems by many researchers (Cruse, 1972; Cruse, 1975; Tan & Fenner, 1979; Blandford et al., 1981). Karami and Fenner (1986) reported that the J-integral was found to generate a good accuracy of the SIF results of a crack. Prasad et al. (1994) used the DBEM and J-integral to evaluate the

SIFs of the crack under thermo-mechanical loading. Farris and Liu (1993) proposed a modified crack closure integral technique into the BEM to calculate the SIFs. Over the years, the applications of BEM to the fracture problem increase significantly. Cisilino and Aliabadi (1999) applied the DBEM for evaluating the linear and non linear fatigue crack growths. Then, they extended the use of the *J*-integral to solve multi crack problems (Cisilino & Aliabadi, 2004). Cisilino and Ortiz (2005) combined the DBEM and the interaction of the J-integral to evaluate the SIFs of mixed-mode crack problems. Ortiz et al. (2006) developed a domain-independent integral technique in the BEM to calculate the SIFs of a straight crack front and edge in 3D solid. Cisilino and Aliabadi (2004) and Wessel et al. (2001) analyzed the multiple cracks that then propagate to coalesce. Wilde and Aliabadi (1999) developed the DBEM formulation for analyzing a mixed-mode crack growth in a three-dimensional solid. Yan (2007) simulated the 2D mixed-mode crack problem by using the displacement discontinuity element of the BEM. The SIF was calculated based on the displacement field, the maximum circumferential stress criteria was used to predict the crack direction and Paris law was employed to calculate the crack extensions. The SIF was calculated based on the displacement field. The direction of crack was predicted by maximum circumferential stress criteria, while the crack extension was calculated by employing Paris law.

A number of researchers have used the boundary element method based software of BEASY for evaluating the LEFM problems. Kramberger et al. (2004) evaluated the SIF and crack growth on a rim spur gear. Yang et al. (2007) used the BEASY software to analyze the crack growth at the weld toe of a square hollow section welded T-joint. Purbolaksono et al. (2009) evaluated SIF of multiple surface cracks in a bi-materials structure. Some extensive researches on fatigue crack growths using BEASY were reported by Mellings et al. (2005), Citarella and Cricrì (2009), Citarella (2011), Armentani and Citarella (2006), Armentani et al. (2011), Citarella and Buchholz (2008),

Citarella and Cricrì (2010), Citarella et al. (2014), Citarella et al. (2015). Another famous software, FRANC2D, has been used by Yan (2007) and Yan (2006b) to evaluate the SIF and crack growth of 2D problems under Mode I and mixed-mode I-II loadings.

2.7 Experimental work

Experimental works are often used to validate the numerical solutions of fatigue crack growth problems. However, there are no standard specimen and experimental method that are universally accepted for mixed-mode fatigue crack growth problems. Richard (1989) summarized the specimens that are often used in investigating such problem, i.e. tensile stress specimen with an oblique central or edge crack, a disk specimen with an oblique inside crack, etc. The uses of the aforementioned specimens and the test methods for evaluating mixed-mode crack problems are presented in Section 2.9 of Chapter 2.

The procedure to introduce a through crack in a specimen is relatively easier than that for a part-through crack. The testing standards for the through crack specimens such as compact tension, centre crack tension, single edge crack tension specimens are available and often used in the fatigue crack experiments. However, the efficient guideline for introducing a part-through (surface or corner) crack in a specimen is not reported in detail in literature. Thompson and Sheppard (1992) and Shin and Cai (2007, 2008) briefly mentioned the use of the electric discharge machining (EDM) for introducing an elliptical surface crack on a solid rod. Yang et al. (2006) used the linear cutting machine to induce a surface crack in a solid cylinder. Recently, Citarella et al. (2014) used the straight wire cutting machine to manufacture a surface crack in a solid cylinder.

2.8 Fractography analysis of mixed-mode fracture surface

Fractographic technique has played an important role in the fracture analysis. The surface morphology and topography can be used to describe the qualitative fatigue crack behaviors such as fracture mechanism and fracture modes. In general, under a single loading mode, the fracture surface of the fatigue crack component can be characterized by the presence of beachmark and striation markings. Both fracture features indicate the conditions of the crack front at some increments during the crack growth. They appear to have a number of concentric lines that resemble ridges and expand away from the initial crack site, frequently forming an elliptical, semi-elliptical, circular or semicircular pattern. Beachmarks are of the macroscopic features that may be observed with naked eye. Meanwhile, fatigue striations are microscopic features in size and can be viewed with an aid of an electron microscope (Bhat & Patibandla, 2011). The striation mark represents the extension of the crack front by a single load cycle. There may be literally thousands of striations within a single beachmark. The striation width increases with increasing of the stress range and vice-versa. The presence of beachmarks and striations on a fractured surface confirms fatigue as the failure mechanism.

The fractography analyses of the fatigue crack growth under combined loading have been reported by some researchers. Shah (1974) observed the fracture surface of a notched round bar made of 4340 steel under tension, torsion and combined tension-torsion as depicted in Figure 2.8. He reported that a pure tension leads to a flat fracture and the torsion will leave a flat fracture with shear rubbing marks. For the combined loading, the texture fracture surface depends upon the tension to torsion stress ratio. For instance, the big stress ratio results in a fracture surface that is similar with that under tension.

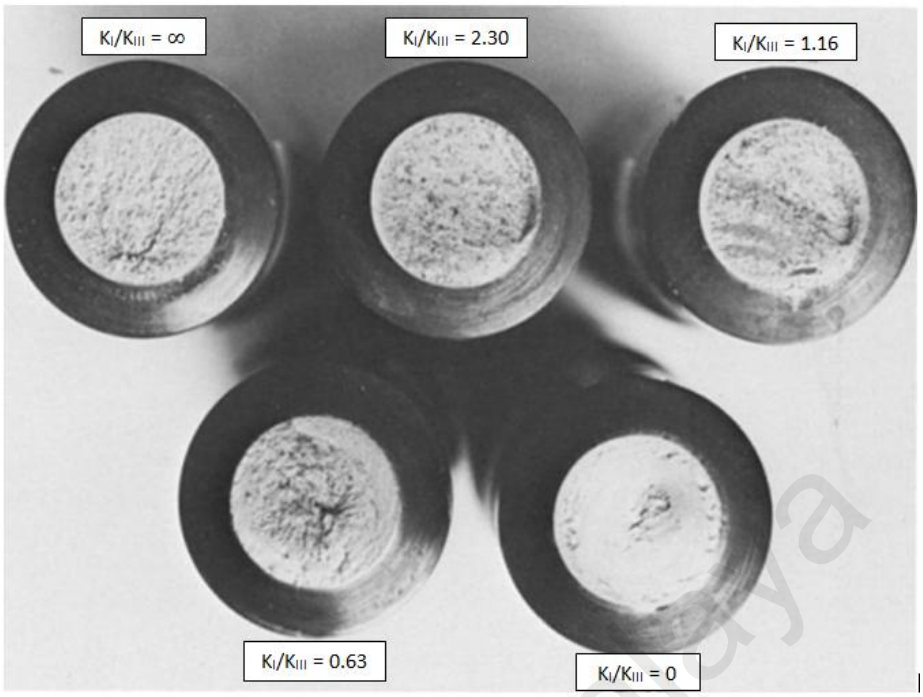

Figure 2.8: Fracture surfaces of notched round bars of 4340 steel under combined mode I-III (Shah, 1974).

Hallbäck and Nilsson (1994) conducted the fractographic analysis on the mixed-mode I-II fracture in aluminium 7075-T6 specimens. They identified two different types of the crack growth. The crack initiation is shown to be straight and macroscopically showed a stable shear separation near Mode II region. In the remaining region, the extensive shearing was observed to occur in a zigzag pattern.

Liu et al. (2004) evaluated the mixed-mode fatigue crack growths on the notched round bars made of Al-7075 alloy. It was observed that under combined tension-torsion loads, the fracture surface was flattened with shear rubbing marks. The radial factory-roof type fracture was clearly observed as shown in Figure 2.9.

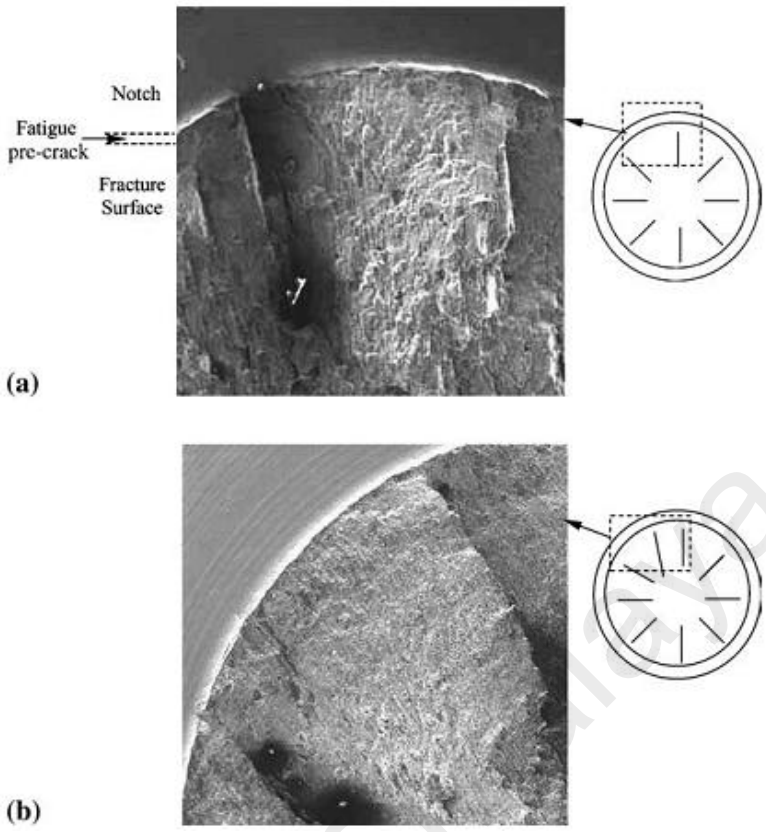

Figure 2.9: Tensile type of factory roof failure of Al7075 (a) K_I/K_{III}=1.674 (b) K_I/K_{III}=0.987 (Liu et al., 2004).

Tarpani et al. (2004) performed fractography analysis to study the fatigue crack initiation and propagation lives under the variable amplitude loads. Slámečka et al. (2007) evaluated the fracture surface roughness of high-strength low-alloy steel under combined bending-torsion fatigue loading. They confirmed the significant influence of the torsion loading on the surface topography. Pokluda et al. (2008) analyzed the fracture surfaces of double circumferential notch cylinder made of austenitic steel. It was observed that Mode II and the mixed-mode I-II mechanism were dominated by the morphological patterns of the fracture surface that occurred under mixed-mode II-III loading. Tanaka (2014) pointed out that the cyclic torsion loading caused a finer factory-roof shape of the fracture surfaces. The superimposed static tension loading reduced the amount of crack growth retardation due to the sliding contact of fracture surfaces, leading to less evidence of the factory-roof shape.

2.9 Mixed-mode SIFs and fatigue crack growth

The SIFs play an important role in the prediction of the fatigue crack growth rate and fatigue life for ensuring the safety of a component during service. In the past decades ago, the evaluation of SIFs and fatigue crack growth were concentrated on the cases where the component is under a simple loading such as either of tension, torsion or bending load. Now a days, the updated knowledge on the SIFs and fatigue crack behaviours under mixed-mode loading are actively sought. Generally, the mixed-mode fatigue crack conditions can be created by two ways: firstly, the crack orientations are inclined with respect to the loading directions and secondly, more than one loading are applied to the cracked components where such loadings may be combined cyclic-static or cyclic-cyclic conditions. Qian and Fatemi (1996) mentioned that it is not easy to draw general conclusions from the experiment result of various specimen geometries.

2.9.1 Mixed-mode I-II

The majority of researchers initially used plate specimens under tension to evaluate the mixed-mode I-II fatigue crack growths. The initial through crack types such as centre crack and edge crack are introduced on specimens where the crack is inclined with respect to the axis loading. The first research on the mixed-mode I-II crack growth carried out by Iida and Kobayashi (1969) who tested centre-cracked plates of aluminium 7075-T6 under cyclic tension. The crack was oriented at various angles (45^0, 60^0, 90^0) to the width direction of the plates. They observed that the crack will be rapidly bifurcated in a direction where the K_I has a maximum value. The similar result was reported by Tanaka (1974). He proposed an equivalent stress intensity factor range for calculating the mixed-mode I-II crack growth rate, that is:

$$\Delta K_{eff} = \left[\Delta K_I^4 + 8\Delta K_{II}^4\right]^{0.25} \quad \textbf{(2.88)}$$

The other similar research on the inclined centre crack was reported by Mageed and Pandey (1992). The crack path and mixed-mode fatigue life obtained by the experimental works were shown to be in good agreements with those predicted by the maximum tensile stress criterion. Paul (1995) evaluated the crack grow path and crack growth rate of an inclined centre crack under tension load in a thin circular plate made of aluminium 2024. The complex crack path and crack growth rate were predicted by the strain energy density theory. The predicted crack growth rates were in close agreement with the experimental results, but the prediction for the kinked initiation angles gave significant deviations from the experimental results. Boljanović and Maksimović (2011) evaluated a crack emanating from the edge of a hole at the centre of Al-2024 T3 alloy plates. The crack was inclined at 45 degree to the applied tension. Fatigue crack growths were simulated using the NASTRAN software to evaluate the fatigue life and crack paths. The SIFs were calculated by the finite element using quarter-point singular elements. The maximum principal stress criterion and K_{eq} were used to determine the crack direction and crack growth, respectively. The results showed that the predicted fatigue life and crack path were in good agreements with the experimental results.

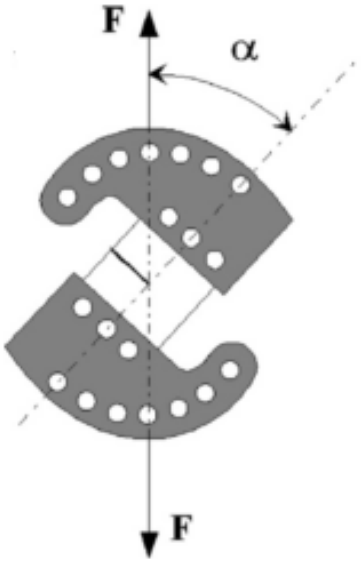

Figure 2.10: The mixed-mode loading device (Richard & Benitz, 1983).

Some researchers used a special mixed-mode loading device (see Figure 2.10) that was firstly developed by Richard and Benitz (1983). The device allows the researcher to easily obtain pure Modes I and II and a few mixed-mode I-II loading conditions on a cracked plate specimen by setting the hole position of tension loading F for different loading angle α as shown in Figure 2.10. Using the mixed-mode loading device, Biner (2001) carried out the experiments on the compact tension shear (CTS) specimens. Four different angles (0^o, 30^o, 45^o, 75^o) of an edge crack with respect to the loading direction were tested. The results indicated that at the low load mixities, both the strain energy density criterion and the maximum stress criterion showed similar crack growth directions. Similar works on aluminium and steel plates for different load angles of 0, 15, 45, 75 degrees have also been conducted by Zhang et al. (2006) to examine the J-integral-plastic mixity parameters of the crack propagation model. They also identified the effects of mixed-mode loading on the fracture modes and the crack bifurcation angle. The maximum circumferential stress criterion was used to determine the crack bifurcation angle. The experimental and numerical results were shown to be in a good agreement. Doquet and Pommier (2004) used the CTS specimen to experimentally evaluate the crack growth under sequential Modes I and II loadings. They concluded that the crack growth rate was a simple sum of the contributions of each mode of the loadings. Song and Lee (2003) used the CTS specimen made of ST304 to evaluate the mixed-mode I-II crack growth experimentally and numerically. The SIFs were analysed by the FEM using the CTOD method and the crack growth direction was determined using the maximum tangential stress criterion. Borrego et al. (2006) carried out the fatigue experiments on an edge crack of the CTS specimen made of AlMgSi1-T6 alloy. The FE analysis was conducted to obtain K_I and K_{II} for different loading angles. They observed that the crack growth direction changed immediately from the initial notch orientation when the load direction is changed. Ding et al. (2007) used a round compact

tension steel specimen to numerically and experimentally evaluate the crack growth and crack growth direction under the mixed-mode I-II loadings. The crack growth rate and direction were calculated based on the critical plane criterion. It was observed that the crack growth direction is perpendicular to the external loading direction and the FE results were in good agreement with the experimental data. Lan et al. (2007) simulated the crack growth of an edge crack in Arcan specimens made of Al-2024 alloy using the CRACK3D finite element software. The CTOD criterion was adopted for calculating the SIFs during the simulations. Smith et al. (2008) used single edge notch (SEN) specimen together with Richard's-like device to evaluate the effect of specimen size on mixed-mode I-II fracture resistance of forged steel. They concluded that specimen size great influence the change of fracture mode from Mode I to Mode II. Benedetti et al. (2009) studied the effect of notch geometry, loading direction, kinking and microstructure on the propagations of fatigue crack emanating from the sharp V-notched plate specimens. They used three loading directions i.e. 0^0, 45^0 and 90^0 for the fatigue testing which result in Mode I, mixed-mode I-II and Mode II loading respectively. The results showed that the driving force for crack propagation is mode I loading. The mode II load did not significantly affect the crack propagation rate. Seo et al. (2010) evaluated the mixed-mode FCG of CTS specimens with and without circular micro defects experimentally and numerically. The interaction between the crack and the circular micro defects was observed. The crack paths observed through experiments were compared with those obtained with the FE analysis using the maximum tangential stress (MTS) criterion. The results indicated that when the crack reached the micro defect, the crack growth rate was found to increase. The predictions of the crack paths with the MTS criterion were found to be inaccurate when the crack reached the micro defect.

The inclined semi-ellipse surface cracks in a rectangular steel plate under tension load were evaluated by Soh and Bian (2001). The inclination angles of the crack vary from 0^o to 90^o. They modified the maximum tensile stress criteria and the minimum strain energy density criteria for the crack growth direction by adopting the von Mises elasto-plastic stress. The crack growth directions obtained using the modified criteria were in good agreement with the experimental data. Bian and Lim (2003) conducted a similar research which incorporated the crack propagation threshold into the effective strain energy density factor range for calculating the crack growth rate. It was found that the behaviour of the fatigue crack extension was influenced by the crack propagation threshold and the crack depth. Forth et al. (2003) used the body force method and experiments to evaluate the crack growth and crack direction of an inclined surface crack in ASTM E740 specimens made of titanium alloy subjected to tension. The maximum circumferential stress criterion was employed to predict the direction of crack propagations. The Paris-like equation by setting ΔK with ΔK_{eff} was used to evaluate the crack growth rates. The predictions of the crack growth and crack direction were found to be in fair agreement with the experimental data. Varfolomeev et al. (2014) conducted experimental and numerical works on the single edge bend and single edge tension specimens under Mode I and mixed-mode I-II loadings. The extended finite element method (XFEM) was used to analyse the crack path and calculate the SIFs. It was concluded that the mixed-mode FCG rate is possible to be predicted by using Mode I FCG data. Ayatollahi and Torabi (2009, 2010) investigated the fracture behavior in the U-notched three-point-bending specimen made of PMMA material under the mixed-mode loads. They proposed a brittle fracture criterion for U-notch specimens. The criterion was developed based on the MTS criterion. Ayatollahi and Aliha (2009) used diagonally loaded square plate (DLSP) specimen made of PMMA to evaluate pure mode I, pure mode II and mixed mode I/II stress intensity factors. A modified MTS

criterion by considering the effects of T-stress have used to evaluate the experiment results obtain by this specimen test configuration.

The mixed-mode I-II fatigue cracks subjected to remote combined tension and shear stress in a plate were evaluated numerically and experimentally by Alegre and Cuesta (2010). They used the ANSYS finite element software to simulate the propagation and direction of an edge crack. The crack propagation rate was predicted using the Paris law by setting ΔK equal to an effective stress intensity factor range ΔK_{eff}. The crack direction was determined by using the maximum tangential stress criterion. Based on the comparison with experimental data, the method was found to have an effective ability in predicting the crack direction in an axisymmetric component. The initial crack angle was found to have insignificant influence on the crack propagation. Sutton et al. (2001) applied combined tension-torsion loading on an edge-cracked plate to evaluate the crack path evolution and crack surface shape based on the COD measurements. It was observed that tunnelling and slant fractures occurred on the crack during loading. The tunnelling was found to increase as the torsion to tension stress ratio decreased.

The calculations of the mixed-mode I-II SIFs have been reported by many researchers. Bittencourt et al. (1992) presented a comparison of the K_I and K_{II} values of an inclined centre crack in a plate under tension. The SIFs analyses were carried out using three different methods that are available in the FRANC finite element code, i.e. the displacement correlation method, the J-integral and the modified crack closure integral method. Beghini et al. (1999) employed the FEM to obtain the analytical expressions for the K_I and K_{II} of an inclined edge crack in a semi-infinite plate under uniform biaxial loads. Xiao et al. (2004) used hybrid crack element (HCE) in the finite element method to evaluate the mixed-mode SIF of an edge crack under combined tension and shear stress. Yan (2006) used the crack-tip element and the constant

displacement discontinuity element of the BEM to calculate the mixed-mode SIF of an offset edge crack in the three point bending and shear specimens. Morais (2007) used the body force method to calculate the K_I and K_{II} of a centre-cracked plate under remote tensile and shear stress using the finite element method. The methods computed the SIFs based on the forces on the nodes along a certain distance from the crack tip. Then, the extrapolation technique was carried out to evaluate the SIFs. Souiyah et al. (2008) determined the K_I and K_{II} values of a single edge-cracked plate containing a hole by using the displacement extrapolation technique. Shahani and Tabatabaei (2008) calculated the mixed-mode I-II SIFs of four point bending specimens for different loading position and crack location by using the FEM. Albinmousa et al. (2011) proposed closed-form solutions of the K_I and K_{II} for any combination of the crack inclination angle and the ratio of the crack length to the plate width in a single edge inclined notch plate tension specimen using the 2D ANSYS finite element codes. Beghini et al. (2012) used the analytical weight function method to evaluate the K_I and K_{II} of an inclined edge kinked crack in a semi-infinite plate. The method considered the principal geometrical parameter such as the initial inclination angle, the kinked angle and the ratio between the lengths of the two crack segments.

2.9.2 Mixed-mode I-III

Mixed-mode I-III crack conditions can be found in many types of engineering components such as vehicle shaft, heavy rotor of turbines and generator and complex shape components. Experimental studies on the angled-slit mild steel beams under the mixed-mode I-III loading were conducted by Pook (1985). He confirmed that the mixed-mode I-III loading produced formations of Mode I branching cracks that were induced by Mode III displacements. Yates and Mohammed (1996) proposed a method to predict the crack propagation rate of an inclined crack in three-point bend specimens by using Mode I fatigue crack growth data. The method was made based on the

relationship between the local mixed-mode conditions of the crack twists and the pure Mode I condition. Lazarus and Leblond (1998) and Lazarus et al. (2001b) evaluated the crack paths of inclined pre-cracked beams subjected to bending load. They observed the variations of the kinked angle along the crack front at the initial crack propagation due to the gradually-twisted crack front. When the crack front is not able to twist as a whole, the segmentation of crack front occurs to split into two zones (the largest of which the twists have the direction leading to Mode I) to form the type of extension as shown in Figure 2.11. The twist rates of the cracks were predicted by maximizing the overall energy release rate. Lazarus et al. (2001a) evaluated analytically the SIFs along the crack front based on the twist and segmentation of the crack by using the combined 3D matched asymptotic expansion and conformal mapping method.

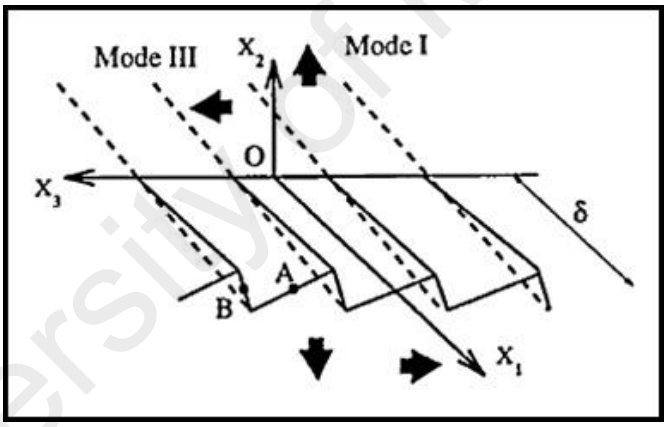

Figure 2.11: Crack front segmentation in mixed-mode I-III (Lazarus & Leblond, 1998).

Pons and Karma (2010) evaluated the mixed-mode I-III crack front evolution through the fracture simulations using the phase-field method. It was found that the unstable crack propagation was observed and the crack front deformed helically which evolved nonlinearly into a segmented array of finger-shaped cracks. Wei et al. (2011) used Richard's special mixed-mode loading device (Richard & Benitz, 1983) to evaluate the crack growth of an edge crack in a thin sheet under combined Modes I-III loads. The CRACK3D FEM software was used for the simulations to verify the experimental

results. Ayatollahi (2015) developed a new loading fixture to perform fatigue crack growth experiment under pure mode I, pure mode III and mixed mode I/III conditions. The fracture load and out-of plane fracture angle obtained from the mode I/III experiments shows a good agreement with those estimates by MTS criterion of finite element analysis. Aliha et al. (2015) used inclined edge crack disc specimen under three point bend loading to evaluate mixed-mode I-III fracture behaviour numerically by ABAQUS finite element code. Mode I, Mode III and mixed-mode I-III SIFs and T-stress were calculated for different crack depths, disc geometry, loadings span and crack inclination angle.

2.9.3 Mixed-mode II-III

Hellier et al. (1987) developed a practical test rig for the fatigue testing of notched steel specimens subjected to any combination of Modes II and III loadings. He and Hutchinson (2000) used the ABAQUS FEM to calculate K_{II} and K_{III} along the crack front of a semi-elliptical surface crack on a semi-infinite solid subjected to shear stress. Doquet et al. (2010) conducted crack growth tests on Maraging steel and Ti-6Al-4V. It was observed that Mode III contributes insignificantly to the crack growth than Mode II as a result of the interlocking and friction of the asperities of the crack surfaces. Vojtek et al. (2014) used a loading device that was able to transform the applied tensile force to the shear loading for investigating the mixed-mode II-III FCG of circumferentially-notched cylindrical specimens.

2.9.4 Mixed-mode I-II-III

The hollow and solid cylindrical specimens were the well known specimens used in analysing the mixed-mode I-II-III crack problems. Socie et al. (1987) tested a small part-through crack in thin-wall tubular specimens made of 1045 steel and Inconel 718 subjected to tension, torsion and combined tension-torsion loads. An equivalent strain

based intensity factor was calculated using the maximum shear strain amplitude and the tensile strain normal to the maximum shear strain amplitude plane. These strain based intensity factors were used to correlate the mixed-mode crack growth rate. It was observed that the nucleation and initial growth of cracks occurred on the planes of the maximum shear strain amplitude for both materials even under tensile loading. Shi et al. (2000) investigated numerically and experimentally the mixed-mode crack initiation and propagation in the internal V-notched circular ring specimen made of austenitic stainless steel. They used the maximum tangential stress and energy release rate criteria in the FEA to identify the crack initiation at the notch root and the direction of the branched cracks initiating from the parent crack. It was concluded that the orientations of crack initiation and propagation were the function of the inclined angle of loading. Tanaka et al. (2006) investigated the fatigue crack propagation of a crack emanating from a circular hole in thin walled tubular specimens made of low-carbon steel subjected to cyclic torsion and the cyclic torsion load with and without the superimposed static and cyclic axial loads. It was observed that the crack paths follow a plane on which the total range of the normal stress was a maximum. The crack paths for cases cyclic torsion were nearly identical with the combined cyclic torsion and static tension. Shahani and Habibi (2007) applied the FEM to calculate the SIFs of a circumferential semi-elliptical surface crack in the outer surface of a hollow cylinder subjected to the combined tension-bending-torsion loads. They used sub-modelling technique to obtain very high fine meshing around the crack front. It was reported that superimposing the torsion load into the tension and bending loads caused a non-symmetrical distribution of the SIFs along the crack front which in turn resulted in the non-symmetric crack growth. Dao and Sellami (2012) used the FEM to determine the SIFs and crack growth of a circumferential semi-elliptical crack on the external surface of a hollow cylinder under the combined bending and tension loads for different ellipse

crack aspect ratios, bending to tension stress ratios and crack depth to cylinder thickness ratios. It was concluded that the ellipse crack aspect ratio at the final increment decreased due to the tension load. For a given cylinder geometry, the final ellipse crack aspect ratio would depend on the ratio of bending to tension stress ratio. Predan et al. (2013) investigated the fatigue crack growth of a surface crack in a hollow cylinder subjected to torsion load by using the ABAQUS FEM. They confirmed that Mode II SIFs of the crack front were found to be dominant. Also, Mode II SIFs were observed to be more significant during the stable crack-initiation than those of Mode III. Moghaddam et al. (2013) used the ABAQUS FEM to evaluate the effects of the gradation of the elastic modulus on the mixed-mode SIFs of a surface crack in the outer and inner wall of a hollow cylinder. They confirmed that the gradation of the elastic modulus had a significant influence on the magnitude and distribution of the mixed-mode SIFs along the crack front.

Thompson and Sheppard (1992) carried out experimental and numerical works on fatigue crack growths of an inclined surface crack in notched and plain shafts under the axial and torsion loadings. Noda and Takase (2003) calculated K_I, K_{II} and K_{III} for various V-shaped notched round bar under tension, bending and torsion using the singular integral equation of the body-force method. The solutions of the integral equations were obtained by approximating the unknown body force densities through the piecewise smooth functions. Citarella and Cricrì (2010) used the BEASY and ANSYS software to analysed the fatigue crack growths and crack paths of a crack initiating from two corner points of a quarter-circular notch on a solid shaft subjected to torsion loads. The mixed-mode I, II, III SIFs along the crack front were evaluated by using the J-integral and crack opening displacement (COD) method and the crack direction was evaluated using the minimum strain energy density criterion. The SIF results obtained from both of software were shown to be in good agreements. Ismail et

al. (2011) calculated the SIFs of a surface crack on a round solid bar under pure tension, pure torsion, combined tension-torsion and bending-torsion load using the ANSYS FEM. The K_{II} and K_{III} values due to the torsion load and the equivalent stress intensity factors K_{eq} due to the combined tension-torsion and bending-torsion loads were presented. However, only the SIF values for the deepest point of the crack front were presented and the K_I and K_{II} values under the combined tension-torsion and bending-torsion loads were not evaluated. Okada et al. (2013) developed the FEM based software which uses the quadratic tetrahedral elements and the virtual crack closure-integral method (VCCI) to evaluate the SIFs and the Paris law based crack growths of an inclined surface crack in smooth and stepped solid cylinders subjected to torsion load. The crack growth of a transverse surface crack in a smooth cylinder subjected to combined tension and torsion loads was also evaluated. Citarella et al. (2014) evaluated the SIFs and fatigue life of a straight front surface crack on cylindrical steel subjected to axial tension and combined tension-torsion load using the BEASY software and conducted the experiments for the purpose of verification. They concluded that the fatigue life decreased when the cyclic torsion load was superimposed on the cyclic tension load. Branco et al. (2014) evaluated numerically and experimentally the fatigue crack growths in a laterally-notched round bar under combined bending-torsion loads. Fatigue test were performed under the constant amplitude with $R = 0$. Three ratios of bending to torsion load were examined. The FE analysis used the Coffin–Manson model for the fatigue life predictions and the crack paths and the initiation sites were controlled by the distribution of the maximum principal stress field along the notch surface. It was concluded that the shear stress amplitude reduced the fatigue life significantly.

Shanyavskiy (2011) evaluated experimentally and numerically the crack growth rate and direction of an edge crack emanating from a hole at the centre of cruciform specimen under the constant and variable amplitude biaxial loads. It was observed that

the striation spacing and the crack-growth rate increased as the angle of the out-of-phase biaxial loads increased (in the range of phase angle from 0^0 to 180^0). Fremy et al. (2014a) and Fremy et al. (2014b) investigated experimentally and numerically the mixed-mode I-II and mixed-mode I-II-III fatigue crack behaviours in cruciform specimens made of 316L stainless steel. They concluded that the load path significantly influenced the crack growth rate. Fatigue crack growth rate increased when Mode III loading was added to Modes I-II loading sequence. Misak et al. (2013) used the ABAQUS software and a biaxial fatigue test machine to evaluate the fatigue crack behaviour of Al 7075-T6 cruciform specimens containing a small hole at the centre. A notch was located at 45 degree to the specimen's arm. The specimens were loaded by the in-plane biaxial tension-tension and uniaxial tension. Two bi-axilialty ratio, λ =1 and 1.5 and stress ratio R = 0.5 were used in the analyses. It was found that stable crack growth rate was same between those under biaxial tension λ = 1 and uniaxial tension. The crack growth under biaxial tension with λ = 1.5 was faster than that under uniaxial tension.

Buchholz et al. (2004) evaluated an inclined crack in single edge notched specimens subjected to three point bending or four point shear loads using the ADAPCRACK3D finite element software. The fatigue crack growths were analysed based on the mixed-mode strain energy release rate (SERR) that was calculated by using the modified virtual crack closure integral (MVCCI) method. They confirmed that under pure in-plane shear and pure out-of-plane shear loadings, both Modes II and III were observed along the crack front. Barlow and Chandra (2005) simulated the crack propagation of corner and side cracks located in the surface contact of the fan blade attachment of an aircraft engine subjected to the multi-axial load using the FRANC3D software. The COD method was used to compute the K_I, K_{II}, K_{III}. The crack growth life and the crack path were determined by using Forman-Newman-de Koning (FNK) crack

growth model and the plane stress criterion, respectively. It was observed the K_I and K_{III} had a strong interaction. Ayhan (2004) and Ayhan (2007) presented the K_I, K_{II} and K_{III} of corner and surface cracks in finite-thickness plates under tensile loading for different crack deflection and inclination angle as well as different plate thickness using the FRANC3D software. They reported that the mixed-mode SIFs increased as the plate thickness decreased. Dhondt (2014) developed finite element software called CRACK-TRACER3D for simulating mixed-mode fatigue crack growths in the four-points bending and compact tension shear rotation specimens.

2.9.5 Mixed-mode SIFs and fatigue crack growth in prismatic bars

Only few studies have been conducted to evaluate the stress intensity factor and fatigue crack growth of non-round components such as prismatic bar under combined loading. Nobile (2000) used the strain energy density theory to analyze the crack growth of edge-cracked beam under Mode I, Mode II and mixed-mode I-II loads. He developed a simple method to calculate the stress intensity factors by using the elementary beam theory. Citarella and Buchholz (2008) investigated the fatigue crack growth behaviour of an inclined edge crack in three-points bending specimen and cantilever beam under bending or torsion loading using the BEASY and ANSYS FEM software. The *J*-integral and minimum strain energy density criterion were used to determine the stress intensity factor and the crack growth direction, respectively. Rozumek and Marciniak (2012) experimentally investigated the fatigue crack growth in rectangular cross-section specimens made of 10 HNAP (S355J2G1W) steel under combined bending and torsion loadings.

2.10 Summary

Relevant literature reviews on the uses of the fracture mechanics concept and the methodologies used for evaluating the SIFs and fatigue crack growth by various loadings were presented. It may be generally summarized as follows:

- Most of the works on the fatigue crack growth that have been reported in literature were using the Paris's crack growth law for the simulations.
- There are no sufficient information for the SIFs and fatigue crack growth behaviours of a surface crack in a solid bar under combined load that have been reported in literature. In particular, not many analyses on fatigue crack growth in the components that have a high stress concentration such as V-shaped notched round bar have been reported. Only a few studies on the fatigue crack growth in the non-round components such as prismatic bar, especially subjected to combined axial-torsion loading were reported. In numerical studies, modelling of a torsional load in a non-round component was found to be quite tedious.
- The guideline for introducing an initial surface or corner crack in a specimen is not reported in detail in literature.

Therefore, any relevant knowledge on the SIFs and fatigue crack growth under combined loadings remains open for updates. With the rapid developments in the computer technology to overcome the high cost of the experimental tests, numerical simulations are always desirable to efficiently simulate the fatigue crack growth under complex/combined loadings. However, the experimental work is necessary and often used to validate the results obtained from the numerical modelling. In the following chapter (Chapter 3), the methodology used to accomplish this research project is presented in detail.

CHAPTER 3

METHODOLOGY

3.1 Introduction

Fatigue crack problems can be evaluated through analytical, numerical and experimental approaches as presented in Chapter 2. Analytical method is not applicable to the complex geometries and problems such as fatigue crack growth under combined loading. The numerical method is desirable due to the rapid development in the computer capability for modelling and simulations. Although the experimental methods are time consuming and expensive, however, they are required to validate the numerical results of fatigue crack solutions. In this work, numerical simulations and experimentations are performed to evaluate the fatigue crack growth under combined loadings. The numerical simulations are carried out by utilizing the boundary element method software package of BEASY (BEASY, 2013). A number of the fatigue crack growth tests using a multi-axial fatigue testing machine are conducted. Fractography analyses are also conducted to identify the fracture surfaces. In particular, a manufacturing technique for generation of an initial surface crack in the specimens is presented. In the following sections, the research methodology used in this research is presented in detail.

3.2 Numerical simulations

The DBEM-based software of BEASY (BEASY, 2013) was developed to evaluate mechanical fatigue crack growth and contact problems. It has been known to provide accurate fracture mechanics solutions for predicting the SIFs, fatigue life, crack growth rate and crack growth direction. BEASY (BEASY, 2013) uses the dual boundary element method (DBEM) formulations developed by Portela et al. (1992) for 2D crack problem and by Mi and Aliabadi (1992) for 3D crack problem. Like other

domain-base numerical analysis software, BEASY (BEASY, 2013) has the pre-processing, processing and post-processing steps to cover the modelling, analyses and plotting of the results of fatigue crack growth simulations.

3.2.1 Dual boundary element method (DBEM)

The DBEM solves general crack problems in a single region by implementing the displacement boundary integral equation (DBIE) at the collocation point on one of the crack surface/boundary and the traction boundary integral equation (TBIE) on the other surface/boundary. The crack surfaces are modelled with the discontinuous elements which allow for accurate integration of finite part integrals without defining the special or grade elements. The advantages of the DBEM become apparent when this technique is applied to the crack growth simulation where crack extension process is simulated by introducing new boundary elements in each crack growth increment (Dirgantara & Aliabadi, 2002).

The dual boundary integral equations for modelling crack problems were described by Aliabadi (2003). Consider a co-planar crack surface as shown in Figure 3.1 where $S=S^{+}+S^{-}+S^{*}$ is domain surface. The displacement integral equation at the collocation point x^{+} on the upper crack surface S^{+} and the traction boundary integral equation at the collocation point x^{-} on the lower crack surface S^{-} can be formulated as Eqs. 3.1 and 3.2 respectively

$$\boldsymbol{C_{ij}(x^{+})u_j(x^{+}) + C_{ij}(x^{-})u_j(x^{-}) + \int_S T_{ij}(x^{+},x)u_j(x)dS} = \boldsymbol{\int_S U_{ij}(x^{+},x)t_j(x)dS} \quad \textbf{(3.1)}$$

$$\boldsymbol{\frac{1}{2}t_j(x^{-}) - \frac{1}{2}t_j(x^{+})} = \boldsymbol{n_i(x^{-})\int_S D_{kij}(x^{-},x)t_k(x)dS - n_i(x^{-})\int_S S_{kij}(x^{-},x)u_k(x)dS} \quad \textbf{(3.2)}$$

where x is boundary point, the notations i and j are the Cartesian components, n is the outward normal vector, T_{ij} and U_{ij} are the Kelvin's traction and displacement fundamental solutions respectively, $D_{kij}(x^-,x)$ and $S_{kij}(x^-,x)$ are the linear combinations of derivatives of $U_{ij}(x^-,x)$ and $T_{ij}(x^-,x)$ respectively, the coefficient C_{ij} is given by δ_{ii} (Kronecker delta function) for a smooth boundary at point x^+ and x^-, u_j and t_j are the known values of displacement and traction on the boundary S.

In order to implement the DBEM numerically, the boundary domains are discretized into a number of elements. The general modelling strategy of 3D crack problem can be roughly summarised as follows (Mi & Aliabadi, 1992):

- Crack surfaces are modelled with the discontinuous quadratic elements;
- The displacement integral equation (Eq. 3.1) and the traction integral equation (Eq. 3.2) are applied for collocation on the upper crack surface S^+ and on the lower crack surface S^-, respectively.
- The remaining surface S^* are modelled with the continuous quadrilateral elements and the displacement integral equation (Eq. 3.1) is applied for collocation on this surface;
- Surface intersecting a crack surface are modelled with edge-discontinuous quadrilateral or triangular elements. Due to this elements, the special treatment does not required for crack-edge corner or crack intersecting because they are not located at nodal point where the collocation is performed.

The DBEM uses the aforementioned discretization method in order to make it more robust, versatile and suitable for model crack propagation (Cisilino & Aliabadi, 1999). It is due to the ability of this method to update the changing on geometry of the numerical model.

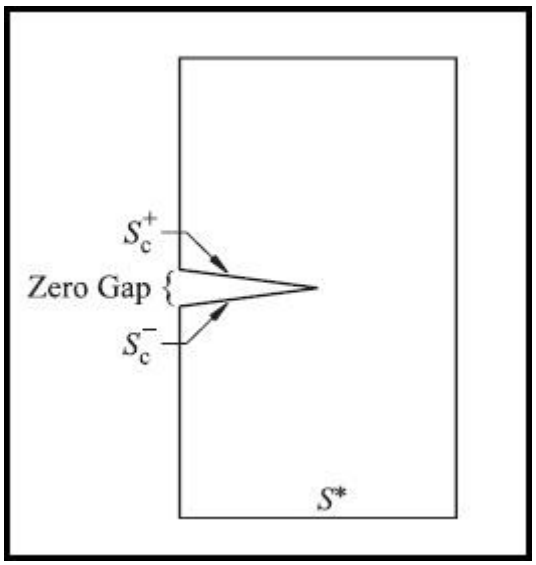

Figure 3.1: Co-planar crack surfaces (Aliabadi, 2003).

3.2.2 Procedure simulations

The general procedures to develop BEM model and crack growth simulations can be presented in the form of a flowchart as shown in Figure 3.2. The BEM models are developed by using the BEASY User Interface wizard that allow a user to create model geometry, define material properties, create boundary mesh, applied load and boundary condition as well as perform a stress analysis. The crack modelling and crack growth simulations are performed in the BEASY Crack Growth wizard.

3.2.2.1 Model generations

The BEM model can be generated using BEASY User Interface for all of the analysis types that are available in the BEASY software package. For 2D problem, the model is constructed by defining coordinate points to create the boundary lines. While, for 3D problem, the model is developed by defining coordinate points to create the boundary lines and then create the boundary surfaces (patches) using the associated boundary lines. A BEM model may consist of several surfaces/patches that may be quadrilateral, triangular or combined shape depending on the shape and complexity of the domain geometry. However, the quadrilateral shape is most commonly applied in

the modelling due to the simplicities in meshing. The quadrilateral shape surface is preferably by four boundary lines while the triangular shape surface is defined by three boundary lines. The orientation of surface patches and lines need to be in outward normal to avoid any overlaps.

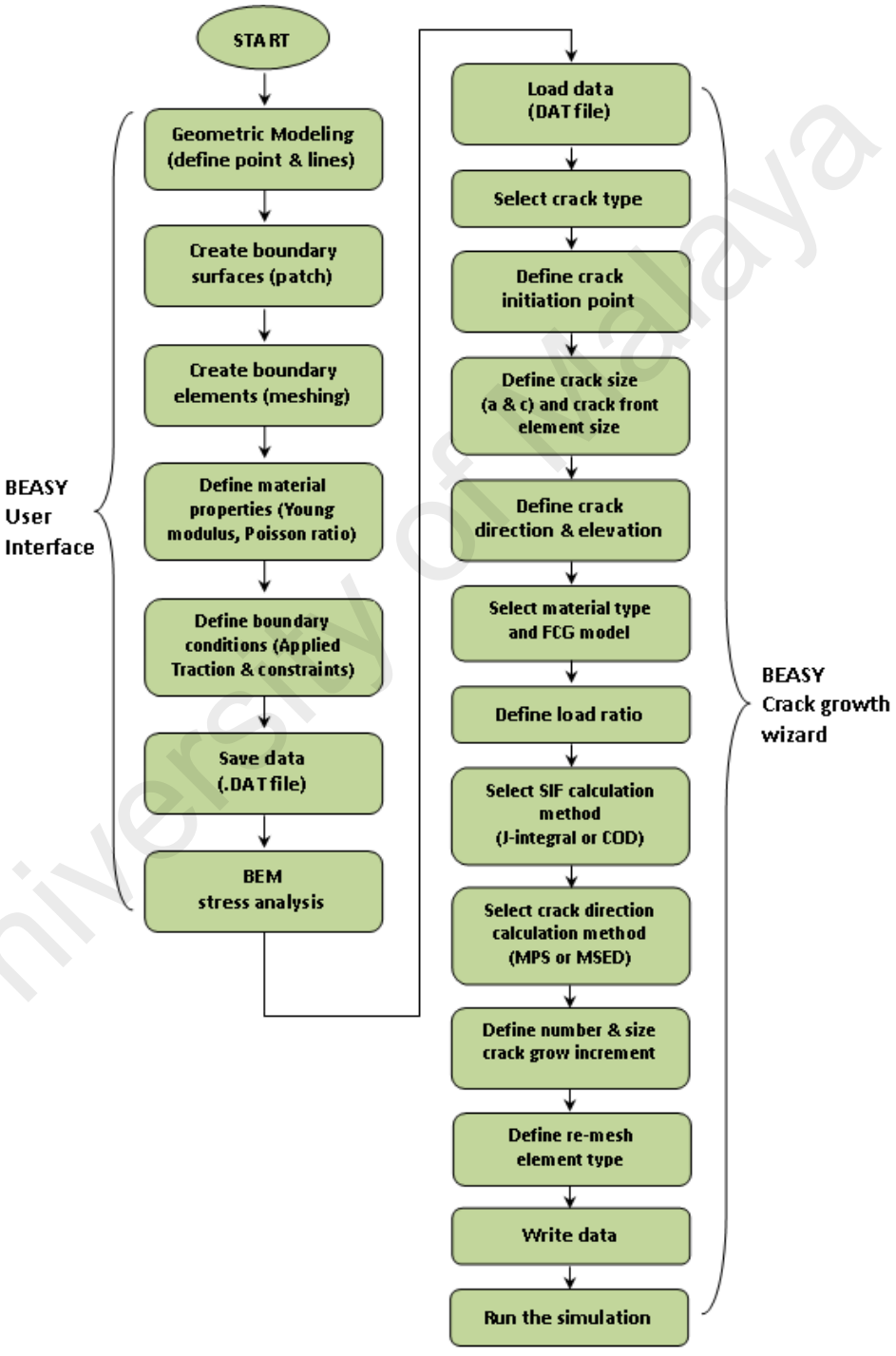

Figure 3.2: Modelling and simulation procedure in BEASY.

Meshing of each boundary surface is performed by defining the mesh element type and mesh grading. The quadrilateral and triangular element types are available for 3D models. The mesh grading is defined by the number of elements on a boundary surface (patch). Different mesh grading can be done in different patches. Summations of elements on each patch are defined the total number element of a BEM model. The displacement constraints and mechanical loadings can be applied on a node or a patch by defining their values and directions. In BEASY (BEASY, 2013), a mechanical loading is defined with a traction which represent the applied stress on the corresponding boundary surface. The mechanical constraints and loadings can be applied to more than one node or boundary surface. The stress analyses are carried out to ensure that the stress distribution under the applied loading is correct. The model generation file is then saved in a data file which is further used for the fatigue crack growth simulations.

3.2.2.2 Crack modelling and crack growth analysis

BEASY Crack Growth wizard module used to analyze the crack growth automatically. In the first stage, the data file (dat.file) of the BEASY model loaded into this module. In this module, a crack type is selected from crack library as shown in Figure 3.3. The initial crack position (defined by the mesh point), initial crack size (crack length and depth), crack direction (defined either by mesh point or coordinate position) and crack front element size are determined for the model as shown in Figures 3.4, 3.5 and 3.6. The minimum crack front element size is used to control the size of the elements along the new crack front and to have a fine representation of the crack front and more accurate SIF values. Decreasing the crack front element size will increase the number of elements which later increases the computational time. The minimum element size at the crack front should be less than one-fifth of the crack depth (BEASY, 2013). When the crack grows, the minimum element size increases and hence reduces

the number of degrees of freedom. However, re-meshing error would occur when the minimum crack front element size becomes too large to represent the crack geometry. It is possible to reduce the minimum crack front element size during the analysis at any increment by using either fracture restart wizard tool or editing the data file manually. The maximum element size at the crack front is used to control the size of the elements away from the crack front to avoid the problem in mesh quality. In BEASY, only a single crack face is modelled with a simple surface mesh, while a second "dual" surface is generated automatically (Mellings et al., 2005).

In next step, the fatigue loading cycle can be defined as either of constant and variable amplitude loads as shown in Figure 3.7. The constant amplitude load is defined by specifying the load ratio value of *R*, while the variable amplitude load has to be defined using a load spectrum file (lsp.file).

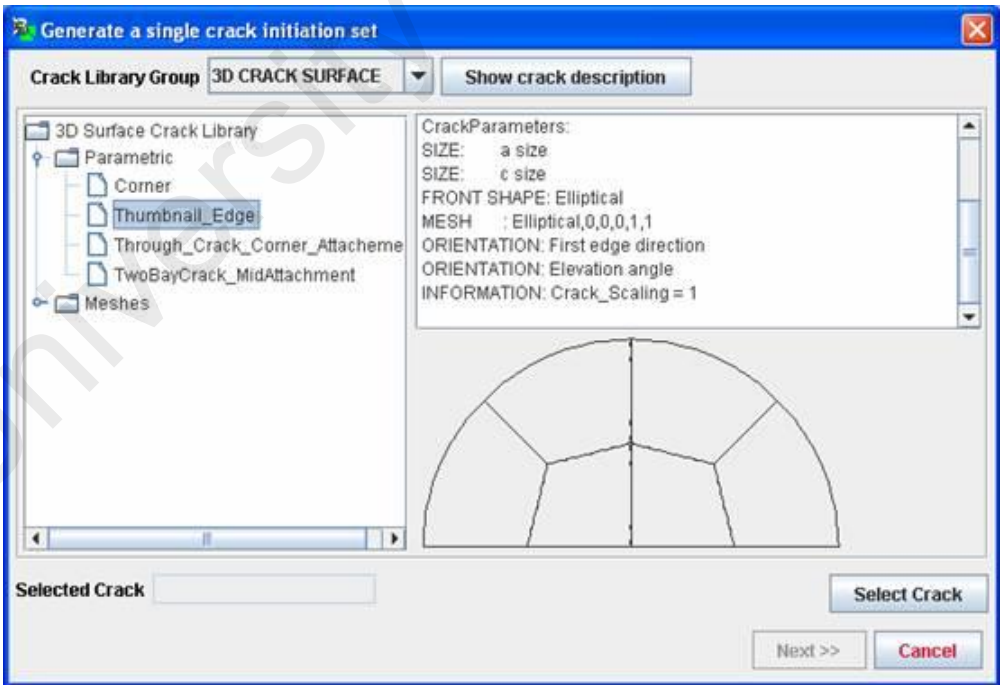

Figure 3.3: Selecting a single thumbnail crack in BEASY (BEASY, 2013).

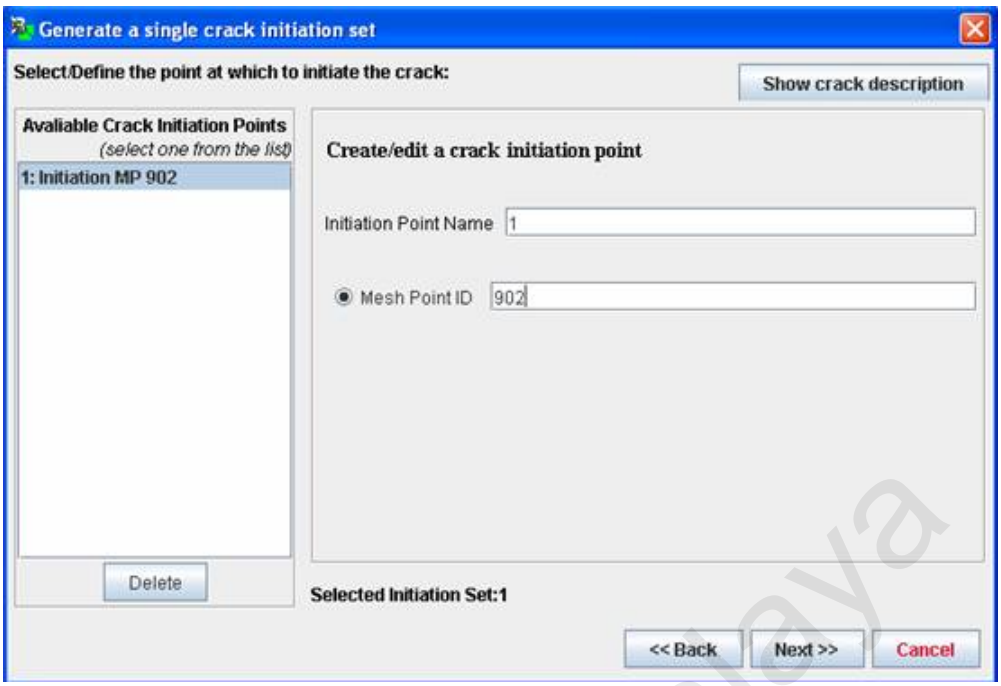

Figure 3.4: Defining crack initial position point in BEASY (BEASY, 2013).

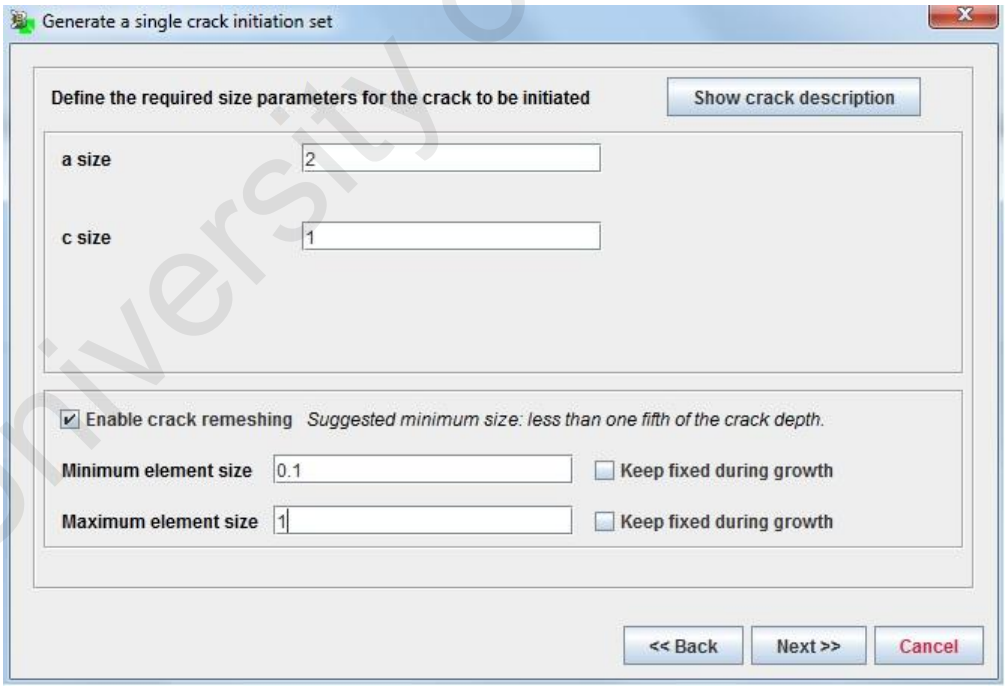

Figure 3.5: Defining crack size and crack front element size in BEASY (BEASY, 2013).

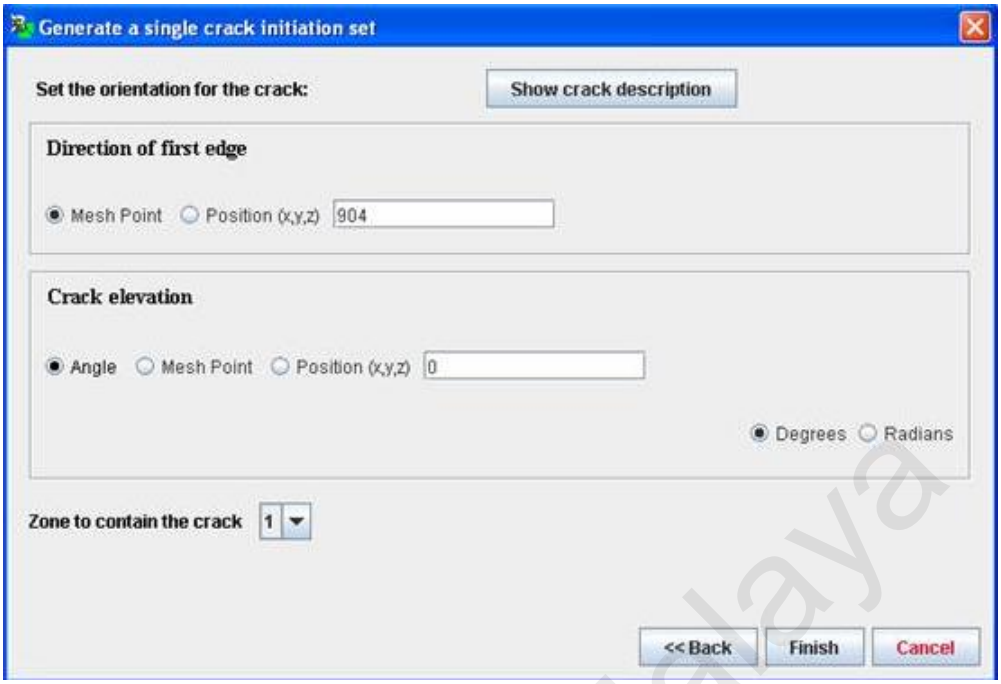

Figure 3.6: Defining crack direction and crack elevation in BEASY (BEASY, 2013).

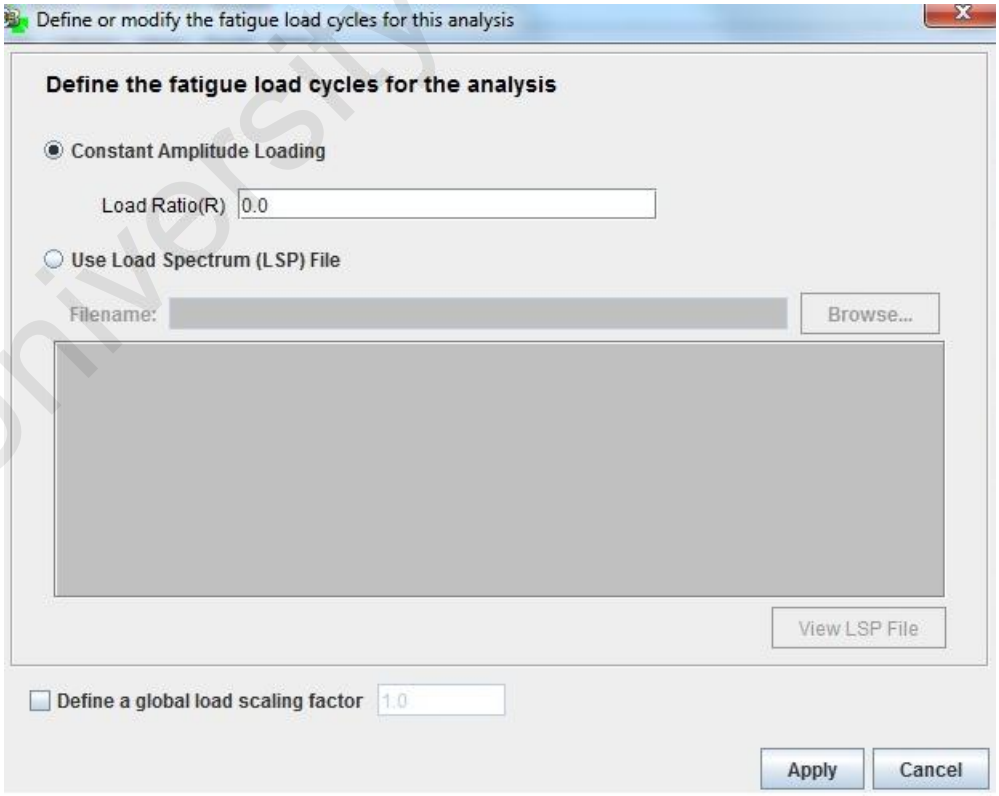

Figure 3.7: Defining the fatigue loading in BEASY (BEASY, 2013).

The iterative computational procedure used to simulate crack growth in BEASY crack growth wizard (BEASY, 2013) is illustrated in Figure 3.8. In the first stage, the initial crack is defined and BEASY uses the DBEM to analyze the stress of the domain. In the second stage, based on stress field around crack front, either of J-integral or COD technique was used to compute the SIFs at crack fronts (see Figure 3.9). In BEASY, the stress intensity factors for different modes (K_I, K_{II}, K_{III}) are computed, and the combination of these three modes of SIFs for an effective stress intensity factor K_{eff} value may then be computed for each point along crack front by either of Tanaka equation (Eq. 2.63), Yaoming Mi equation (Eq. 2.64), Sum of Square equation (Eq. 2.65), Maximum Principal Method equation (Eq. 2.66) (see Figure 3.10). At the third stage, the crack growth is modelled by computing the crack growth rate, the crack extension, the number of cycle and the crack growth direction. The relationship between incremental size and the number of cycle is represented by crack growth model. These models are function of the range of stress intensity factor ($da/dN=f(dK)$) that represents the change in SIF value over the loading cycle. Some crack growth models are available in the BEASY Crack Growth module including Paris, Forman, Rhodes, NASGRO models as shown in Figure 3.11. For the NASGRO crack growth model, the module includes the NASGRO database of the properties of some common materials. At fourth stage, the crack growth direction that function of the stress field around the crack front is computed by using either of the minimum strain energy density, the maximum principle stress, grow in Mode I only and multiaxiality Q-plane (see Figure 3.12). At fifth stage, after the magnitute and direction of the crack extension are known along the crack front, the model geometry is updated by adding new crack front boundary elements and a remeshing was performed to the boundary surface. At final stage, the DBEM stress analysis is repeated for the new configurations of the crack model until the defined crack growth increments are completed, or the calculated SIF exceed the

fracture toughness of the material. Figures 3.13 and 3.14 show the option for defining the number of crack growth increments, the crack growth extension per increment and the element type for remeshing crack surfaces and remain boundary surfaces.

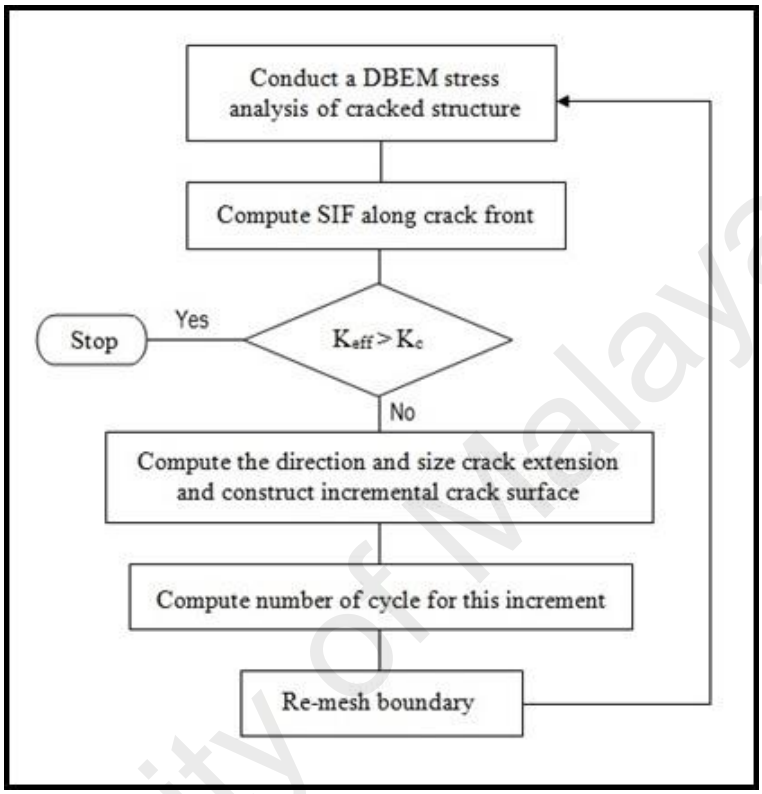

Figure 3.8: Flow chart crack growth simulation in BEASY (BEASY, 2013).

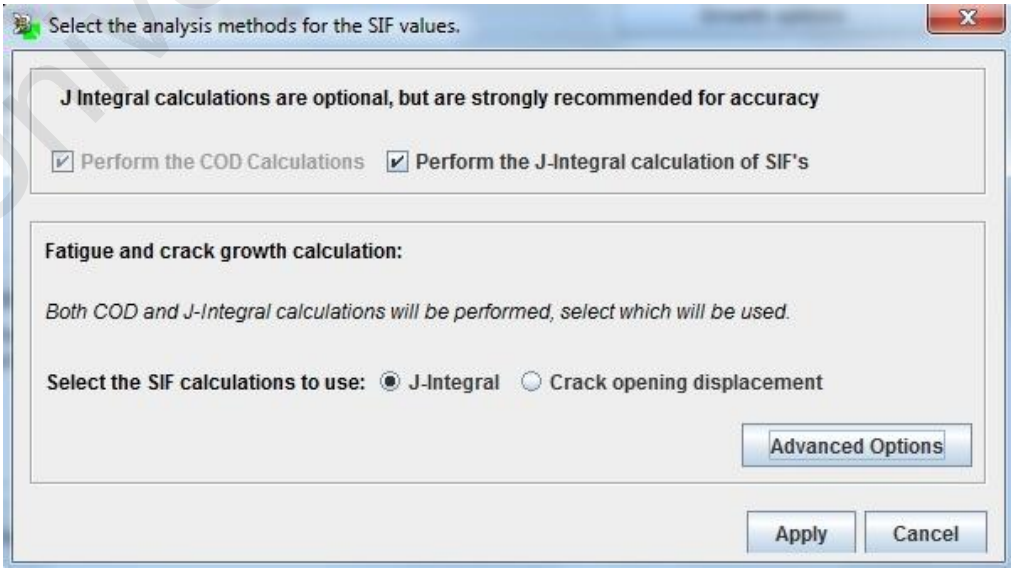

Figure 3.9: Defining the SIFs calculation methods in BEASY (BEASY, 2013).

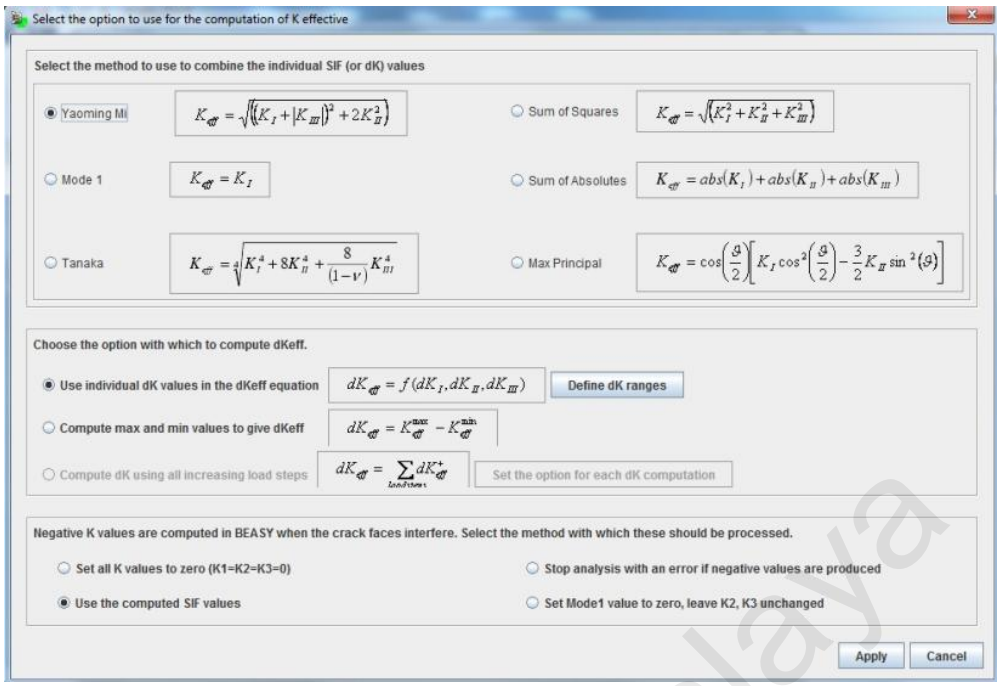

Figure 3.10: Defining the K_{eff} calculation methods in BEASY (BEASY, 2013).

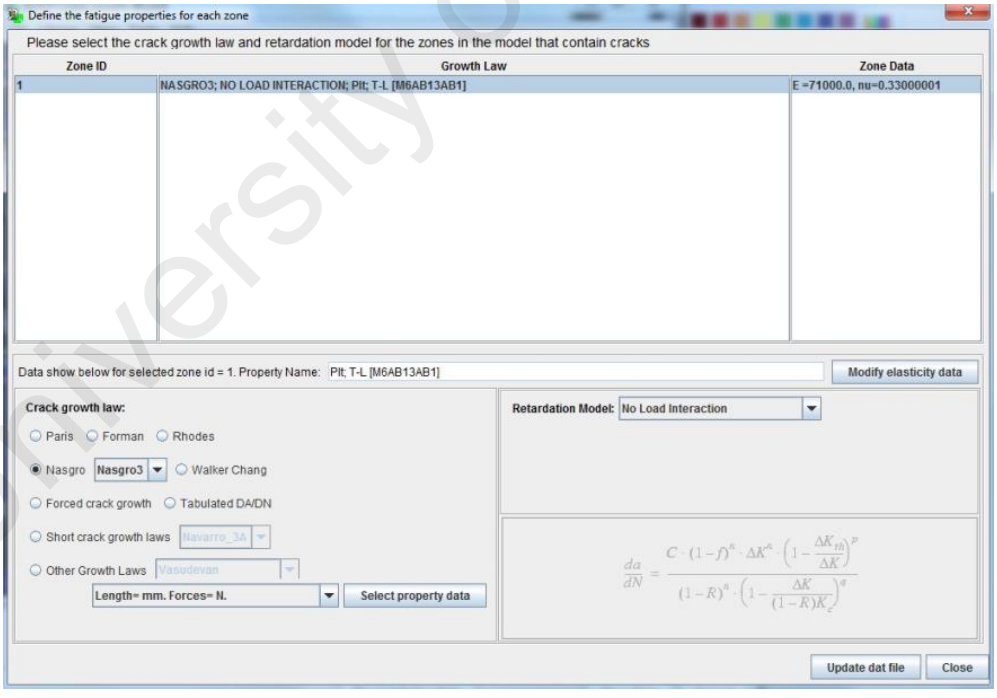

Figure 3.11: Defining the crack growth model in BEASY (BEASY, 2013).

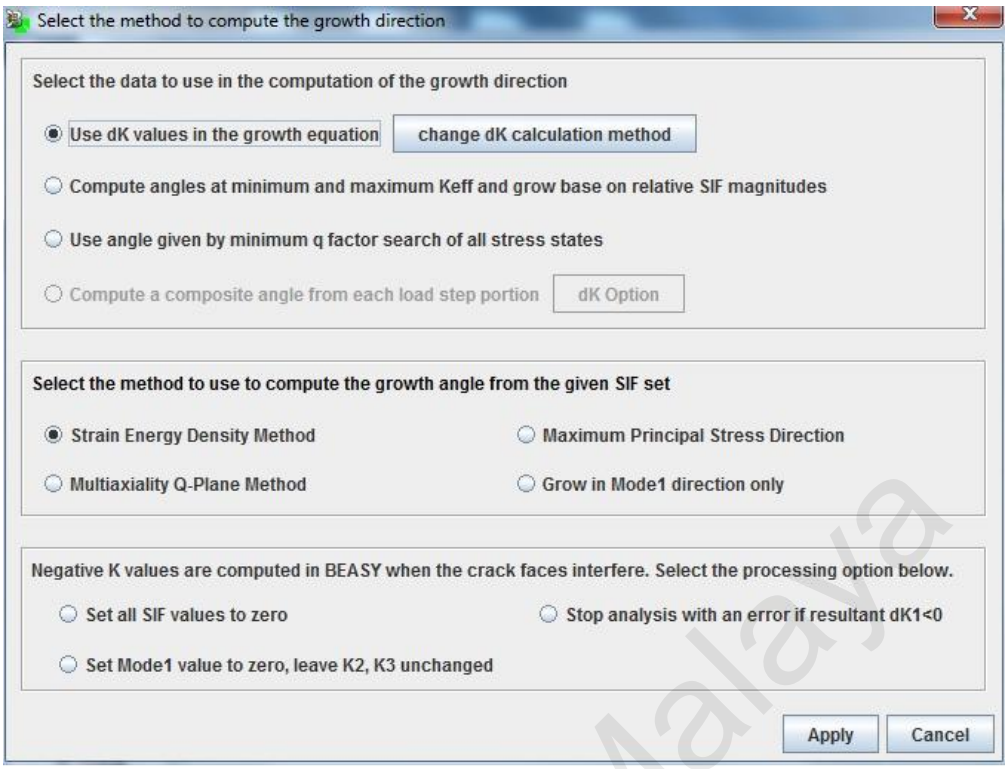

Figure 3.12: Defining the crack growth direction angle computation in BEASY (BEASY, 2013).

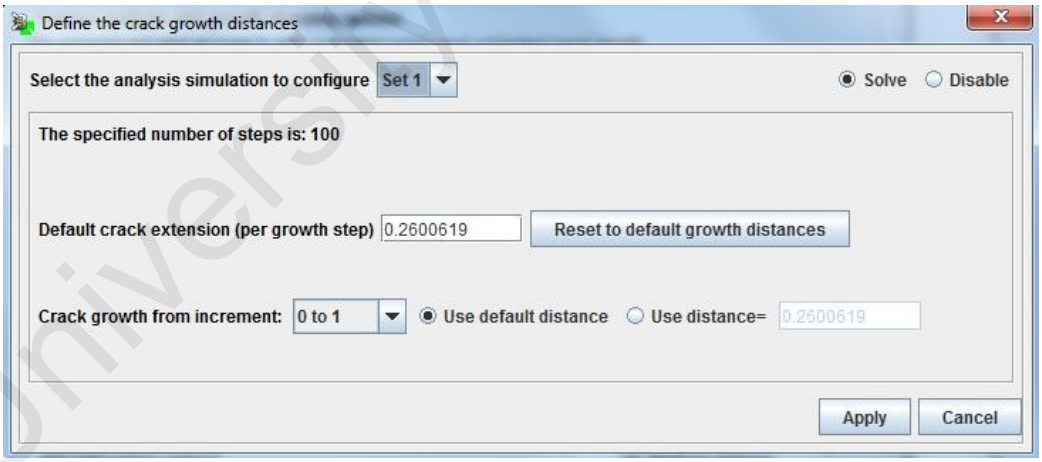

Figure 3.13: Defining the crack extension per increment in BEASY (BEASY, 2013)

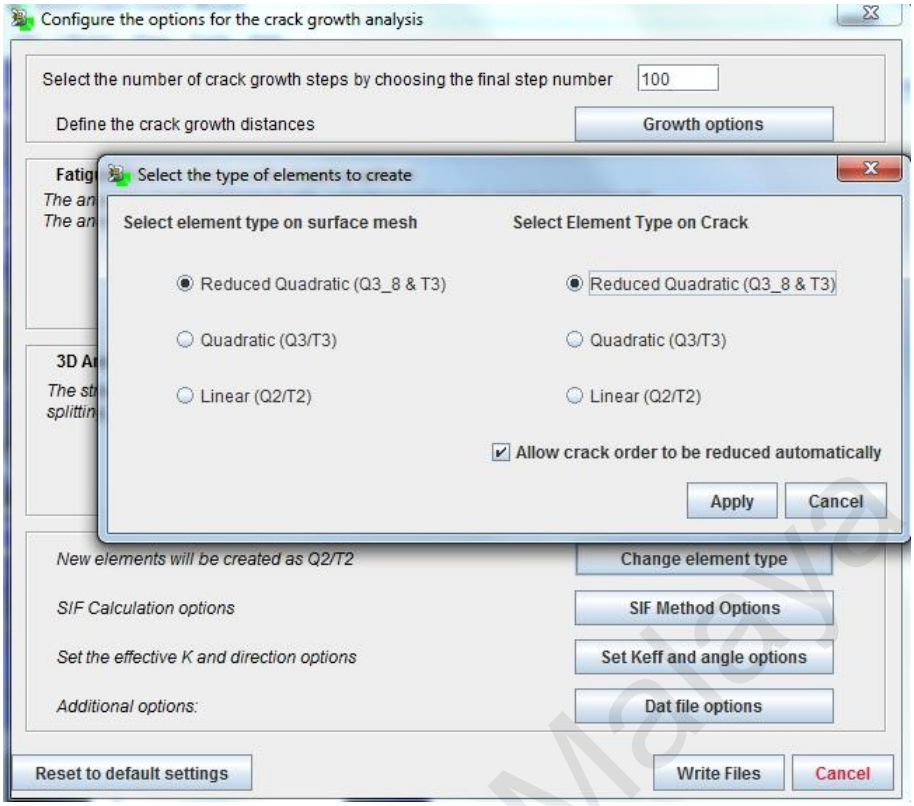

Figure 3.14: Defining the number of crack growth increments, the surface mesh and crack element types in BEASY (BEASY, 2013).

3.2.3 Surface crack in a V-notched cylinder under cyclic tension

Some studies on surface cracks in a notched cylinder have been carried out. Lin and Smith (1998; 1999) investigated crack shape evolution, crack shape deviation, and variation of the aspect ratio of a surface crack in a semi-circular notched round bar. They utilized a linear elastic 3D-FEA to estimate SIFs along the crack front and used Paris's equation for simulating fatigue crack growths. Guo et al. (2003) studied the effects of the stress concentration coefficients K_t and notch geometry on the SIFs of a semi-elliptical surface crack in notched round bars under tension load by using ANSYS FEA software. They also carried out evaluations of the SIFs of a semi-elliptical surface crack in various semi-circular types of V- and U-type annular notches. Carpinteri et al. (2006) used a 3D-FEM to compute and evaluate the SIFs and fatigue growth of an elliptical-arc surface crack in a notched round bar under cyclic tension and bending using the Paris-Erdogan law.

The present study evaluated the FCG, the SIF, and the crack shape evolution of a semi-elliptical surface crack in a full model of a V-shaped notched round bar under cyclic tension. The NASGRO crack growth rate law is used to simulate the fatigue crack growths.

3.2.3.1 Geometric modelling

Crack growth analysis of a surface crack in V-notched cylinder under tension is a preliminary study in this research. This is to examine the capability and accuracy of the BEASY software to evaluate the model that contains a crack in a high stress concentration region. The BEM model with circumferentially V-shaped notch has outer diameter cylinder *D* of 12.7 mm, length *L* of 107.95 mm, diameter notch cross section *d* of 6.35 mm, notch depth *t* of 3.175 mm, notch opening angle of 60 degree and either a notch root radius *r* of 0.529 mm or 1.588 mm as shown in Figure 3.15a. The geometries are similar to those used in (Zeng & Fatemi, 2001). The steps that are used to generate the models for notch radius of 1.588 mm and 0.529 mm are shown in Figures 3.16 and 3.17, respectively. All patches must be defined to be in outward normal direction. It is important to check the connectivity all boundary surfaces after modeling to avoid any error during stress analysis.

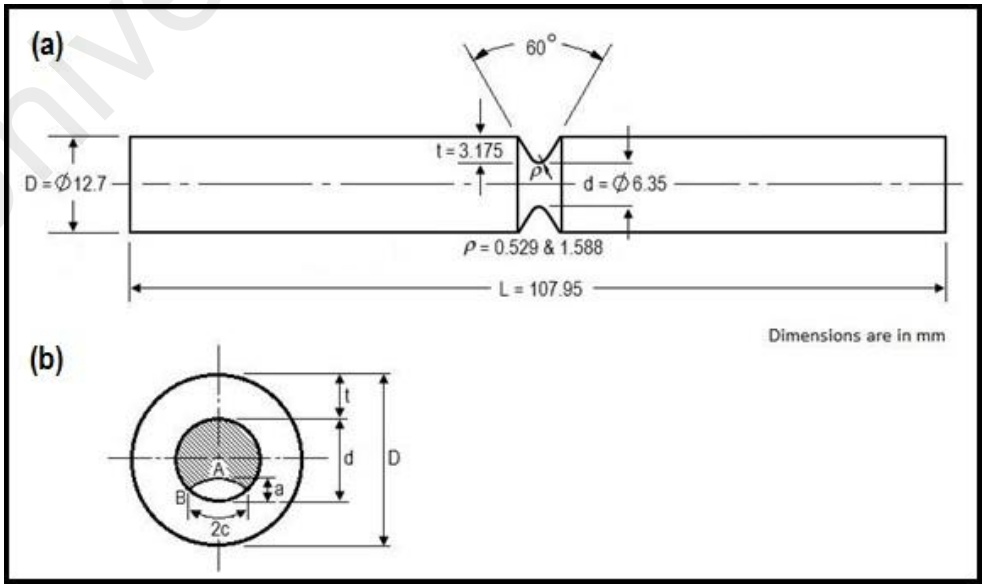

Figure 3.15: (a) Geometry and dimensions of V-notched cylinder (b) Definition of surface crack.

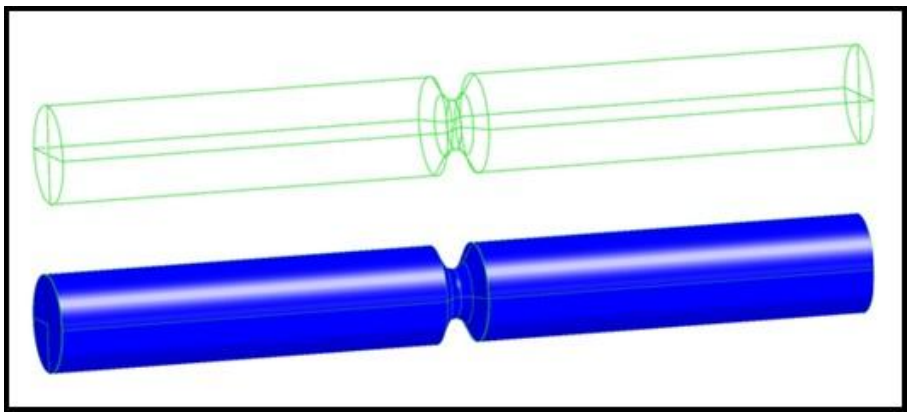

Figure 3.16: The steps to defining the boundary surfaces of a V-notched cylinder (r=1.588).

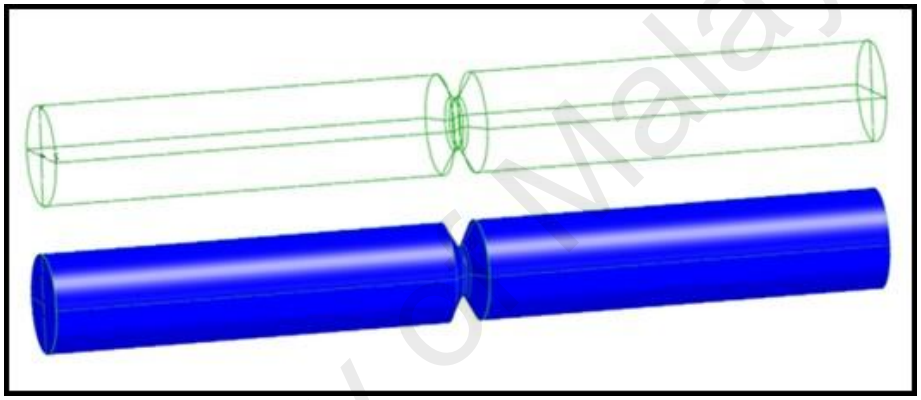

Figure 3.17: The steps to defining the boundary surfaces of a V-notched cylinder (r=0.529).

3.2.3.2 Boundary element model

The quadrilateral and triangular shape elements (485 elements) were used to discretize the entire surfaces of the model as depicted in Figure 3.18. To improve the accuracy of the stress and strain evaluations, the mesh size refinement of around 0.3 mm in the vicinity of the notch root was made. It is important to check the overlapping elements of whole model and merger any duplicate mesh points to avoid any error during the analysis. A uniform tensile stress of 30 MPa was applied to either end of the model and a fixed displacement boundary condition in *x*, *y* and *z* directions was applied to another end as shown in Figure 3.19. An initial semi-elliptical surface crack was introduced on the notch root. The crack plane was set to be normal to the axis of the

round bar. The crack geometries are set to have a crack depth a = 0.5 mm and the crack aspect ratios a/c = 0.5, 1 and 2. The details of the crack depth a and the crack length c are depicted in Figure 3.15b. Points A and B shown in Figure 3.15b, respectively, denote the deepest point and the surface point on the crack front. The material used in the V-shaped notched round bar model is magnesium alloy AZ-6A-T5. This material is widely used in aerospace and automotive components. Table 3.5 lists the mechanical and fracture properties of magnesium alloy AZ-6A-T5 taken from BEASY material database containing NASGRO constants/parameters.

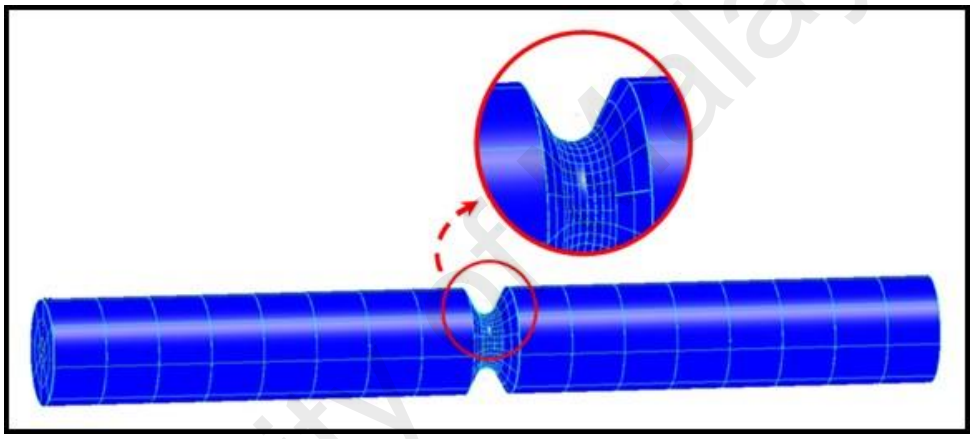

Figure 3.18: Meshed V-shaped notched cylinder model.

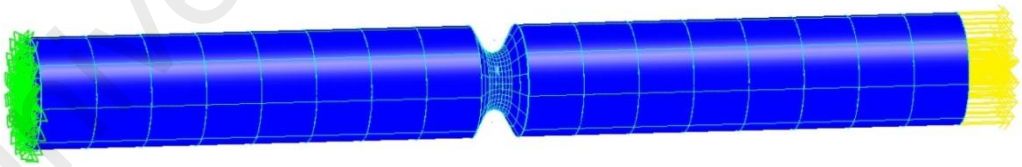

Figure 3.19: Fixed constraint and tension stress at the end of the model.

3.2.3.3 Crack growth analysis

The crack growth analyses are conducted using the BEASY Crack Growth wizard that allows the user to define single or multiple crack, crack elevation, crack position and direction, material type, fatigue loading (constant or variable amplitude load), crack front element size. User can also configure the analysis options, define element type,

examine and check the results. It is important to ensure that the crack mesh is well refined during the crack growth to avoid any error corresponding to the element distortion. For this model, the crack aspect ratio is defined by specifying the crack depth value, a = 0.5 mm and half crack length value c, for instance c = 0.25 mm, to set a/c = *2*. The minimum crack front element size is set to be less than one-fifth of crack depth that is 0.08. This value will result in a good balance between the accuracy and computational time.

Incremental crack extension

BEASY (BEASY, 2013) offers several equations for incremental crack growth prediction such as Paris law, Forman model, Rodhes model and NASGRO model. The NASGRO model (Eqs. 2.52-2.58) is a comprehensive equation because it takes into account some factors that influence the FCG such as the mean stress and crack closure. It is able to describe the crack behavior in all three stage of fatigue crack; initiation, propagation and unstable crack growth. Therefore, the NASGRO crack propagation law was chosen to simulate the fatigue crack growth.

Incremental crack direction

BEASY (BEASY, 2013) provides some criterions to predict the incremental crack growth direction. In this work, the minimum strain energy density criterion was selected for determining crack growth direction. According to this criterion, the crack growth direction angle θ at any point along crack front goes towards the region where the strain energy density factor S is the minimum as compared to other region on the same spherical surface surrounding the point. The spherical coordinat (r, θ, φ) at point O along the crack front shown in Figure 3.20 where z is unit vector normal to the crack surface, t is tangent unit vector of the crack front, and n is unit vector in crack surface and normal to crack front.

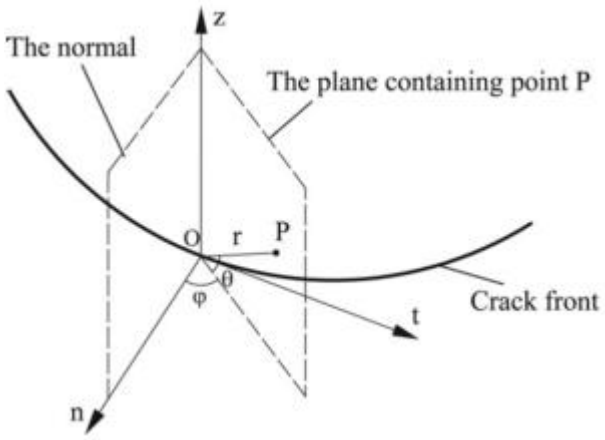

Figure 3.20: Spherical coordinat at point O along the crack front (Yang et al, 2007).

The derivative of strain energy density factor S with respect to θ can be obtained from Eq. 2.73. BEASY compute the stationary points of strain energy density factor S by solving $dS/d\theta = 0$ ($-\pi<\theta<\pi$). Finally, BEASY obtain the minimum strain energy density factor S_{min} by comparing the value of S at stationary points where $d^2S/d\theta^2>0$ (Aliabadi, 2003). Referring to Figure 3.20, the minimum of strain energy density factor S occurs in the normal plane of the crack front, namely when φ equal to zero. Therefore, the crack growth direction at a point on the crack front is decided solely by the angle θ in the normal plane (Yang et al., 2007).

Calculation of SIFs

There are two different ways to calculate the stress intensity factors in BEASY (BEASY, 2013) i.e. using the crack opening displacement (COD) and J-integral. In this work, the J-integral technique is used to evaluate stress intensity factors due to its accuracy, effective and capability. The interior elastic field can be accurately determined along the contour path of the J-integral using the boundary element method, since the exact variation of the interior elastic field is built into the fundamental solution. Figure 3.21 shows a sample of different circular contour paths of J- integral (J-integral ring) used in BEASY (BEASY, 2013) to evaluate the SIFs around the crack

front. The J-integral ring comprises of a number internal points created around the crack front. The options for the J-Integral calculation can be defined such as J-integral positions on crack front (by defining the radius of outer ring), the number of the J-integral positions per 90 degrees curvature of crack front and radius of each of the J-Integral rings. The Yaoming Mi equation, Eq. 2.64 (Mi, 1995) is used to estimate K_{eff} to account the crack growth increment. Furthermore, during the analysis, it is essential to evaluate dK_{eff}. Here, the method considers individual dK_I, dK_{II} and dK_{III} to evaluate $dK_{eff.}$ as shown in Figure 3.10.

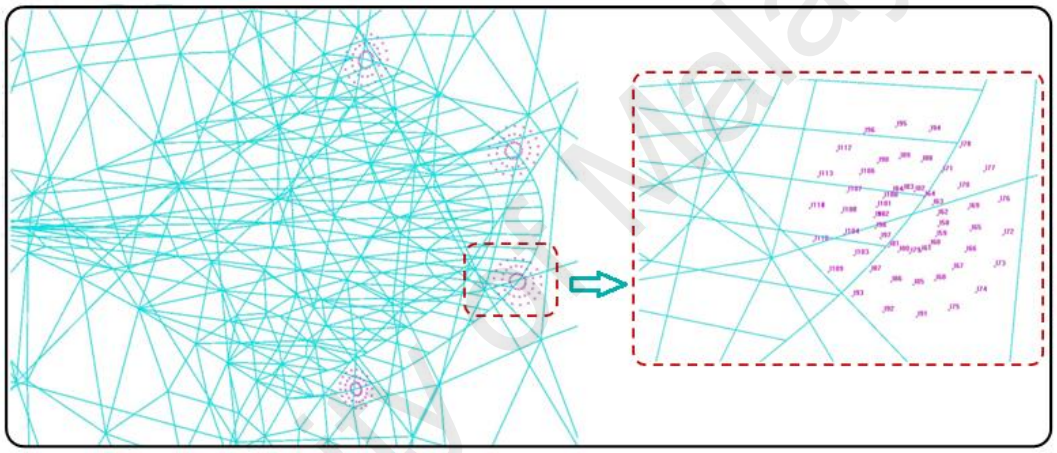

Figure 3.21: J-integral path at the crack front (BEASY, 2013).

The V-shaped notched cylinder model is then subjected to a constant amplitude cyclic tension with stress amplitude ratio R = 0 where the maximum load cycle is 30 MPa and the minimum load is zero. The reduced quadratic element is selected for re-meshing the crack surface and remaining surface during the crack growth simulations. An adjustment on the crack front element size is sometimes taken if the error occurs at the corresponding crack growth increment during the simulation. When the SIFs reach the critical stress intensity factor (refer to the fracture toughness of the material), the analysis would stop. The results are then plotted and saved in an excel file format.

3.2.4 Corner crack in square prismatic bar under combined tension-torsion load

Fatigue crack growth have been observed in non-round bar or square bar-like components such as in an automatic coupler of railway carriage (Mouzavi et al., 2007), in a wobbler of heavy plate mill (Hubner et al., 2009), in a traveling hook of elevator (Faqian et al., 2007), in an overhead power line yoke connector (Dzupon et al., 2013), in a connecting rod of air compressor (Ilman & Barizy, 2015), in railway bridge hanger (Klinger et al., 2014), in counterweight boom supporting truss column of bucket chain excavator (Bosnjak et al., 2013), in fork end of the conveyor chain link (Sujata et al., 2006).

A few researchers have investigated fatigue crack growth in the non-round components such as prismatic bar. Raju and Newman Jr (1988) performed finite element analysis to result in SIF solution for a corner crack in rectangular bar under tension loading. Forman and Mettu (1990) investigated fatigue crack growth behaviour of corner crack in square and rectangular bar made of Al-Ti alloy subjected to tension and bending loads. Naresh et al. (2013) performed FEA using Ansys code to evaluate SIF of quarter circular edge crack in a square bar under tension. The strain energy density theory was used to analyze the crack growth of edge cracked beam under Mode I, Mode II and mixed-mode I-II loads (Nobile, 2000). Rozumek and Marciniak (2008) experimentally investigated the fatigue crack growth of rectangular bar under out-of-phase bending and torsion loadings. Varfolomeev et al. (2014) investigated mixed-mode I-II fatigue crack growth and crack path of modified single edge notch bar under bending. This present study evaluated SIF, crack path and FCG behaviour of different crack aspect ratio of corner crack in square bar under combined cyclic tension-torsion loading.

3.2.4.1 Geometric modelling

The square prismatic bar model used in this work consists of two zones, i.e. bar (zone 1) and cylinder regions (zone 2). The cylinder part was needed to model the torsional load to be transferred to the square bar. Bar has a width of 155 mm, height of 155 mm and 1000 mm in length. Cylinder has diameter and length of 240 mm and 50 mm, respectively. The model is developed by creating some coordinate points, then creating boundary lines by connecting two associated points as shown in Figure 3.22a. The quadrilateral boundary surfaces are generated by connecting the corresponding four boundary lines as shown in Figure 3.22b. Figure 3.23 shows the interface that connects zones 1 and 2.

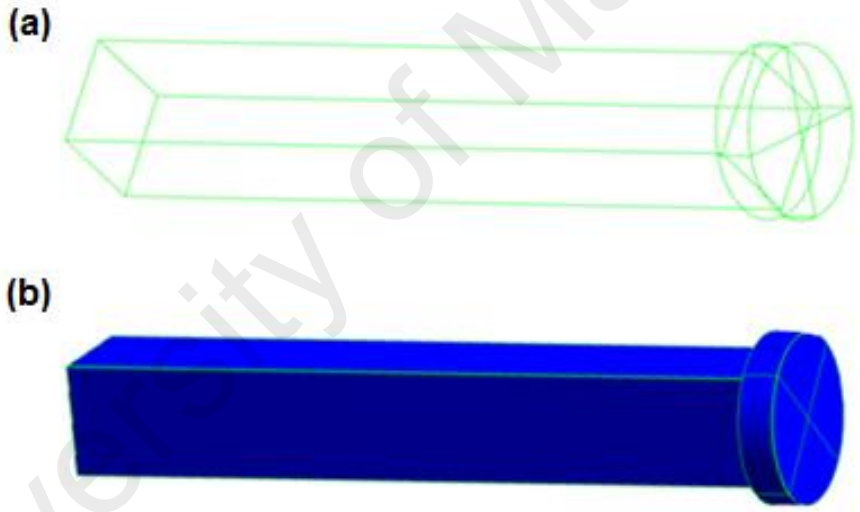

Figure 3.22: The steps to define boundary surfaces of square bar model.

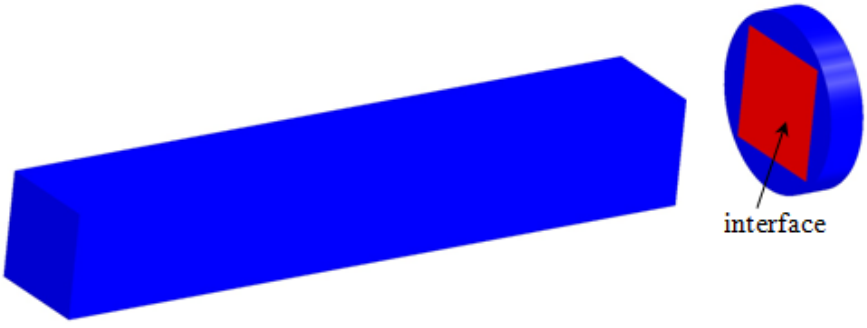

Figure 3.23: The interface connecting zones 1 and 2.

3.2.4.2 Boundary element model

Basically, the analysis using BEASY (BEASY, 2013) is less sensitive to the number of elements if no irregular geometries are included. However, it is necessary to consider the balance between the accuracy and analysis time when discretizing the model. The meshed model of the square prismatic bar containing a corner crack is illustrated in Figure 3.24. All the surfaces of bar region are defined to be in outward normal direction. Next, for the cylinder part, the surface which is the interface between the bar and cylinder regions has to be defined to be in the inward normal direction, whereas the rest of the surfaces are defined in the outward normal direction. Two-dimensional quadratic elements were used to discretize all the surfaces. To avoid the distortion element and any error during analysis, it is necessary to merge mesh points to remove any coincident mesh points generated at the ends of lines or at the intersections of patches. Every BEASY model must be restrained against the rigid body motion in the three coordinate directions. As shown in Figure 3.24, the displacement constraints in *x*, *y* and *z* directions are applied on one end of bar region and a combination of torsional (anti-clock wise direction) and tension stresses is applied on one end of cylinder.

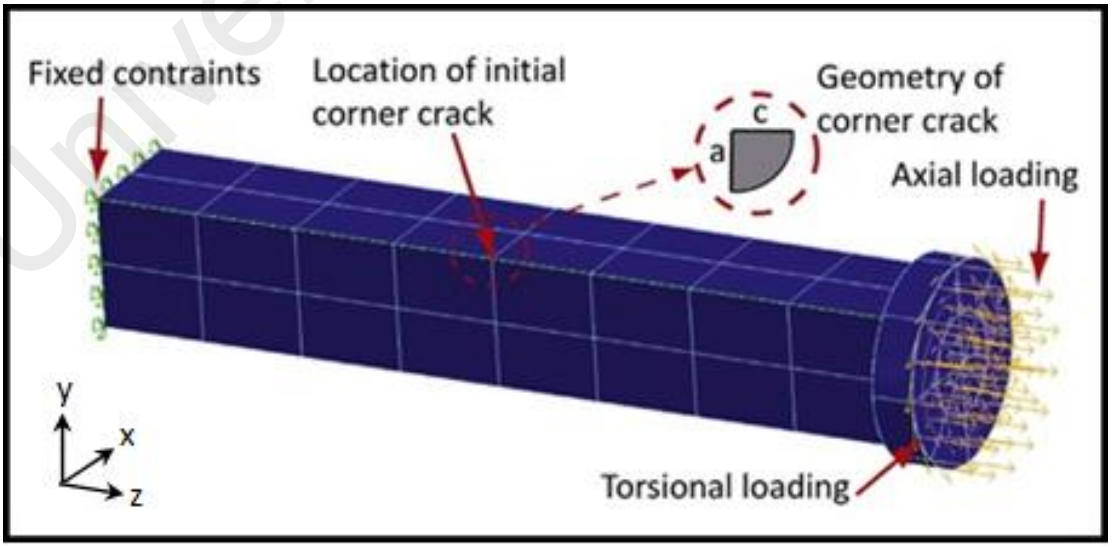

Figure 3.24: Boundary conditions of the meshed square bar model with a corner crack

The cases for different torsional and tension stress acting on the prismatic bar are defined and presented in Table 3.1. As can be seen in Table 3.1, there are six square bar models with different crack sizes and combined stresses to be simulated. The torsion and tension stress defined in Table 3.1 are the maximum value of such stresses which was occured at the middle lateral point of each side of the outer boundary surface and at any point of all boundary surface of the square bar, respectively. The state of stresses at any point in the bar can be given by the principle stress. Figure 3.25 shows the principle stress distributions in a square bar without crack under combined tension of 125 MPa and torsion of 100 MPa.

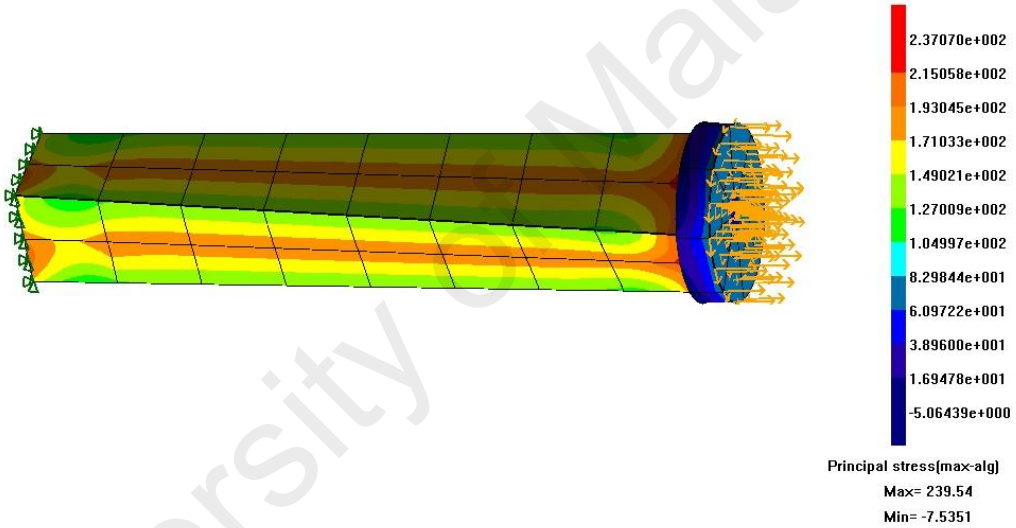

Figure 3.25: Principal stress distribution under combined tension of 125 MPa and torsion of 100 MPa in square bar model.

3.2.4.3 Crack growth analysis

Fatigue crack growths of a corner crack in a square prismatic bar are carried out following the procedure presented in Sections 3.2.2.2 and 3.2.3.3. The material used in the square prismatic bar model is magnesium alloy AZ-6A-T5. Table 3.2 lists the mechanical and fracture properties of the magnesium alloy AZ-6A-T5 that are used in the NASGRO equation. An initial quarter-corner crack with crack depth of a = 4 mm or a = 6 mm is introduced at the mid-length of one longitudinal edge of bar as illustrated in

Figure 3.24. The crack plane was set to be normal to the axis of the square bar. Three different crack aspect ratios *a/c* = 4/6, 4/4 and 6/4 are specified. The quarter elliptical corner cracks for three aspect ratios are illustrated in Figure 3.26. To obtain a good balance between the accuracy and computational time, the minimum and maximum crack front element sizes were set to be 0.4 and 4 mm respectively.

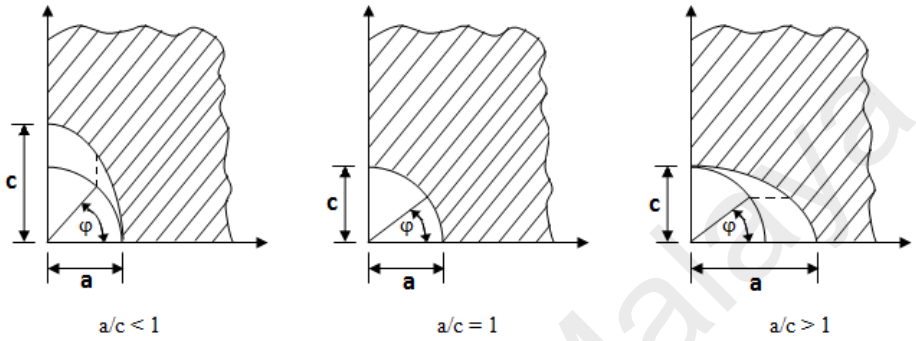

Figure 3.26: Schematic quarter elliptical corner crack.

The square prismatic bar model is subjected to combined proportional tension-torsion load with constant amplitude and stress ratio, $R = \frac{\sigma_{max}}{\sigma_{min}} = \frac{\tau_{max}}{\tau_{min}} = 0$, where σ and τ denote the axial and torsion stresses respectively. The subscripts for max and min refer to the maximum and minimum values. For example, Figure 3.27 illustrates the sinusoidal form of the stress cycles for the load case C as defined in Table 3.1. The NASGRO crack propagation law is chosen to simulate fatigue crack growth. The minimum strain energy density criterion is used to determine crack growth direction and the J-integral is used to evaluate stress intensity factors.

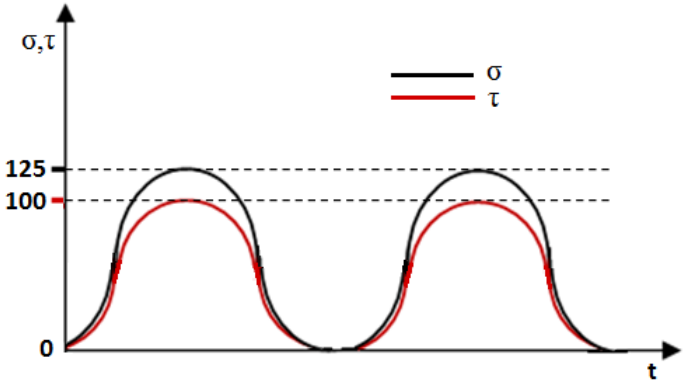

Figure 3.27: Illustration of stress for case C of square bar simulations.

Table 3.1: Combinations of loadings acting on the square bar.

Case	Tension (MPa)	Torsion (MPa)
A	75	100
B	100	100
C	125	100
D	100	200
E	125	0
F	100	0

Table 3.2: Mechanical and fracture properties of AZ-6A-T5 magnesium alloy (BEASY, 2013).

Modulus of elasticity (GPa)	45
Poisson's ratio	0.35
Yield stress (0.2%) (MPa)	268.89
Ultimate tensile strength (Mpa)	344.738
Plane stress fracture toughness, K_c (MPa√mm)	972.9575
Plane strain fracture toughness, K_{Ic} (MPa√mm)	694.9696
Crack growth rate coefficient (C)	7.95714E-10
Crack growth exponent coefficient (N)	2.576
NASGRO coefficient (P)	0.25
NASGRO coefficient (Q)	0.25
Threshold SIF at R=0, (ΔK_{th}) (Mpa√mm)	48.6478
Plane stress/strain constraint factor	1.5
The ratio of the peak stress to the material flow stress in a stress cycle	0.3

3.3 Experimental and numerical work on a surface crack in a solid cylinder

The cylindrical bars are widely used in engineering applications for machine components and structures. A number of initial crack shapes such as circular-arc, elliptical-arc, straight-fronted, sikle and irregular shape have been used by many researchers for numerical and experimental evaluations of the fatigue crack growth of a surface crack in solid round bar. Yang et al. (2006) evaluated crack growth behavior of straight front crack in a round bar under cyclic axial loading with steady torsion. Fonte et al. (2006) investigated a semi elliptical surface crack growth and its evolution in a solid shaft under combined cyclic bending and static torsion loads. Recently, Branco et al. (2014) predicted the fatigue life of a straight-front surface crack in a round bar under

combined bending-torsion loads. Citarella (2014) used straight-front surface crack under combined tension-torsion stress and evaluate fatigue crack growth using Paris-law.

In this present study, fatigue growth of a semi-circular and semi-elliptical surface crack in a solid round bar under combined cyclic tension-torsion loading was evaluated numerically and experimentally. The NASGRO crack propagation law and MSED criterion are used to simulate fatigue crack growth and crack growth direction respectively.

3.3.1 Numerical modeling

Prior to conducting the experiment, the corresponding numerical modelling is carried out. The meshed model of a solid cylinder containing a surface crack and its notations are illustrated in Figure 3.28. The cylindrical model has diameter D = 10 mm and length L = 80 mm. Displacement constraints in x, y and z directions are applied on either end of the cylindrical model. Meanwhile, a combination of axial and torsional stresses is applied on another end. Figure 3.29 shows the stress distributions in the solid cylinder model without crack under combined torsion of 125 MPa and tension of 100 MPa.

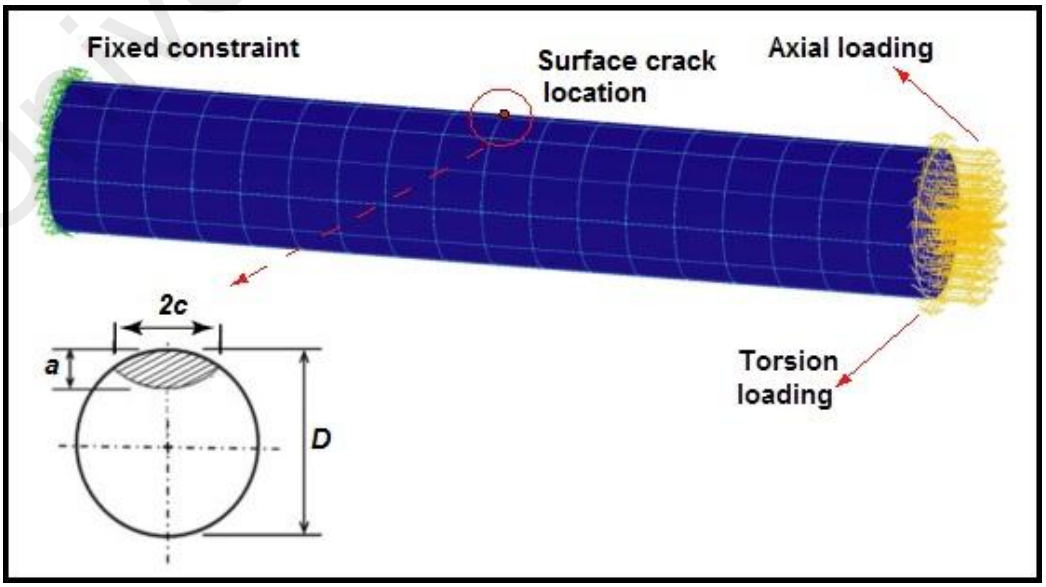

Figure 3.28: Meshed solid cylinder model with the boundary conditions in BEASY.

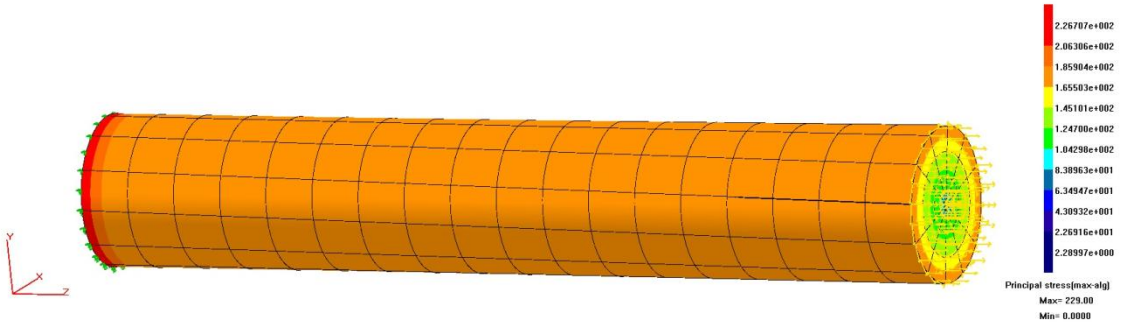

Figure 3.29: Stress distribution in un-cracked solid cylinder under combined torsion of 125 MPa and tension of 100 MPa.

A semi-elliptical surface crack is introduced at the mid-length of the model. The crack plane is set to be normal to the axis of the round bar. Table 3.3 lists the mechanical and fracture properties of the Al-6061-T6 for the NASGRO constants/parameters taken from BEASY material database (BEASY, 2013). In Table 3.3, plane stress fracture toughness K_c is a function of specimen thickness and other geometric variables. Plate or sheet specimens with difference thickness are tested to obtain K_c value. If fracture stress for a test is below 80 % of the material yield strength (the ASTM criterion for validation), the K_c value for given thickness should be the same, regardless of which type of specimen was used. The optimum thickness where the toughness reaches its highest level is usually considered to be the real plane-stress fracture toughness K_c (Liu, 1998).

All the surfaces of the model are defined to be in outward normal direction and discretized by two-dimensional quadratic elements. The NASGRO crack propagation law with a stress ratio R = 0 (as set for the experiments) is chosen to simulate fatigue crack growths. The J-integral method is used to quantify the stress intensity factors during the crack growth. Figure 3.30 shows J-integral paths for surface crack in solid cylinder used in simulations. The cases for different crack size and torsional-tension stress acting on the solid cylinder are defined and presented in Table 3.4.

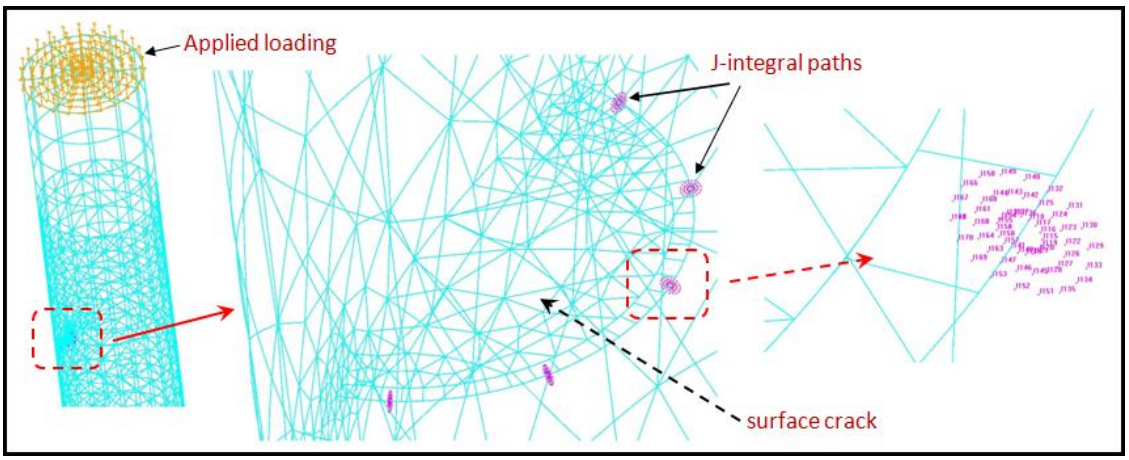

Figure 3.30: J-integral paths for surface crack in solid cylinder model.

Table 3.3: Mechanical and fracture properties of 6061-T6 aluminum alloy (BEASY, 2013).

Poisson's ratio	0.33
Yield stress (0.2%) (MPa)	282.69
Ultimate tensile strength (MPa)	310.26
Plane stress fracture toughness, K_C (MPa√mm)	1250.95
Plane Strain fracture toughness, K_{IC} (MPa√mm)	903.46
Crack growth rate coefficient (C)	6.53E-10
NASGRO N exponent (N)	2.3
NASGRO P coefficient (P)	0.5
NASGRO Q coefficient (Q)	0.5
Threshold SIF range at $R = 0$ (ΔK_{th}) (MPa√mm)	121.62
Plane stress/strain constraint factor, α	2.0
S_{max}/S_0	0.3

Table 3.4: Combination of crack size and loading on smooth solid cylinder.

No	a (mm)	c (mm)	Tension (MPa)	Torsion (MPa)
1	1	0.5	100	100
2	1	0.5	100	125
3	1	1	100	100
4	1	1	100	125

3.3.2 Experimental methods

3.3.2.1 Materials

Aluminium alloy 6061-T6 is typically used for heavy duty structures such as in rail coaches, truck frames, ship building, bridges, etc. Prior to doing the fatigue crack growth experiments, the uniaxial tensile test based on ASTM B557 standard was performed on this material using a universal testing machine Instron 5569. Four round tension test specimens have been loaded uniaxially with constant rate until the final fracture. The average measured yield strength and ultimate tensile strength were found to be around 260 MPa and 286 MPa, respectively.

3.3.2.2 Fatigue crack growth test specimens

The nominal diameter of the specimen is 10 mm with dimension tolerance of +/- 0.05 mm and nominal length of 120 mm. The surface finish is performed to the specimen by using multi-grade sand paper to obtain the fine surfaces roughness. Next, an initial surface crack for different crack length and crack depth is generated at the mid-length of specimen by using the Electric Discharge Machining (EDM) machine. The techniques used to manufacture an initial surface crack on the specimen presented in Chapter 4. The crack plane was set to be normal to the axis of the bar. The schematic shape and dimensions of the crack specimen is shown in Figure 3.31.

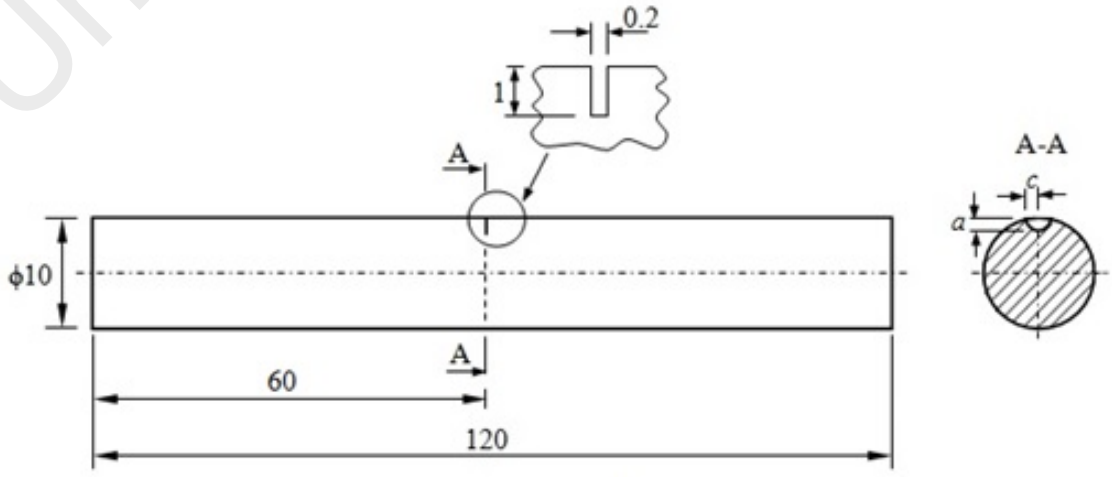

Figure 3.31: Schematic of crack specimen geometry.

3.3.2.3 Setting-up of the fatigue testing

Fatigue crack growth experiments are carried out by using the Instron Model 8874 Table Top Axial Servo-Hydraulic Dynamic Testing Machine as shown in Figure 3.32. The machine has axial and torsional load cells with maximum capacity of 25 kN and 100 Nm, respectively. The machine is equipped with the WaveMatrix® calculation module that enables the user to set up and perform various real-time calculations as part of a testing. Here, all fatigue crack tests are conducted at room temperature under a constant amplitude sinusoidal loading (combined cyclic tension-torsion) with the stress ratio $R = 0$ at the frequency of 3 Hz. Two different crack aspect ratios a/c of 1 and 2 are considered.

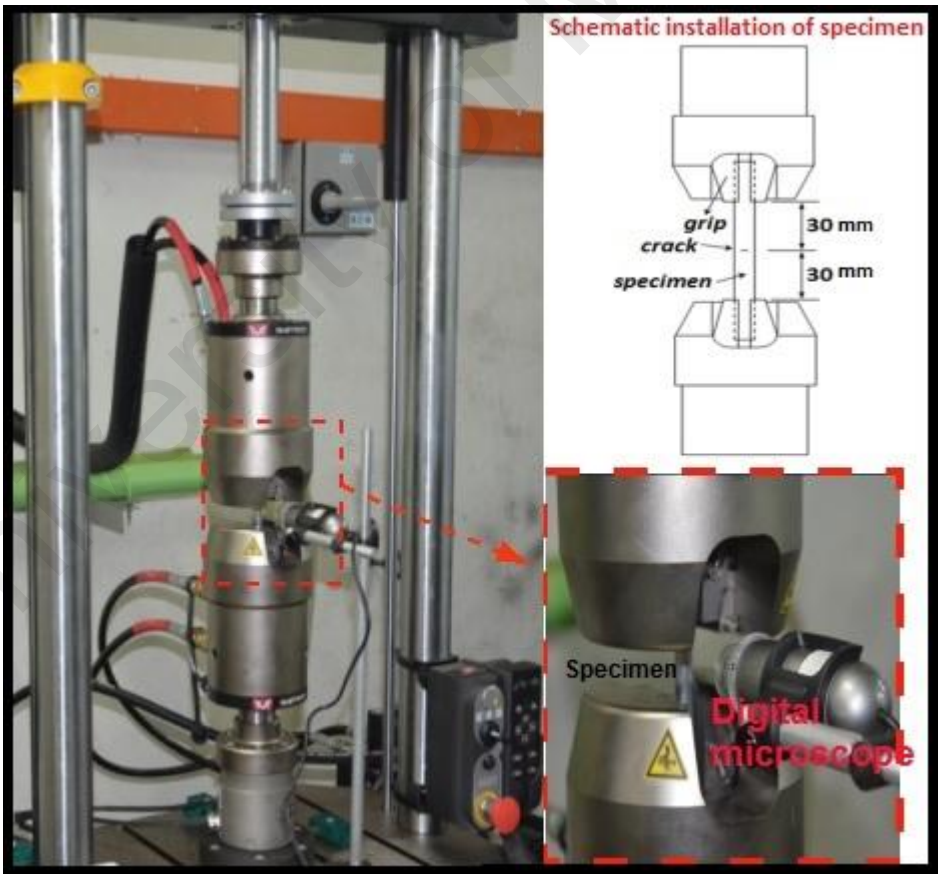

Figure 3.32: The set-up of fatigue testing and the schematic of the specimen clamping.

The specimen is clamped using hydraulically-actuated wedge grips. The V-jaw wedge grips are specifically used for a cylindrical specimen. It is necessary to ensure that the crack position after clamping is located at the middle between the grips as schematically shown in Figure 3.32. The crack growth paths at the crossed surface points of the specimen are constantly monitored by using a digital microscope (Figure 3.32) which is connected the computer. The digital microscope used in this work has a maximum magnification of about 200 times and is equipped with snapshoot and video recording features. The crack length tracking for a given number of cycles can be measured with the aid of the video recording. This measurement technique allows the user to acquire the data for plotting the crack lengths versus the number of cycles. The detail of crack length measurement is presented as follow:

First, before running the crack growth test, the cracked specimen is installed in fatigue test machine, and a digital microscope that connected to the computer is properly placed in the front of specimen. A snapshot of initial surface crack is taken using digital microscope, and is displayed in the screen of the computer. The crack length size c of initial surface crack is measured and scaled by using a digital caliper with accuracy +/- 0.0005 mm. Second, after conducting the crack growth test, the video recording of crack growth test is displayed. The crack length for a given number of cycles can be tracked by stopping the video recording at a record time that fits to the respective number of cycle. Then, a digital caliper used to measure the crack length extension displaying on the screen of the computer. Finally, this measurement result together with the previous scaled value of crack length was used to determine the actual crack length extensions for this number of cycles. The procedure can be repeated up to the final fracture to obtain the crack length for any number of cycles.

3.3.3 Fractography analysis

Typically, observations of fracture surface begins with a visual examination by naked eye or under favorable lighting where general features, surface roughness and nature of the fracture path can be revealed. Fractographic techniques then can be used to reveal microscopic features. The failed cracked component may be properly sectioned for preparation of metallographic samples and examination under a microscope.

3.3.3.1 Material and equipments

This research utilized a digital microscope for fractograpic analysis of fracture surface specimens. The Acetone solutions are used to cleaning the fracture surface specimens in an ultrasonic cleaner prior to the microscopic observation. Then, the fracture surface is dried with an electric dryer. Specimen should be carefully handled during the preparation to avoid any contamination and touching of the fracture surfaces.

3.3.3.2 Procedures

A simple fractography technique has been performed by using a digital microscope which was connected to the computer. The details of this technique are as follows:

- Take tested fracture specimen of fatigue crack growth.
- Examine the fracture surfaces of the provided fracture specimens by naked eyes before putting it into the cleaner.
- Clean the specimen using Acetone solution in an ultrasonic cleaner.
- Dry the specimens using electric dryer.
- Observe the specimen surfaces using a digital microscope as shown in Figure 3.33.
- Take snapshot of the observed specimen surface for several magnifications.
- Analyze the snapshot of the specimen surfaces.

Figure 3.33: Observing the specimen surfaces using digital microscope.

3.4 Summary

The methodology used in this research has been presented in this chapter. In Chapter 4, various results on the SIFs and fatigue crack growths in a V-sharp notched cylinder, a square prismatic bar and a solid cylinder are presented and discussed. The procedures and results of inducing an initial surface crack in a solid cylinder are also presented in Chapter 4.

CHAPTER 4

RESULT AND DISCUSSIONS

4.1 Introduction

In this chapter, preliminary numerical works of evaluating the fatigue crack growths of a surface crack in a V-notched cylinder under cyclic tension were carried out. Next, the numerical works were further carried out to evaluate the stress intensity factors and fatigue crack growths of a corner crack in a square prismatic bar under combined cyclic torsion-tension loads. In particular, with a consideration of a practical interest, surface crack growths in a solid cylinder under combined cyclic tension-torsion loading were evaluated through experimentation and numerical modeling.

4.2 Numerical results

4.2.1 Benchmarking studies

To show the accuracy of the results obtained by using BEASY, comparisons with the published solutions are made. Four different cracked models are considered for benchmarking studies. The SIFs of a semi-elliptical surface crack in smooth round bar and a quarter-elliptical corner crack in a prismatic bar under tension load were evaluated by BEASY (BEASY, 2013) and the results were compared with the Raju-Newman solution (Raju & Newman, 1986) and Newman-Raju solution (Newman & Raju, 1986), respectively. Both Newman-Raju solutions used 3D finite element analysis results to develop semi-empirical SIF equations for semi-elliptical surface crack and corner crack in a prismatic bar under tension loads. Mode I SIFs along the crack front was given as:

$$K_I = \sigma \sqrt{\pi \frac{a}{Q}}\, F \tag{4.1}$$

where σ is tension stress, a is depth of crack, F is the boundary correction factor along the crack front, Q is shape factor for elliptical crack that is given as:

$$Q = 1 + 1.464(a/c)^{1.65} \quad \text{for } a/c \leq 1 \tag{4.2}$$

and

$$Q = 1 + 1.464(c/a)^{1.65} \quad \text{for } a/c > 1 \tag{4.3}$$

The smooth round bar has diameter *D* of 10 mm, crack depth *a* of 2 mm, crack length *c* of 2 mm and the tension stress of 70 MPa is used. While, the square bar has a width of 155 mm, height of 155 mm, 1000 mm in length, aspect ratio *a/c* of 1 with the crack length *c* of 4 mm and the tension stress used is 200 MPa. Both surface and corner cracks were oriented on a plane normal to the longitudinal axis of smooth round and square bar. The results are plotted in Figures 4.1 and 4.3 for smooth round bar and square bar respectively. It can be seen from Figures 4.1 and 4.3 that the results are shown to be in a good agreement. For round bar model, the largest difference is found at the mid-point of the crack front and is within 8%, while for square bar model, the largest difference is found at cross surface points (angle 0^0 and 90^0) and is within 5%.

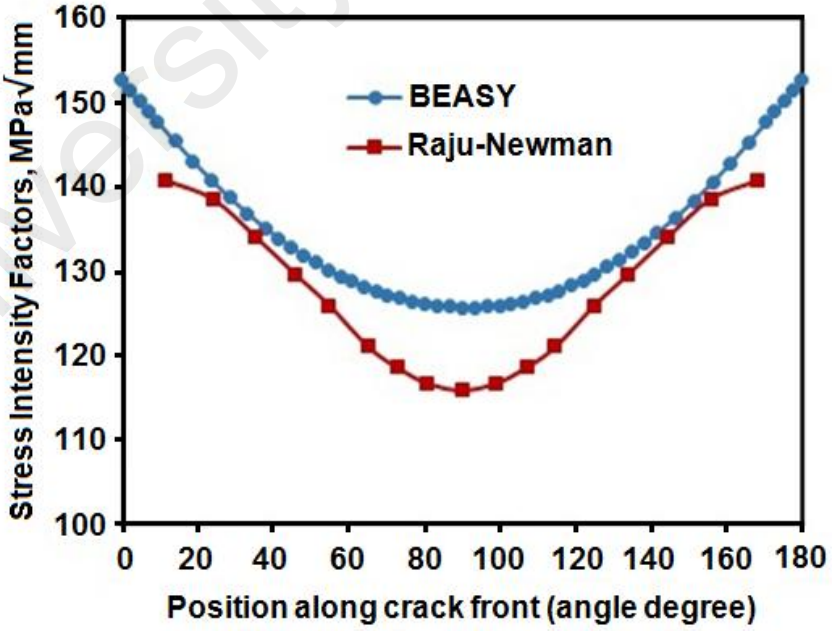

Figure 4.1: Comparison of the SIFs for semi-elliptical surface crack on a solid cylinder obtained by BEASY (BEASY, 2013) and Raju-Newman solution (Raju & Newman, 1986).

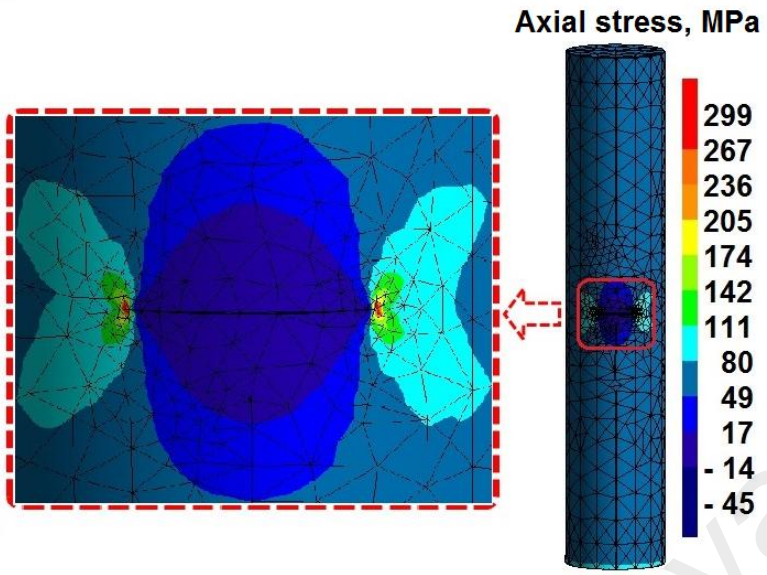

Figure 4.2: The corresponding axial stresses around the crack region on a solid cylinder.

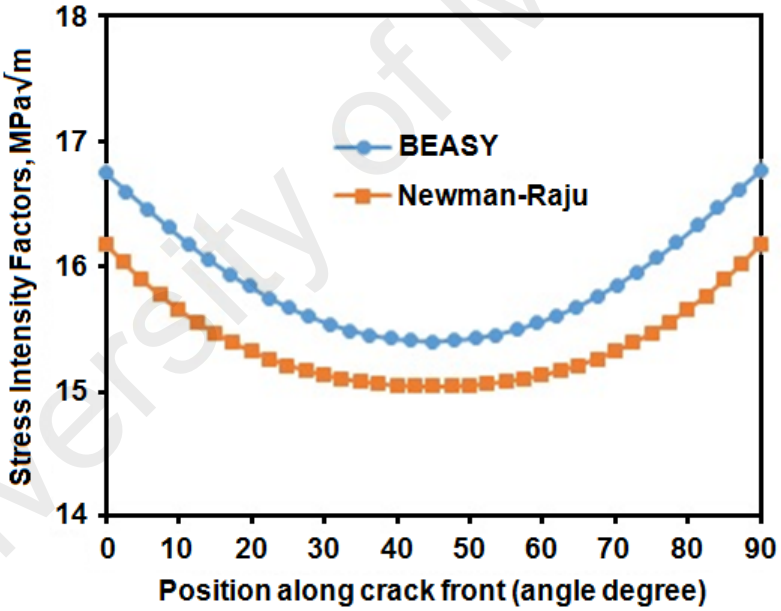

Figure 4.3: Comparison of mode I SIFs for quarter-elliptical corner crack on prismatic bar by BEASY (BEASY, 2013) and Newman-Raju solution (Newman & Raju, 1986).

The axial stress contour around the crack tip and the mesh refinement generated using BEASY are shown in Figure 4.2 for the smooth round bar and in Figure 4.4 for the square bar. It shows that the tool possesses the advantages in generating mesh refinements around the crack front.

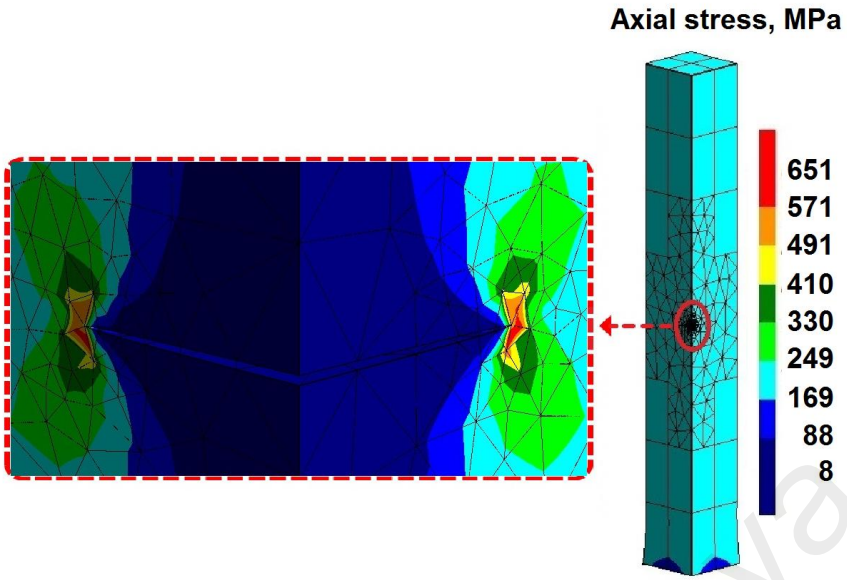

Figure 4.4: The corresponding axial stresses around the crack tips on a square bar.

Further, a semi-elliptical outer surface crack in a hollow cylinder under torsion was modeled by BEASY to making a comparison of Modes II and III stress intensity factors (K_{II} and K_{III}) with the finite element solutions by Predan et al. (2013). The hollow cylinder has an outer diameter of 12 mm, a wall thickness of 2 mm and a length of 117 mm. The principal stresses and crack mesh of the hollow cylinder are shown in Figure 4.5. The K_{II} and K_{III} results for crack aspect ratio a/c = 0.5 are presented in Figure 4.6. The equivalent stress intensity factors K_{eq} shown in Figure 4.6 is defined as $K_{eq} = \sqrt{K_{II}^2 + (1+\nu)K_{III}^2}$. where ν is Poisson's ratio of the material. Very good agreements on both K_{II} and K_{III} results are noticeable.

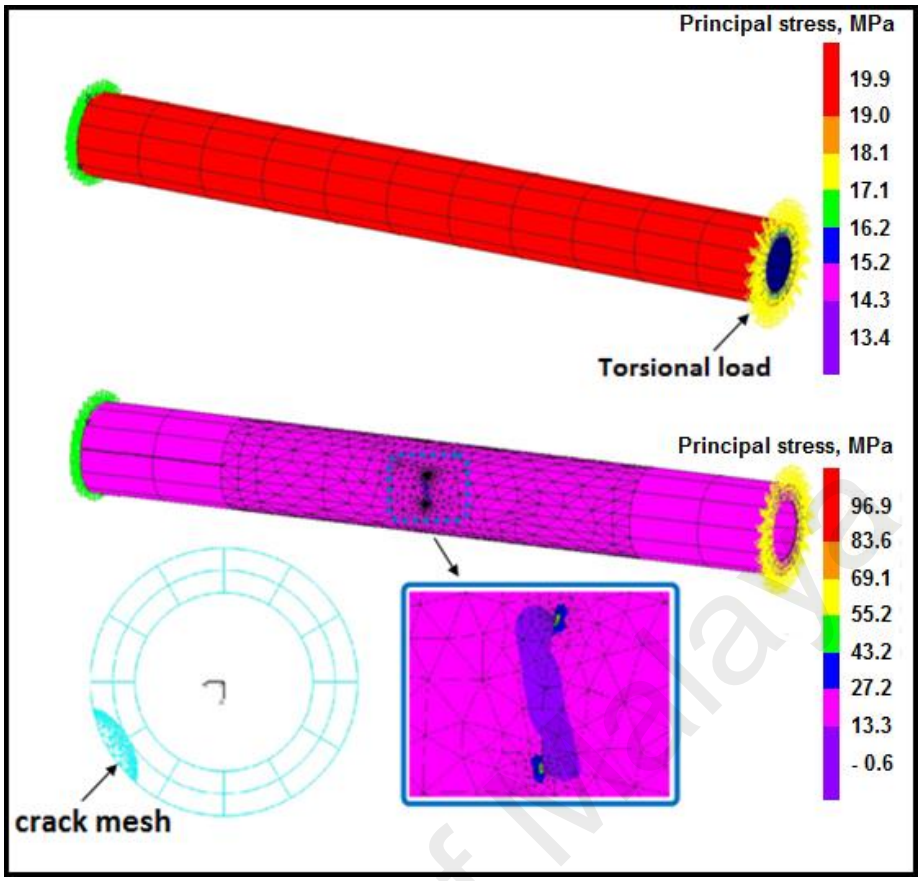

Figure 4.5: BEASY model, principal stress and crack mesh of hollow cylinder under torsion.

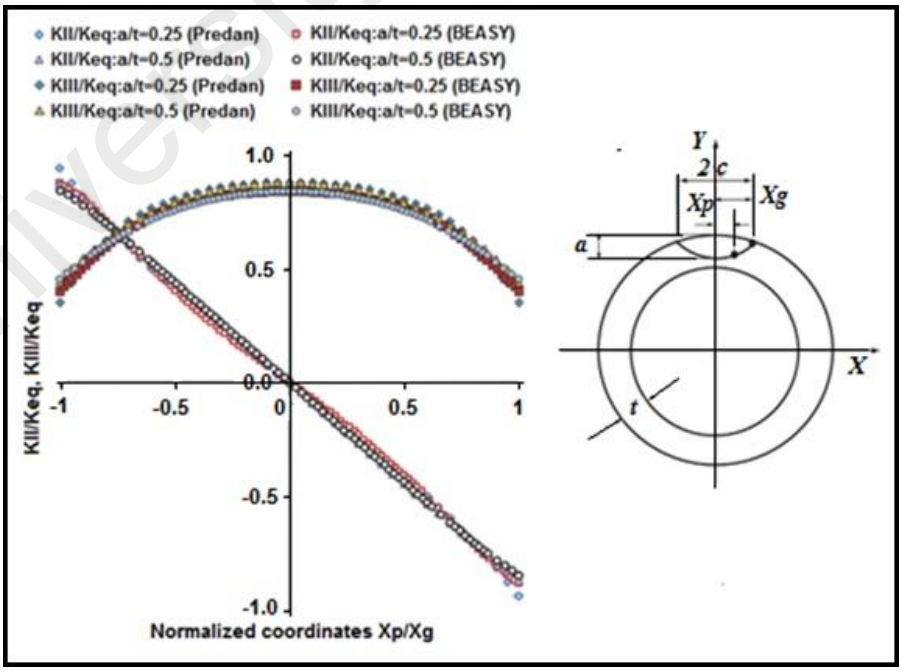

Figure 4.6: Comparison of Modes II and III SIFs for semi-elliptical surface crack (*a/c*=0.5) on a hollow cylinder under torsion loading by BEASY (BEASY, 2013) and Predan et al. (2013).

Next, an experimental work of fatigue growth of an inclined semi-elliptical surface crack (angle of 45^0) of Al 2024-T351 reported by Thompson and Sheppard (1992) was chosen to validate the results estimated by BEASY. Figure 4.7 shows the cracked model at final increment (fracture) and the close-up of the maximum principal stresses. The surface crack mesh and crack front at the inner of specimen are shown in Figure 4.8. It can be seen in Figure 4.8 that fatigue crack growth of inclined surface crack under cyclic tension results in a wave-shaped and inclined crack surface and crack fronts which is induced by the mode II and III stress portions. The fatigue crack growth curves are plotted in Figure 4.9. The estimation of the fatigue crack growth by the simulation is shown to result in a shorter fatigue life though fairly showing similar trend of the crack growth by the experimentation. Similar pattern of the crack growth for Al 2024-T3 was also observed but the fatigue life is longer than that of Al 2024-T351. Although the numerical simulation is intended to reduce experimentation, it is not always be perfect when the initial crack size has a very small ratio to the component/structure. As consequence, re-meshing around the crack region during the crack growth is the concern.

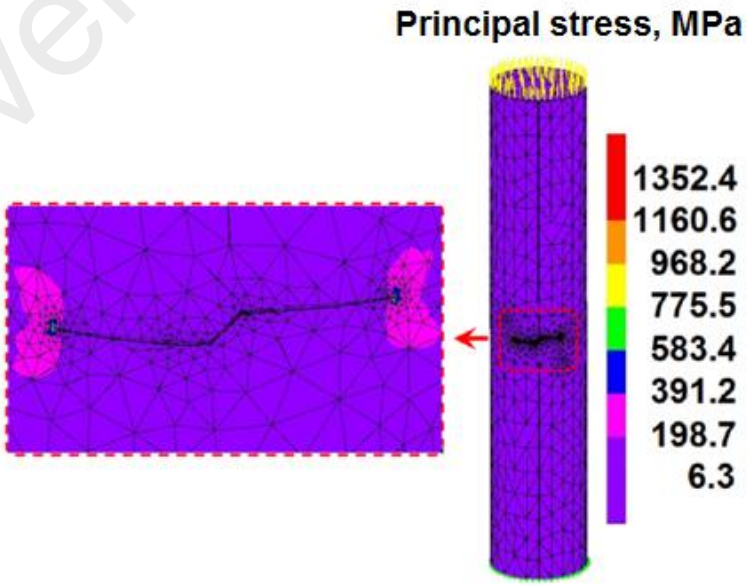

Figure 4.7: The inclined semi-elliptical surface crack on solid cylinder model at final increment (fracture) and the close-up of the maximum principal stresses obtained by BEASY (BEASY, 2013).

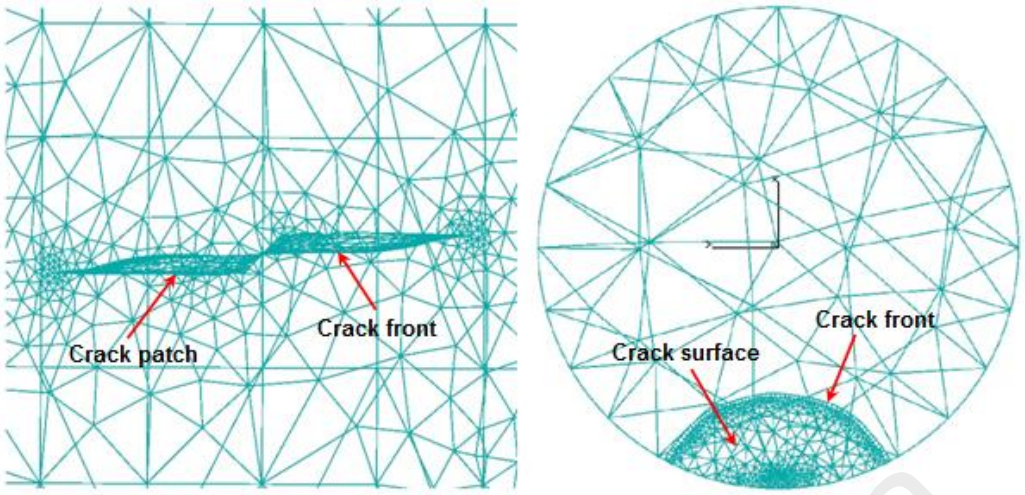

Figure 4.8: The crack surface mesh and crack patch on solid cylinder model at final increment (fracture) obtained by BEASY (BEASY, 2013).

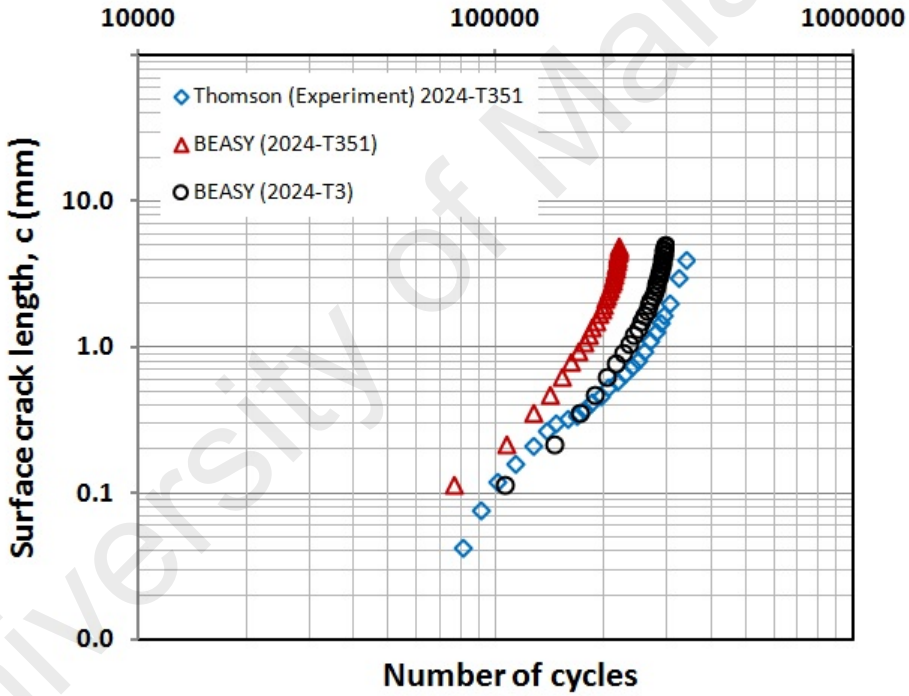

Figure 4.9: Fatigue growth of an inclined surface crack (angle=45^0) under cyclic tension by experiment (Thomson & Sheppard, 1992) and BEASY (BEASY, 2013).

4.2.2 Surface crack in a V-shaped notched round bar under cyclic tension

4.2.2.1 Stress intensity factors

It can be seen from Figure 4.10 and 4.11 that the axial stress contours for the initial and final increments around the crack fronts and the final crack opening modes can be identified. For a given crack depth a, the axial stresses for cracks with $a/c \neq 1$ are shown to be larger than those for $a/c = 1$. However, a greater axial stress around the

crack front does not necessarily result in a higher stress intensity factor. The SIF values are largely dependent on the applied remote stress and geometry factors. Figures 4.10 and 4.11 also show highly stressed zones around the notch root surface, causing the dislocations' shielding stress. The shielding effect leads to the maximum elastic stress shifting away from the notch root surface as a result of a condition where the regions around the crack front would physically experience plastic deformation.

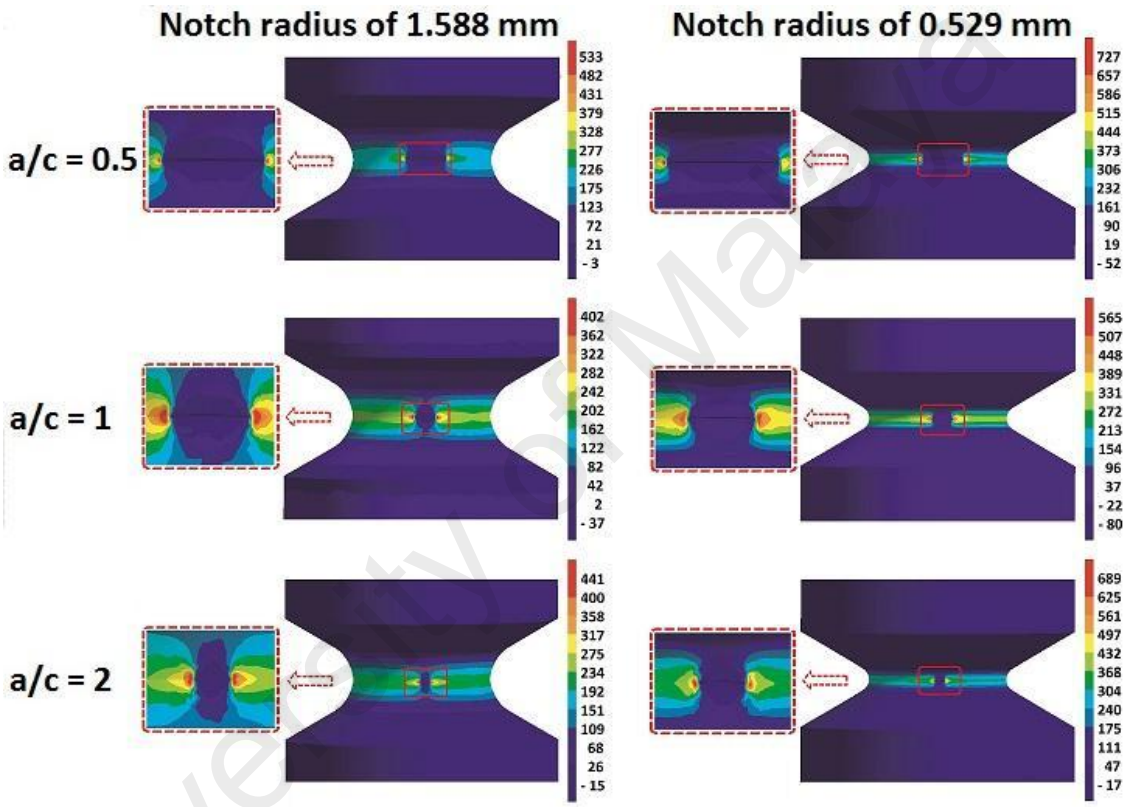

Figure 4.10: The axial stress contours around the surface crack of V-notched cylinder at the initial increment.

The normalized SIFs *K* along the crack front for three different crack aspect ratios (*a/c*) and two different notch radii *r* of the selected increments during fatigue crack growths are presented in Figure 4.12. The stress intensity factor K_o shown in Figure 4.12 is defined as:

$$\boldsymbol{K_o = \sigma\sqrt{\pi a}} \qquad \textbf{(4.4)}$$

where σ is remote applied tension stress and *a* is crack depth.

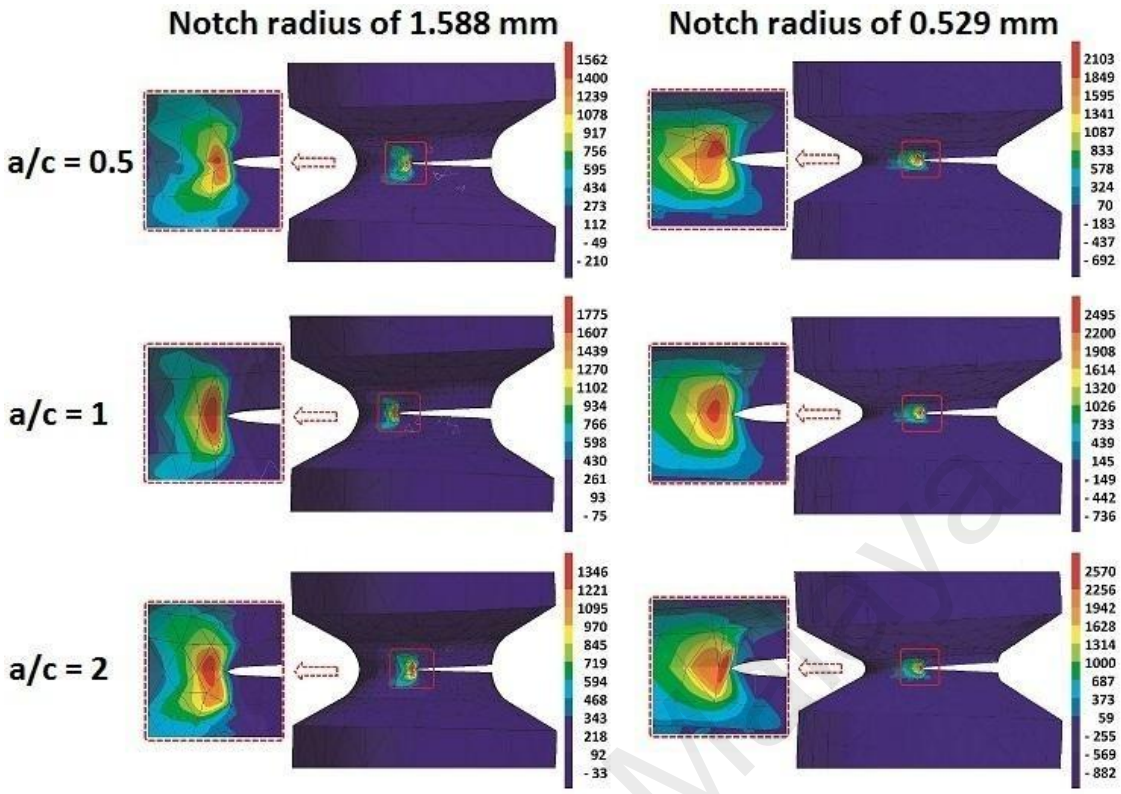

Figure 4.11: The axial stress contours around the crack fronts of V-notched cylinder at the final increment.

In Figure 4.12, the mid-point of the elliptical crack front is defined as the point 0.5 of the *x*-axis, while the surface points of the crack front are denoted by the points 0 and 1. The maximum and minimum normalized SIFs along the crack front at each increment during the crack propagation are, respectively, found at the crossed surface points and the mid-point. As expected, for a given crack aspect ratio, more fatigue loading cycles to failure are seen in the blunt notch model compared to those of the sharp notch model. In all cases, the largest SIFs are found at the surface points.

At the initial stage (increment 0), the stress intensity factors along the crack front for *a/c* = 0.5 are shown to have slight different values (Figure 4.12). Meanwhile, the differences in the SIF values along the crack front for the larger crack aspect ratios, i.e. *a/c* of 1 and 2, are noticeably larger as evidenced by the SIFs patterns which forms a U-shaped curve. The SIF patterns along the crack front for the larger crack aspect ratios *a/c* tend to form flat-shaped curves in the first few increments and then appear to form

U-shaped curves in the following increments. The shape evolution of the SIF patterns at the crack fronts for a/c = 1 and 2 are shown to be different from those at the smaller crack aspect ratio (a/c = 0.5), which immediately forms U-shaped curves until fracture. It may be estimated from Table 4.1 that the unstable crack extensions during crack growth are observed when the crack aspect ratio a/c evolves to be between 0.6 and 0.7.

4.2.2.2 Fatigue life and crack shape evolution

The crack shape evolutions for three different crack aspect ratios and two different notch radii are depicted in Figure 4.13-4.18. At the initial increment of the crack growth, the crack surfaces form an almond shape. Then, in the following increments, the shapes of the cracks evolve to form a nearly straight line at the crack front. It can also be observed from Figure 4.13-4.18 that unstable crack growth is observed after the crack front has formed a straight shape.

A careful consideration should be taken if the cylinder contains a defect like a 'shallow surface crack' with a straight crack front shape or with a smaller crack aspect ratio. Previous studies on the crack shape evolutions of a surface crack in smooth and notched cylinders have been reported (Carpinteri, 1993), (Carpinteri & Brighenti, 1996), (Carpinteri, Brighenti, & Vantadori, 2006), (Carpinteri, Ronchei, & Vantadori, 2013) and (Lin & Smith, 1998).

They used linear Paris's equation for the crack growth simulations. Paris's equation does not consider the effect of crack closure during the crack growth, resulting in very conservative estimations and much shorter fatigue lives. Figures 4.13-4.18 also show that the size of the initial crack aspect ratio would have a significant influence on the crack shape evolution during the crack growth.

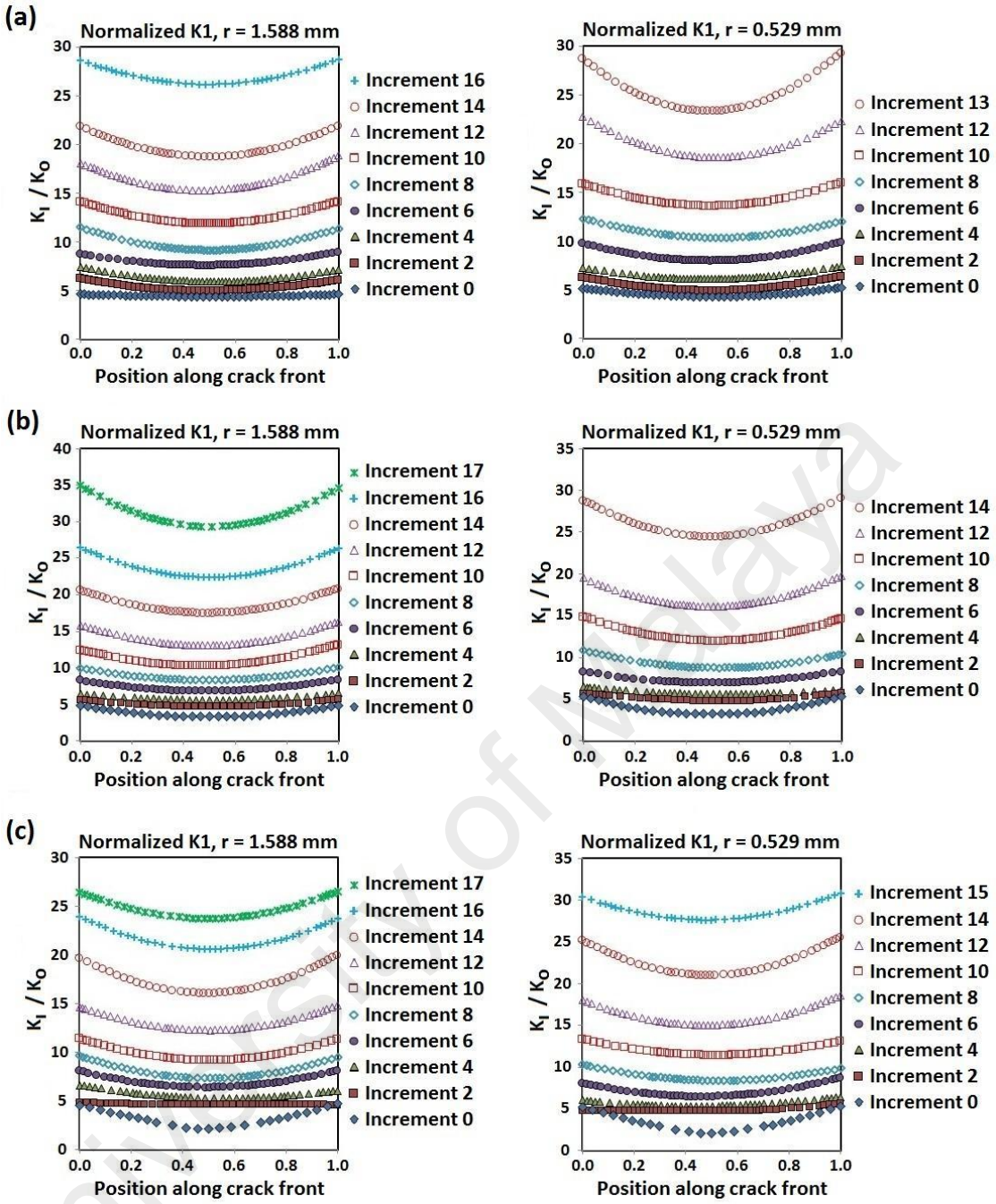

Figure 4.12: Normalized SIFs of surface crack in V-notched cylinder for (a) a = 0.5 mm and c = 1 mm; (b) a = 0.5 mm and c = 0.5 mm; (c) for a = 0.5 mm and c = 0.25 mm.

Figure 4.19 and 4.20 shows that the smaller crack aspect ratio clearly leads to a shorter fatigue life. The effect of the crack aspect ratio on the fatigue life is shown to be more significant than the notch radius. Unstable crack growth is expected when the corresponding stress intensity factors K_I approaches the plane strain fracture toughness. It can be seen from Figure 4.21 that unstable crack growths begin to happen when the

SIF of the cracks is about 400 MPa√mm (see Table 3.2 for the plane strain fracture toughness). The specimens fail when the stress intensity factors attain the plane stress fracture toughness.

Table 4.1: Crack geometries during fatigue crack growths

c **mm**	***Initial*** ***a/c***	**increment**	**Notch radius *r* = 1.588**			**Notch radius *r* = 0.529**		
			total cycle	crack depth *a*	crack length *c*	total cycle	crack depth *a*	crack length *c*
1	0.5	0	0	0.5000	0.9668	0	0.5000	0.9668
		2	3738	0.9662	1.5325	3683	0.9253	1.6067
		4	5998	1.3841	2.2242	5944	1.3358	2.3357
		6	7332	1.8155	2.8784	7213	1.8066	3.0212
		8	8063	2.2690	3.573	7866	2.3191	3.6378
		10	8467	2.7462	4.175	8172	2.8609	4.1712
		12	8693	3.3587	4.6655	8316	3.4837	4.6829
		13	8760	3.6587	4.8955	8330	3.8548	4.9431
		14	8811	3.9683	5.1146			
		16	8848	4.5750	5.5344			
0.5	1	0	0	0.5000	0.4997	0	0.5000	0.4997
		2	4910	0.8733	1.3296	4779	0.8349	1.4631
		4	7729	1.3079	1.9576	7553	1.2873	2.0498
		6	9450	1.7554	2.5767	9230	1.7324	2.6441
		8	10412	2.1671	3.2353	10134	2.1579	3.3089
		10	10940	2.5793	3.8609	10543	2.6329	3.9114
		12	11245	3.0940	4.4315	10740	3.1960	4.4658
		14	11413	3.7172	4.9134	10804	3.9296	4.9937
		16	11490	4.3289	5.3469			
		17	11490	4.8035	5.5857			
0.25	2	0	0	0.5000	0.2501	0	0.5000	0.2501
		2	6289	0.7873	1.1688	5289	0.7426	1.241
		4	9546	1.2562	1.7199	8525	1.1963	1.8579
		6	11419	1.6680	2.3985	10375	1.6021	2.5568
		8	12527	2.0801	3.0590	11318	2.0028	3.2369
		10	13211	2.4934	3.6706	11814	2.4935	3.8144
		12	13560	2.8989	4.2853	12049	3.0515	4.3357
		14	13770	3.5525	4.7649	12154	3.7187	4.8559
		15	13824	3.8344	5.0019	12157	4.0326	5.1343
		16	13861	4.1219	5.2197			
		17	13877	4.4347	5.4267			

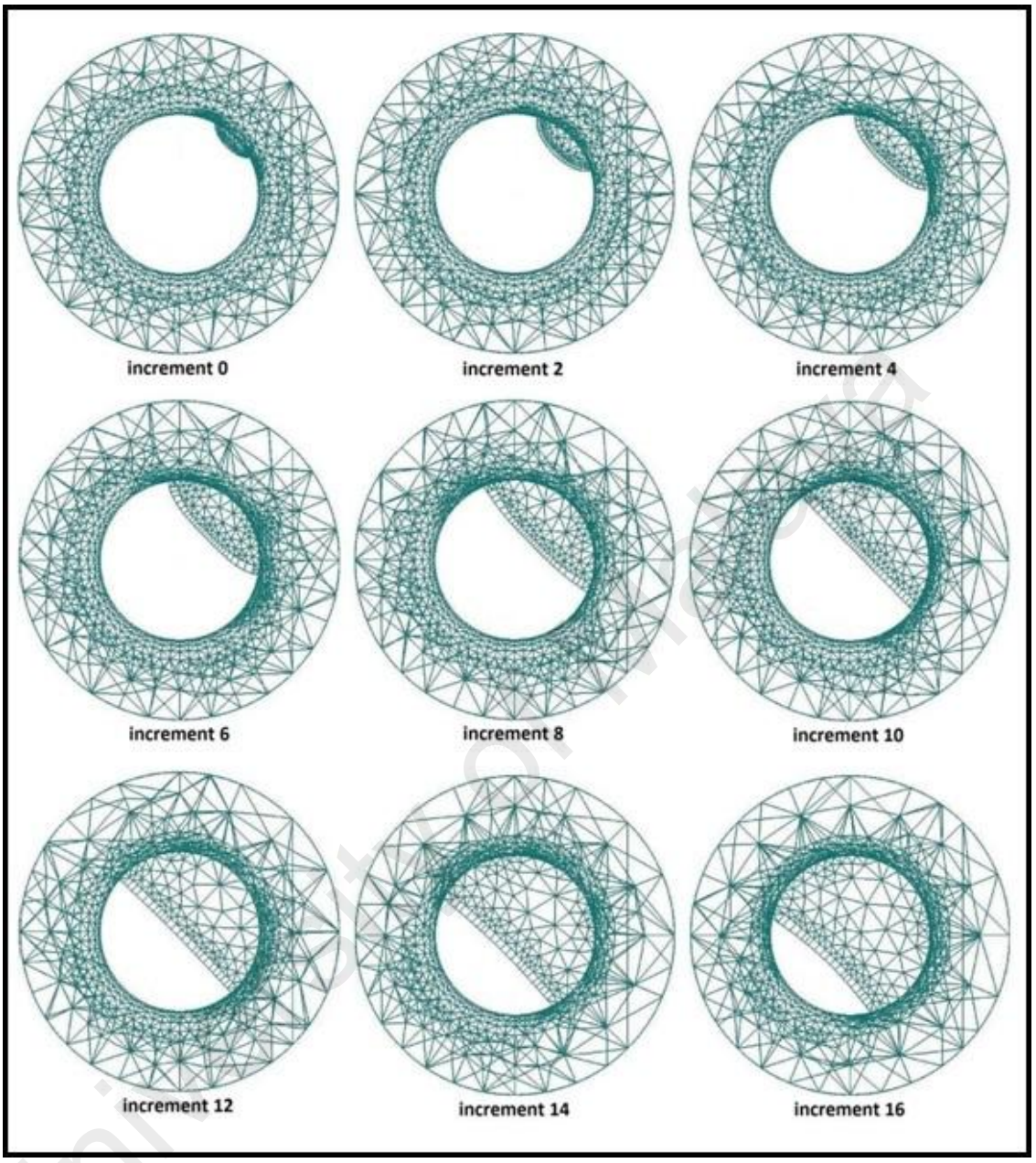

Figure 4.13: Crack shape evolutions for *a/c* = 0.5 and *r* = 1.558.

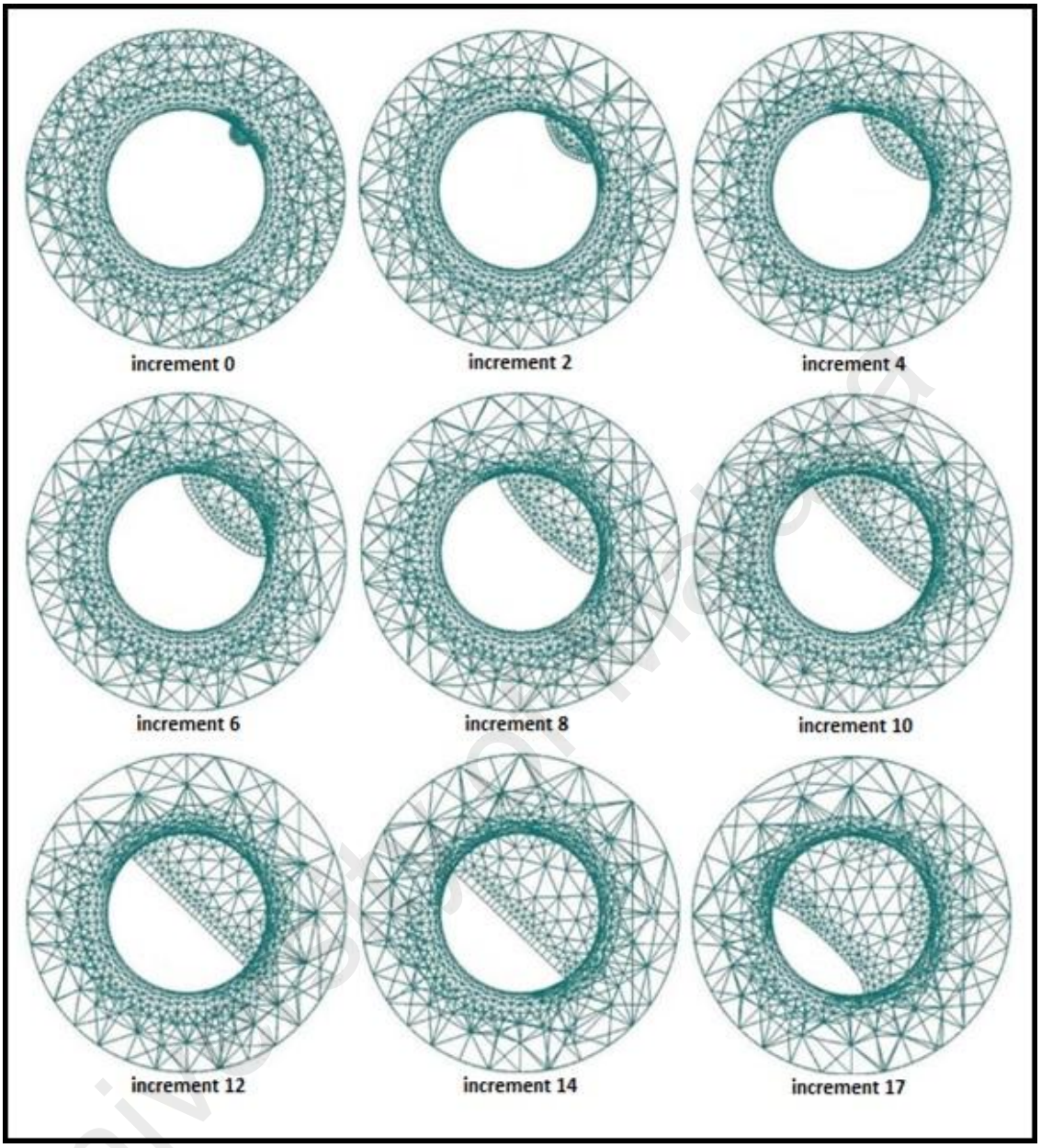

Figure 4.14: Crack shape evolutions for *a/c* = 1 and *r* = 1.558.

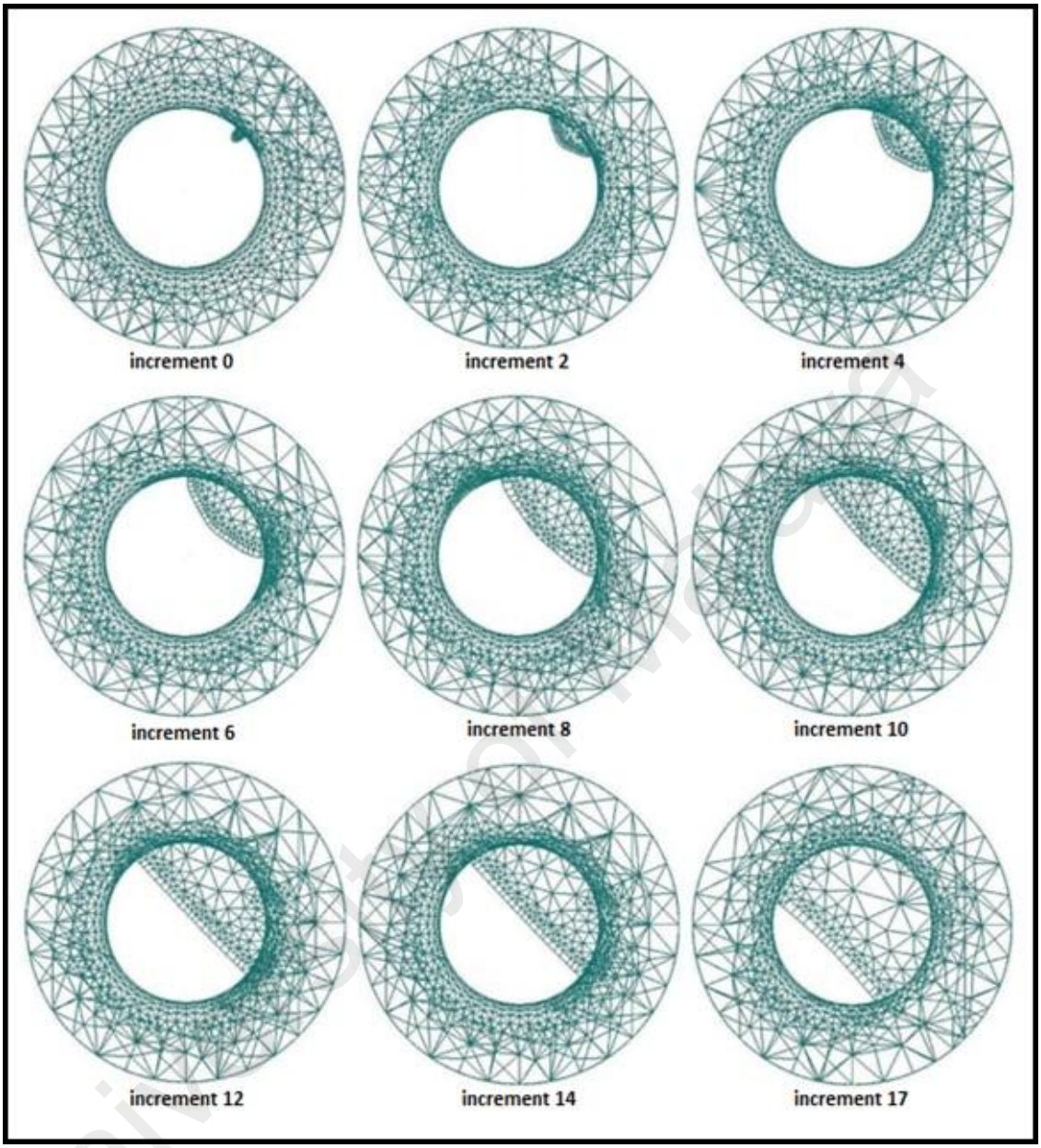

Figure 4.15: Crack shape evolutions for *a/c* = 2 and *r* = 1.558.

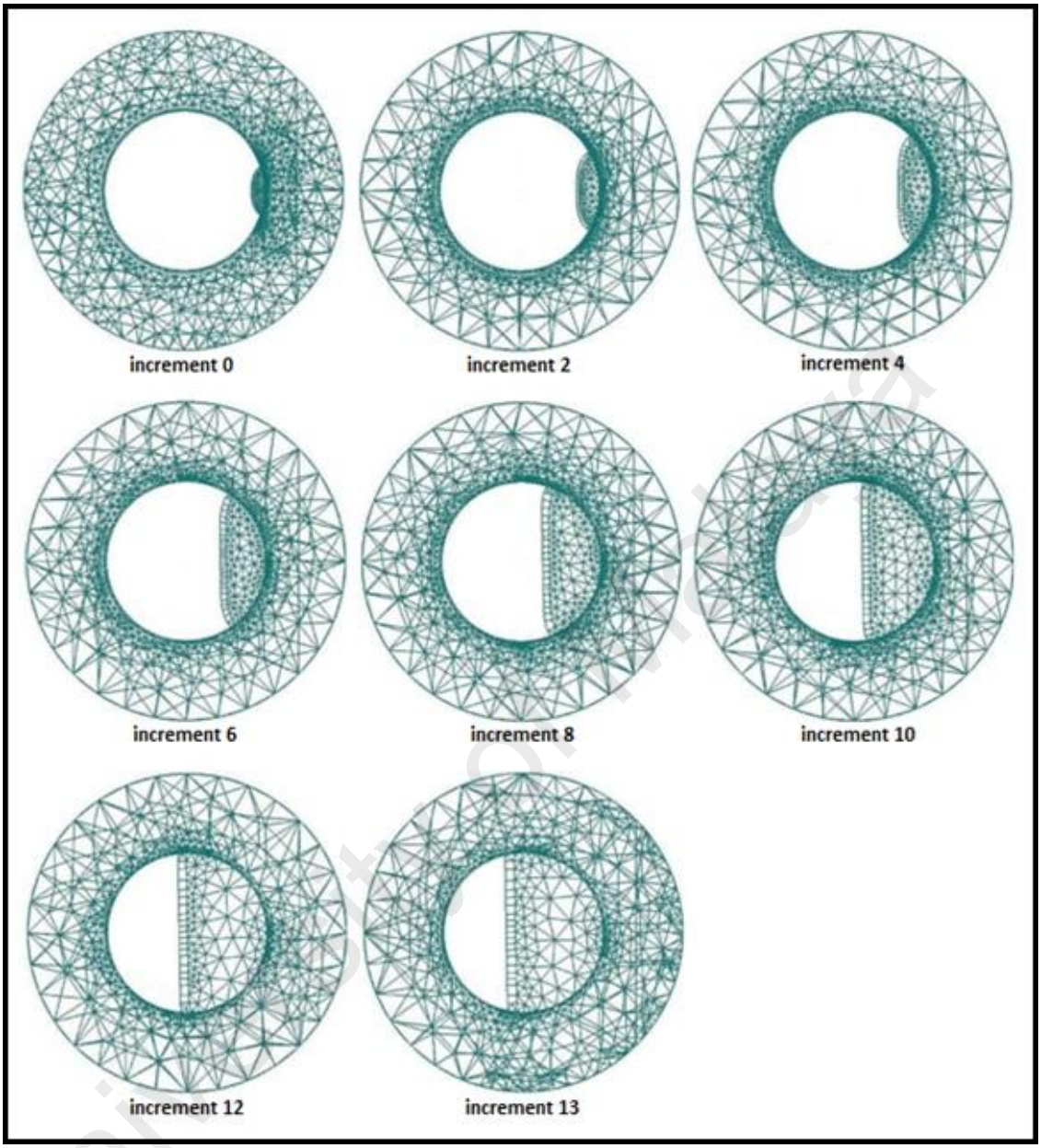

Figure 4.16: Crack shape evolutions for *a/c* = 0.5 and *r* = 0.529.

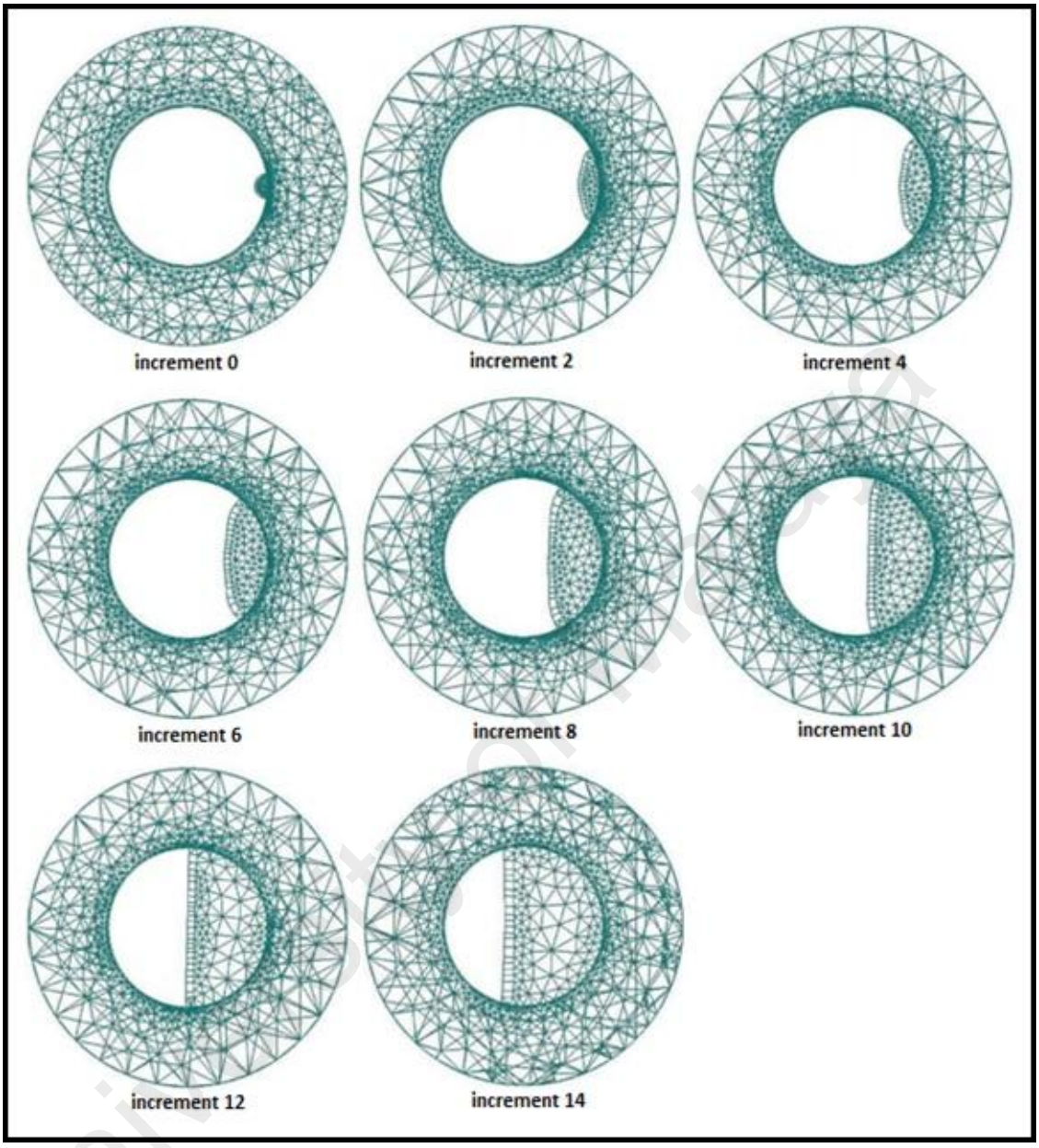

Figure 4.17: Crack shape evolutions for *a/c* = 1 and *r* = 0.529.

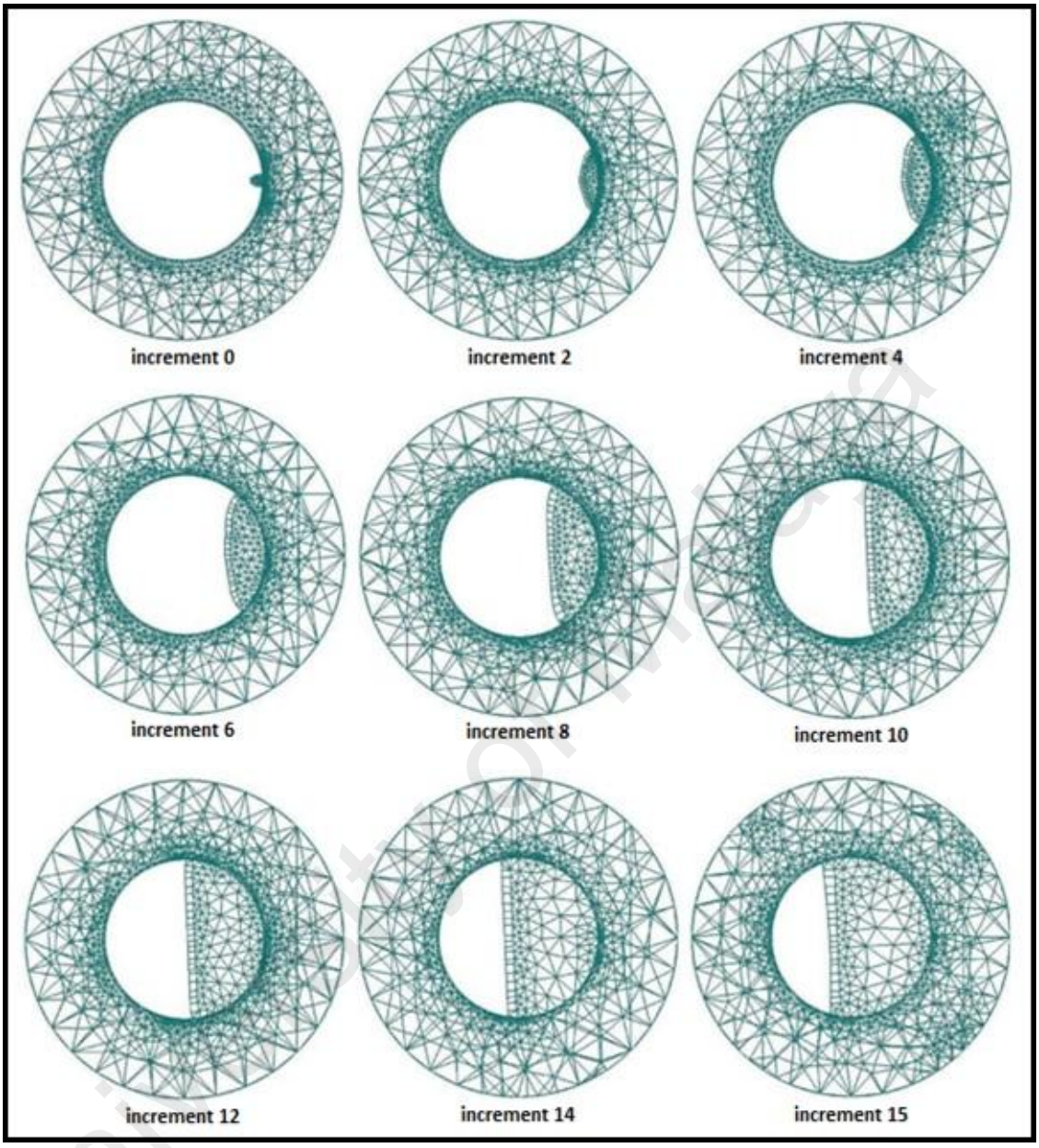

Figure 4.18: Crack shape evolutions for *a/c* = 2 and *r* = 0.529.

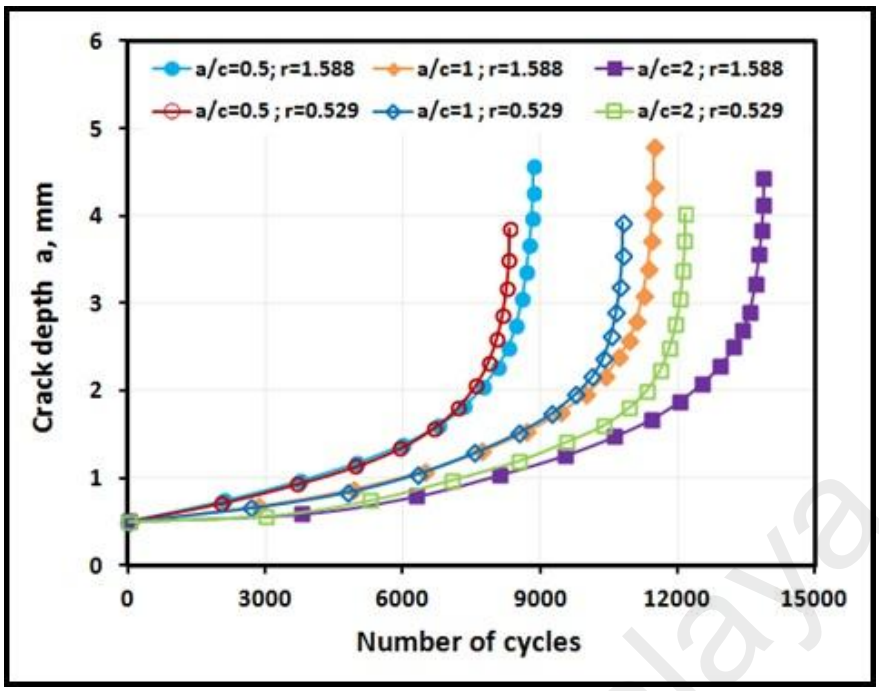

Figure 4.19: Fatigue life versus crack depth.

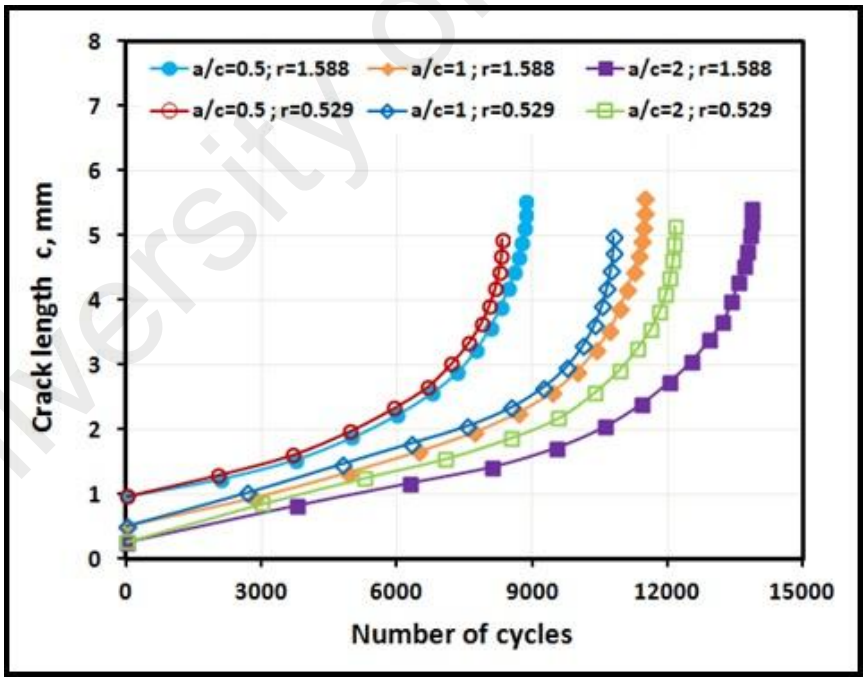

Figure 4.20: Fatigue life versus crack length.

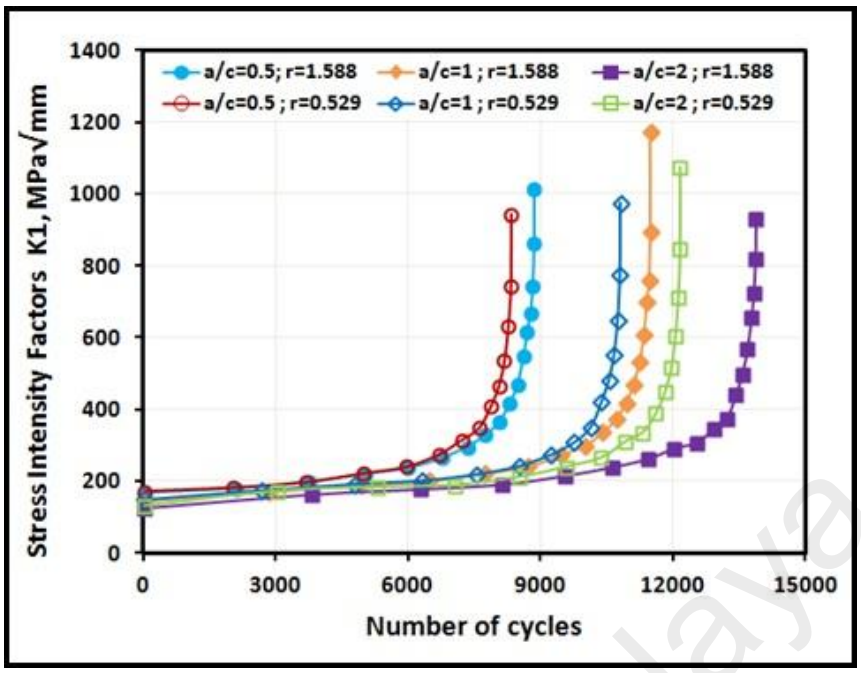

Figure 4.21: Fatigue life versus the SIFs (K_I).

4.2.3 Corner crack in a square prismatic bar under combined torsion–tension loading

4.2.3.1 Stress Intensity Factors

The stress intensity factors K_I, K_{II}, K_{III} and K_{eff} along the crack front of a corner crack in a prismatic bar for different loading ratios and aspect ratio *a/c* at the initial increment are presented in Figures 4.22–4.25. Zero point of horizontal axis in Figures. 4.22–4.25 is defined to be at the crossed surface point *c*. Cases E and F (refer to Table 3.1) shown in Figures. 4.22–4.25 denote the zero torsional loading. For a given aspect ratio *a/c* in Figure 4.22, a combination of a larger tension loading and a smaller torsional loading leads to greater K_I value. Figure 4.22 also confirms that there is no effect of the torsional stress on the K_I values at the initial increment. In all cases, the larger K_I value is found at the crossed surface point which has the smaller crack depth of *a* or crack length of *c*.

Figure 4.23 confirms that at the initial increment there is no effect of tension loading on the K_{II} values as evidenced by the coincided values for the configurations for a given crack aspect ratio *a/c*. In contrast to Mode I SIFs, the larger absolute K_{II} value is found at the crossed surface point which has the larger crack depth of *a* or crack length of *c*. As expected, the greater Mode II SIFs are shown to be under a larger torsional loading. The SIFs (K_{III}) for the tearing mode are presented in Figure 4.24. For a given crack aspect ratio *a/c*, the K_{III} values along the crack front for different loading ratios (but having the same torsion loading) are shown to coincide each other. The K_{III} values for zero torsional loading (Cases E and F) in Figure 4.24b indicates that the shearing load is predominant. In all cases under combined torsion–tension loadings, the greatest Mode III SIFs are shown at the mid-point of the crack fronts. Larger Mode III SIFs are found at the model with a larger torsional loading and a crack aspect ratio $a/c \neq 1$. At the initial increment (static condition), the K_I values are only induced by tension loading and the torsion load contributes to the K_{II} and K_{III} values. However, the torsion and tension loads will further interact in the following increments to produce the maximum principal stress that determines the crack paths. The interaction of the combined torsion–tension loadings would also contribute to the effective stress intensity factor K_{eff} that is defined as:

$$\boldsymbol{K_{eff} = \sqrt{(K_I + |K_{III}|)^2 + 2K_{II}^2}} \qquad \textbf{(4.5)}$$

The K_{eff} values along the crack fronts presented in Figure 4.25 shows similar patterns with the K_I values presented in Figure 4.22, indicating that the tension load is predominant in the fatigue crack growth based on the given loading ratios used in this study. Effect of the crack aspect ratio *a/c* on the SIFs is shown to be significant in all loading modes.

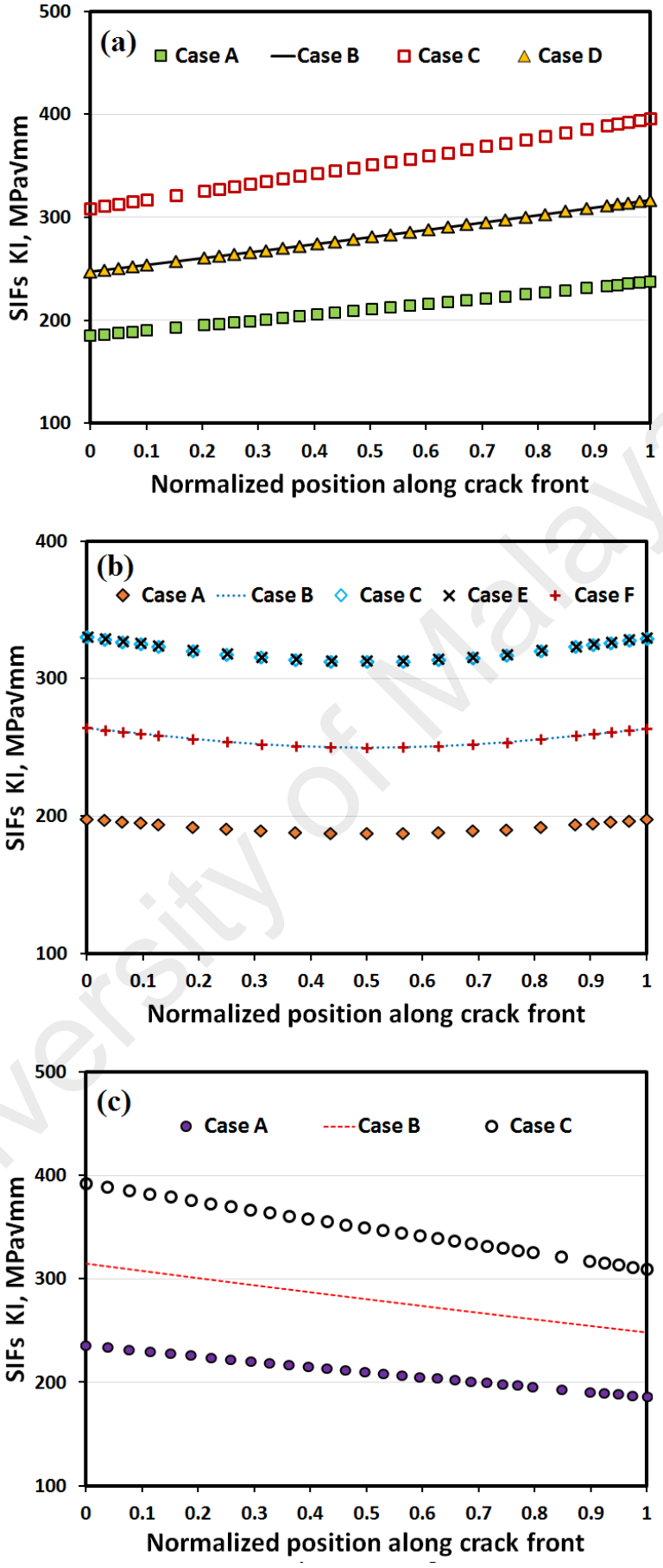

Figure 4.22: Stress intensity factor KI (opening mode) for different loading and crack aspect ratios at the initial condition (a) *a/c*=0.66; (b) *a/c*=1; (c) *a/c*=1.

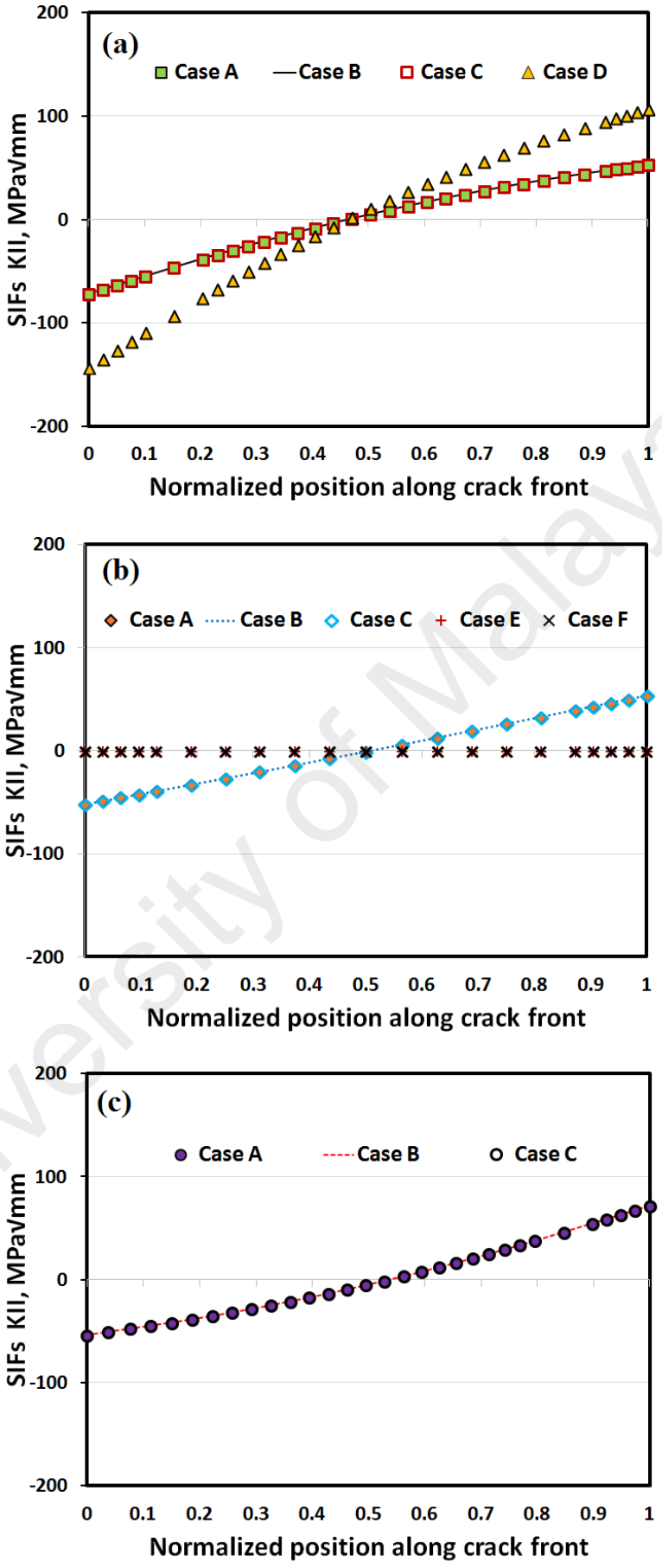

Figure 4.23: Stress intensity factor KII (shearing mode) for different loading and crack aspect ratios at the initial condition (a) *a/c*=0.66; (b) *a/c*=1; (c) *a/c*=1.5

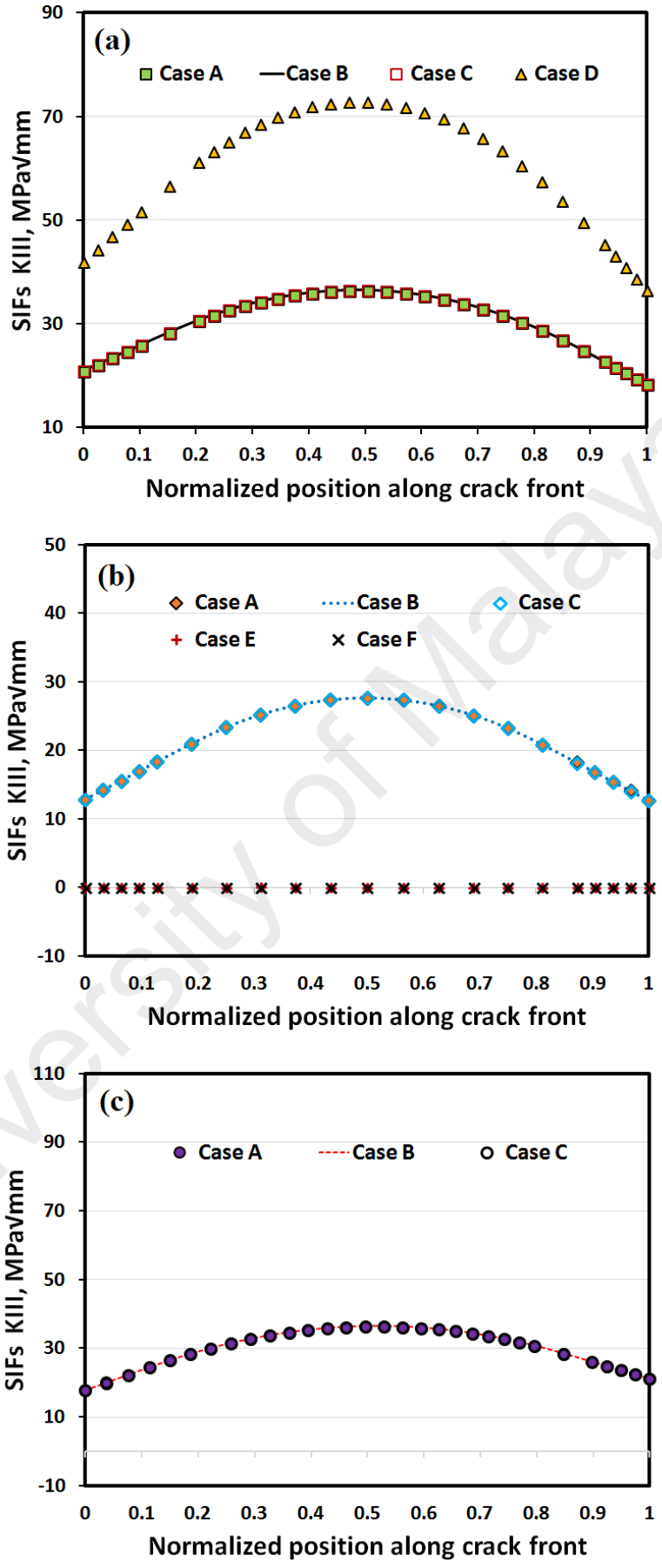

Figure 4.24: Stress intensity factor KIII (tearing mode) for different loading and crack aspect ratios at the initial condition (a) *a/c*=0.66; (b) *a/c*=1; (c) *a/c*=1.5

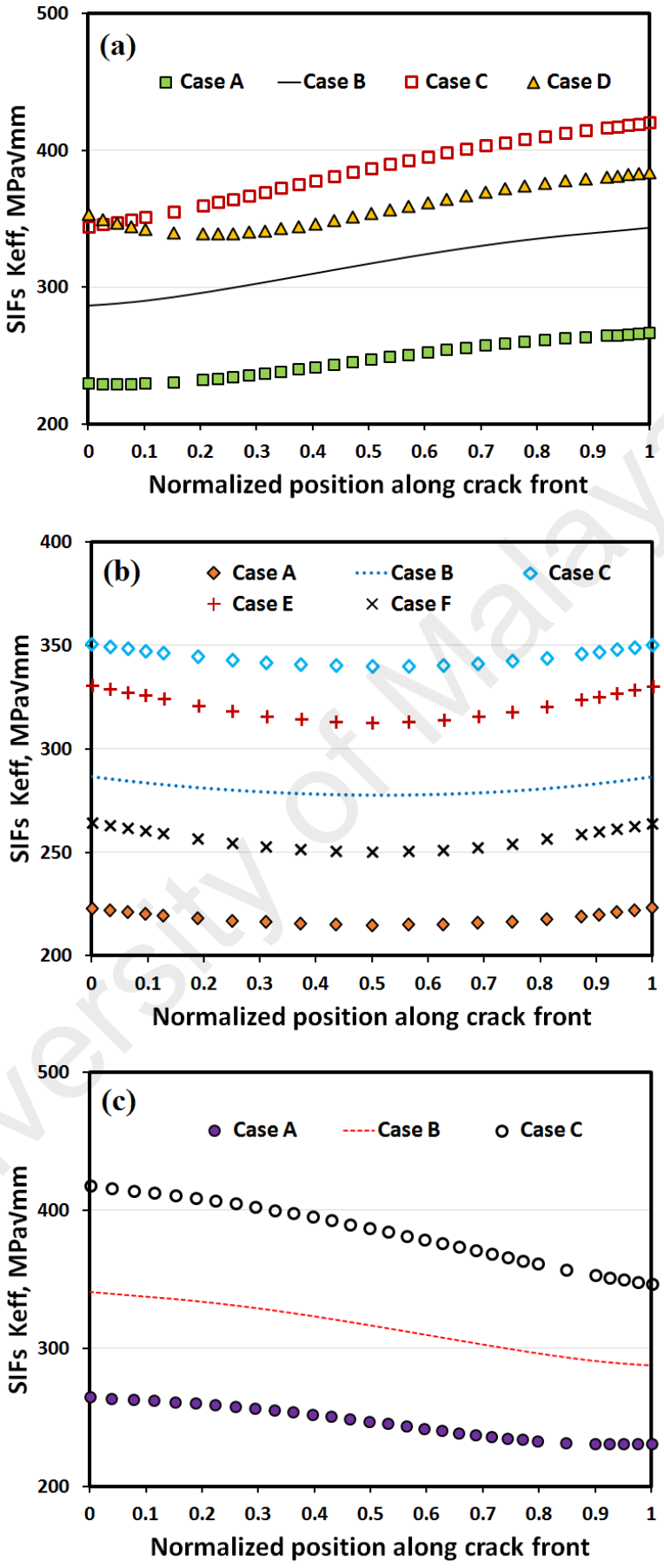

Figure 4.25: Stress intensity factor K_{eff} (mixed-mode) for different loading and crack aspect ratios at the initial condition (a) *a/c*=0.66; (b) *a/c*=1; (c) *a/c*=1.5

4.2.3.2 Fatigue life and crack evolution/direction

Figure 4.26 shows the crack shapes and the distributions of the principal stresses for *a/c* = 0.66 under a tension of 125 MPa and a torsion of 100 MPa at the initial increment and the final fracture. At the initial increment, a corner crack is introduced at the edge of the prismatic bar (Figure 4.26a). Upon the final fracture, an inclining shape of the crack surface against the bar longitudinal axis is observed in Figure 4.26b. The inclined crack path is triggered by the cyclic torsion load. For quantitative comparisons of inclined crack patch, the shapes of crack for *a/c* = 0.66 under combined tension of 75 MPa-torsion of 100 MPa and for *a/c* = 0.66 under combined tension of 100 MPa-torsion of 100 MPa at final increment are given in Figure 4.27. It can be seen from Figure 4.27, crack patch angle drawn from the initial to final increment of crack front for *a/c* = 0.66 under combined tension of 75 MPa-torsion of 100 MPa and for *a/c* = 0.66 under combined tension of 100 MPa-torsion of 100 MPa were approximately 35^0 and 25^0 , respectively. Whereas, from Figure 4.26, the crack patch angle was observed 16^0 for *a/c* = 0.66 under combined tension of 125 MPa-torsion of 100 MPa.

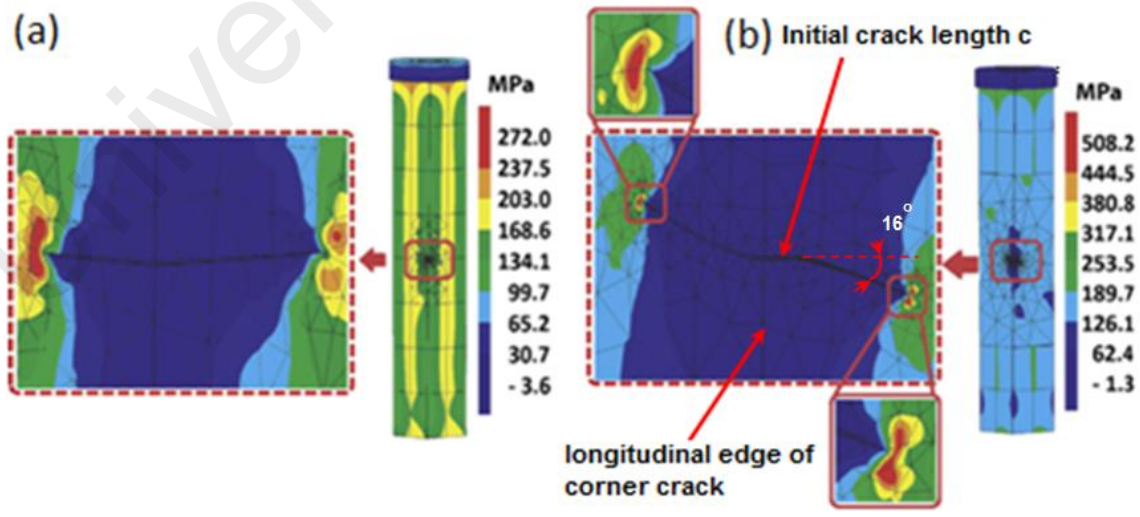

Figure 4.26: The shapes of crack in square bar and the corresponding principal stresses for *a/c*=0.66 under tension of 125 MPa and torsion of 100 MPa at (a) the initial increment; (b) the final fracture.

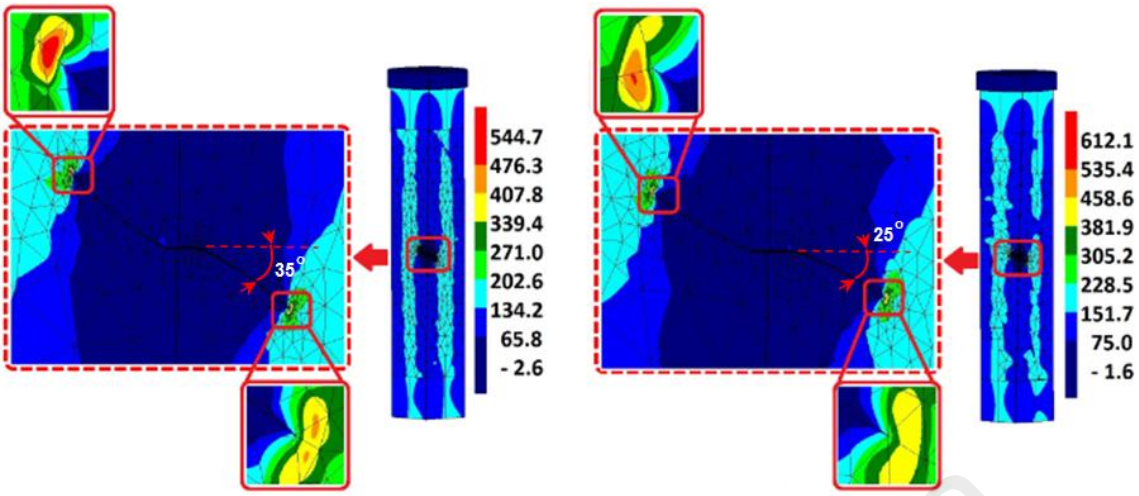

Figure 4.27: The shapes of crack (a) for *a/c*=0.66 under tension of 75 MPa and torsion of 100 MPa (b) for *a/c*=0.66 under tension of 100 MPa and torsion of 100 MPa

Figures 4.28 and 4.30 show the y-z plane view and x-y plane view of crack shape evolution during incremental crack extension respectively (see Figure 3.24 for coordinate system of the square bar model). Each line in Figures 4.28 and 4.30 indicates the crack front of corner crack at each increment of crack growth. For more details of the y-z plane view in Figure 4.28, one example of the y-z plane view of crack patch and mesh crack surface for crack aspect ratio a/c = 0.66 under a combined tension of 125 MPa-torsion of 100 MPa was given in Figure 4.29.

It can be seen from Figures 4.28 that the inclination of crack path for a given torsion load increase as the tension to torsion stress ratio is decrease. Figure 4.28 also show that the model with crack aspect ratio a/c = 0.66 and a/c = 1.5 relatively to have similar crack patch and crack growth angles. Figure 4.30 indicated that for aspect ratio $a/c \neq 1$, crack extension at the crossed surface point which has the smaller crack depth of a or crack length of c larger for the first few increments.

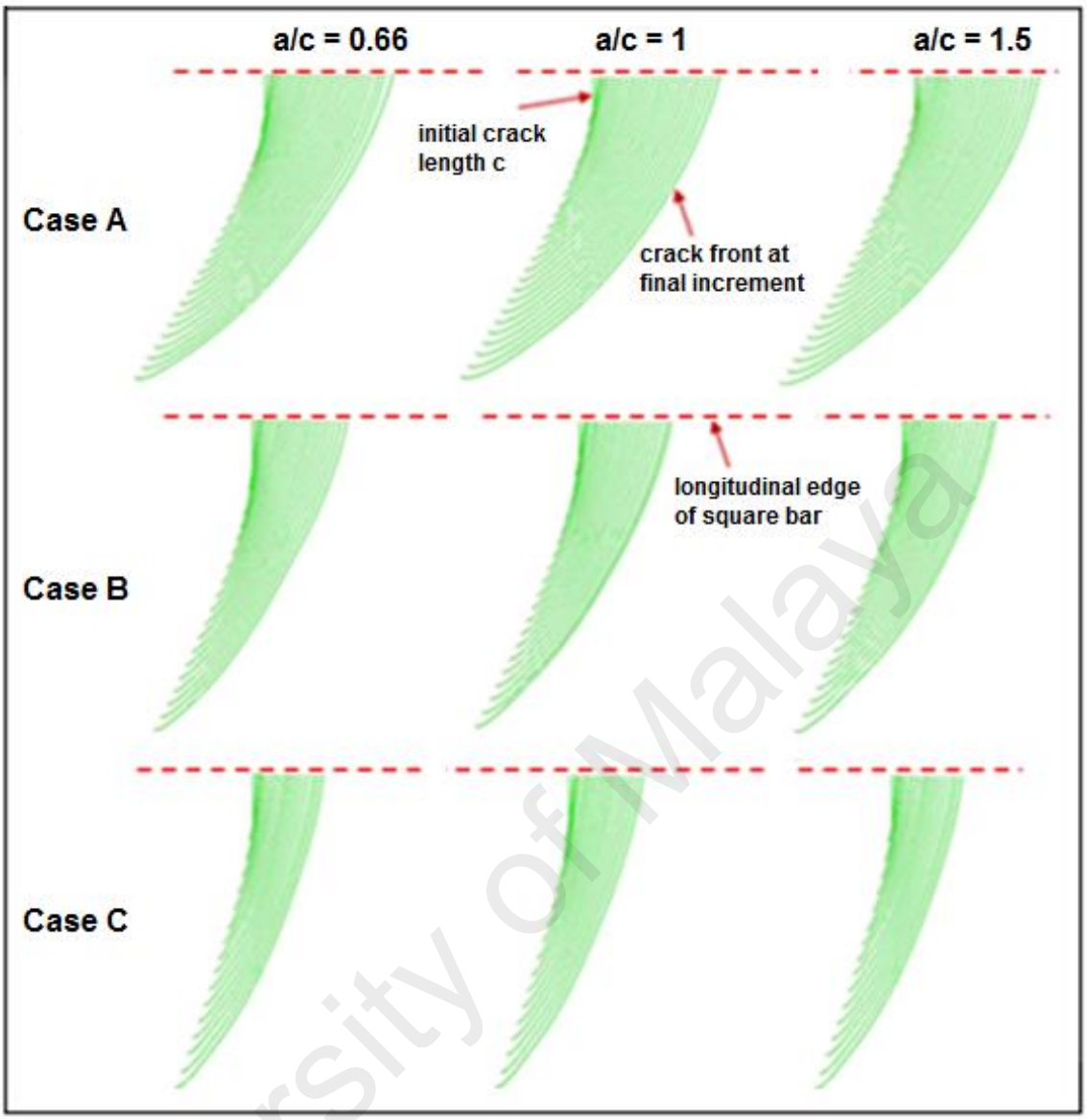

Figure 4.28: The y-z plane view of crack shape evolution in square bar.

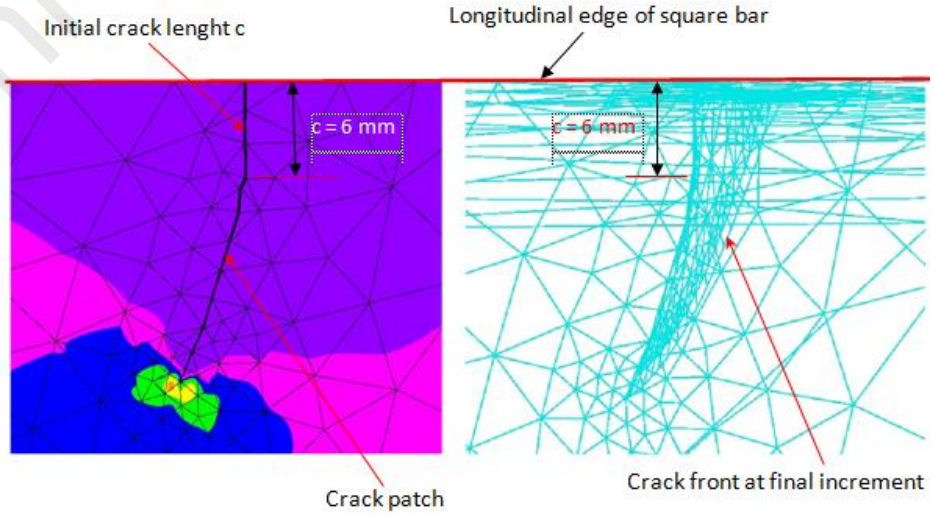

Figure 4.29: The y-z plane view of crack patch and mesh crack surface for *a/c*=0.66 under tension of 125 MPa and torsion of 100 MPa (Case C with *a/c* =0.66)

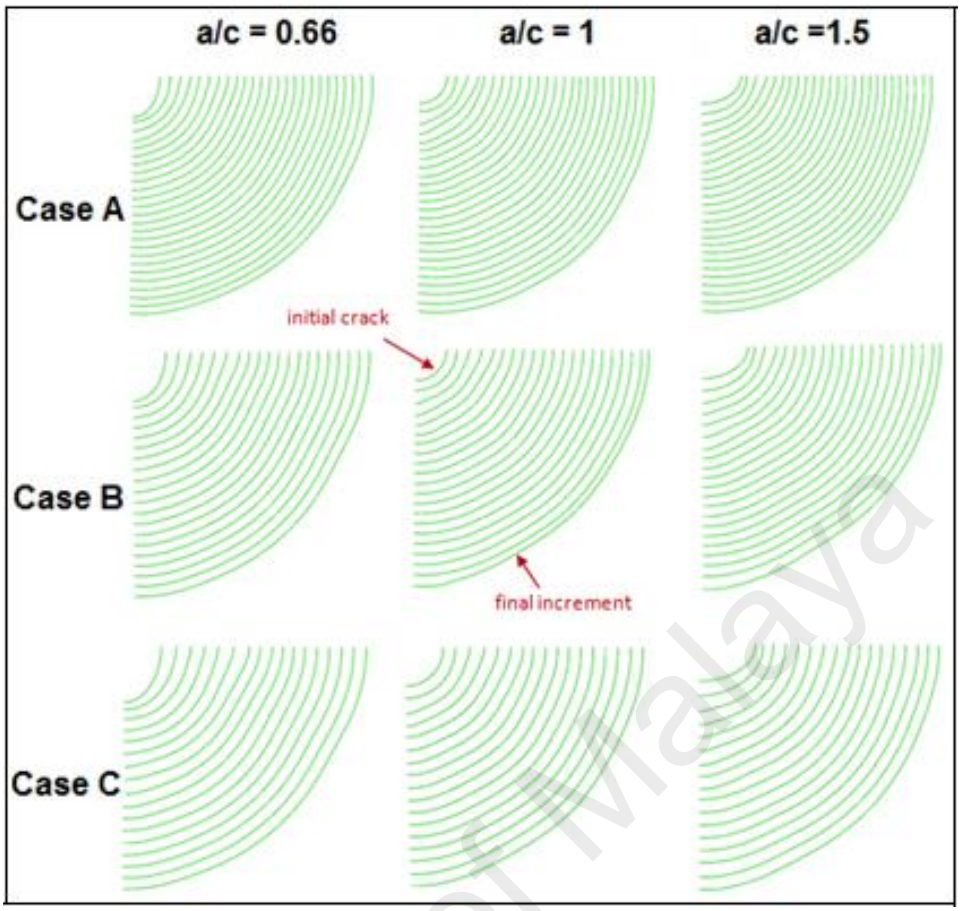

Figure 4.30: The x-y plane view of crack shape evolution in square bar.

Figures 4.31 and 4.32 show the crack depth a and the K values against the number of cycles. The crack depth a (= a_o+ Δa) is measured at the crossed surface point, where a_o and Δa are the initial crack depth and the crack increment, respectively. It is similarly defined for the crack length c (= c_o+ Δc). In square prismatic bars subjected to cyclic loadings, for the given crack aspect ratios a/c = 0.66 (4/6) and a/c = 1.5 (6/4) shown in Figure 4.31, the crack depth would coincide each other at a number of cycles, indicating that the crack aspect ratio is evolving to a unity ($a/c \approx 1$). The asymptotic aspect ratio $a/c \approx 1$ is then maintained until reaching the fracture condition. For a given tension loading, a shorter fatigue life is found at the model with a larger torsional loading and the crack aspect ratio $a/c \neq 1$. It can be seen from Figure 4.32, the K_{eff} values at the crack depth a (cross surface point) for the zero torsional loading are found to smoothly form a hyperbolic curve in comparison to those under combined loadings which have

some stepped increases in SIFs as the number of cycles is increasing. The stepped increases of the SIFs at those particular periods are due to the changes of the crack plane orientation (non-planar) with regard to the maximum principal stresses.

The results of evaluation stress intensity factors, crack patch and fatigue life of a corner crack in square bar under combined tension-torsion loading can be used for prediction of fracture behavior and fatigue life of the similar cracked components under mode I/III condition. However, this prediction requires the understanding, experience and engineering judgement to obtain the accurate and reliable results. It may begin by identifying whether the corresponding cracked component can be represented by the square bar model or not. Then, due to the crack patch and fatigue life are independent to applied stress intensity factor and critical fracture toughness, it is necessary to identify the mode and range of applied load (or stress), crack size and geometry and material of the component. The crack patch and fatigue life behaviour obtained from present study can be considered to approximate the prediction of the crack patch and fatigue life of such the similar cracked component of the same material under similar cyclic condition (range of stress intensity factor and stress ratio).

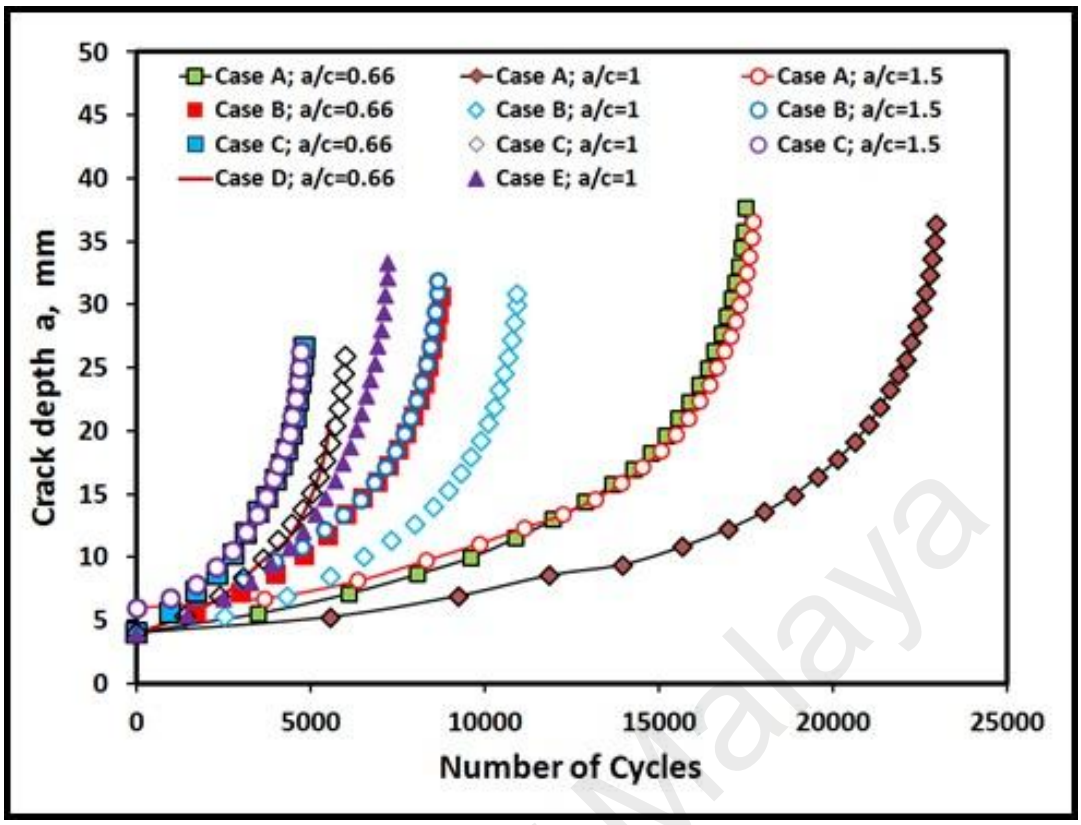

Figure 4.31: The crack depth *a* against the number of cycles.

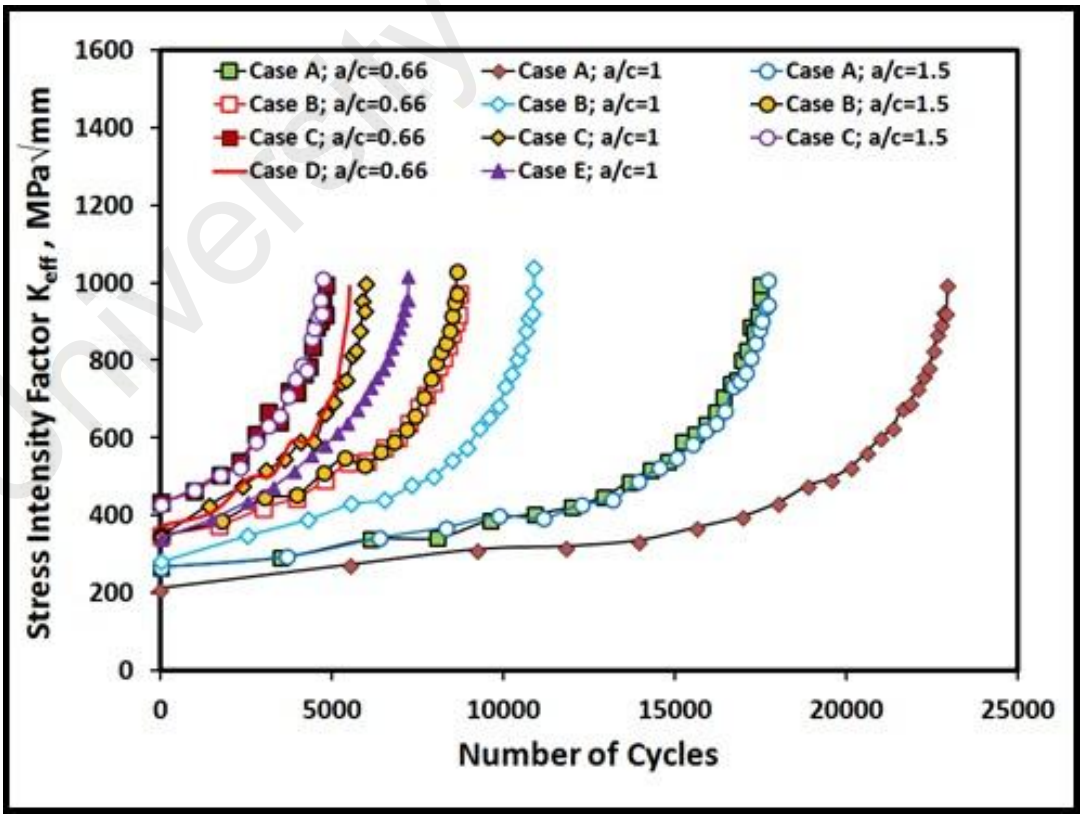

Figure 4.32: The K_{eff} values against the number of cycles.

4.3 Experimental and numerical results of surface crack growth in solid cylinder under combined axial-torsion loading

4.3.1 Crack growth path/direction of a surface crack

Fatigue crack growth paths for different loading cases and crack aspect ratios by experimentations and numerical simulations are presented in Figures 4.33-4.36. It may be observed from Figures 4.33-4.36 that the crack growth paths estimated by the numerical simulations are generally shown to have similar patterns with those by experimentations. However, these patterns do not necessarily have similar crack lengths for a given approximated cycle. For the given loading case and crack depth, a larger crack aspect ratio is observed to result in a larger angle of the inclined crack path. During stable crack growth, the larger crack aspect ratio would geometrically lead to a larger mixed shearing and tearing mode, causing the crack extension to grow towards a larger angle. For a given crack aspect ratio, a larger torsion is also observed to result in a larger angle of the inclined crack path. The torsion loading reasonably promote the shearing and tearing effects on the crack extension.

Fatigue crack growth data at the first increment obtained by experiments and simulations for all load cases are shown in Table 4.2. Figures 4.37-4.40 compare the measured and predicted crack path angle at the first increment for all load cases. It can be observed from Figures 4.37-4.40 and Table 4.2, for all load cases, the crack growth angle at the initial crack growth obtained by the simulation is slightly larger than the one obtained by experiment. The largest difference crack growth angle obtained by the experiment and the simulation is 0.8 degree (1.5%) which is found on the specimen with crack aspect ratio a/c = 2 and load case of tension of 100 MPa-torsion of 125 MPa.

Table 4.2: Fatigue crack growth data at first increment

Load case		crack depth (a)	crack length (c)	Number of cycle		crack length (mm)		growth angle (deg)	
Tension (Mpa	Torsion (Mpa)			Exp	BEASY	Exp	BEASY	Exp	BEASY
100	100	1	0.5	13505	13505	0.712	0.796	47.8	48.2
100	125	1	0.5	12686	12686	0.801	0.855	52.0	52.8
100	100	1	1	6277	6277	1.132	1.192	46.8	47.1
100	125	1	1	6086	6086	1.184	1.251	51.4	52.0

The crack path at the second increment for all load cases was shown by the second figures from top in Figures 4.33-4.36. At this increment, the crack growth tends to deviate from the previous direction, forming a zig-zag or fluctuating crack path as shown in Figure 4.41 for load case of tension of 100 MPa-torsion 100 MPa and crack aspect ratio a/c = 2 after 23951 number of cycle. The crack length at each increment for load case of tension of 100 MPa-torsion 100 MPa and crack aspect ratio a/c = 2 is shown in Table 4.4. It can be seen from Table 4.4 that the crack lengths at the second increment estimated by the simulation and the experiment are 1.048 mm and 0.951 mm, respectively, indicating a good agreement between the results of the simulation and the experiment. However, as shown in Figure 4.41, the measured and predicted crack growth angles observed at this increment have a significant different where the values were -28 degree and 3 degree, respectively.

The predicted crack path and crack length up to the third increment (after 30014 number of cycle) for crack aspect ratio a/c = 2 and load case of tension of 100 MPa-torsion of 100 MPa were compared with the experimental result shown in Figure 4.42 and Table 4.4. From the comparison in Figure 4.42, it is found that the crack growth angle estimated by the simulation is 33 degree which is smaller than 38 degree measured by the experiment. Whereas, the predicted crack length was observed larger than those obtained by experiment as shown in Table 4.4. The predicted and measured crack length at this increment was found of 1.296 mm and 1.182 mm, respectively.

Figure 4.43 compares the measured and predicted crack paths up to the fourth increment (after 34935 number of cycle) for load case of tension of 100 MPa-torsion of 100 MPa and crack aspect ratio a/c = 2. It can be seen from Figure 4.43 that the crack growth angle estimated by the simulation and the experiment was found approximately -5.8 degree and 7 degree, respectively. Whereas, the measured and predicted crack length for load case of tension of 100 MPa-torsion of 100 MPa (crack aspect ratio a/c = 2) were found of 1.351 mm and 1.532 mm, respectively, as shown in Table 4.4.

The prediction of crack growth angle and its experimental results at the first and third increments were in a good agreement as shown in Figures 4.37-4.40 and Figure 4.42, respectively. However, the crack growth angle cannot be precisely achieved at the second and fourth increments as shown in Figures 4.41 and 4.43, respectively. Although there is a small deviation, the trend of overall crack growth was well predicted. Therefore, the prediction of crack growth direction with MSED criterion is acceptable.

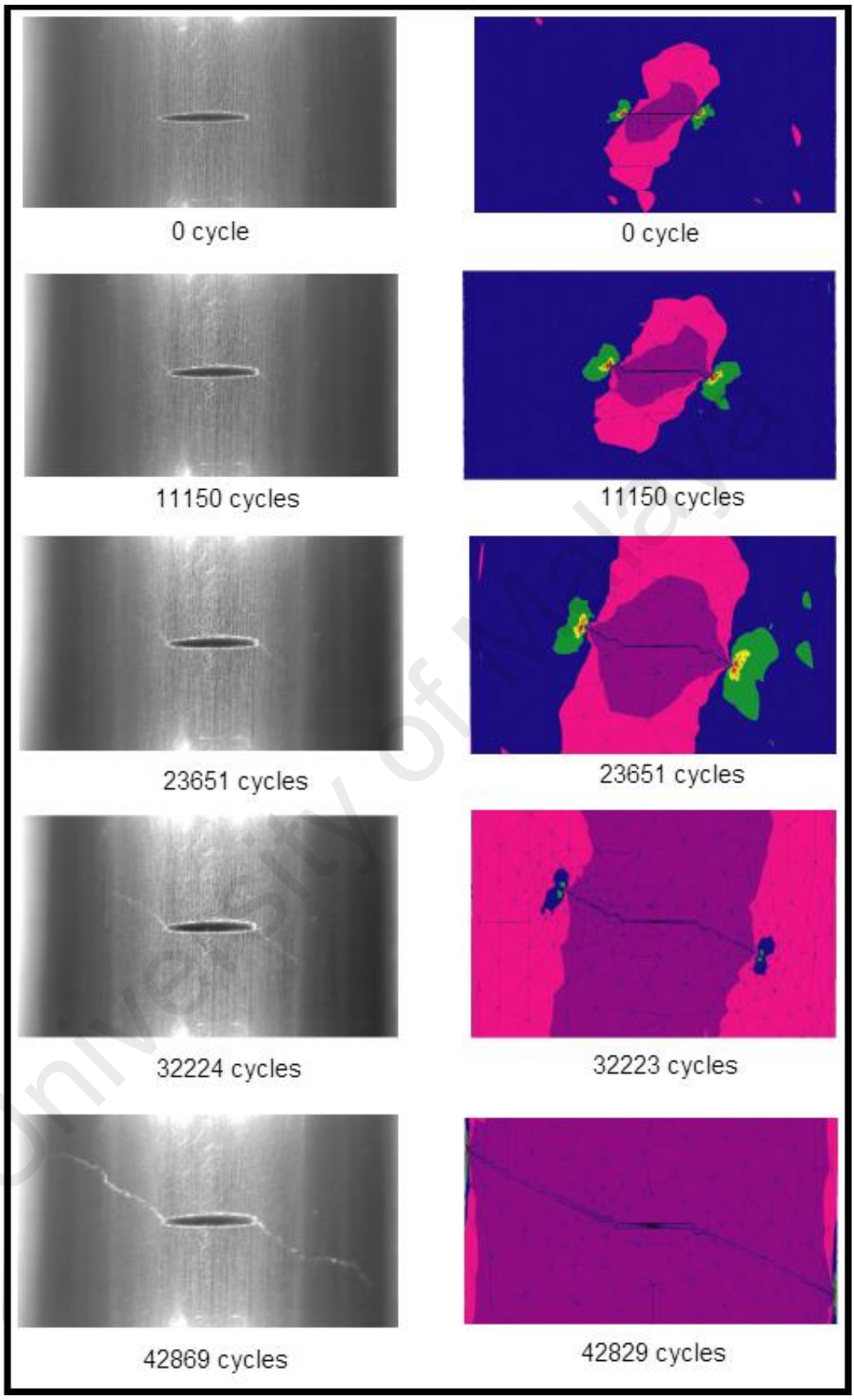

Figure 4.33: The crack growth path over the given approximated number of cycles by the experiment and numerical simulation for *a/c* = 1 under combined cyclic tension (= 100 MPa) – torsion (= 100 MPa) loading.

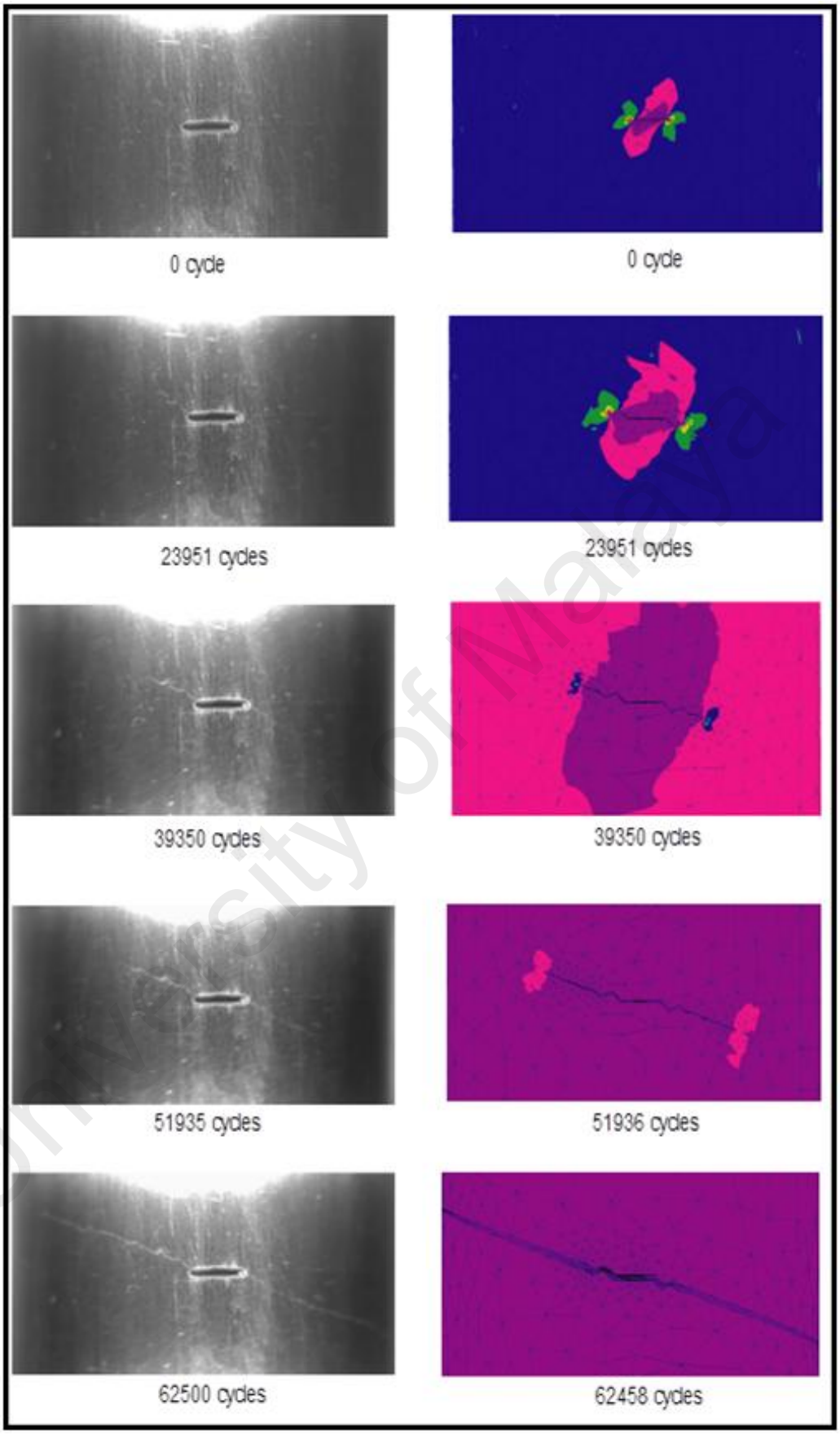

Figure 4.34: The crack growth path over the given approximated number of cycles by the experiment and numerical simulation for *a/c* = 2 under combined cyclic tension (= 100 MPa) – torsion (= 100 MPa) loading.

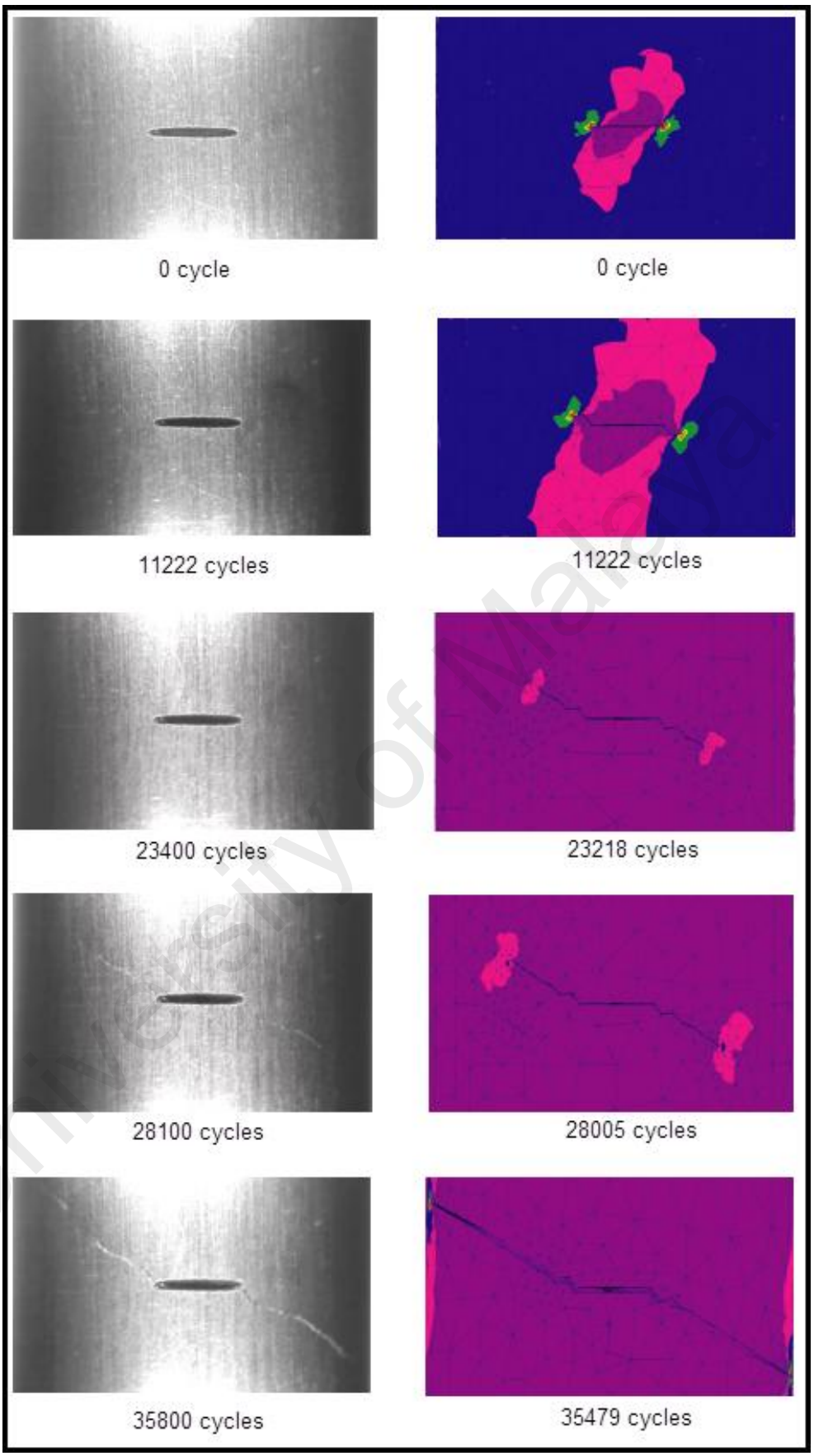

Figure 4.35: The crack growth path over the given approximated number of cycles by the experiment and numerical simulation for *a/c* = 1 under combined cyclic tension (= 100 MPa) – torsion (= 125 MPa) loading.

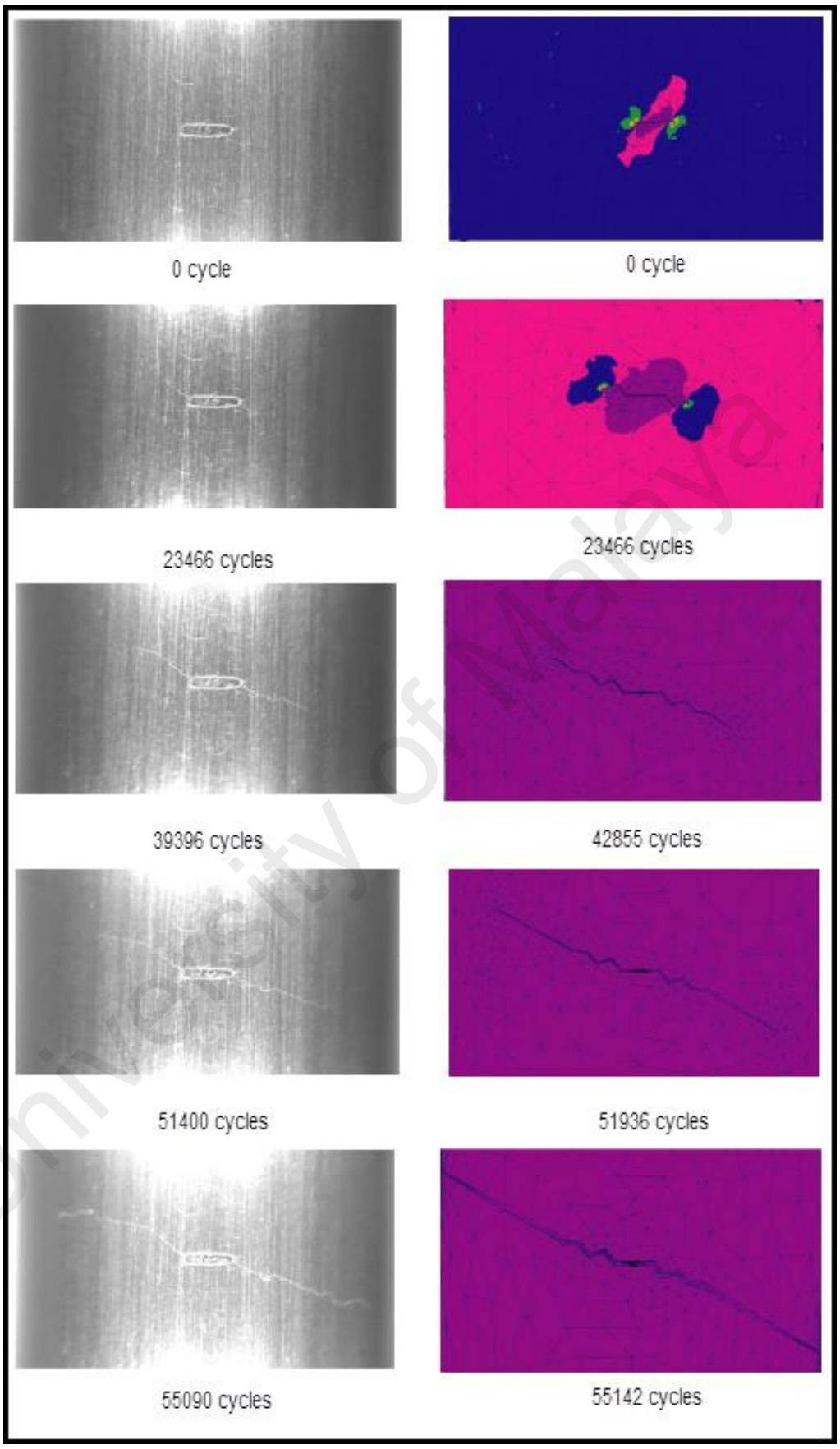

Figure 4.36: The crack growth path over the given approximated number of cycles by the experiment and numerical simulation for *a/c* = 2 under combined cyclic tension (= 100 MPa) – torsion (= 125 MPa) loading.

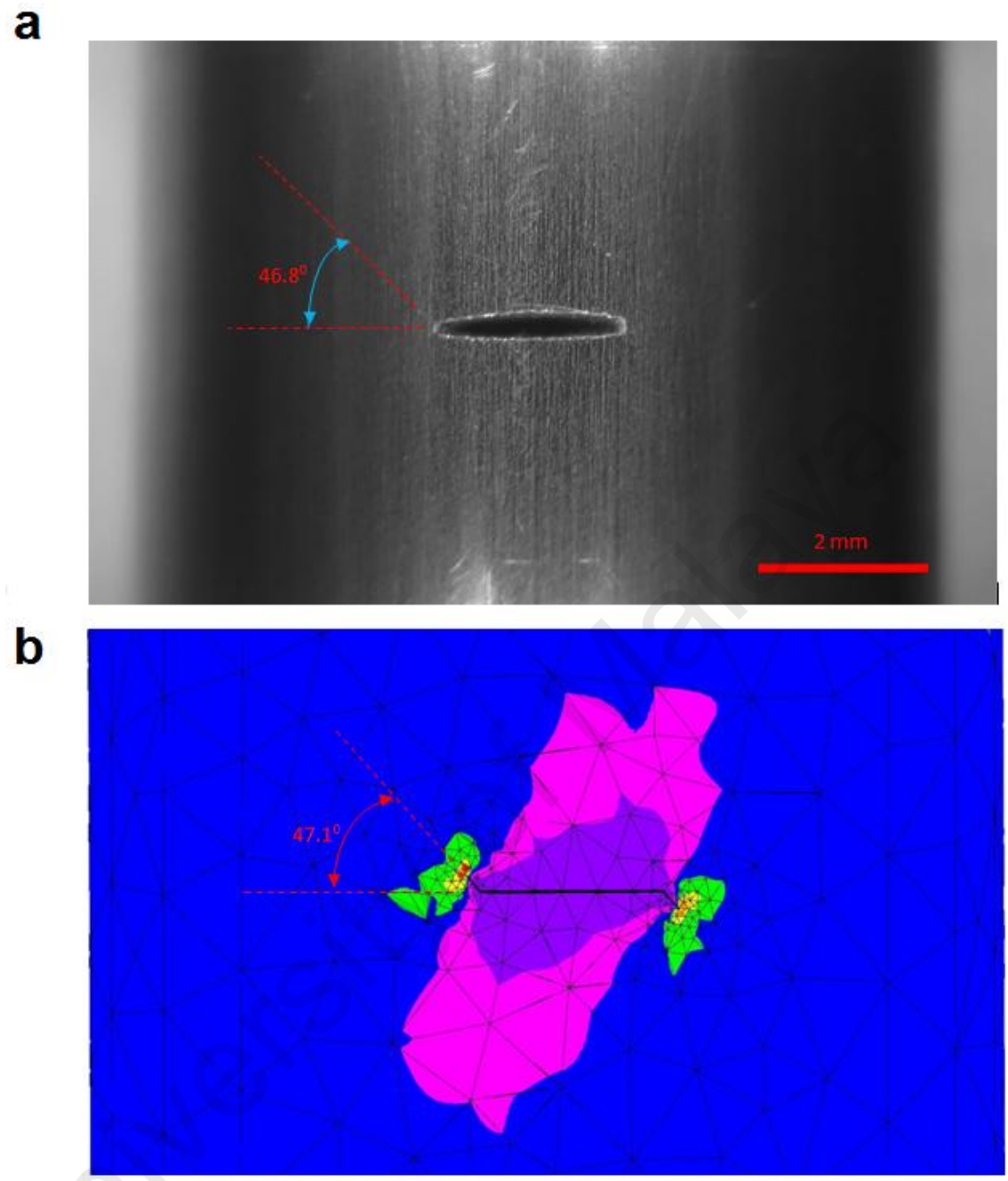

Figure 4.37: The crack growth path at first increment (6277 cycles) for *a/c* = 1 under combined cyclic tension (= 100 MPa) – torsion (= 100 MPa) loading by (a) the experiment and (b) the numerical simulation

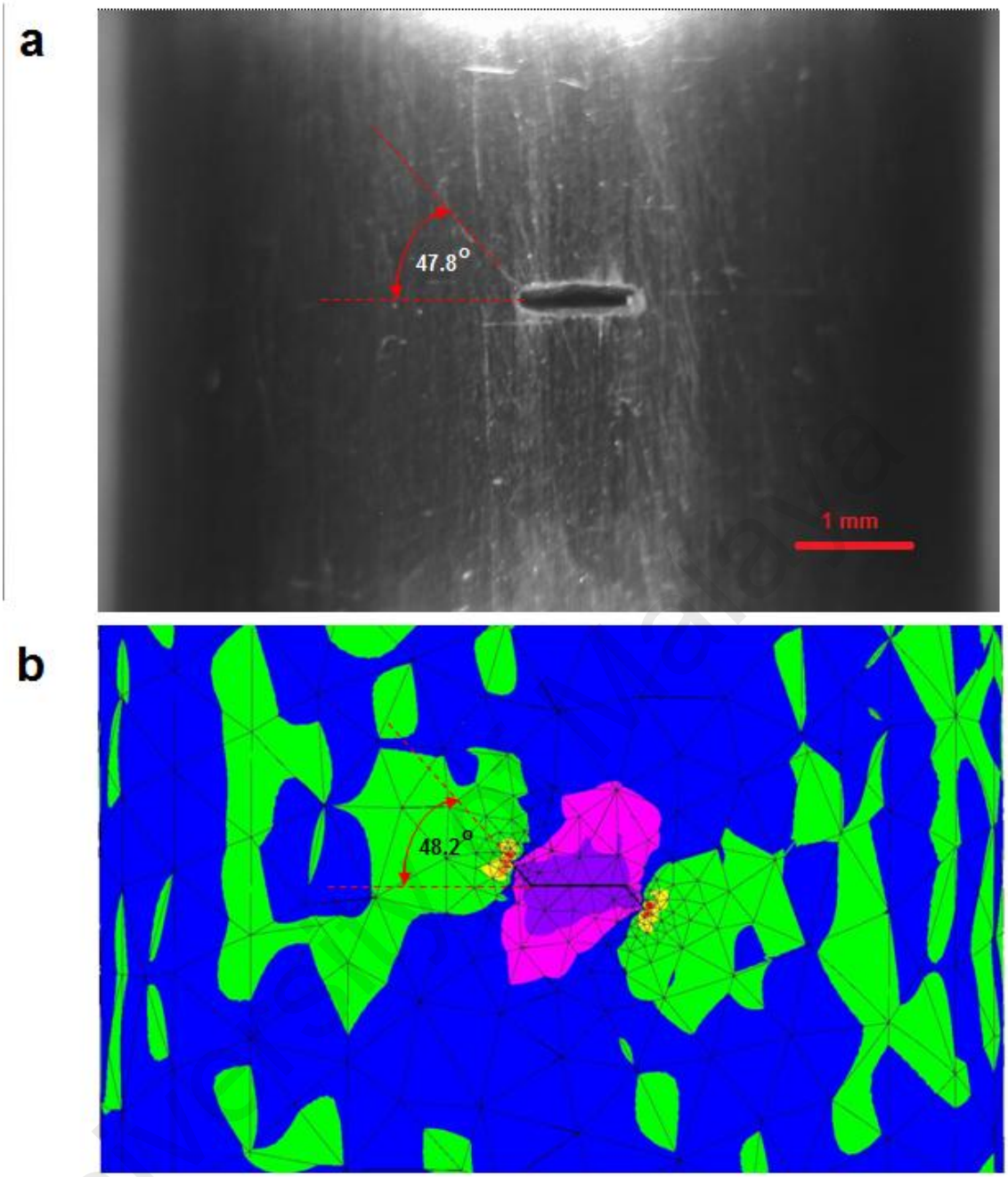

Figure 4.38: The crack growth path at first increment (13505 cycles) for *a/c* = 2 under combined cyclic tension (= 100 MPa) – torsion (= 100 MPa) loading by (a) the experiment and (b) the numerical simulation.

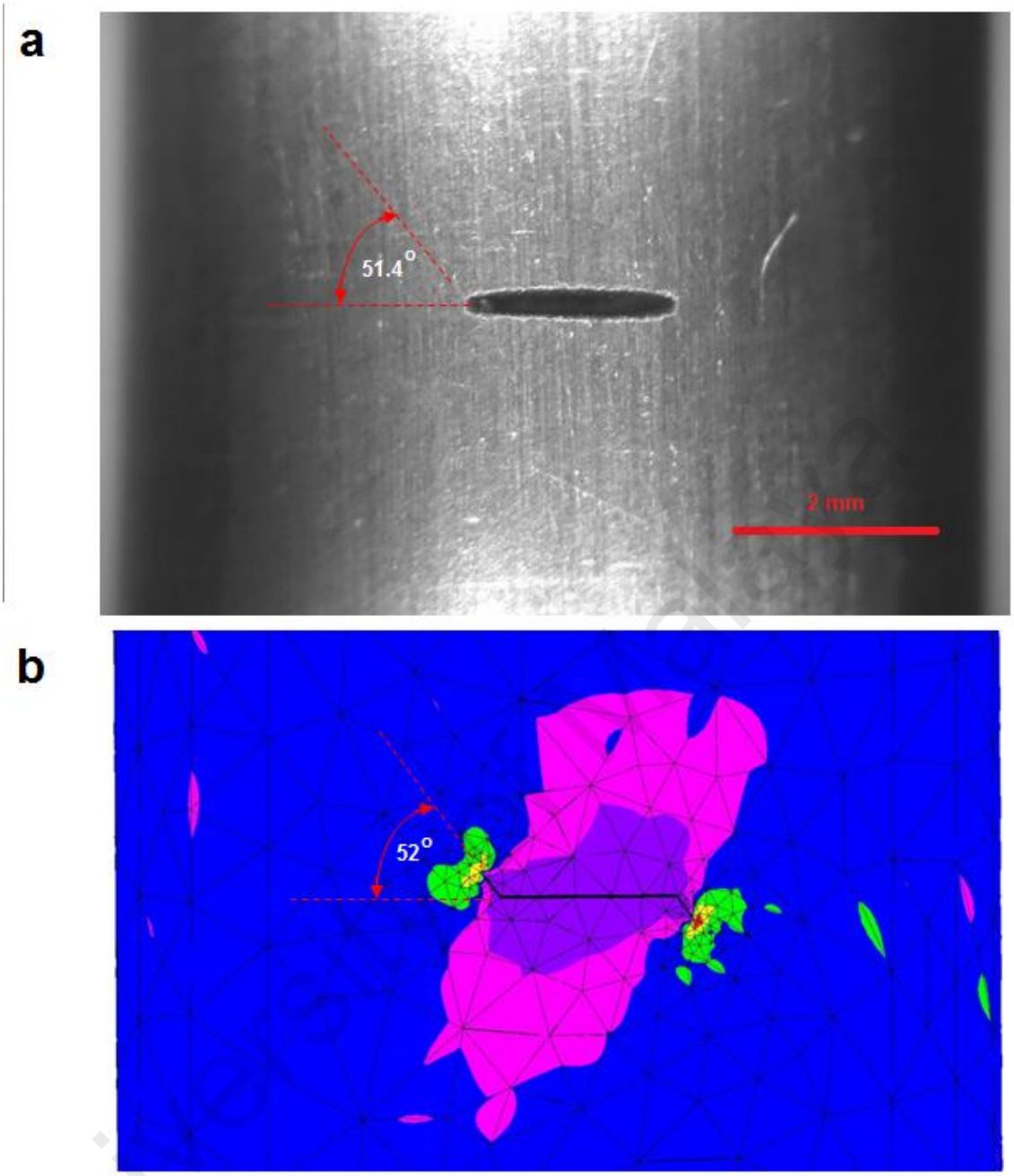

Figure 4.39: The crack growth path at first increment (6086 cycles) for *a/c* = 1 under combined cyclic tension (= 100 MPa) – torsion (= 125 MPa) loading by (a) the experiment and (b) the numerical simulation.

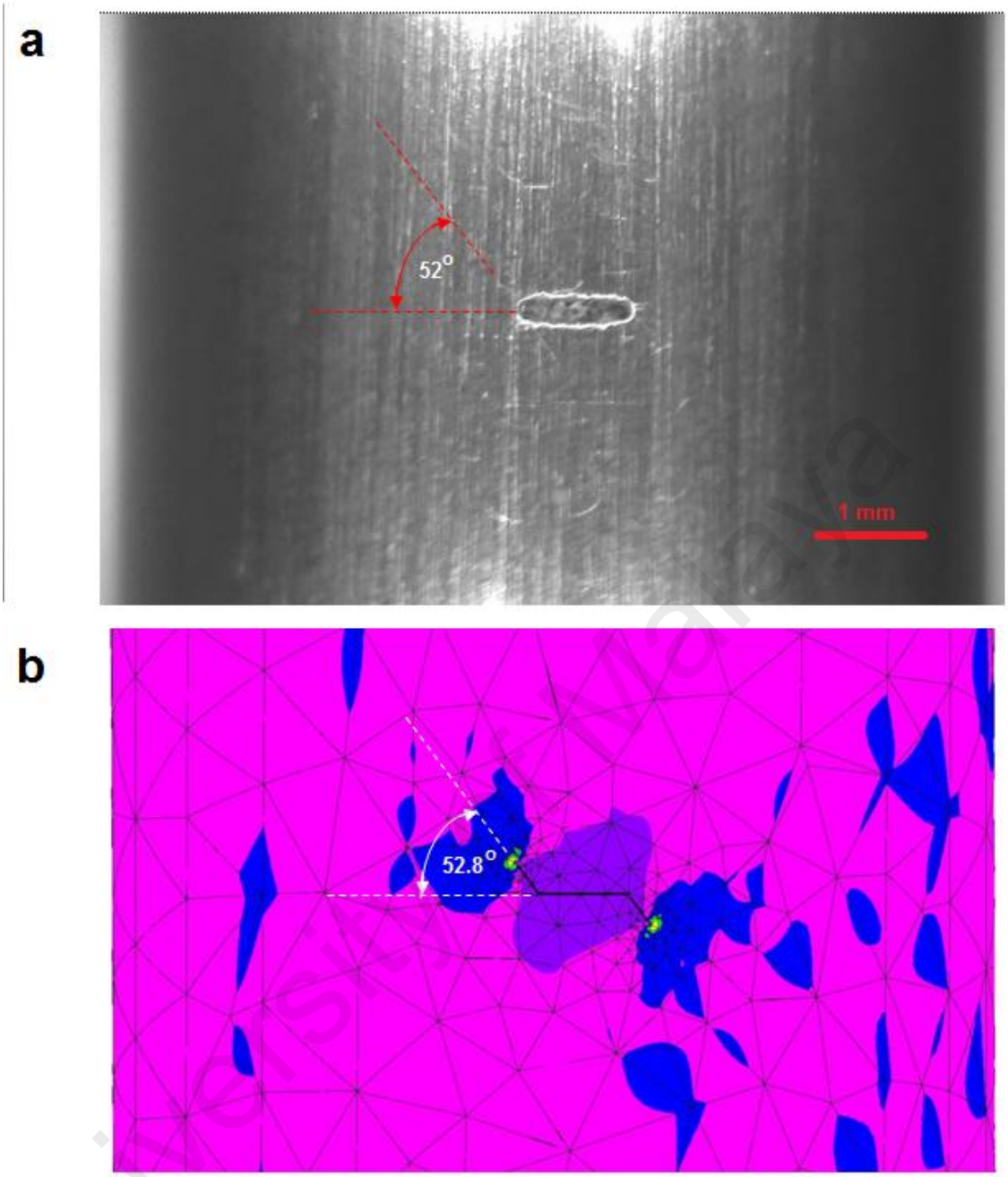

Figure 4.40: The crack growth path at first increment (12686 cycles) for *a/c* = 2 under combined cyclic tension (= 100 MPa) – torsion (= 125 MPa) loading by (a) the experiment and (b) the numerical simulation

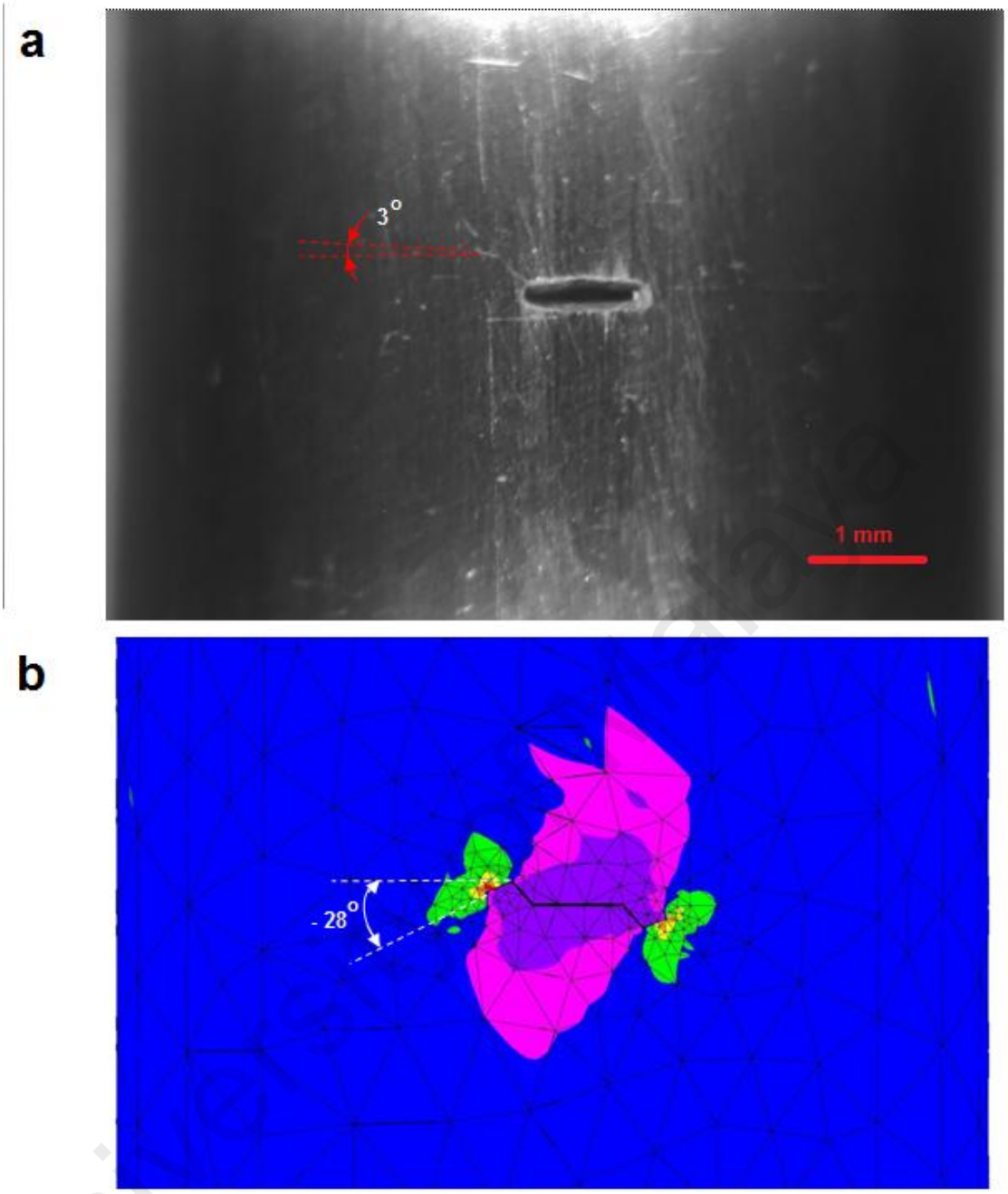

Figure 4.41: The crack growth path at second increment (23951 cycles) for *a/c* = 2 under combined cyclic tension (= 100 MPa) – torsion (= 100 MPa) loading by (a) the experiment and (b) the numerical simulation.

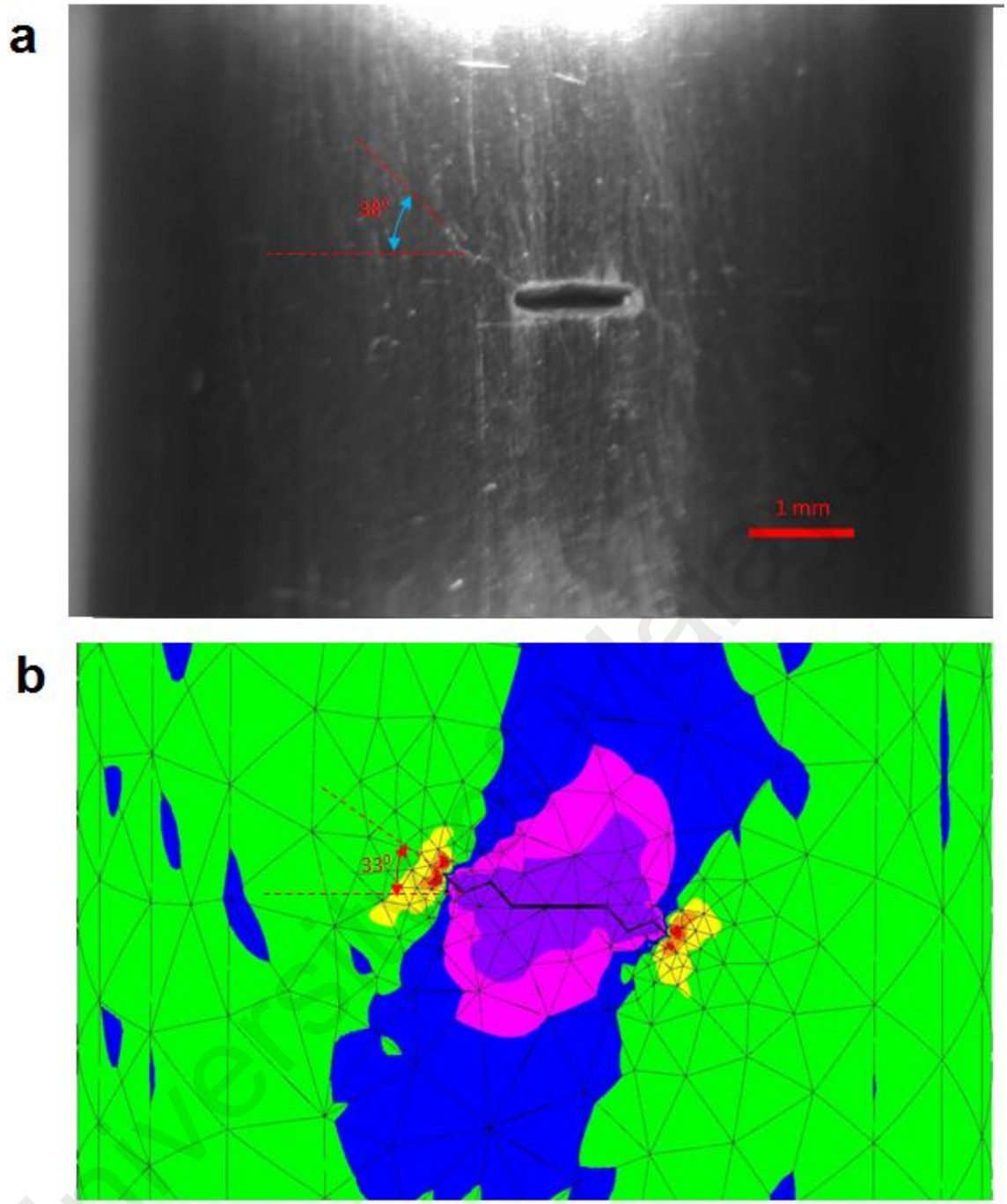

Figure 4.42: The crack growth path at third increment (30014 cycles) for *a/c* = 2 under combined cyclic tension (= 100 MPa) – torsion (= 100 MPa) loading by (a) the experiment and (b) the numerical simulation.

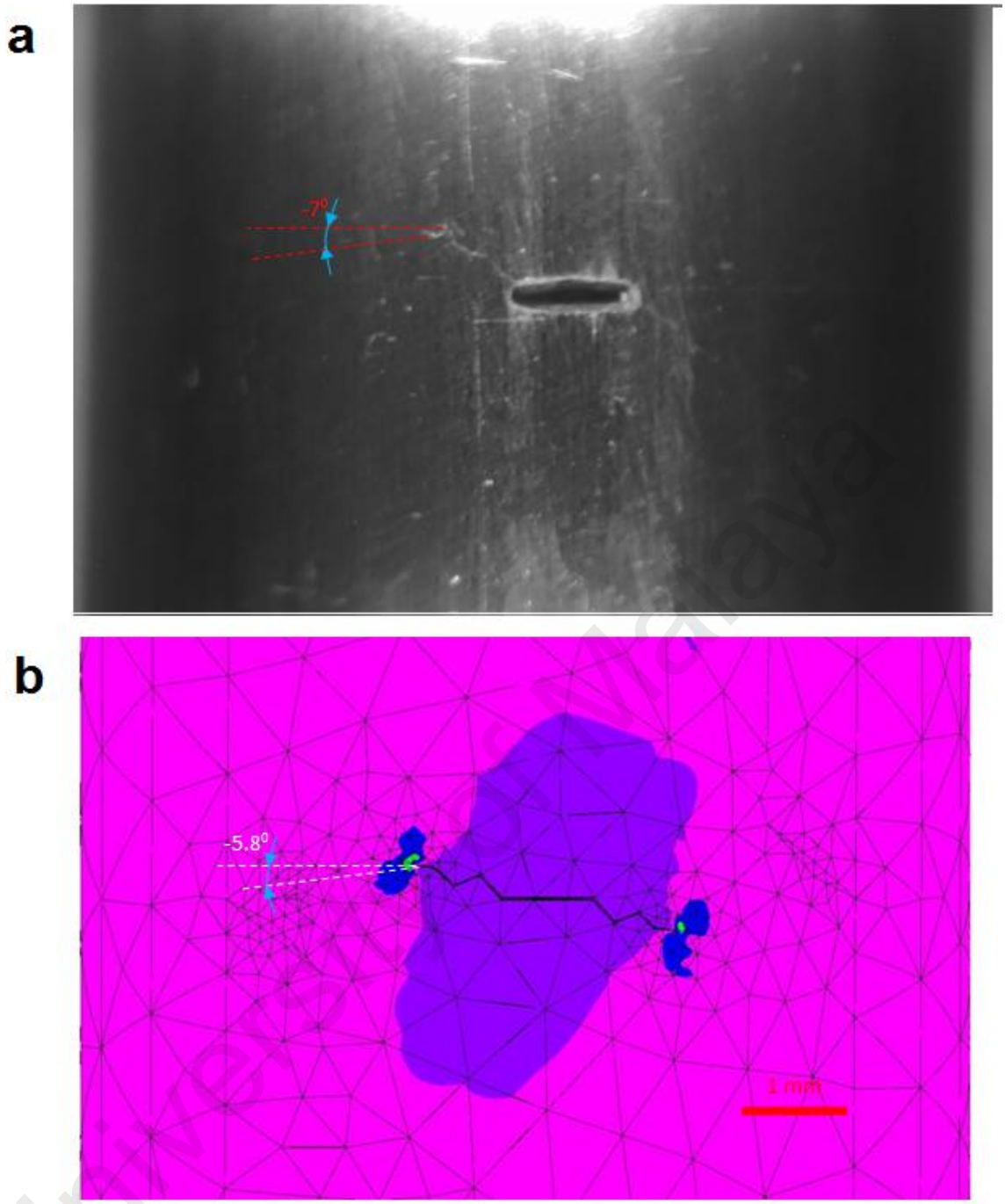

Figure 4.43: The crack growth path at fourth increment (34935 cycles) for *a/c* = 2 under combined cyclic tension (= 100 MPa) – torsion (= 100 MPa) loading by (a) the experiment and (b) the numerical simulation

The crack extension angles along the crack front for different loading case and crack aspect ratio at the first increment obtained from the numerical simulations are presented in Figure 4.44. It is obviously seen from Figure 4.44 that the effect of the torsion loading on the crack extension angle at the crossed surface point seems more

dominant than that due to the crack aspect ratio. However, the crack aspect ratio is observed to give more dominant effect on the crack extension angle at the around crack deepest point.

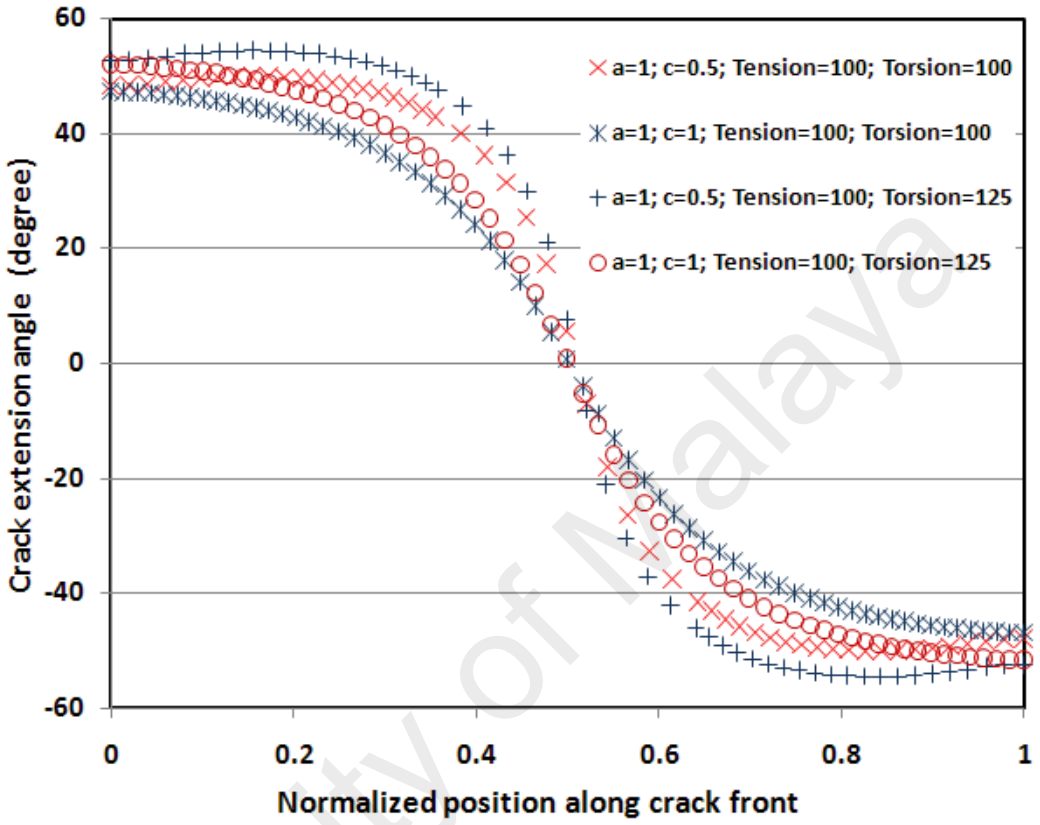

Figure 4.44: Crack extension angles at the first increments.

The changes of the crack extension angle at the crossed surface (c) at each increment of the crack growth are presented in Table 4.3 and depicted in Figures 4.45a. The fluctuated angles indicate the alterations of the crack growth direction as a result of the combined cyclic tension-torsion (mixed-mode fracture condition). Significant changes of the crack growth direction at the crossed surface points are observed during stable crack growth. Meanwhile, smaller alterations of the crack growth direction are seen during rapid crack propagation. It can be seen from Table 4.3 that during stable crack growth, the model with larger torsion load tends to have the larger crack growth angle at cross surface point for a given crack aspect ratio. During stable crack growth,

the largest difference crack growth angle between combined tension of 100 MPa-torsion of 125 MPa and tension of 100 MPa-torsion of 100 MPa for crack aspect ratio *a/c* = 2 was 6.7^0 which is occured at fourth increment. While, for crack aspect ratio *a/c* =1, the largest difference crack growth angle is occured at first increment that is 4.7^0. As shown in Table 4.3, the largest change of crack growth angle for load case of tension of 100 MPa-torsion of 100 MPa and crack aspect ratio *a/c* = 2 was occured from first increment (48.2^0) to second increment (-28^0). While, for load case of tension of 100 MPa-torsion of 125 MPa and crack aspect ratio *a/c* = 2, the largest change of crack growth angle was observed from first increment (52.8^0) to second increment (-34.1^0). For crack aspect ratio *a/c* = 1, the largest change of crack growth angle was occured from first increment to second increment, that is from 47.2^0 to -18.3^0 and from 52^0 to -22.6^0 for load case of tension of 100 MPa-torsion of 100 MPa and tension of 100 MPa-torsion of 125 MPa, respectively.

The changes of the crack extension angle at the crack deepest (*a*) points at each increment of the crack growth are depicted in Figure 4.45b. The scales of change in the crack growth direction at the crack deepest points are relatively small in comparison to those at the crossed surface points. It is likely due to the smaller shearing stress distribution around the crack deepest point.

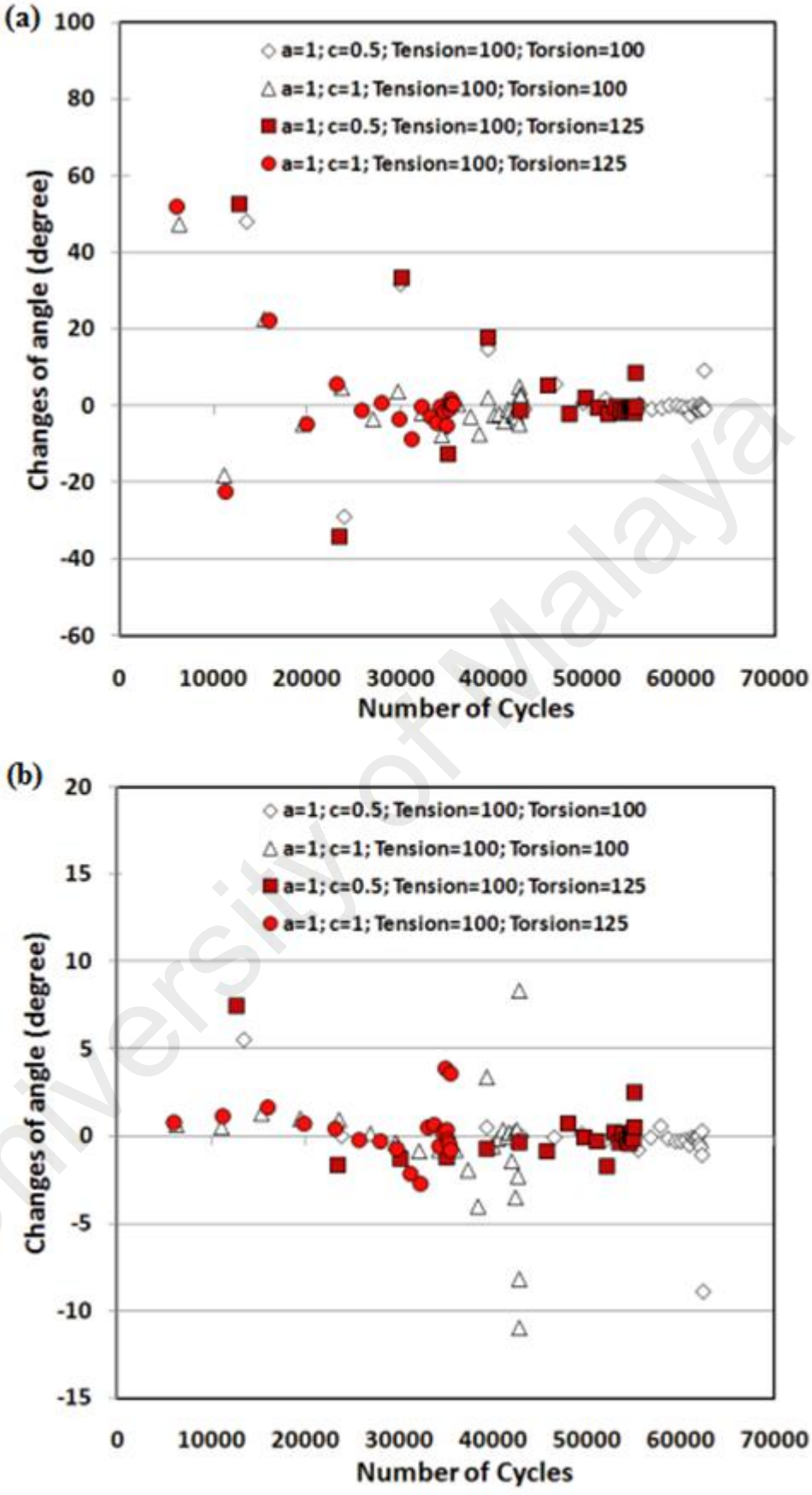

Figure 4.45: The changes of crack growth angles over a number of cycles: (a). at the crossed surface point; (b). at the crack deepest point.

Table 4.3: Crack growth angle at cross surface point at each increment obtained by BEASY (BEASY, 2013)

increment	a/c = 2 (Tension = 100 MPa, Torsion = 100 MPa)		a/c = 2 (Tension = 100 MPa, Torsion = 125 MPa)		a/c = 1 (Tension = 100 MPa, Torsion = 100 MPa)		a/c = 1 (Tension = 100 MPa, Torsion = 125 MPa)	
	Number of cycle	growth angle (degree)	Number of cycle	growth angle (degree)	Number of cycle	growth angle (degree)	Number of cycle	growth angle (degree)
0	0	0.0	0	0.0	0	0.0	0	0.0
1	13505	48.2	12686	52.8	6277	47.2	6086	52.0
2	23951	-28.0	23466	-34.1	11150	-18.3	11222	-22.6
3	30014	33.0	30166	34.4	15374	22.4	15985	22.5
4	34935	-5.8	35087	-12.5	19559	-4.7	19945	-5.0
5	39350	14.7	39396	17.6	23651	4.8	23218	5.7
6	43152	-0.8	42855	-1.2	27007	-3.5	25812	-1.3
7	46546	5.6	45736	5.2	29707	3.8	28005	0.9
8	49469	-0.7	48088	-2.3	32223	-2.0	29805	-3.4
9	51935	1.9	49825	1.9	34365	-7.6	31202	-8.8
10	53925	-1.8	51151	-0.5	36085	0.5	32317	-0.1
11	55536	0.3	52172	-2.1	37430	-3.0	33184	-3.0
12	56847	-0.8	52934	-0.3	38467	-7.5	33830	-4.6
13	57897	-0.5	53500	-1.1	39322	2.0	34316	-0.2
14	58767	0.0	53938	-1.8	40022	-2.6	34674	-1.6
15	59490	0.0	54277	-1.4	40607	-2.3	34939	-5.2
16	60102	-0.1	54544	-0.3	41084	-4.0	35139	-0.8
17	60594	-0.5	54748	-0.5	41476	-0.9	35285	1.7
18	60990	-2.4	54897	-1.1	41786	-1.3	35396	0.5
19	61312	0.2	55009	-1.8	42040	-2.4	35479	0.3
20	61578	-1.0	55090	-0.1	42259	-2.2	35535	0.4
21	61795	-1.2	55142	8.5	42429	-3.3	35560	-9.6
22	61970	-1.3			42561	0.3		
23	62112	0.3			42664	4.9		
24	62227	-0.4			42742	-4.8		
25	62312	0.1			42799	1.3		
26	62375	-0.9			42839	3.1		
27	62424	-0.9			42869	2.5		
28	62458	9.2			42879	0.9		
29	62459	1.7						

4.3.2 The SIFs and fatigue crack growths of a surface crack

For both experimental and simulation works, the crack length c (= c_0 + Δc).is measured at the crossed surface point, where c_0 and Δc are the initial crack length and the crack increment, respectively. The measurements of the crack lengths by the experimentation over the number of cycles are made based on the displays of the video

recording. Careful and tidy readings of the crack length measurement are certainly required. The crack length at the selected number of cycle for all load cases obtained from experiment and simulations are presented in Tables 4.4-4.7 and plotted in Figure 4.46. It can be seen from Figure 4.46, for all cases, the fatigue crack growths done by the experimentation and numerical simulations are shown to be in satisfactory agreements. As shown in Tables 4.4-4.7, the largest difference between the measured and predicted crack length at the initial increment was 0.084 mm or 10.6% which was found for the specimen with crack aspect ratio a/c = 2 and load case of combined tension of 100 MPa-torsion of 100 MPa. During stable fatigue crack growth, the difference between the measured and predicted crack length slightly increase with increasing the number of cycle. For all loading cases and crack aspect ratio, the unstable crack growth would occur approximately at the last 5-7% of the fatigue life of the specimen where crack growth was relatively fast. It can also be seen from Tables 4.4-4.7, for a given number of cycle, the largest difference between the measured and predicted crack length prior unstable crack growth is 30.5% (1.349 mm) that is observed in specimen with aspect ratio a/c = 2 and load case of combined tension of 100 MPa-torsion of 100 MPa. At the fracture condition, for crack aspect ratio a/c =2, the difference between measured and predicted crack length is of 2.312 mm (32.5%) for load case of combined tension of 100 MPa-torsion of 100 MPa and is of 1.914 mm (26.7%) for load case of combined tension of 100 MPa-torsion of 125 MPa. Whereas for crack aspect ratio a/c =1, the difference crack length at fracture condition are 1.853 mm (24.7%) and 1.112 mm (15.1%) for combined tension of 100 MPa-torsion of 100 MPa and combined tension of 100 MPa-torsion of 125 MPa, respectively. Table 4.8 summarized the fatigue life of specimen obtained by the experiment and the simulation. It can be observed from Table 4.8 and Figure 4.46 that for the given loading case and crack aspect ratio, the fatigue crack growths obtained from the simulation slightly show

more conservative (shorter fatigue life) than those from the experimentation. This fact is likely due to the degree of sharpness of the crack front of the surface crack. When producing an initial surface crack using the die-sinking EDM machine, the electrode may experience a slight blunting along the crack front edge during the penetration into the specimen. Referring to Table 4.8, the largest difference between the measured and predicted fatigue life was found around 7.7% which was occurred on specimen with crack aspect ratio a/c = 1 and load case of tension of 100 MPa and torsion of 125 MPa.

Figure 4.46 shows that a larger torsion load would expectedly lead to a shorter fatigue life for a given crack aspect ratio. The quatitative comparisons of fatigue life for all load cases are presented in Table 4.8. It can be seen from Table 4.8, for specimens with crack aspect ratio a/c = 2, fatigue life in the fatigue crack growth experiment under combined tension of 100 MPa-torsion of 125 MPa is 10% shorter than those under combined tension of 100 MPa-torsion of 100 MPa. Whereas, numerical simulation under combined tension of 100 MPa-torsion of 125 MPa results in 12% shorter fatigue life than those under combined tension of 100 MPa-torsion of 100 MPa. It can also be seen from Table 4.8, for specimens with crack aspect ratio a/c = 1, the experimental and numerical simulation of fatigue crack growth under combined tension of 100 MPa-torsion of 125 MPa result in 14% and 17% shorter fatigue life than those under combined tension of 100 MPa-torsion of 100 MPa, respectively. This comparison results indicate that the NASGRO fatigue crack growth law that applied in BEASY software was able to satisfactory predict fatigue life of cracked components. The corresponding effective SIFs obtained from the numerical simulations are presented in Figure 4.47. Prior to having an unstable stage, the effective SIFs are shown to be fluctuated during the crack growth. This is as a result of the change of the crack path orientation to be inclined and twisted during the crack growth.

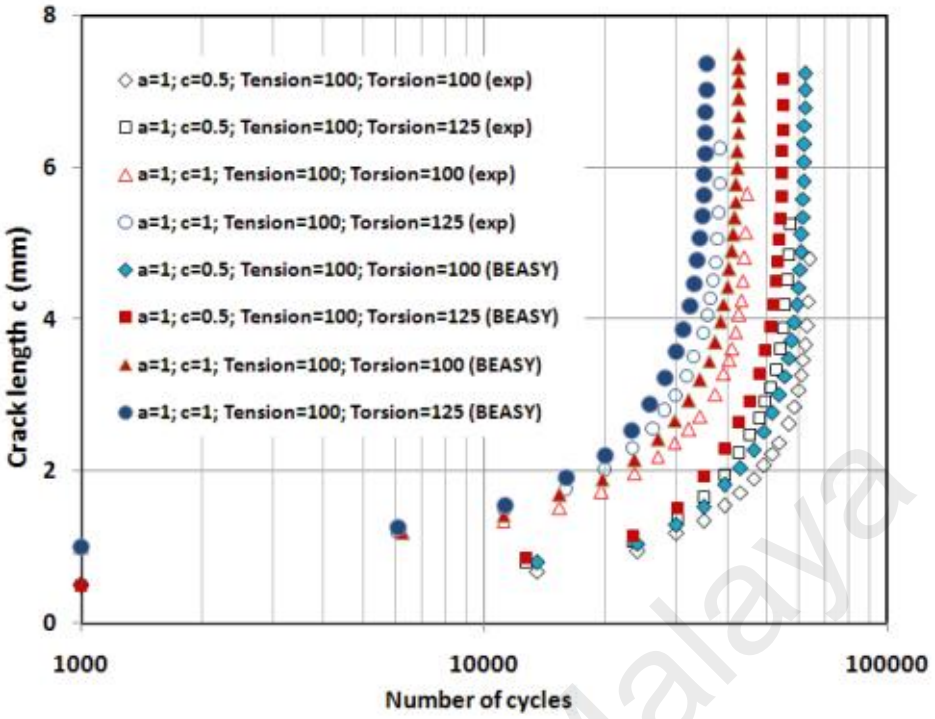

Figure 4.46: The crack length *c* over a number of cycles.

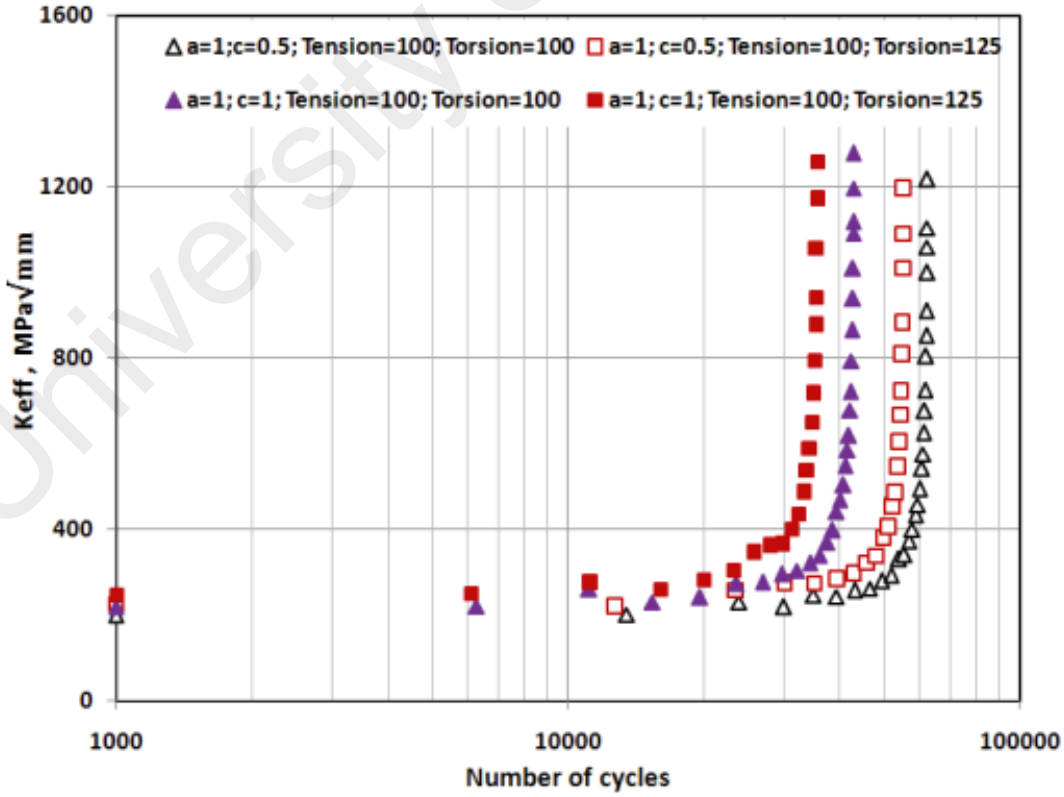

Figure 4.47: The K_{eff} values over a number of cycles.

Table 4.4: Crack length and number of cycle for *a/c* = 2 under tension of 100 MPa and torsion of 100 MPa by BEASY and experiment

Number of cycle (Exp)	crack length (Exp) (mm)	Number of cycle (BEASY)	crack length (BEASY) (mm)	difference of crack length (mm)	difference of crack length (%)
0	0.504	0	0.510	0.006	1.2
13505	0.712	13505	0.796	0.084	10.6
23951	0.951	23951	1.048	0.097	9.2
30014	1.182	30014	1.296	0.114	8.8
34935	1.351	34935	1.532	0.181	11.8
39350	1.552	39350	1.815	0.263	14.5
43152	1.721	43152	2.046	0.325	15.9
46546	1.902	46546	2.282	0.380	16.7
49469	2.071	49469	2.522	0.451	17.9
51935	2.228	51935	2.765	0.537	19.4
53925	2.379	53925	3.007	0.628	20.9
56847	2.621	56847	3.487	0.866	24.8
58767	2.851	58767	3.953	1.102	27.9
60102	3.070	60102	4.419	1.349	30.5
60990	3.271	60990	4.888	1.617	33.1
61795	3.469	61795	5.584	2.115	37.9
62500	3.668	62458	7.107	3.439	48.4
63100	3.921				
63400	4.239				
63900	4.795				

Table 4.5: Crack length and number of cycle for *a/c* = 2 under tension of 100 MPa and torsion of 125 MPa by BEASY and experiment

Number of cycle (Exp)	crack length (Exp) (mm)	Number of cycle (BEASY)	crack length (BEASY) (mm)	difference of crack length (mm)	difference of crack length (%)
0	0.502	0	0.500	0.002	0.4
12686	0.801	12686	0.855	0.054	6.3
23466	1.091	23466	1.148	0.058	5.0
30166	1.386	30166	1.518	0.132	8.7
35087	1.651	35087	1.931	0.280	14.5
39396	1.949	39396	2.290	0.341	14.9
42855	2.239	42855	2.647	0.408	15.4
45736	2.481	45736	2.926	0.445	15.2
48088	2.702	48088	3.279	0.577	17.6
49825	2.919	49825	3.590	0.671	18.7

Table 4.5, continued

Number of cycle (Exp)	crack length (Exp) (mm)	Number of cycle (BEASY)	crack length (BEASY) (mm)	difference of crack length (mm)	difference of crack length (%)
51400	3.102	51151	3.897	0.795	20.4
52934	3.331	52934	4.497	1.167	25.9
54277	3.619	54277	5.331	1.712	32.1
55090	3.889	55090	6.818	2.930	43.0
55800	4.201	55142	7.162	2.961	41.3
56300	4.518				
56800	4.848				
57200	5.248				

Table 4.6: Crack length and number of cycle for *a/c* = 1 under tension of 100 MPa and torsion of 100 MPa by BEASY and experiment

Number of cycle (Exp)	crack length (Exp) (mm)	Number of cycle (BEASY)	crack length (BEASY) (mm)	difference of crack length (mm)	difference of crack length (%)
0	1.004	0	1.000	0.004	0.4
6277	1.132	6277	1.192	0.060	5.0
11150	1.341	11150	1.420	0.079	5.6
15374	1.512	15374	1.689	0.177	10.5
19559	1.729	19559	1.894	0.165	8.7
23651	1.971	23651	2.151	0.180	8.4
27007	2.189	27007	2.426	0.237	9.8
29707	2.378	29707	2.671	0.293	11.0
32224	2.549	32223	2.939	0.390	13.3
34365	2.725	34365	3.210	0.485	15.1
37430	3.012	37430	3.693	0.681	18.4
39322	3.282	39322	4.203	0.921	21.9
40607	3.471	40607	4.664	1.193	25.6
41250	3.619	41084	4.896	1.277	26.1
42040	3.838	42040	5.548	1.710	30.8
42869	4.059	42869	7.304	3.245	44.4
43400	4.248	42879	7.501		
43850	4.502				
44300	4.808				
44600	5.149				
44900	5.648				

Table 4.7: Crack length and number of cycle for *a/c* = 1 under tension of 100 MPa and torsion of 125 MPa by BEASY and experiment

Number of cycle (Exp)	crack length (Exp) (mm)	Number of cycle (BEASY)	crack length (BEASY) (mm)	difference of crack length (mm)	difference of crack length (%)
0	1.005	0	1.000	0.005	0.5
6086	1.184	6086	1.251	0.067	5.3
11222	1.486	11222	1.558	0.071	4.6
15985	1.763	15985	1.913	0.150	7.8
19945	2.018	19945	2.211	0.193	8.7
23400	2.296	23218	2.540	0.243	9.6
26200	2.551	25812	2.878	0.326	11.3
28100	2.805	28005	3.233	0.428	13.2
29805	2.991	29805	3.579	0.587	16.4
31800	3.245	31202	3.874	0.628	16.2
33184	3.501	33184	4.472	0.981	21.9
34940	3.809	34940	5.627	1.828	32.5
35800	4.051	35285	6.175	2.123	34.4
36430	4.269	35479	6.721	2.451	36.5
36950	4.502	35560	7.360	2.858	38.8
37570	4.749				
37900	5.051				
38230	5.398				
38460	5.788				
38560	6.248				

Table 4.8: Summary of fatigue life and crack length for all load cases by BEASY and experiment

Load case		crack depth (*a*)	crack length (*c*)	Number of cycle at fracture (N_f)		Crack length at fracture (c_f)	
Tension (Mpa	Torsion (Mpa)			Exp	BEASY	Exp	BEASY
100	100	1	0.5	63900	62458	4.795	7.107
100	125	1	0.5	57200	55142	5.248	7.162
100	100	1	1	44900	42879	5.648	7.501
100	125	1	1	38560	35560	6.248	7.360

4.3.3 Fractography analysis

The fracture surfaces of the corresponding testing specimens for different loading cases and crack aspect ratios are presented in Figures 4.48, 4.49 and 4.50. It can be seen from Figure 4.48a that the fracture surface of a cracked specimen under pure cyclic tension loading noticeably leaves beach marks on the surface which was marked by the white color lines. The semi circular or semi elliptical surface crack under tension grew in a self-similar way forming a curved crack front, which was always observed in other experiments. Meanwhile, the torsion loading results in deformed draw marks and rolling scratches on the fracture surface as shown in Figure 4.48b. Under combined cyclic tension-torsion loading, combinations of flat fracture and shear lips are noticed at the lower regions of the fracture surfaces (Figures 4.49 and 4.50). This surface appearance is the manifestation of mixed-mode fracture condition during the stable crack growth. The middle regions show the change of fracture surface roughness, indicating a transition from stable to unstable stages of the crack growth. Next, the top regions of the fracture surfaces show brittle fractures as an indication of rapid crack propagation.

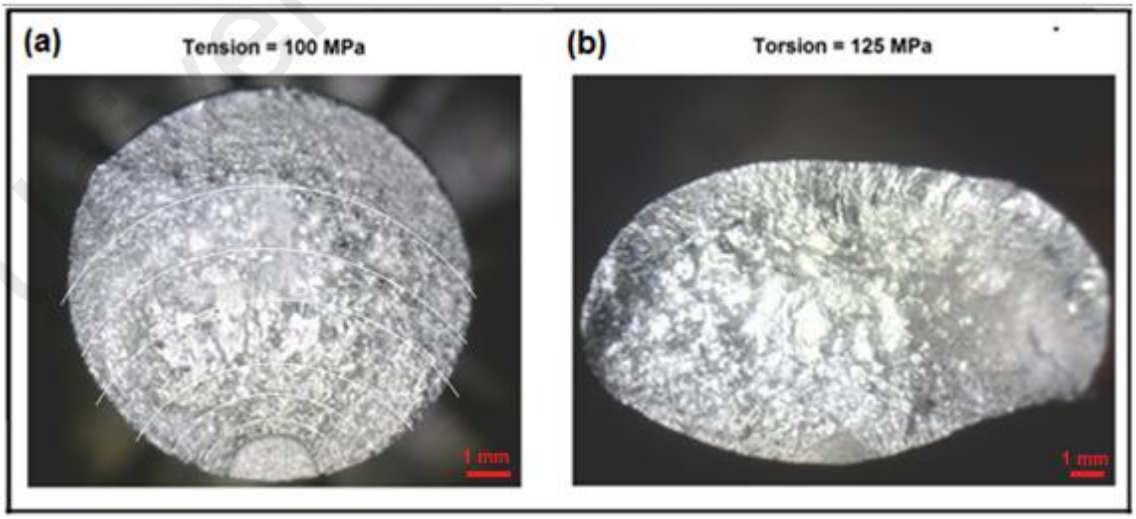

Figure 4.48: Fracture surface conditions of surface cracks (*a/c* = 1) (a) under tension load; (b) under torsion load.

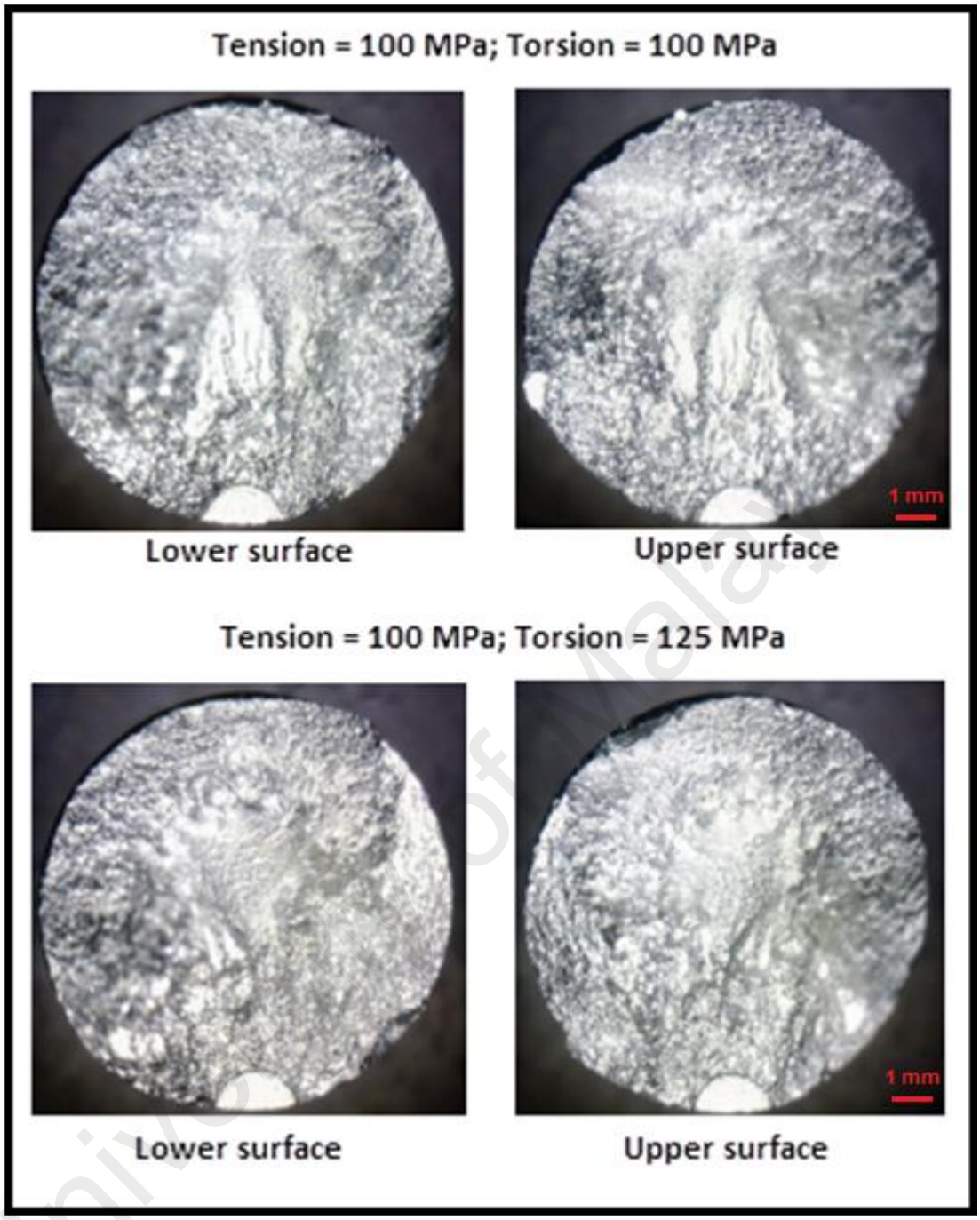

Figure 4.49: Fracture surface conditions of surface cracks (*a/c* = 1) on solid cylinder under combined tension-torsion loading.

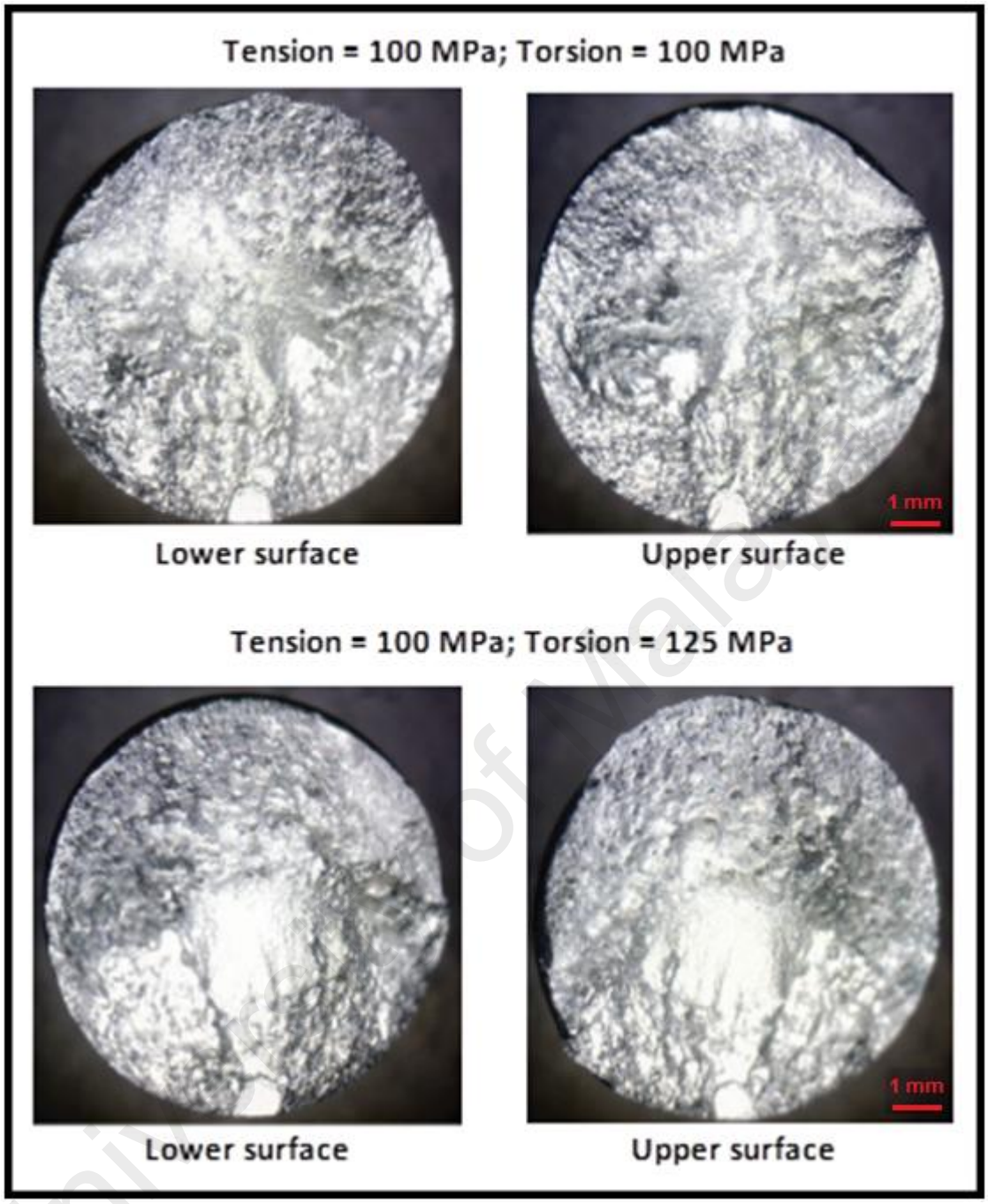

Figure 4.50: Fracture surface conditions of surface cracks (*a/c* = 2) on solid cylinder under combined tension-torsion loading.

4.4 Procedure for generation of initial surface crack

The experimental results are often sought to validate the numerical solutions of fatigue crack growth problems. The standard laboratory specimens such as compact tension specimen, single edge specimen, and center crack specimen are widely used in the through-crack fatigue tests (Citarella & Cricri, 2009; Beretta & Carboni, 2011;

Zheng & Jiang, 2013). However, the guideline for introducing a surface crack in a specimen is not reported in detail in literature. Shin and Cai (2007, 2008) briefly mentioned the use of the electric discharge machining (EDM) for preparing an elliptical surface crack on a solid rod. Yang et al. (2006) used the linear cutting machine to induce a surface crack in a solid cylinder. Recently, Citarela et al. (2014) used the straight wire cutting machine to manufacture a straight edge surface crack in solid cylinder. In this study, the procedure for introducing an initial semi circular and semi elliptical surface crack in a solid cylinder using the die-sinking EDM machine is presented in detail.

The die-sinking electric discharge machine is utilized to prepare a semi-elliptical surface crack in a solid cylinder bar. Generally, the die-sinking EDM machine is used for machining hard metal or certain shape contour that is very difficult to do with a conventional tooling machine. The tooling in the EDM machine consists of an electrode, a work piece (specimen) and the supporting holders that are submerged in an insulating liquid such as oil or another dielectric fluid. The electrode and work piece are connected to a suitable power supply which generates an electrical potential between them. As the electrode approaches the specimen, a dielectric breakdown occurs in the fluid, forming a plasma channel and a small-sparking jump. The procedures used to introduce an initial surface crack in a solid cylinder using the die-sinking EDM machine are presented in the following sections.

Electrode preparation

As the electrode serves as a die, its shape and dimension would affect the quality of the crack front shapes (semi-circular or semi-elliptical). Therefore, during the electrode preparation, the accuracy of the shape and dimension shall be highly considered. The detailed electrode preparation is explained as follow:

- *First step*: the wire cutting EDM machine is utilized to cut a copper plate (thickness of 0.3 mm, length of 50 mm and width of 25 mm) for the electrodes. Figure 4.51 shows the set-up of the electrode preparation using the wire cutting EDM machine.
- *Second step*: Thinning process on the crack-shaping region of the electrode is carried out by using the sand papers with different grades (coarse to fine) to produce a thickness with a maximum size of around 0.15 mm.
- *Third step*: Further refinement in shaping of a semi-circular or semi-elliptical crack profile for having a thinner-edge thickness is again made by using sand papers. A digital microscope is used to observe and ensure the crack-shaping region of the electrode to have a semi-circular or semi-elliptical shape (a/c = 1 = 1 mm/1 mm and a/c = 2 = 1 mm/0.5 mm as shown in Figure 4.52).

-

Figure 4.51: The setting-up of the electrode preparation.

Preparation of an initial surface crack in specimens

When preparing a surface crack using the die-sinking EDM, the electrode and work piece (specimen) are submerged in an insulating liquid. The detailed steps used for introducing an initial surface crack in the specimen are as follows:

- *First step*: When running the die-sinking EDM machine, the file containing the program for making crack on the menu is selected. Next, the feed depth of electrode into the work piece (in the *z*-direction) can be set by entering the desired value for the crack depth.
- *Second step*: The specimen is gently placed at the holder on the magnetic table of the die-sinking EDM (see Figure 4.53). The position of the holder shall be ensured to be in *x*- and *y*- directions using the dial indicator.
- *Third step*: The electrode is installed on the holder of the die-sinking EDM (see Figure 4.53). To produce correct transverse crack planes, the electrode must be ensured to be perpendicular to the longitudinal axis of the specimen. To obtain the correct crack depth, the centre point of the electrode has to coincide with the top surface point of the specimen.
- *Fourth step*: After the installation of the electrode on the specimen has been completed, the oil pumping button of the EDM machine is switched ON to flow the oil into the tank until both specimen and electrode are submerged. Next, the Start button of the die-sinking EDM machine is switched ON to drive the electrode to penetrate into the specimen up to the specified depth (in *First step*).
- *Fifth step*: Once the surface crack has been produced, the specimen and electrode can be removed from the apparatus of the die-sinking EDM machine. Figure 4.54 shows the initial surface crack in the specimens for the crack aspect ratio of 1 and 2 before fatigue crack growth test. The shapes and sizes of the initial surface crack after fatigue crack growth test are shown in Figure 4.55 for the different crack aspect ratio. It can be seen from Figures 4.54 and 4.55 that a good accuracy of the shape and size of the semi-circular and semi-elliptical surface crack can be obtained through the developed procedure.

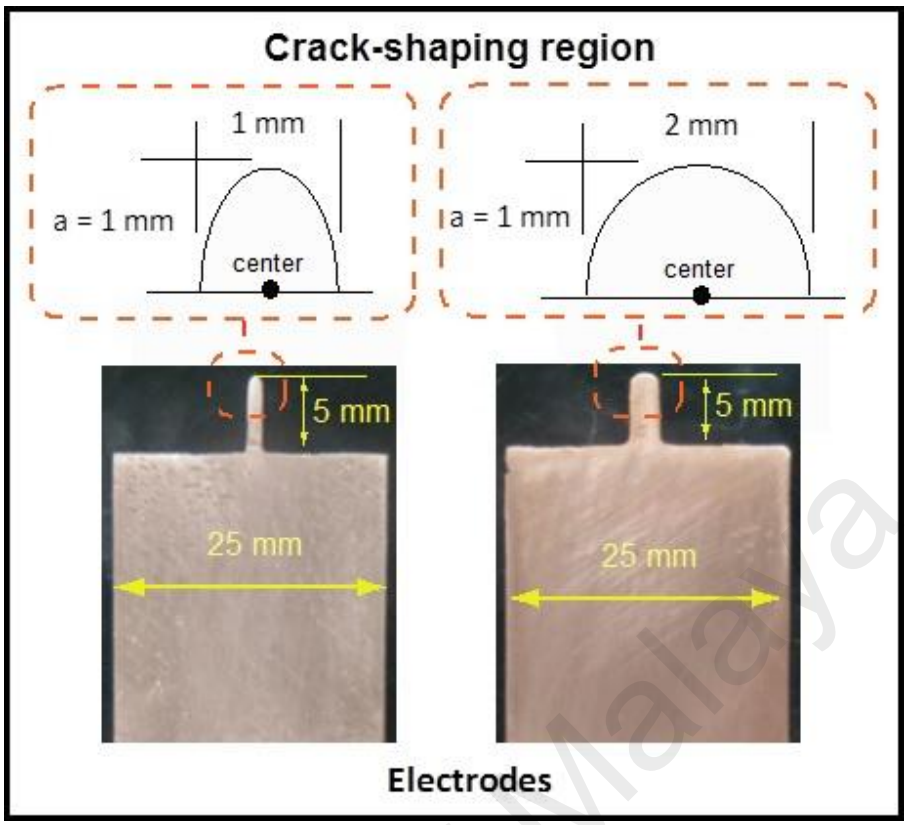

Figure 4.52: The electrodes in a semi-circular or semi-elliptical shape.

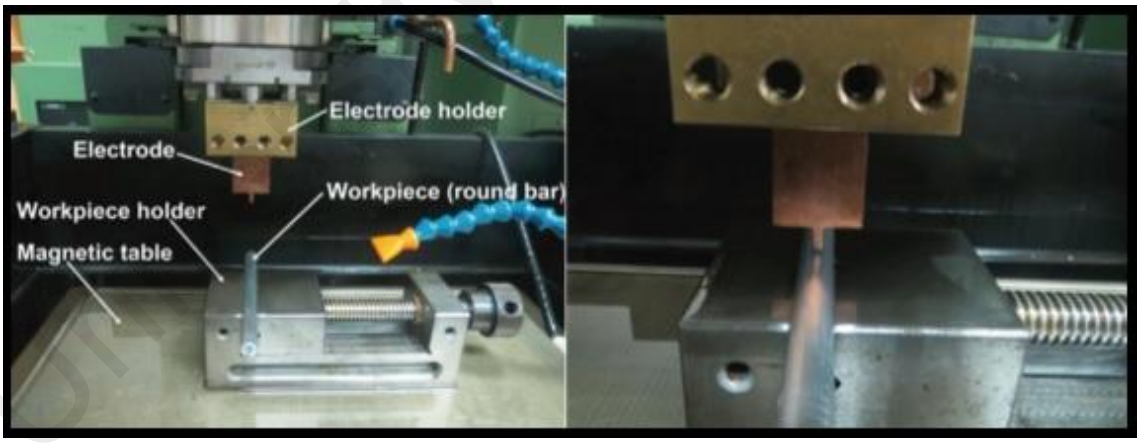

Figure 4.53: The setting-up for preparing an initial surface crack in a specimen using the die-sinking EDM machine.

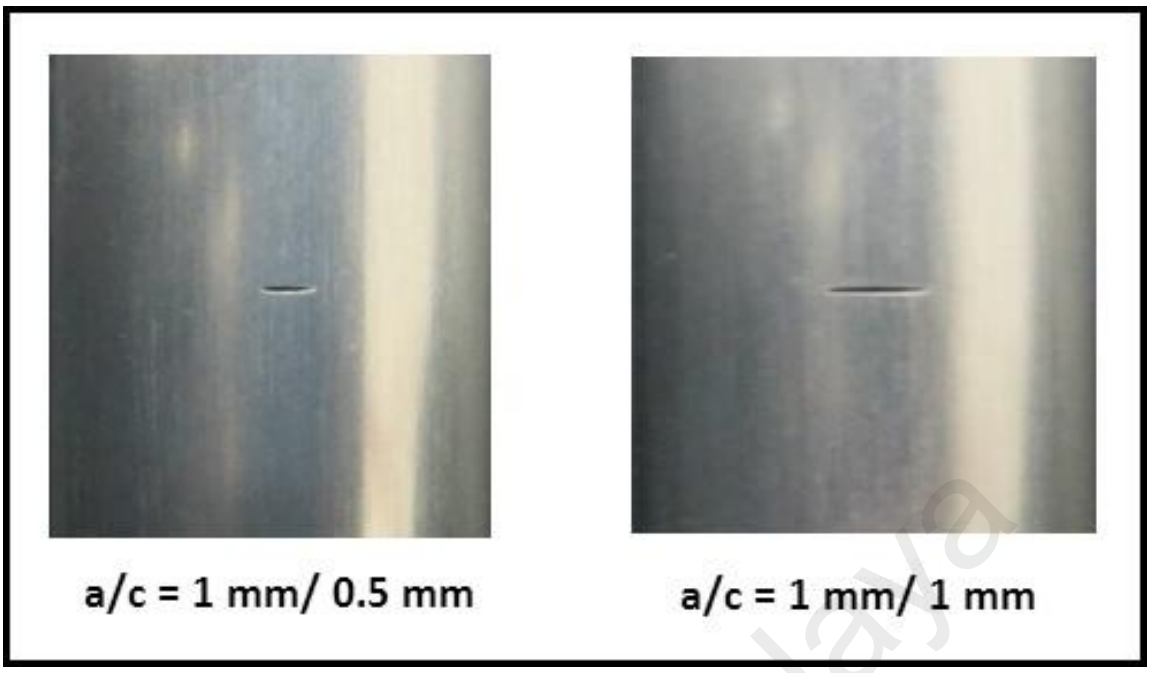

Figure 4.54: Cracked specimens prepared using the die-sinking EDM machine.

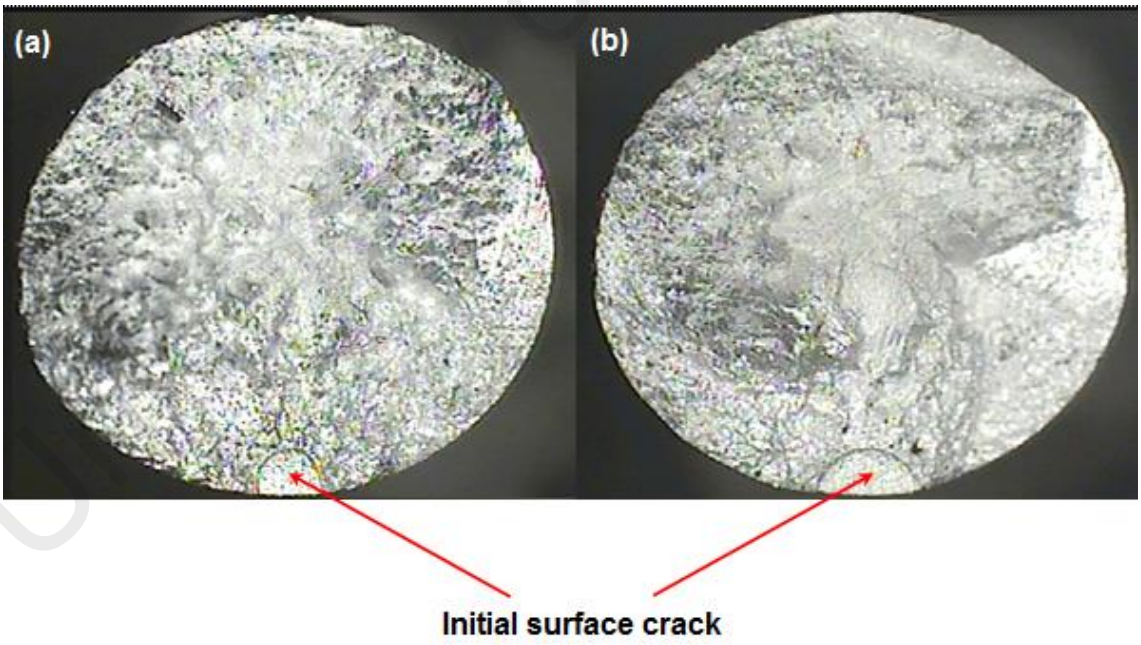

Figure 4.55: Shapes of surface crack prepared using the die-sinking EDM machine after fatigue crack test (a) *a/c*=1/0.5 mm (b) *a/c* = 1/1 mm

4.5 Summary

Benchmarking of the present results for a typical geometry with the available solution in literature was made. The SIFs, fatigue life and crack growth direction/path of a surface crack in a V-notched solid cylinder, a surface crack in a solid cylinder and a corner crack in square prismatic bar have been presented and discussed. The procedure for generating an initial surface crack have also been presented. The conclusions of the findings of this work are presented in Chapter 5.

CHAPTER 5

CONCLUSIONS AND FUTURE WORKS

5.1 Conclusions

The stress intensity factors, crack evolution/directions, fatigue crack growth and fatigue life of a surface crack in a V-notched solid cylinder and in a solid cylinder and a corner crack in square prismatic bar have been presented and discussed in Chapter 4. The effects of the crack aspect ratio (*a/c*) and the tension to torsion stress ratio on the SIFs, crack evolution/direction, fatigue crack growth and fatigue life were studied. Numerical simulations of FCG are conducted by use of a boundary element method based software of BEASY. NASGRO FCG model and MSED criterion were used to calculate the magnitude of crack growth and to predict the crack growth path/direction, respectively. J-integral technique was used to evaluate the SIF around crack front. The effective SIF range for a mixed mode condition was calculated from each of the mode components using Yaoming Mi equation (Eq. 2.64). The procedure for generating an initial surface crack in solid round bar by use of a die-sinking EDM machine has also been presented. Based on the findings presented in Chapter 4, the following conclusions are made.

First, as preliminary study, FCG of surface crack in a V-notched solid cylinder under cyclic tension is numerically evaluated for different crack aspect ratio and notch root radius. It is found that the size of the initial crack aspect ratio has significant influence on the crack shape evolution during crack growth. At the initial increment of the crack growth, the crack surfaces form an almond shape. In the few following increments, larger positively curved crack front of crack surfaces were observed on larger crack aspect ratio. Then, in the following increments, the shapes of the cracks evolve to form a nearly straight line at the crack front. Correlating the SIFs value and crack shapes for each increments, the unstable crack growth was observed when the crack front had evolved to form a straight shape.

The V-shaped notched cylinder with smaller crack aspect ratio shall be given more careful attentions because for a given crack depth, the smaller crack aspect ratio clearly leads to a shorter fatigue life. The effect of the crack aspect ratio on fatigue life is more significant than the notch radius. Based on the SIFs value and crack sizes at each increment, the unstable crack extension during the crack growth was observed when the crack aspect ratio *a/c* evolved to be between 0.6 and 0.7.

Second, the SIF, crack path and fatigue life of corner crack in square bar under combined cyclic tension-torsion loads were numerically evaluated for different initial crack aspect ratio. It is observed that a combination of a larger tension loading and a smaller torsional loading leads to greater K_I values. The larger absolute K_{II} value was found at the crossed surface point having the larger crack length of *a* or *c* in which the feature is in contrast to Mode I SIFs. Larger Mode III SIFs are found at the square bar models with a larger torsional loading and a crack aspect ratio $a/c \neq 1$. During the fatigue crack growth, the initial crack aspect ratio $a/c \neq 1$ was evolving to a unity ($a/c \approx 1$) at a number of cycles prior to fracture. It implies that FCG of a corner crack on square bar model tends to have the same crack length and crack depth size at the final fracture. The present results of FCG computed by using NASGRO law indicate that for a given tension loading, the larger Mode III SIFs and the shorter fatigue life were found at the square bar model with a larger torsional loading and the crack aspect ratio $a/c \neq 1$. The predictions of crack growth path by use of MSED criterion results in an inclining shape of the crack surface/crack path against the bar longitudinal axis which is triggered by the cyclic torsion load. It is observed that for a given torsion load, the inclination of crack path of corner crack increases as the tension to torsion stress ratio decreases.

Third, the FCG of surface crack on solid cylinder under combined tension-torsion load were evaluated numerically and experimentally for different crack aspect ratio. Experimental results related to crack length, crack growth direction/path and fatigue life

were compared with simulation results. The predictions of crack growth direction by use of MSED criterion indicate that at the first increment, the torsion loading gave a more dominant effect on the crack extension angle at the crossed surface point than that due to the crack aspect ratio. Meanwhile, the effect of the crack aspect ratio on the crack extension angle was observed to be more dominant at the crack deepest point. It is found that the crack growth paths estimated by the numerical simulations (MSED criterion) are generally shown to have similar patterns with those by experimentations. The crack growth direction at the crossed surface points fluctuated significantly during stable crack growth. The crack growth angle at first increment predicted in simulations were in a good agreement with the experimental results. The largest difference of crack growth angle at first increment obtained by the experiment and the simulation is 0.8 degree (1.5%) that is observed in the specimen with crack aspect ratio a/c = 2 under combined tension of 100 MPa-torsion of 125 MPa. The larger torsion load would expectedly lead to a shorter fatigue life for a given crack aspect ratio. Numerical computations of SIFs show that prior to having an unstable stage the effective SIFs are fluctuated during the crack growth. This is as a result of the change of the crack path orientation to be inclined and twisted during the crack growth. Fractography analysis on fracture surface reveals that the combinations of flat fracture and shear lips are noticed at region around of initial crack front of the fracture surfaces due to mixed-mode fracture during stable crack growth. The middle regions show the change of fracture surface roughness, indicating a transition from stable to unstable stages of the crack growth. The remaining regions of the fracture surfaces show brittle fractures as an indication of rapid crack propagation.

Fourth, a guideline was developed for generation of the initial surface crack in solid round bar using die-sinking EDM machine. The copper electrode utilized as dies of crack shape in conjunction with die sinking EDM machine and fixture has a simple

geometry and it can be made easily using wire cut EDM machine. The performance and accuracy of shape and size of the generated initial surface crack can be observed from the fracture surface of fatigue crack growth test specimen. It was shown that relatively good consistency and accuracy was found between the shape and size of crack surface produced by die-sinking EDM processes and the shape and size of crack shaping area of the electrode. The developed guideline and its associated EDM machine and electrode can be used as a practical approach for introducing an initial surface crack in solid bar specimen.

5.2 Recommendations for future works

This research has provided some results that are intended to update the knowledge in the field of fatigue and fracture mechanics, particularly for the cases of part-through cracks in a solid bar. Further researchs are however encouraged to analyse the following tentative topics:

- Numerical and experimental analyses of the fatigue growth of a surface/corner crack in a solid bar under non proportional tension-torsion loads.
- Effects of the combinations of variable amplitude and non-proportional loadings on the fatigue crack growth behaviors of a part-through crack.

REFERENCES

Abreu, L. M. P., Costa, J. D., & Ferreira, J. A. M. (2009). Fatigue behaviour of AlMgSi tubular specimens subjected to bending–torsion loading. *International Journal of Fatigue, 31*(8–9), 1327-1336. http://dx.doi.org/10.1016/j.ijfatigue.2009.03.004.

Albinmousa, J., Merah, N., & Khan, S. M. A. (2011). A model for calculating geometry factors for a mixed-mode I–II single edge notched tension specimen. *Engineering Fracture Mechanics, 78*(18), 3300-3307. http://dx.doi.org/10.1016/j.engfracmech.2011.09.005.

Alegre, J. M., & Cuesta, I. I. (2010). Some aspects about the crack growth FEM simulations under mixed-mode loading. *International Journal of Fatigue, 32*(7), 1090-1095. http://dx.doi.org/10.1016/j.ijfatigue.2009.12.002.

Aliabadi, M. (1997). Boundary element formulations in fracture mechanics. *Applied Mechanics Reviews, 50*(2), 83-96.

Aliabadi, M. H. (2003). Boundary Element Methods in Linear Elastic Fracture Mechanics. In I. M. Editors-in-Chief: R. O. Ritchie, & B. Karihaloo (Eds.), *Comprehensive Structural Integrity* (pp. 89-125). Oxford: Pergamon.

Aliha, M. R. M., Bahmani, A., & Akhondi, S. (2015). Numerical analysis of a new mixed mode I/III fracture test specimen. *Engineering Fracture Mechanics, 134*(0), 95-110. http://dx.doi.org/10.1016/j.engfracmech.2014.12.010

Anderson, T. L. (2005). *Fracture mechanics: fundamentals and applications*: CRC press.

Armentani, E., & Citarella, R. (2006). DBEM and FEM analysis on non-linear multiple crack propagation in an aeronautic doubler-skin assembly. *International Journal of Fatigue, 28*(5–6), 598-608. http://dx.doi.org/10.1016/j.ijfatigue.2005.06.050

Armentani, E., Citarella, R., & Sepe, R. (2011). FML full scale aeronautic panel under multiaxial fatigue: Experimental test and DBEM Simulation. *Engineering Fracture Mechanics, 78*(8), 1717-1728. http://dx.doi.org/10.1016/j.engfractmech.2011.02.020.

Ayatollahi, M. R., & Torabi, A. R. (2009). A criterion for brittle fracture in U-notched components under mixed mode loading. *Engineering Fracture Mechanics, 76*(12), 1883-1896. http://dx.doi.org/10.1016/j.engfracmech.2009.04.008.

Ayatollahi, M. R., & Torabi, A. R. (2010). Investigation of mixed mode brittle fracture in rounded-tip V-notched components. *Engineering Fracture Mechanics, 77*(16), 3087-3104. http://dx.doi.org/10.1016/j.engfracmech.2010.07.019.

Ayhan, A. O. (2004). Mixed mode stress intensity factors for deflected and inclined surface cracks in finite-thickness plates. *Engineering Fracture Mechanics, 71*(7–8), 1059-1079. http://dx.doi.org/10.1016/S0013-7944(03)00153-X.

Ayhan, A. O. (2007). Mixed mode stress intensity factors for deflected and inclined corner cracks in finite-thickness plates. *International Journal of Fatigue, 29*(2), 305-317. http://dx.doi.org/10.1016/j.ijfatigue.2006.03.006.

Barenblatt, G. I. (1959). The formation of equilibrium cracks during brittle fracture. General ideas and hypotheses. Axially-symmetric cracks. *Journal of Applied Mathematics and Mechanics, 23*(3), 622-636.

Barlow, K. W., & Chandra, R. (2005). Fatigue crack propagation simulation in an aircraft engine fan blade attachment. *International Journal of Fatigue, 27*(10–12), 1661-1668. http://dx.doi.org/10.1016/j.ijfatigue.2005.06.016

Barsoum, R. S. (1976). On the use of isoparametric finite elements in linear fracture mechanics. *International Journal for Numerical Methods in Engineering, 10*(1), 25-37.

BEASY. (2013). V10r14. BEASY Ashurst Lodge. Southampton, United Kingdom.

Beghini, M., Benedetti, M., Fontanari, V., & Monelli, B. D. (2012). Stress intensity factors of inclined kinked edge cracks: A simplified approach. *Engineering Fracture Mechanics, 81*(0), 120-129. http://dx.doi.org/1016/j.engfracmech.2011.11.005

Beghini, M., Bertini, L., & Fontanari, V. (1999). Stress intensity factors for an inclined edge crack in a semiplane. *Engineering Fracture Mechanics, 62*(6), 607-613. http://dx.doi.org/10.1016/S0013-7944(99)00011-9

Benedetti, M., Beghini, M., Fontanari, V., & Monelli, B. (2009). Fatigue cracks emanating from sharp notches in high-strength aluminium alloys: The effect of loading direction, kinking, notch geometry and microstructure. *International Journal of Fatigue, 31*(11–12), 1996-2005.

Benthem, J., & Koiter, W. (1973). Asymptotic approximations to crack problems *Methods of analysis and solutions of crack problems* (pp. 131-178): Springer

Bhat, S., & Patibandla, R. (2011). *Metal Fatigue and Basic Theoretical Models: A Review*: INTECH Open Access Publisher.

Bian, L. C., & Lim, J. K. (2003). Fatigue life prediction of the plates with an inclined surface crack. *International Journal of Fatigue, 25*(6), 521-531. http://dx.doi.org/10.1016/S0142-1123(02)00172-X

Biner, S. B. (2001). Fatigue crack growth studies under mixed-mode loading. *International Journal of Fatigue, 23, Supplement 1*(0), 259-263. http://dx.doi.org/10.1016/S0142-1123(01)00146-3

Bittencourt, T. N., Barry, A., & Ingraffea, A. R. (1992). Comparison of mixed-mode stress-intensity factors obtained through displacement correlation, J-integral formulation and modified crack-closure integral. *ASTM special technical publication, 1131*, 69-69.

Blandford, G. E., Ingraffea, A. R., & Liggett, J. A. (1981). Two-dimensional stress intensity factor computations using the boundary element method. *International Journal for Numerical Methods in Engineering, 17*(3), 387-404.

Boljanović, S., & Maksimović, S. (2011). Analysis of the crack growth propagation process under mixed-mode loading. *Engineering Fracture Mechanics, 78*(8), 1565-1576. http://dx.doi.org/10.1016/j.engfracmech.2011.02.003

Borrego, L. P., Antunes, F. V., Costa, J. M., & Ferreira, J. M. (2006). Mixed-mode fatigue crack growth behaviour in aluminium alloy. *International Journal of Fatigue, 28*(5–6), 618-626. http://dx.doi.org/10.1016/j.ijfatigue.2005.07.047

Bowie, O. (1973). Solutions of plane crack problems by mapping technique *Methods of Analysis and Solutions of Crack Problems* (pp. 1-55): Springer

Branco, R., Costa, J. D., & Antunes, F. V. (2014). Fatigue behaviour and life prediction of lateral notched round bars under bending–torsion loading. *Engineering Fracture Mechanics, 119*, 66-84. http://dx.doi.org/10.1016/j.engfracmech.2014.02.009.

Brebbia, C. A., & Dominguez, J. (1996). *Boundary elements: an introductory course*: WIT press.

Buchholz, F. G., Chergui, A., & Richard, H. A. (2004). Fracture analyses and experimental results of crack growth under general mixed mode loading conditions. *Engineering Fracture Mechanics, 71*(4–6), 455-468. http://dx.doi.org/10.1016/S0013-7944(03)00015-8

Bueckner, H. (1971). Weight functions for the notched bar. *ZAMM-Journal of Applied Mathematics and Mechanics/Zeitschrift für Angewandte Mathematik und Mechanik, 51*(2), 97-109.

Carpinteri, A. (1992). Stress intensity factors for straight-fronted edge cracks in round bars. *Engineering Fracture Mechanics, 42*(6), 1035-1040. http://dx.doi.org/10.1016/0013-7944(92)90142-2

Carpinteri, A. (1993). Shape change of surface cracks in round bars under cyclic axial loading. *International Journal of Fatigue, 15*(1), 21-26. http://dx.doi.org/10.1016/0142-1123(93)90072-X

Carpinteri, A., & Brighenti, R. (1996a). Fatigue propagation of surface flaws in round bars: A three-parameter theoretical model. *Fatigue & Fracture of Engineering Materials & Structures, 19*(12), 1471-1480.

Carpinteri, A., & Brighenti, R. (1996b). Part-through cracks in round bars under cyclic combined axial and bending loading. *International Journal of Fatigue, 18*(1), 33-39. http://dx.doi.org/10.1016/0142-1123(95)00076-3

Carpinteri, A., De Freitas, M., & Spagnoli, A. (2003). *Biaxial/Multiaxial Fatigue and Fracture* (Vol. 31): Elsevier.

Carpinteri, A., & Vantadori, S. (2009). Sickle-shaped cracks in metallic round bars under cyclic eccentric axial loading. *International Journal of Fatigue, 31*(4), 759-765. http://dx.doi.org/10.1016/j.ijfatigue.2008.03.006

Chambers, A., Hyde, T., & Webster, J. (1991). Mixed mode fatigue crack growth at 550 C under plane stress conditions in Jethete M152. *Engineering Fracture Mechanics, 39*(3), 603-619.

Chang, J., Xu, J.-q., & Mutoh, Y. (2006). A general mixed-mode brittle fracture criterion for cracked materials. *Engineering Fracture Mechanics, 73*(9), 1249-1263. http://dx.doi.org/10.1016/j.engfracmech.2005.12.011.

Cheung, Y. K., Woo, C. W., & Wang, Y. H. (1989). Stress intensity factors for a circular arc crack by boundary collocation method. *Engineering Fracture Mechanics, 34*(4), 841-849. http://dx.doi.org/10.1016/0013-7944(89)90221-X.

Cisilino, A. P., & Aliabadi, M. H. (1999). Three-dimensional boundary element analysis of fatigue crack growth in linear and non-linear fracture problems. *Engineering Fracture Mechanics, 63*(6), 713-733. http://dx.doi.org/10.1016/S0013-7944(99)00047-8.

Cisilino, A. P., & Aliabadi, M. H. (2004). Dual boundary element assessment of three-dimensional fatigue crack growth. *Engineering Analysis with Boundary Elements, 28*(9), 1157-1173. http://dx.doi.org/10.1016/j.enganabound.2004.01.005.

Cisilino, A. P., & Ortiz, J. (2005). Boundary element analysis of three-dimensional mixed-mode cracks via the interaction integral. *Computer Methods in Applied Mechanics and Engineering, 194*(9–11), 935-956. http://dx.doi.org/10.1016/j.cma.2003.08.014.

Citarella, R. (2011). MSD crack propagation by DBEM on a repaired aeronautic panel. *Advances in Engineering Software, 42*(10), 887-901. http://dx.doi.org/10.1016/j.advengsoft.2011.02.014.

Citarella, R., & Buchholz, F. G. (2008). Comparison of crack growth simulation by DBEM and FEM for SEN-specimens undergoing torsion or bending loading. *Engineering Fracture Mechanics, 75*(3–4), 489-509. http://dx.doi.org/10.1016/j.engfracmech.2007.03.039.

Citarella, R., Carlone, P., Lepore, M., & Palazzo, G. S. (2015). Numerical–experimental crack growth analysis in AA2024-T3 FSWed butt joints. *Advances in Engineering Software, 80*(0), 47-57. http://dx.doi.org/10.1016/j.advengsoft.2014.09.018.

Citarella, R., & Cricrì, G. (2009). A two-parameter model for crack growth simulation by combined FEM–DBEM approach. *Advances in Engineering Software, 40*(5), 363-377. http://dx.doi.org/10.1016/j.advengsoft.2008.05.001.

Citarella, R., & Cricrì, G. (2010). Comparison of DBEM and FEM crack path predictions in a notched shaft under torsion. *Engineering Fracture Mechanics, 77*(11), 1730-1749. http://dx.doi.org/10.1016/j.engfracmech.2010.03.012.

Citarella, R., Cricrì, G., Lepore, M., & Perrella, M. (2014). Thermo-mechanical crack propagation in aircraft engine vane by coupled FEM–DBEM approach. *Advances in Engineering Software, 67*(0), 57-69. http://dx.doi.org/10.1016/j.advengsoft.2013.07.006.

Citarella, R., Lepore, M., Shlyannikov, V., & Yarullin, R. (2014). Fatigue surface crack growth in cylindrical specimen under combined loading. *Engineering Fracture Mechanics, 131*(0), 439-453. http://dx.doi.org/10.1016/j.engfracmech.2014.08.017.

Couroneau, N., & Royer, J. (1998). Simplified model for the fatigue growth analysis of surface cracks in round bars under mode I. *International Journal of Fatigue, 20*(10), 711-718. http://dx.doi.org/10.1016/S0142-1123(98)00037-1

Couroneau, N., & Royer, J. (2000). Simplifying hypotheses for the fatigue growth analysis of surface cracks in round bars. *Computers & Structures, 77*(4), 381-389. http://dx.doi.org/10.1016/S0045-7949(00)00030-4

Crouch, S. L., Starfield, A. M., & Rizzo, F. (1983). Boundary element methods in solid mechanics. *Journal of Applied Mechanics, 50,* 704.

Cruse, T. (1972). Numerical evaluation of elastic stress intensity factors by the boundary-integral equation method. Retrieved from http://trid.trb.org

Cruse, T. (1975). Boundary-Integral Equation Method for Three-Dimensional Elastic Fracture Mechanics Analysis: DTIC Document.

Dao, N. H., & Sellami, H. (2012). Stress intensity factors and fatigue growth of a surface crack in a drill pipe during rotary drilling operation. *Engineering Fracture Mechanics, 96*(0), 626-640. http://dx.doi.org/10.1016/j.engfracmech.2012.09.025

Dhondt, G. (2014). Application of the Finite Element Method to mixed-mode cyclic crack propagation calculations in specimens. *International Journal of Fatigue, 58*(0), 2-11. http://dx.doi.org/10.1016/j.ijfatigue.2013.05.001

Ding, F., Zhao, T., & Jiang, Y. (2007). A study of fatigue crack growth with changing loading direction. *Engineering Fracture Mechanics, 74*(13), 2014-2029. http://dx.doi.org/10.1016/j.engfracmech.2006.10.013.

Dirgantara, T., & Aliabadi, M. (2002). Numerical simulation of fatigue crack growth in pressurized shells. *International Journal of Fatigue, 24*(7), 725-738.

Doquet, V., Bui, Q.-H., Bertolino, G., Merhy, E., & Alves, L. (2010). 3D shear-mode fatigue crack growth in maraging steel and Ti-6Al-4V. *International Journal of Fracture, 165*(1), 61-76.

Doquet, V., & Pommier, S. (2004). Fatigue crack growth under non-proportional mixed-mode loading in ferritic-pearlitic steel. *Fatigue & Fracture of Engineering Materials & Structures, 27*(11), 1051-1060.

Dugdale, D. (1960). Yielding of steel sheets containing slits. *Journal of the Mechanics and Physics of Solids, 8*(2), 100-104.

Džupon, M., Falat, L., Slota, J., & Hvizdoš, P. (2013). Failure analysis of overhead power line yoke connector. *Engineering Failure Analysis, 33*, 66-74. doi: http://dx.doi.org/10.1016/j.engfailanal.2013.04.024

Elbert, W. (1971). The significance of fatigue crack closure. *ASTM STP, 486*, 230-243.

Erdogan, F., & Sih, G. (1963). On the crack extension in plates under plane loading and transverse shear. *Journal of basic engineering, 85*(4), 519-525.

Farris, T., & Liu, M. (1993). Boundary element crack closure calculation of three-dimensional stress intensity factors. *International Journal of Fracture, 60*(1), 33-47.

Faqian, L., Shuanlu, L., Helin, L., Changyi, Q., Jie, Z., Jiping, T., & Jun, C. (2007). Analysis of causes of casing elevator fracture. *Engineering Failure Analysis, 14*(4), 606-613. doi: http://dx.doi.org/10.1016/j.engfailanal.2006.03.012

Fawaz, S. (1998). Application of the virtual crack closure technique to calculate stress intensity factors for through cracks with an elliptical crack front. *Engineering Fracture Mechanics, 59*(3), 327-342.

Fischer-Cripps, A. C. (2007). Linear Elastic Fracture Mechanics. *Introduction to Contact Mechanics*, 31-48.

Fonte, M., Reis, L., Romeiro, F., Li, B., & Freitas, M. (2006). The effect of steady torsion on fatigue crack growth in shafts. *International Journal of Fatigue, 28*(5–6), 609-617. http://dx.doi.org/10.1016/j.ijfatigue.2005.06.051

Fonte, M., Gomes, E., & de Freitas, M. (1999). Stress intensity factors for semi-elliptical surface cracks in round bars subjected to mode I (bending) and mode III (torsion) loading. In W. B. E. Macha & T. Łagoda (Eds.), *European Structural Integrity Society* (Vol. Volume 25, pp. 249-260): Elsevier

Forman, R. G., & Mettu, S. R. (1990). Behavior of surface and corner cracks subjected to tensile and bending loads in Ti-6Al-4V alloy. NASA technical memorandum.

Forman, R. (1972). Study of fatigue crack initiation from flaws using fracture mechanics theory. *Engineering Fracture Mechanics, 4*(2), 333-345.

Forth, S. C., Favrow, L. H., Keat, W. D., & Newman, J. A. (2003). Three-dimensional mixed-mode fatigue crack growth in a functionally graded titanium alloy. *Engineering Fracture Mechanics, 70*(15), 2175-2185. http://dx.doi.org/10.1016/S0013-7944(02)00237-0

Fremy, F., Pommier, S., Galenne, E., Courtin, S., & Le Roux, J.-C. (2014b). Load path effect on fatigue crack propagation in I+II+III mixed mode conditions – Part 2: Finite element analyses. *International Journal of Fatigue, 62*(0), 113-118.

Fremy, F., Pommier, S., Poncelet, M., Raka, B., Galenne, E., Courtin, S., & Roux, J.-C. L. (2014a). Load path effect on fatigue crack propagation in I+II+III mixed mode conditions – Part 1: Experimental investigations. *International Journal of Fatigue, 62*(0), 104-112.

Griffith, A. (1920). VI. The Phenomena of Rupture and F low in Solids. *Phil. Trans. Roy. Soc.(Lon.) A, 221*, 163-198.

Gross, B., Srawley, J. E., & Brown Jr, W. F. (1964). Stress-intensity factors for a single-edge-notch tension specimen by boundary collocation of a stress function: DTIC Document.

Hallbäck, N., & Nilsson, F. (1994). Mixed-mode I/II fracture behaviour of an aluminium alloy. *Journal of the Mechanics and Physics of Solids, 42*(9), 1345-1374. http://dx.doi.org/10.1016/0022-5096(94)90001-9

Hartranft, R., & Sih, G. C. (1972). Alternating method applied to edge and surface crack problems. NASA-TR-72-1, Lehigh University.

He, M. Y., & Hutchinson, J. W. (2000). Surface crack subject to mixed mode loading. *Engineering Fracture Mechanics, 65*(1), 1-14. http://dx.doi.org/10.1016/S0013-7944(99)00129-0

Hellen, T. (1975). On the method of virtual crack extensions. *International Journal for Numerical Methods in Engineering, 9*(1), 187-207.

Hellen, T., & Blackburn, W. (1975). The calculation of stress intensity factors for combined tensile and shear loading. *International Journal of Fracture, 11*(4), 605-617.

Hellier, A. K., Corderoy, D. J. H., & McGirr, M. B. (1987). A practical mixed Mode II/III fatigue test rig. *International Journal of Fatigue, 9*(2), 95-101. http://dx.doi.org/10.1016/0142-1123(87)90050-8

Hussain, M., Pu, S., & Underwood, J. (1974). Strain Energy Release Rate for a Crack Under Combined Mode I and Mode. *Fracture analysis, 560*(1).

Hübner, P., Zerbst, U., Berger, M., & Brecht, T. (2009). The fracture of a wobbler in a heavy plate mill. *Engineering Failure Analysis, 16*(4), 1097-1108. doi: http://dx.doi.org/10.1016/j.engfailanal.2008.06.021

Iida, S., & Kobayashi, A. S. (1969). Crack-propagation rate in 7075-T6 plates under cyclic tensile and transverse shear loadings. *Journal of Fluids Engineering, 91*(4), 764-769.

Ilman, M. N., & Barizy, R. A (2015). Failure analysis and fatigue performance evaluation of a failed connecting rod of reciprocating air compressor. *Engineering Failure Analysis*(0). doi: http://dx.doi.org/10.1016/j.engfailanal.2015.03.010

Inglis, C. (1913). Stresses in a cracked plate due to the presence of cracks and sharp corners. *Transaction of Naval Architects (London), 60*, 213.

Irwin, G. R. (1948). Fracture dynamics. *Fracturing of metals, 152*.

Irwin, G. R. (1956). *Onset of fast crack propagation in high strength steel and aluminum.* Paper presented at the Proc. Sec. Sagamore Conf.

Irwin, G. R., & Paris, P. (1960). Proceedings of the 7th Sagamore Ordnance Materials Research Conference. *Syracuse University Research Institute, August*, 661-611.

Irwin, G. R. (1957). Analysis of stresses and strains near the end of a crack traversing a plate. *J. appl. Mech.*

Ishikawa, H. (1980). A finite element analysis of stress intensity factors for combined tensile and shear loading by only a virtual crack extension. *International Journal of Fracture, 16*(5), R243-R246.

Isida, M. (1973). Method of Laurent series expansion for internal crack problems *Methods of analysis and solutions of crack problems* (pp. 56-130): Springer

Ismail, A. E., Ariffin, A. K., Abdullah, S., & Ghazali, M. J. (2011). Stress intensity factors for surface cracks in round bar under single and combined loadings. *Meccanica, 47*(5), 1141-1156. doi: 10.1007/s11012-011-9500-7

Karami, G., & Fenner, R. (1986). Analysis of mixed mode fracture and crack closure using the boundary integral equation method. *International Journal of Fracture, 30*(1), 13-29.

Kramberger, J., Šraml, M., Potrč, I., & Flašker, J. (2004). Numerical calculation of bending fatigue life of thin-rim spur gears. *Engineering Fracture Mechanics, 71*(4–6), 647-656. http://dx.doi.org/10.1016/S0013-7944(03)00024-9

Lan, W., Deng, X., & Sutton, M. A. (2007). Three-dimensional finite element simulations of mixed-mode stable tearing crack growth experiments. *Engineering Fracture Mechanics, 74*(16), 2498-2517. http://dx.doi.org/10.1016/j.engfracmech.2006.12.026

Lazarus, V., & Leblond, J. B. (1998). Propagation de fissures en mode mixte (I + III) ou (I + II + III). *Comptes Rendus de l'Académie des Sciences - Series IIB - Mechanics-Physics-Chemistry-Astronomy, 326*(3), 171-177. http://dx.doi.org/10.1016/S1251-8069(99)89004-6

Lazarus, V., Leblond, J. B., & Mouchrif, S. E. (2001a). Crack front rotation and segmentation in mixed mode I+III or I+II+III. Part I: Calculation of stress intensity factors. *Journal of the Mechanics and Physics of Solids, 49*(7), 1399-1420.

Lazarus, V., Leblond, J. B., & Mouchrif, S. E. (2001b). Crack front rotation and segmentation in mixed mode I+III or I+II+III. Part II: Comparison with experiments. *Journal of the Mechanics and Physics of Solids, 49*(7), 1421-1443. http://dx.doi.org/10.1016/S0022-5096(01)00008-4

Leblond, J., & Amestoy, M. (2013). *The stress intensity factors at the tip of a kinked and curved crack.* Paper presented at the ICF7, Houston (USA) 1989.

Li, C. (1989). Vector CTD criterion applied to mixed mode fatigue crack growth. *Fatigue & Fracture of Engineering Materials & Structures, 12*(1), 59-65.

Li, F. Z., Shih, C. F., & Needleman, A. (1985). A comparison of methods for calculating energy release rates. *Engineering Fracture Mechanics, 21*(2), 405-421.

Lin, X. B., & Smith, R. A. (1997). Shape growth simulation of surface cracks in tension fatigued round bars. *International Journal of Fatigue, 19*(6), 461-469. http://dx.doi.org/10.1016/S0142-1123(97)00012-1

Lin, X. B., & Smith, R. A. (1998). Fatigue growth simulation for cracks in notched and unnotched round bars. *International Journal of Mechanical Sciences, 40*(5), 405-419. http://dx.doi.org/10.1016/S0020-7403(97)00039-8

Liu, S., Chao, Y. J., & Zhu, X. (2004). Tensile-shear transition in mixed mode I/III fracture. *International Journal of Solids and Structures, 41*(22), 6147-6172.

Liu. A. F. (1998). *Structural Life Assessment Methods*. USA: ASM International.

Liu, S., & Duan, S. (2014). Analytical solutions of cracks emanating from an elliptical hole under shear. *Chinese Journal of Aeronautics, 27*(4), 829-834. http://dx.doi.org/10.1016/j.cja.2014.06.007

Mageed, A. M., & Pandey, R. K. (1992). Studies on cyclic crack path and the mixed-mode crack closure behaviour in Al alloy. *International Journal of Fatigue, 14*(1), 21-29. http://dx.doi.org/10.1016/0142-1123(92)90149-7.

Mahajan, R., & Ravi-Chandar, K. (1989). Experimental determination of stress-intensity factors using caustics and photoelasticity. *Experimental mechanics, 29*(1), 6-11.

Maligno, A. R., Rajaratnam, S., Leen, S. B., & Williams, E. J. (2010). A three-dimensional (3D) numerical study of fatigue crack growth using remeshing techniques. *Engineering Fracture Mechanics, 77*(1), 94-111. http://dx.doi.org/10.1016/j.engfracmech.2009.09.017

Mellings, S., Baynham, J., & Adey, R. A. (2005). Automatic crack growth prediction in rails with BEM. *Engineering Fracture Mechanics, 72*(2), 309-318. http://dx.doi.org/10.1016/j.engfracmech.2004.04.013

Mi, Y. (1995). *Three dimensional dual boundary element analysis of crack growth.* University of Portsmouth.

Mi, Y., & Aliabadi, M. (1992). Dual boundary element method for three-dimensional fracture mechanics analysis. *Engineering Analysis with Boundary Elements, 10*(2), 161-171.

Mikheevskiy, S., Glinka, G., & Algera, D. (2012). Analysis of fatigue crack growth in an attachment lug based on the weight function technique and the UniGrow fatigue crack growth model. *International Journal of Fatigue, 42*(0), 88-94. http://dx.doi.org/10.1016/j.ijfatigue.2011.07.006

Misak, H. E., Perel, V. Y., Sabelkin, V., & Mall, S. (2013). Crack growth behavior of 7075-T6 under biaxial tension–tension fatigue. *International Journal of Fatigue, 55*(0), 158-165. http://dx.doi.org/10.1016/j.ijfatigue.2013.06.003

Moghaddam, A. S., Alfano, M., & Ghajar, R. (2013). Determining the mixed mode stress intensity factors of surface cracks in functionally graded hollow cylinders. *Materials & Design, 43*(0), 475-484. http://dx.doi.org/10.1016/j.matdes.2012.07.027

Morais, A. B. (2007). Calculation of stress intensity factors by the force method. *Engineering Fracture Mechanics, 74*(5), 739-750. http://dx.doi.org/10.1016/j.engfracmech.2006.06.017

Mousavi zadeh Noughabi, S. M., Dehghani, K., & Pouranvari, M. (2007). Failure analysis of automatic coupler SA-3 in railway carriages. *Engineering Failure Analysis, 14*(5), 903-912. doi: http://dx.doi.org/10.1016/j.engfailanal.2006.11.039

Muskhelishvili, N. I. (1977). *Some basic problems of the mathematical theory of elasticity*: Springer Science & Business Media.

Mukhopadhyay, N. K., Maiti, S. K., & Kakodkar, A. (2000). A review of SIF evaluation and modelling of singularities in BEM. *Computational Mechanics, 25*(4), 358-375.

Naresh, S., Naik, B., Madhu, S., & Mohan, A. (2013). Computational Analysis of Stress Intensity Factor for a Quarter Circular Edge Crack under Mode-I loading. *Research Journal of Engineering Sciences, 2*(7),38-42.

Newman, J., & Raju, I. (1981). An empirical stress-intensity factor equation for the surface crack. *Engineering Fracture Mechanics, 15*(1), 185-192.

Newman, J., & Raju, I. (1983). Stress-intensity factor equations for cracks in three-dimensional finite bodies. *ASTM STP*, *791*, 238-265.

Newman Jr, J., & Raju, I. (1986). Stress-intensity factor equations for cracks in three-dimensional finite bodies subjected to tension and bending loads. *Computational methods in the mechanics of fracture*, *2*(S N), 312-334.

Nobile, L. (2000). Mixed mode crack initiation and direction in beams with edge crack. *Theoretical and Applied Fracture Mechanics*, *33*(2), 107-116.

Noda, N. A., & Takase, Y. (2003). Generalized stress intensity factors of V-shaped notch in a round bar under torsion, tension and bending. *Engineering Fracture Mechanics*, *70*(11), 1447-1466. http://dx.doi.org/10.1016/S0013-7944(02)00115-7

Okada, H., Kawai, H., Tokuda, T., & Fukui, Y. (2013). Fully automated mixed mode crack propagation analyses based on tetrahedral finite element and VCCM (virtual crack closure-integral method). *International Journal of Fatigue*, *50*(0), 33-39. http://dx.doi.org/10.1016/j.ijfatigue.2012.04.009

Orowan, E. (1949). Fracture and strength of solids. *Rep. Prog. Phys*, *12*, 185-232.

Ortiz, J. E., Mantič, V., & París, F. (2006). A domain-independent integral for computation of stress intensity factors along three-dimensional crack fronts and edges by BEM. *International Journal of Solids and Structures*, *43*(18–19), 5593-5612. http://dx.doi.org/10.1016/j.ijsolstr.2005.08.003

Paris, P. C., Gomez, M. P., & Anderson, W. E. (1961). A rational analytic theory of fatigue. *The trend in engineering*, *13*(1), 9-14.

Paul, T. K. (1995). Plane stress mixed mode fatigue crack propagation. *Engineering Fracture Mechanics*, *52*(1), 121-137. http://dx.doi.org/10.1016/0013-7944(94)00256-H

Pirondi, A. (2003). Suitability of mixed-mode I/II assessment methods for implementation into the SINTAP procedure. *Engineering Fracture Mechanics*, *70*(13), 1597-1609.

Pokluda, J., Trattnig, G., Martinschitz, C., & Pippan, R. (2008). Straightforward comparison of fatigue crack growth under modes II and III. *International Journal of Fatigue*, *30*(8), 1498-1506. http://dx.doi.org/10.1016/j.ijfatigue.2007.09.009

Pons, A. J., & Karma, A. (2010). Helical crack-front instability in mixed-mode fracture. *Nature, 464*(7285), 85-89.

Pook, L. P. (1985). The fatigue crack direction and threshold behaviour of mild steel under mixed mode I and III loading. *International Journal of Fatigue, 7*(1), 21-30. http://dx.doi.org/10.1016/0142-1123(85)90004-0

Portela, A., Aliabadi, M., & Rooke, D. (1992). The dual boundary element method: effective implementation for crack problems. *International Journal for Numerical Methods in Engineering, 33*(6), 1269-1287.

Prasad, N., Aliabadi, M., & Rooke, D. (1994). The dual boundary element method for thermoelastic crack problems. *International Journal of Fracture, 66*(3), 255-272.

Predan, J., Močilnik, V., & Gubeljak, N. (2013). Stress intensity factors for circumferential semi-elliptical surface cracks in a hollow cylinder subjected to pure torsion. *Engineering Fracture Mechanics, 105*(0), 152-168. http://dx.doi.org/10.1016/j.engfracmech.2013.03.033

Purbolaksono, J., Ali, A. A., Khinani, A., & Rashid, A. Z. (2009). Evaluation of stress intensity factors for multiple surface cracks in bi-material tubes. *Engineering Analysis with Boundary Elements, 33*(11), 1339-1343. http://dx.doi.org/10.1016/j.enganabound.2009.05.004

Qian, J., & Fatemi, A. (1996). Mixed mode fatigue crack growth: a literature survey. *Engineering Fracture Mechanics, 55*(6), 969-990.

Raju, I., & Newman, J. (1986). Stress-intensity factors for circumferential surface cracks in pipes and rods under tension and bending loads. *ASTM special technical publication*(905), 789-805.

Raju, I., & Newman Jr, J. (1988). *Stress-intensity factors for corner cracks in rectangular bars.* Paper presented at the Fracture Mechanics: Nineteenth Symposium, ASTM STP.

Rice, J. R. (1968). A path independent integral and the approximate analysis of strain concentration by notches and cracks. *Journal of Applied Mechanics, 35*(2), 379-386.

Richard, H., & Benitz, K. (1983). A loading device for the creation of mixed mode in fracture mechanics. *International Journal of Fracture, 22*(2), R55-R58.

Richard, H. A. (1989). Specimens for investigating biaxial fracture and fatigue processes. *Biaxial and Multiaxial Fatigue*, ed. M. W. Brown and K. J. Miller. Mechanical Engineering Publication, London, 217-229.

Richard, H., Fulland, M., & Sander, M. (2005). Theoretical crack path prediction. *Fatigue & Fracture of Engineering Materials & Structures, 28*(1-2), 3-12.

Richard, H. A., Schramm, B., & Schirmeisen, N. H. (2014). Cracks on Mixed Mode loading – Theories, experiments, simulations. *International Journal of Fatigue, 62*(0), 93-103.

Rozumek, D., & Marciniak, Z. (2012). The investigation of crack growth in specimens with rectangular cross-sections under out-of-phase bending and torsional loading. *International Journal of Fatigue, 39*(0), 81-87. http://dx.doi.org/10.1016/j.ijfatigue.2011.02.013

Rybicki, E. F., & Kanninen, M. (1977). A finite element calculation of stress intensity factors by a modified crack closure integral. *Engineering Fracture Mechanics, 9*(4), 931-938.

Sarangi, H., Murthy, K., & Chakraborty, D. (2012). Optimum strain gage locations for accurate determination of the mixed mode stress intensity factors. *Engineering Fracture Mechanics, 88*, 63-78.

Schijve, J. (1981). Some formulas for the crack opening stress level. *Engineering Fracture Mechanics, 14*(3), 461-465. http://dx.doi.org/10.1016/0013-7944(81)90034-5

Seo, K.-J., Choi, B.-H., Lee, J.-M., & Shin, S.-M. (2010). Investigation of the mixed-mode fatigue crack growth of a hot-rolled steel plate with a circular microdefect. *International Journal of Fatigue, 32*(7), 1190-1199. http://dx.doi.org/10.1016/j.ijfatigue.2009.12.015

Sha, G. T. (1984). On the virtual crack extension technique for stress intensity factors and energy release rate calculations for mixed fracture mode. *International Journal of Fracture, 25*(2), R33-R42.

Shah, R. (1974). Fracture under combined modes in 4340 steel. *ASTM STP, 560*, 29-52.

Shahani, A., & Tabatabaei, S. (2008). Computation of mixed mode stress intensity factors in a four-point bend specimen. *Applied Mathematical Modelling, 32*(7), 1281-1288.

Shahani, A. R., & Habibi, S. E. (2007). Stress intensity factors in a hollow cylinder containing a circumferential semi-elliptical crack subjected to combined loading. *International Journal of Fatigue, 29*(1), 128-140. http://dx.doi.org/10.1016/j.ijfatigue.2006.01.017

Shanyavskiy, A. (2011). Fatigue cracking simulation based on crack closure effects in Al-based sheet materials subjected to biaxial cyclic loads. *Engineering Fracture Mechanics, 78*(8), 1516-1528. http://dx.doi.org/10.1016/j.engfracmech.2011.01.019

Shi, H. J., Niu, L. S., Mesmacque, G., & Wang, Z. G. (2000). Branched crack growth behavior of mixed-mode fatigue for an austenitic 304L steel. *International Journal of Fatigue, 22*(6), 457-465. doi: http://dx.doi.org/10.1016/S0142-1123(00)00027-X

Shi, X., Zhang, X., & Pang, J. (2006). Determination of interface fracture toughness of adhesive joint subjected to mixed-mode loading using finite element method. *International Journal of Adhesion and Adhesives, 26*(4), 249-260.

Shih, C., Moran, B., & Nakamura, T. (1986). Energy release rate along a three-dimensional crack front in a thermally stressed body. *International Journal of Fracture, 30*(2), 79-102.

Shih, Y.-S., & Chen, J.-J. (2002). The stress intensity factor study of an elliptical cracked shaft. *Nuclear Engineering and Design, 214*(1–2), 137-145. doi: http://dx.doi.org/10.1016/S0029-5493(02)00022-5

Shin, C., & Cai, C. (2004). Experimental and finite element analyses on stress intensity factors of an elliptical surface crack in a circular shaft under tension and bending. *International Journal of Fracture, 129*(3), 239-264.

Shin, C. S., & Cai, C. Q. (2007). Evaluating fatigue crack propagation properties using a cylindrical rod specimen. *International Journal of Fatigue, 29*(3), 397-405. http://dx.doi.org/10.1016/j.ijfatigue.2006.06.006

Shin, C. S., & Cai, C. Q. (2008). Surface fatigue crack growth suppression in cylindrical rods by artificial infiltration. *International Journal of Fatigue, 30*(3), 560-567. http://dx.doi.org/10.1016/j.ijfatigue.2007.03.005

Shivakumar, K., & Raju, I. (1992). An equivalent domain integral method for three-dimensional mixed-mode fracture problems. *Engineering Fracture Mechanics, 42*(6), 935-959.

Shivakumar, K., Tan, P., & Newman, J. (1988). A virtual crack-closure technique for calculating stress intensity factors for cracked three dimensional bodies. *International Journal of Fracture, 36*(3), R43-R50.

Sih, G., & Barthelemy, B. (1980). Mixed mode fatigue crack growth predictions. *Engineering Fracture Mechanics, 13*(3), 439-451.

Sih, G., & Macdonald, B. (1974). Fracture mechanics applied to engineering problems-strain energy density fracture criterion. *Engineering Fracture Mechanics, 6*(2), 361-386.

Singh, V. K., & Gope, P. C. (2013). Experimental Evaluation of Mixed Mode Stress Intensity Factor for Prediction of Crack Growth by Phoelastic Method. *Journal of failure analysis and prevention, 13*(2), 217-226.

Slámečka, K., Ponížil, P., & Pokluda, J. (2007). Quantitative fractography in bending-torsion fatigue. *Materials Science and Engineering: A, 462*(1–2), 359-362. http://dx.doi.org/10.1016/j.msea.2006.03.153

Smith, D. J., Swankie, T. D., Pavier, M. J., & Smith, M. C. (2008). The effect of specimen dimensions on mixed mode ductile fracture. *Engineering Fracture Mechanics, 75*(15), 4394-4409. http://dx.doi.org/10.1016/j.engfracmech.2008.04.005

Sneddon, I. N. (1975). *Application of integral transforms in the theory of elasticity*: Springer Wien.

Snyder, M., & Cruse, T. (1975). Boundary-integral equation analysis of cracked anisotropic plates. *International Journal of Fracture, 11*(2), 315-328.

Socie, D., Hua, C., & Worthem, D. (1987). Mixed mode small crack growth. *Fatigue & Fracture of Engineering Materials & Structures, 10*(1), 1-16.

Soh, A. K., & Bian, L. C. (2001). Mixed mode fatigue crack growth criteria. *International Journal of Fatigue, 23*(5), 427-439. http://dx.doi.org/10.1016/S0142-1123(00)00105-5

Song, S. H., & Lee, J. M. (2003). Fatigue crack propagation behavior in STS304 under mixed-mode loading. *KSME international journal, 17*(6), 796-804.

Souiyah, M., Alshoaibi, A., Muchtar, A., & Ariffin, A. (2008). Finite element model for linear-elastic mixed mode loading using adaptive mesh strategy. *Journal of Zhejiang University SCIENCE A, 9*(1), 32-37.

Sujata, M., Venkataswamy, M. A., Parameswara, M. A., & Bhaumik, S. K. (2006). Failure analysis of conveyor chain links. *Engineering Failure Analysis, 13*(6), 914-924. doi: http://dx.doi.org/10.1016/j.engfailanal.2005.07.002

Sutton, M. A., Helm, J. D., & Boone, M. L. (2001). Experimental study of crack growth in thin sheet 2024-T3 aluminum under tension-torsion loading. *International Journal of Fracture, 109*(3), 285-301.

Tada, H., Paris, P., & Irwin, G. (2000). *The analysis of cracks handbook*: New York: ASME Press.

Tan, C., & Fenner, R. (1979). Elastic fracture mechanics analysis by the boundary integral equation method. *Proceedings of the Royal Society of London. A. Mathematical and Physical Sciences, 369*(1737), 243-260.

Tan, P., Newman, J., & Bigelow, C. (1996). Three-dimensional finite-element analyses of corner cracks at stress concentrations. *Engineering Fracture Mechanics, 55*(3), 505-512.

Tanaka, K. (1974). Fatigue crack propagation from a crack inclined to the cyclic tensile axis. *Engineering Fracture Mechanics, 6*(3), 493-507.

Tanaka, K. (2014). Crack initiation and propagation in torsional fatigue of circumferentially notched steel bars. *International Journal of Fatigue, 58*(0), 114-125. http://dx.doi.org/10.1016/j.ijfatigue.2013.01.002

Tanaka, K., Takahash, H., & Akiniwa, Y. (2006). Fatigue crack propagation from a hole in tubular specimens under axial and torsional loading. *International Journal of Fatigue, 28*(4), 324-334. http://dx.doi.org/10.1016/j.ijfatigue.2005.08.001

Tarpani, J. R., Ruckert, C. O. F. T., Milan, M. T., Silva, R. V., Rosato Jr, A., Pereira, R. N.,Spinelli, D. (2004). Estimating fatigue life under variable amplitude loading through quantitative fractography – A case study. *Engineering Failure Analysis, 11*(4), 547-559. http://dx.doi.org/10.1016/j.engfailanal.2003.09.004

Thompson, K., & Sheppard, S. (1992). Fatigue crack growth in notched and plain shafts subjected to torsion and axial loading. *Engineering Fracture Mechanics, 43*(1), 55-71.

Tong, P., Mau, S., & Pian, T. (1974). Derivation of geometric stiffness and mass matrices for finite element hybrid models. *International Journal of Solids and Structures, 10*(8), 919-932.

Toribio, J., Matos, J. C., González, B., & Escuadra, J. (2009). Numerical modelling of crack shape evolution for surface flaws in round bars under tensile loading. *Engineering Failure Analysis, 16*(2), 618-630. http://dx.doi.org/10.1016/j.engfailanal.2008.02.014

Toribio, J., Matos, J. C., González, B., & Escuadra, J. (2011). Compliance evolution in round cracked bars under tensile fatigue. *Engineering Fracture Mechanics, 78*(18), 3243-3252. http://dx.doi.org/10.1016/j.engfracmech.2011.09.013

Toribio, J., Matos, J. C., González, B., & Escuadra, J. (2014). Numerical modelling of cracking path in round bars subjected to cyclic tension and bending. *International Journal of Fatigue, 58*(0), 20-27. http://dx.doi.org/10.1016/j.ijfatigue.2013.03.017

Tracey, D. M. (1971). Finite elements for determination of crack tip elastic stress intensity factors. *Engineering Fracture Mechanics, 3*(3), 255-265. http://dx.doi.org/10.1016/0013-7944(71)90036-1

Valvo, P. S. (2014). A Physically Consistent Virtual Crack Closure Technique for I/II/III Mixed-mode Fracture Problems. *Procedia Materials Science, 3*, 1983-1987.

Varfolomeev, I., Burdack, M., Moroz, S., Siegele, D., & Kadau, K. (2014). Fatigue crack growth rates and paths in two planar specimens under mixed mode loading. *International Journal of Fatigue, 58*(0), 12-19. http://dx.doi.org/10.1016/j.ijfatigue.2013.04.013

Vojtek, T., Pokluda, J., Šandera, P., Horníková, J., Hohenwarter, A., & Pippan, R. (2014). Analysis of fatigue crack propagation under mixed mode II+III in ARMCO iron. *International Journal of Fatigue.* http://dx.doi.org/10.1016/j.ijfatigue.2014.09.018

Walker, K. (1970). The effect of stress ratio during crack propagation and fatigue for 2024-T3 and 7075-T6 aluminum. *Effects of environment and complex load history on fatigue life, ASTM STP, 462*, 1-14.

Wei, Z., Deng, X., Sutton, M. A., Yan, J., Cheng, C. S., & Zavattieri, P. (2011). Modeling of mixed-mode crack growth in ductile thin sheets under combined in-plane and out-of-plane loading. *Engineering Fracture Mechanics, 78*(17), 3082-3101. http://dx.doi.org/10.1016/j.engfracmech.2011.09.004

Wells, A. A. (1961). *Unstable crack propagation in metals: cleavage and fast fracture.* Paper presented at the Proceedings of the crack propagation symposium.

Wessel, C., Cisilino, A., Santi, O., Otegui, J., & Chapetti, M. (2001). Numerical and experimental determination of three-dimensional multiple crack growth in fatigue. *Theoretical and Applied Fracture Mechanics, 35*(1), 47-58. http://dx.doi.org/10.1016/S0167-8442(00)00048-3

Westergaard, H. (1939). Bearing Pressures and Cracks. *Journal of Applied Mechanics,* 49-53.

Wilde, A., & Aliabadi, M. (1999). A 3-D Dual BEM formulation for the analysis of crack growth. *Computational mechanics, 23*(3), 250-257.

Wilson, W. (1973). Finite element methods for elastic bodies containing cracks *Methods of analysis and solutions of crack problems* (pp. 484-515): Springer

Wolf, E. (1970). Fatigue crack closure under cyclic tension. *Engineering Fracture Mechanics, 2*(1), 37-45.

Woo, C., Cheung, Y., & Wang, Y. (2013). *J-integral calculation by using collocation method and elasto-viscoplastic theory.* Paper presented at the ICF7, Houston (USA) 1989.

Wu, L., Zhang, L., & Guo, Y. (2012). Extended finite element method for computation of mixed-mode stress intensity factors in three dimensions. *Procedia Engineering, 31,* 373-380.

Xiao, Q., Karihaloo, B., & Liu, X. (2004). Direct determination of SIF and higher order terms of mixed mode cracks by a hybrid crack element. *International Journal of Fracture, 125*(3-4), 207-225.

Yan, X. (2006a). A boundary element modeling of fatigue crack growth in a plane elastic plate. *Mechanics Research Communications, 33*(4), 470-481.

Yan, X. (2006). Numerical analysis of the stress intensity factor for two kinds of mixed-mode crack specimens. *The Journal of Strain Analysis for Engineering Design, 41*(1), 9-18.

Yan, X. (2006b). Stress intensives and propagation of mixed-mode cracks. *Engineering Failure Analysis, 13*(6), 1022-1027. http://dx.doi.org/10.1016/j.engfailanal.2005.04.007

Yan, X. (2007). Automated simulation of fatigue crack propagation for two-dimensional linear elastic fracture mechanics problems by boundary element method. *Engineering Fracture Mechanics, 74*(14), 2225-2246. http://dx.doi.org/10.1016/j.engfracmech.2006.10.020

Yang, F., Kuang, Z., & Shlyannikov, V. N. (2006). Fatigue crack growth for straight-fronted edge crack in a round bar. *International Journal of Fatigue, 28*(4), 431-437. http://dx.doi.org/10.1016/j.ijfatigue.2005.07.036

Yang, S., Ni, Y. L., & Li, C.-Q. (2013). Weight function method to determine stress intensity factor for semi-elliptical crack with high aspect ratio in cylindrical vessels. *Engineering Fracture Mechanics, 109*, 138-149.

Yang, Z. M., Lie, S. T., & Gho, W. M. (2007). Fatigue crack growth analysis of a square hollow section T-joint. *Journal of Constructional Steel Research, 63*(9), 1184-1193. http://dx.doi.org/10.1016/j.jcsr.2006.11.013

Yates, J. R., & Mohammed, R. A. (1996). The determination of fatigue crack propagation rates under mixed mode (I+III) loading. *International Journal of Fatigue, 18*(3), 197-203. http://dx.doi.org/10.1016/0142-1123(96)00110-7

Zeng, Z., & Fatemi, A. (2001). Elasto-plastic stress and strain behaviour at notch roots under monotonic and cyclic loadings. *The Journal of Strain Analysis for Engineering Design, 36*(3), 287-300.

Zhang, R., & He, L. (2012). Measurement of mixed-mode stress intensity factors using digital image correlation method. *Optics and Lasers in Engineering, 50*(7), 1001-1007.

Zhang, X. B., Ma, S., Recho, N., & Li, J. (2006). Bifurcation and propagation of a mixed-mode crack in a ductile material. *Engineering Fracture Mechanics, 73*(13), 1925-1939. http://dx.doi.org/10.1016/j.engfracmech.2005.12.013

LIST OF PUBLICATIONS

1. Fatigue crack growth of a corner crack in a square prismatic bar under combined cyclic torsion-tension loading.
   (*International Journal of Fatigue*, 64, 2014, 67-73)

2. Fatigue growth of a surface crack in a V-shaped nothed round bar under cyclic tension.
   (*Journal of Zhejiang University-SCIENCE A*, 2014, 15 (11): 873-882)

3. Fatigue growth analysis of a surface crack in a solid cylinder under combined cyclic axial-torsion loading.
   (Paper has been accepted for publication in *Experimental Techniques*)